



A universe of sky and snow: site-testing for optical astronomy at Dome C, Antarctica

Author:

Kenyon, Suzanne Laura

Publication Date:

2007

DOI:

<https://doi.org/10.26190/unsworks/6656>

License:

<https://creativecommons.org/licenses/by-nc-nd/3.0/au/>

Link to license to see what you are allowed to do with this resource.

Downloaded from <http://hdl.handle.net/1959.4/40822> in <https://unsworks.unsw.edu.au> on 2024-04-30

UNSW



>013751735

THE UNIVERSITY OF NEW SOUTH WALES
Thesis/Dissertation Sheet

Surname or Family name: Kenyon

First name: Suzanne

Other name/s: Laura

Abbreviation for degree as given in the University calendar:

PhD

School: Physics

Faculty: Science

Title: A universe of sky and snow: site-testing for optical astronomy at Dome C, Antarctica

Abstract:

The unique advantages for astronomy on the Antarctic plateau are now well established. In particular, Dome C, Antarctica is potentially one of the best new sites for optical, infrared and sub-millimeter astronomy, presenting the opportunity to build unique astronomical instruments. Located high on the Antarctic plateau, Dome C offers low wind, clear skies, and negligible precipitation. This thesis addresses three additional properties of the site relevant to optical astronomy—sky brightness, atmospheric extinction and optical turbulence.

The sky at an optical astronomy site must be dark, and the atmosphere very clean with minimal light extinction. At present little is known from an astronomer's perspective about the optical sky brightness and atmospheric extinction at most Antarctic sites. The high latitude of Dome C means that the Sun spends a relatively small amount of time far below the horizon, implying longer periods of astronomical twilight and less optical dark time than other sites, especially those close to the equator. We review the contributions to sky brightness at high-latitude sites, and calculate the amount of usable dark time at Dome C. We also explore the implications of the limited sky coverage of high-latitude sites, and review optical extinction data from the South Pole. A proposal to extend the amount of usable dark time through the use of polarising filters is examined, and we present the design and calibration of an instrument (called Nigel) to measure the brightness, spectrum and temporal characteristics of the twilight and night sky.

The atmospheric turbulence profile above an astronomical site limits the achievable resolution and sensitivity of a telescope. The atmospheric conditions above high plateau Antarctic sites are different to temperate sites; the boundary layer of turbulence is confined very close to the surface, and the upper atmosphere turbulence very weak. We present the first winter-time turbulence profiles of the atmosphere above Dome C, and characterise the site in terms of the achievable precision for photometry and astrometry, and the isoplanatic angle and coherence time for the adaptive optics.

Declaration relating to disposition of project thesis/dissertation

I hereby grant to the University of New South Wales or its agents the right to archive and to make available my thesis or dissertation in whole or in part in the University libraries in all forms of media, now or here after known, subject to the provisions of the Copyright Act 1968. I retain all property rights, such as patent rights. I also retain the right to use in future works (such as articles or books) all or part of this thesis or dissertation.

I also authorise University Microfilms to use the 350 word abstract of my thesis in Dissertation Abstracts International (this is applicable to doctoral theses only).

Witness

Date

The University recognises that there may be exceptional circumstances requiring restrictions on copying or conditions on use. Requests for restriction for a period of up to 2 years must be made in writing. Requests for a longer period of restriction may be considered in exceptional circumstances and require the approval of the Dean of Graduate Research.

FOR OFFICE USE ONLY

Date of completion of requirements for Award:

THIS SHEET IS TO BE GLUED TO THE INSIDE FRONT COVER OF THE THESIS

**A UNIVERSE OF SKY AND SNOW:
SITE-TESTING FOR OPTICAL ASTRONOMY AT
DOME C, ANTARCTICA**

by

Suzanne L. Kenyon

A thesis submitted in satisfaction of
the requirements for the degree of

Doctor of Philosophy

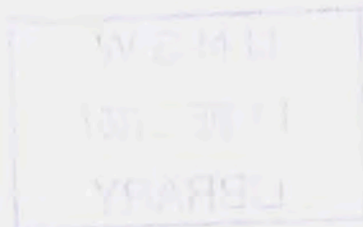
in the Faculty of Science.

2007

**THE UNIVERSITY OF
NEW SOUTH WALES**



SYDNEY • AUSTRALIA



UNSW

11 DEC 2007

LIBRARY

Statement of Originality

'I hereby declare that this submission is my own work and to the best of my knowledge it contains no materials previously published or written by another person, or substantial proportions of material which have been accepted for the award of any other degree or diploma at UNSW or any other educational institution, except where due acknowledgment is made in the thesis. Any contribution made to the research by others, with whom I have worked at UNSW or elsewhere, is explicitly acknowledged in the thesis. I also declare that the intellectual content of this thesis is the product of my own work, except to the extent that assistance from others in the project's design and conception or in style, presentation and linguistic expression is acknowledged.'

Signed: .

Date: 25 August 2007

Copyright Statement

'I hereby grant the University of New South Wales or its agents the right to archive and to make available my thesis or dissertation in whole or part in the University libraries in all forms of media, now or here after known, subject to the provisions of the Copyright Act 1968. I retain all proprietary rights, such as patent rights. I also retain the right to use in future works (such as articles or books) all or part of this thesis or dissertation.

I also authorise University Microfilms to use the 350 word abstract of my thesis in Dissertation Abstract International.

I have either used no substantial portions of copyright material in my thesis or I have obtained permission to use copyright material; where permission has not been granted I have applied/will apply for a partial restriction of the digital copy of my thesis or dissertation.'

Signed:..

Date:.....*25 August 2007*.....

Authenticity Statement

'I certify that the Library deposit digital copy is a direct equivalent of the final officially approved version of my thesis. No emendation of content has occurred and if there are any minor variations in formatting, they are the result of the conversion to digital format.'

Signed:

Date:.....*25 August 2007*.....

Abstract

The unique advantages for astronomy on the Antarctic plateau are now well established. In particular, Dome C, Antarctica is potentially one of the best new sites for optical, infrared and sub-millimeter astronomy, presenting the opportunity to build unique astronomical instruments. Located high on the Antarctic plateau. Dome C offers low wind, clear skies, and negligible precipitation. This thesis addresses three additional properties of the site relevant to optical astronomy—sky brightness, atmospheric extinction and optical turbulence.

The sky at an optical astronomy site must be dark, and the atmosphere very clean with minimal light extinction. At present little is known from an astronomer's perspective about the optical sky brightness and atmospheric extinction at most Antarctic sites. The high latitude of Dome C means that the Sun spends a relatively small amount of time far below the horizon, implying longer periods of astronomical twilight and less *optical* dark time than other sites, especially those close to the equator. We review the contributions to sky brightness at high-latitude sites, and calculate the amount of usable dark time at Dome C. We also explore the implications of the limited sky coverage of high-latitude sites, and review optical extinction data from the South Pole. A proposal to extend the amount of usable dark time through the use of polarising filters is examined, and we present the design and calibration of an instrument (called Nigel) to measure the brightness, spectrum and temporal characteristics of the twilight and night sky.

The atmospheric turbulence profile above an astronomical site limits the achievable resolution and sensitivity of a telescope. The atmospheric conditions above high plateau Antarctic sites are different to temperate sites; the boundary layer of turbulence is confined very close to the surface, and the upper atmosphere turbulence very weak. We present the first winter-time turbulence profiles of the atmosphere above Dome C, and characterise the site in terms of the achievable precision for photometry and astrometry, and the isoplanatic angle and coherence time for the adaptive optics.

Contents

Abstract	i
List of tables	viii
List of figures	xi
Acknowledgments	xiii
Preface	xv
1 Introduction	1
1-1 Site testing for ground based astronomy	2
1-1.1 Atmospheric turbulence	3
1-1.2 Atmospheric extinction	4
1-1.3 Sky brightness	5
1-2 Why Antarctica?	5
1-3 Where in Antarctica?	6
1-4 Site testing at Dome C	7
1-5 Thesis motivations	10
2 Atmospheric extinction	13
2-1 Atmospheric extinction	14
2-2 Molecular scattering	15
2-2.1 Simple model	15
2-2.1.1 Results	17
2-2.2 Improved model	17
2-2.2.1 Results	20
2-3 Molecular absorption	22
2-3.1 Water vapour and clouds	22

2-3.2	Ozone optical depth	23
2-4	Aerosol scattering and absorption	24
2-4.1	Aerosols at Dome C	25
2-5	Conclusions	26
3	Optical twilight and formal dark-time	29
3-1	Twilight, formal dark-time and cloud cover	30
3-1.1	Sky coverage	34
3-2	Using a polariser to reduce sky background	36
3-3	The polarised sky	37
3-4	Polarisation at the South Pole and effects of ice precipitation	40
3-5	Polarisation measurements during twilight	40
3-6	Conclusions	44
4	Optical sky brightness	45
4-1	Moonlight	47
4-1.1	Model of the moonlight contribution to sky brightness	50
4-1.2	Results	51
4-2	Aurorae	52
4-2.1	Implications for Dome C	53
4-3	Airglow	56
4-3.1	Airglow reactions and emissions lines	56
4-3.2	A reduction in airglow over Antarctica?	56
4-3.3	Airglow measurements	58
4-4	Zodiacal light	59
4-4.1	Results	60
4-5	Integrated starlight	61
4-6	Diffuse Galactic light	61
4-7	Integrated cosmic light	61
4-8	Light pollution	62
4-9	Conclusions	62
5	Nigel, monitoring the sky brightness at Dome C	65
5-1	Instrument description	66

5-2	Control and communication	68
5-3	Wavelength Calibration	71
5-4	Flux calibration	76
5-4.1	Theoretical sensitivity	77
5-4.2	Measured sensitivity	78
5-5	Conclusions on calibration methods	80
5-6	Discussion and Nigel's plans for the future	82
6	Atmospheric turbulence in Antarctica	83
6-1	Turbulent flow in fluids	84
6-2	Optical turbulence	85
6-2.1	Statistical description of turbulence	88
6-3	Turbulence measurements in Antarctica	91
6-4	Measuring the night time turbulence profile at Dome C	93
6-4.1	Dome C SODAR	93
6-4.2	MASS	93
6-4.3	Dome C MASS	95
6-4.4	MASS data filtering	97
6-4.5	Combining SODAR and MASS data	100
6-5	Turbulence profiles	100
6-5.1	Lower atmosphere turbulence profiles	100
6-5.2	Upper atmosphere turbulence profiles	102
6-6	Seeing, isoplanatic angle and coherence time	106
6-7	Discussion	108
7	Atmospheric scintillation	109
7-1	Scintillation	110
7-1.1	Scintillation index for a very small aperture	112
7-1.2	Scintillation index for a large aperture	112
7-1.3	Scintillation index for a long integration time and large aperture	113
7-2	Photometric noise	114
7-3	Astrometric precision	115
7-4	Wind profiles	116

7-5	Results using fixed wind profiles	117
7-5.1	Photometry	118
7-5.2	Astrometry	120
7-6	Results using dynamic wind profiles	123
7-6.1	Photometry and astrometry reanalysed	127
7-7	Correlation between wind shear and turbulence	129
7-8	Conclusions	134
8	Conclusions	135
	Appendices	139
A	Acronyms	139
B	Daily turbulence profiles at Dome C	141
C	Published papers	155
C-1	A review of the optical sky brightness and extinction at Dome C	157
C-2	Atmospheric scintillation at Dome C, Antarctica	171
C-3	Nigel and the optical sky brightness at Dome C, Antarctica	181
	References	191

List of Tables

2.1	Site parameters	14
2.2	Data for the simple Rayleigh model.	17
2.3	Rayleigh optical depth at Dome C, Dome A and Mauna Kea.	18
3.1	The observable sky at Dome C compared to other sites	35
3.2	Typical behaviour of the degree of polarisation	42
4.1	Contributions to the light of the night sky	46
4.2	Typical auroral emissions in the visible.	54
4.3	Distance and elevation angle of aurorae as viewed from Dome C	55
4.4	Nightglow emissions at zenith in the visible range.	57
5.1	Characteristics of the fibre and spectrograph used in Nigel	69
5.2	Europium IV transitions and wavelengths	72
5.3	Terbium IV transitions and wavelengths	72
5.4	The most intense Mercury transitions in the visible range.	73
5.5	Probable identification of fluorescent lines	73
5.6	Fraunhofer lines in the visible	74
5.7	Twilight glow emission features	74
5.8	Emissivity of tungsten	78
6.1	Data sets for each site	104
6.2	Isoplanatic angles and coherence times for adaptive optics.	106
6.3	Comparison of seeing, isoplanatic angle and coherence time at various sites	107
7.1	Isoplanatic angles and coherence times for adaptive optics.	121
7.2	Average results for astrometric errors using three methods	128

7.3	Average results for photometric errors using three methods	128
-----	--	-----

List of Figures

1.1	Elevation map of Antarctica.	7
1.2	Photograph of Concordia station at Dome C, Antarctica	8
2.1	The Rayleigh optical depth at Dome C, Dome A and Mauna Kea	21
2.2	The short wavelength Rayleigh optical depth at Dome C and Dome A	22
2.3	Precipitable water vapour at four sites	23
2.4	Average ozone content in the atmosphere	24
2.5	Histogram of $\tau_A(\lambda = 440 \text{ nm})$ values measured at Dome C by Six et al. (2005).	26
3.1	The solar elevation angle at Dome C, South Pole and Mauna Kea over 2005	32
3.2	Comparison of the usable dark-time at Dome C and Mauna Kea	33
3.3	The observable sky as a function of latitude	35
3.4	The degree of polarisation for a Rayleigh model	39
3.5	Polarisation as a function of solar zenith angle	43
4.1	Lunar phase, and solar and lunar elevation angles over one year at Dome C	48
4.2	Lunar phase, and solar and lunar elevation angles over one year at Mauna Kea	49
4.3	Scattered moonlight brightness	51
4.4	Schematic of the typical southern auroral oval	53
4.5	Schematic illustrating the geometry of aurorae relative to Dome C	55
4.6	The zodiacal contribution to sky brightness at Dome C and Mauna Kea	60
5.1	Schematic and photograph of the Nigel fibre positions	67
5.2	Light path in the spectrograph used in Nigel	69
5.3	Raw CCD image taken with Nigel	70
5.4	Spectra of a compact fluorescent tube and the daytime sky	75
5.5	Absolute flux calibration using a tungsten bulb	76

5.6	Theoretical sensitivity of the Nigel instrument	79
5.7	Measured sensitivity of the Nigel instrument	81
6.1	Laminar and turbulent flow in a pipe	84
6.2	Formation of optical turbulence	87
6.3	Schematic illustrating wavefront distortion and a typical temperature profile .	87
6.4	Diffraction and seeing limited images	90
6.5	Ideal MASS response function	94
6.6	MASS installation in the AASTINO	96
6.7	Histograms of the flux in channel D for every MASS measurement at Dome C	98
6.8	Histograms of filtering criteria for the Dome C MASS data	98
6.9	Flux through channel <i>D</i> on 25 and 27 March, and 2 May 2004	99
6.10	SODAR temperature structure constant profiles measured at Dome C in 2004	101
6.11	Turbulence intensity profiles measured using the MASS at Dome C in 2004 .	103
6.12	Floating turbulence layers	104
6.13	Comparison of the integrated turbulence in each MASS layer at three sites .	105
6.14	Histograms of the atmospheric time constant, seeing and isoplanatic angle . .	107
7.1	Schematic illustrating the formation of atmospheric scintillation	111
7.2	Wind speed profiles at Dome C, Cerro Tololo and Cerro Pachón	118
7.3	Photometric precision at Dome C, Cerro Tololo and Cerro Pachón	119
7.4	Astrometric precision at Dome C, Cerro Tololo and Cerro Pachón	122
7.5	Wind speed and direction at Dome C from the NCEP/NCAR database . . .	124
7.6	Schematic showing how the wind speeds were chosen for each MASS altitude	125
7.7	Comparison of the two extraction methods for wind speed.	126
7.8	C_1 , C_2 and S_3 calculated using NCEP wind speeds	127
7.9	Wind shear and turbulence in the four lowest MASS layers at Dome C . . .	130
7.10	Wind shear and turbulence in the 8 and 16 km MASS layers at Dome C . .	131
7.11	Wind shear and turbulence in the five lowest MASS layers at Cerro Tololo . .	132
7.12	Wind shear and turbulence in the 16 km MASS layer at Cerro Tololo	133
B.1	MASS turbulence intensity profiles for 24 March 2004 and 25 March 2004. . .	142
B.2	MASS turbulence intensity profiles for 26 March 2004 and 27 March 2004. . .	143
B.3	MASS turbulence intensity profiles for 30 March 2004 and 31 March 2004. . .	144

B.4	MASS turbulence intensity profiles for 1 April 2004 and 4 April 2004.	145
B.5	MASS turbulence intensity profiles for 5 April 2004 and 6 April 2004.	146
B.6	MASS turbulence intensity profiles for 7 April 2004 and 8 April 2004.	147
B.7	MASS turbulence intensity profiles for 9 April 2004 and 10 April 2004.	148
B.8	MASS turbulence intensity profiles for 11 April 2004 and 28 April 2004.	149
B.9	MASS turbulence intensity profiles for 30 April 2004 and 1 May 2004.	150
B.10	MASS turbulence intensity profiles for 2 May 2004 and 3 May 2004.	151
B.11	MASS turbulence intensity profiles for 4 May 2004 and 5 May 2004.	152
B.12	MASS turbulence intensity profiles for 11 May 2004 and 14 May 2004.	153
B.13	MASS turbulence intensity profiles for 16 May 2004	154

Acknowledgments

Frank Herbert once said, “the beginning of knowledge is the discovery of something we do not understand”, well I have a lot of people to thank for helping me discover things I didn’t understand.

Firstly to my supervisor, John Storey, who has guided me through these last three years with patient support and a bit of prodding. John has helped me to develop professionally, and taught me the art of public speaking and a lot of grammar. Of all things, I most admire John’s ability to find the best beer wherever you are in the world. To my co-supervisor Michael Ashley for help with all things computerised and with putting Nigel together. I’d especially like to thank John and Michael for giving me the opportunity to visit Dome C in Antarctica. I’ll never forget the day Michael walked into my office and casually asked if I wanted to go to Antarctica—in two weeks. To Jon Lawrence, the ideas man, for his dedication to the project, advice and help. Thanks for being a great companion on my Antarctic trip, and not being afraid to give a girl a power tool—it was safer in the end. To Jon Everett for helping to put Nigel together, working right up to the last minute. Thanks to Tony Travouillon for on-going support with all things turbulent and Anna Moore for advice, encouragement and a 12 hour tour of Los Angeles. And a big thank you to the remainder of the UNSW Antarctica research group: Michael Burton, Jessie Christiansen, Daniel Luong-Van, Balthasar Indermuehle and Shane Hengst.

I’d like to thank my international colleagues who have given advice and contributed many ideas to the project. In particular, thanks to the LUAN team at the University of Nice, especially Eric Aristidi and Karim Agabi, for their assistance with the AASTINO project at Dome C. To Andrei Tokovinin for continuing advice with the MASS instrument and data. I’d also like to thank Andrei and his wife for their kind hospitality while I was in La Serena.

A big thank you to my family—Mum, Dad, Melanie, Emilie, Granny, Chris, Sheebe, Murphy, Bucket and Studley—for their love and encouragement (hey Dad, maybe now I’ll get a real job!) To Matt for his amazing love and support, always ready to tell me everything will be alright—especially if chocolate is involved. To my office mates, Cormac, Steve and Nadia for keeping me on the right side of sane, and to the past and present pirates and wenches at UNSW, you know who you are.

I am grateful to the Australian government for financial support, through an Australian Postgraduate Award and an Australian Antarctic Division top-up scholarship. For logistical support of the UNSW AASTINO Antarctic adventures I would like to say *merci beaucoup* to the French (Institut Polaire Français Paul Emile Victor; IPEV) and *grazie mille* to the Italian (Programma Nazionale di Ricerca in Antartide; PRNA) Antarctic programs. The research of the UNSW AASTINO project is financially supported by the Australian Research Council and the Australian Antarctic Division.

Finally, I'd like to thank my examiners for taking time to read this thesis.

Preface

A large part of this thesis was published in the following papers, copies of these papers are reproduced in the appendices as noted.

- **Kenyon & Storey 2006:** *A review of the optical sky brightness and extinction at Dome C, Antarctica.* Chapters 2, 3 and 4. Appendix C-1.
- **Kenyon et al. 2006a:** *Nigel and the optical sky brightness at Dome C, Antarctica.* Chapter 5. Appendix C-3.
- **Kenyon et al. 2006b:** *Atmospheric scintillation at Dome C, Antarctica: implications for photometry and astrometry.* Chapters 6 and 7. Appendix C-2.

Additional papers that I co-authored during the thesis are:

- **Lawrence et al. 2004:** *A robotic instrument for measuring high altitude atmospheric turbulence from Dome C, Antarctica*
- **Lawrence et al. 2006b:** *Site testing Dome A, Antarctica*
- **Moore et al. 2006a:** *Ground-layer turbulence profiling using a lunar SHABAR*
- **Moore et al. 2006b:** *The Gattini cameras for optical sky brightness measurements in Antarctica*

See Appendix C for full details.

During this project I was involved in the development of two instruments and the software and data analysing tools for these instruments; however, there were many other researchers involved in these projects. Below I clarify my contributions and the contributions of others to these projects. These contributions are also referenced in the text.

- Nigel was developed using the components and general idea behind the Antarctic Fibre Optic Spectrometer (AFOS). The AFOS instrument and software was primarily designed and developed by Maxime Boccas and Michael Ashley. With the help of the Antarctic group I modified the instrument, adapted the software, and installed and

calibrated Nigel at Dome C. I was responsible for the operation and data analysis of Nigel.

- The Dome C MASS was installed by Jon Lawrence and Tony Travouillon in the summer of 2003/2004. I was involved in some pre-deployment work on the instrument and software, and the calibration of the instrument during the 2004/2005 summer season. I carried out my own analysis of the MASS data using software I based on scripts by Andre Tokovinin.
- All data collection from instruments in the AASTINO was aided by scripts written by Michael Ashley and Jon Lawrence.

“No cloud above, no earth below,
A universe of sky and snow.”

John Greenleaf Whittier (1807-1892)

Snow-Bound: A Winter Idyll (1866)

Chapter 1

Introduction

Optical astronomy is entering a new stage of telescope design as larger and more complex astronomical facilities are being proposed. The science demands of astronomers require higher resolution and greater sensitivity than ever before. We will soon be leaving behind the first generation of very large telescopes (8–10 m apertures) and entering the era of Extremely Large Telescopes (ELTs; 20–30 m apertures). This is a step towards the even bigger telescopes of the future which may have aperture sizes up to 100 m. The potential sites of these expensive facilities have to be rigorously tested, with more in-depth characterisation than in the past, to ensure that the best available sites are chosen.

Dome C, Antarctica is potentially one of the best locations on the Earth on which to site a telescope. This thesis assesses three fundamental areas of astronomical site testing for optical astronomy at Dome C—sky brightness, atmospheric extinction, and atmospheric turbulence. This research uses on-site measurements, and models that incorporate data from the South Pole and satellite-based instruments.

In this introductory chapter the characteristics of an ideal astronomical site are described and the choice of Antarctica, and in particular Dome C, is explained.

1-1 Site testing for ground based astronomy

The atmosphere places the final limit on the resolution and, sometimes, the sensitivity of a ground-based optical telescope. The light from every astronomical object has to pass through our turbulent, cloudy, rainy atmosphere before reaching the telescope. Space-based telescopes are used to get above the atmosphere, removing these atmospheric problems. However, space based telescopes have their own disadvantages: they are extremely expensive to design, manufacture and launch; the size of the telescope and associated instruments are limited by the size of the Shuttle or other launch vehicle; and access to repair or upgrade the instrument is very limited and incurs even more cost. Ground-based telescopes are a more economical and versatile option, as long as they are placed at the best possible, high altitude, sites on the Earth. With larger apertures and advanced imaging techniques, ground-based telescopes of the future will rival space-based telescopes in terms of sensitivity and resolution.

Below the characteristics of an *ideal* optical astronomical site are listed:

High altitude: a high altitude site is necessary to minimise the amount of atmosphere that the light from an astronomical object must travel through, resulting in lower extinction. A high altitude location will also be above some cloud layers.

Dry atmosphere: a dry atmosphere reduces the absorption of light by water vapour

No precipitation: a telescope dome is closed in the event of rain, fog, hail and snow, minimising the available observing time.

No lightning: lightning can damage the surface of the telescope and the sensitive electronics of the instruments.

No cloud cover: clouds attenuate the light reaching a telescope. In the event of thick cloud, no measurements can be taken.

Weak surface wind speed and low seismic activity: these both have implications for the design of the telescope structure and dome. The telescope dome must be able to withstand the strongest gusts of wind at a site, and the telescope structure needs to remain still for precision measurements and tracking. These criteria are becoming more important as telescope sizes are increasing.

No close-by towns and cities: artificial lighting in nearby towns and cities can increase the sky brightness. The pollution in the atmosphere from a city can increase the scattering of light in the atmosphere, and also result in the mirror requiring more frequent cleaning. The potential growth of the city needs to be predicted because telescope facilities can be in use for decades.

Access to the site: the telescope site needs to be accessible in some form, with access to power, communications, accommodation, food, and water.

Weak atmospheric turbulence: atmospheric turbulence distorts the light travelling through the atmosphere. A calm, stable atmosphere is necessary to minimise this turbulence.

Low sky brightness: most astronomical observations require the background sky to be as dark as possible.

Minimal atmospheric extinction: particles in the atmosphere scatter and absorb the light from astronomical object, attenuating the signal that reaches the telescope.

Preliminary site evaluations typically use historical meteorological records or satellite measurements to assess the climate of the site. If the site looks promising, on-site measurements are then conducted using a variety of instruments. These can include sky cameras to monitor cloud cover, and weather stations to measure precipitation, wind speed, and temperature.

The focus of this thesis is on the last three characteristics in the list. These are now explained further.

1-1.1 Atmospheric turbulence

The light from a star, or other astronomical object, is distorted as it passes through the turbulent atmosphere of the Earth. This distortion places limits on the resolution and sensitivity of ground-based optical telescopes. Astronomical telescopes should be located at sites where the atmosphere is calm and stable, and the turbulence is weak.

In the context of astronomy, turbulence refers to optical turbulence created in the atmosphere. Optical turbulence is generated when wind in the atmosphere mixes air of

different temperature. This mixing results in the formation of “cells” each with a slightly different temperature, humidity and refractive index. The light from a star enters the atmosphere as a plane undistorted wavefront. As the wave propagates towards the Earth these cells act as positive or negative “lenses” changing the wavefront curvature and producing phase and amplitude fluctuations. The effect of these fluctuations can be seen on an image taken through a telescope. With a small aperture telescope the image is seen to randomly move around and change intensity. With a larger aperture the image will be blurred and a “speckle” pattern is formed.

Astronomers usually consider optical turbulence in three regimes: dome, surface and free atmosphere turbulence. Dome turbulence is usually related to temperature gradients inside the telescope dome itself, and temperature gradients between the inside and outside of the dome. These gradients can usually be overcome by equalising internal and external temperatures; for example, by opening side panels on the dome to let air flow through. Surface layer turbulence is caused by the lower atmosphere interacting with the surface of the Earth. Wind shear in this layer is caused as the wind interacts with the local terrain and man-made structures and temperature gradients are formed by the diurnal cycle of solar heating of the ground. The free atmosphere turbulence is associated with wind shears (for example, caused by strong jet-stream winds), and convection in the tropopause. Atmospheric turbulence is discussed further in Chapter 6.

1-1.2 Atmospheric extinction

Atmospheric extinction describes the attenuation of light by absorption and scattering as it passes through the atmosphere. Light can be scattered and absorbed in the atmosphere by gaseous molecules (at optical wavelengths the most important are oxygen, ozone, nitrogen and water), and by aerosols—solid particles or liquid droplets that are suspended in the atmosphere. Scattering has two effects on astronomical observations: it increases the overall sky brightness and decreases the flux received from the object being observed. Atmospheric absorption reduces the amount of light reaching a telescope mirror, lowering the flux from both the sky background and the observed object.

The amount of molecular scattering and absorption can be minimised by choosing a site at a high altitude with minimal water vapour in the atmosphere. In terms of

aerosols, each site has to be considered individually because aerosols come from assorted sources including dust from the ground, particles of sea salt, and pollution. Sites near major cities may experience more pollution in the atmosphere in the future. Estimating the long-term concentrations of aerosols above current and potential astronomical sites is essential to evaluating the future of the site.

1-1.3 Sky brightness

To make the best use of an astronomical site you need a large quantity of good quality dark skies. The Sun sets the limit on the amount of dark-time at a site. During the day the surface of the Earth is illuminated by direct sunlight and sunlight scattered by atmospheric molecules and particles. After sunset, the surface of the Earth is only illuminated by scattered sunlight; the direct component illuminates the atmosphere above the level of the Earth's shadow. Over the course of twilight the scattered sunlight contribution to sky brightness decreases to negligible levels and night begins. The length of the night depends on the latitude of the site and the season of year.

Even after the Sun has fully set the sky is never completely dark at optical wavelengths. At any site the optical night sky is always brightened with airglow, zodiacal light, integrated starlight, diffuse Galactic light and extra-galactic light. Further brightening can be caused by aurorae, moonlight and artificial sources. Atmospheric scattering of the flux from each of these sources adds significantly to the sky brightness. Each of these sources has to be considered individually when assessing a site.

1-2 Why Antarctica?

Antarctica brings to mind images of howling winds, blizzards, heavy snow, and penguins. But, as discussed earlier, the ideal astronomical site has slow winds and little precipitation; penguins are not a problem. It begs the question, why would Antarctica be chosen? Most of the Antarctic continent is actually a high, almost flat plateau of ice ranging from about 2000 to 4000 m above sea level. While the coast of Antarctica experiences some of the most violent blizzards in the world, on the highest parts of the plateau the wind speed and weather is very calm.

The winds in Antarctica are partly katabatic in nature. Katabatic winds form as cold, dense air moves downward in altitude. From the highest places on the plateau the gradient of the ice is very slight; only near the coast does the gradient become very steep. The katabatic winds in Antarctica form as the cold air on the summits slowly rolls down towards the coast, gaining speed as the gradient increases. On reaching the coast the wind increases to impressive speeds; for example, a wind speed of 345 km h^{-1} ($\approx 96 \text{ m s}^{-1}$) was measured from an 80 metre high tower on the coastal base of Dumont D'Urville (Wendler et al. 1997, and references therein.). Lower lying areas on the plateau can also experience strong winds. Figure 1.1 shows the prevailing wind directions on the Antarctic continent.

The potential of the Antarctica plateau as a prime site for astronomy has been recognised for a number of years. See Indermuehle et al. (2005) for a history of astronomy in Antarctica. The Antarctic plateau is the highest and driest continent in the world, fulfilling the first two criteria for an ideal site. There is no lightning, the cloud cover is very low, and as just discussed, the wind speeds on the summits are very slow. There is very little seismic activity, and of course there are no nearby major cities to pollute the atmosphere.

The scientific exploration of the Antarctica plateau has come a long way since the first scientific expedition in 1898. In the early 1900's the race was on to trek to the geographic South Pole. The men in these expeditions experienced severe conditions and many lost their lives. Scientific exploration on the plateau is now a lot more comfortable. There are now permanent stations on the plateau that house people all year round, supplied during the summer months by airplane or tractor traverse.

1-3 Where in Antarctica?

Not every place on the Antarctic plateau is suitable for optical astronomy. Figure 1.1 shows an elevation map of the Antarctic continent; marked on the map are the South Pole and the three highest places on the plateau: Dome A, Dome F, and Dome C (in order of height). The highest summit, Dome A, is possibly the best site for astronomy on the plateau. However, there is no permanent station as yet at Dome A; indeed the site was only first visited in January 2005 by a Chinese expedition. While there

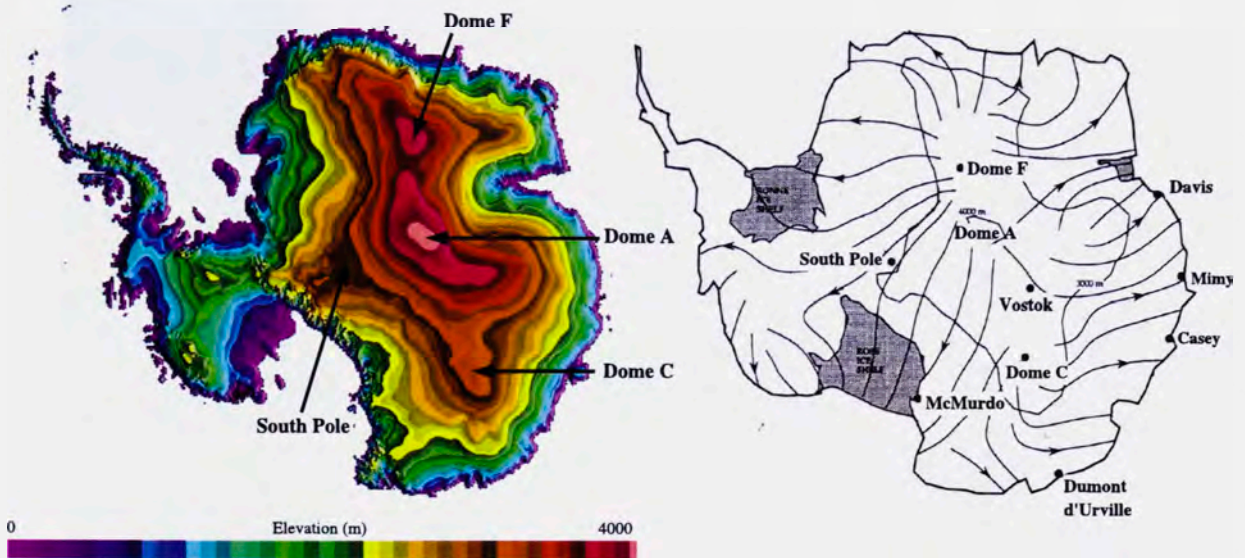


Figure 1.1. *Left:* elevation map of Antarctica from the U.S. Geological Survey website (<http://terraweb.wr.usgs.gov/projects/Antarctica/antdemsr.html>). The positions of the South Pole and the three highest summits, Domes A, F and C, on the Antarctic plateau are shown. *Right:* map of Antarctica showing the prevailing surface wind directions (Marks et al. 1999, and references therein).

are plans to deploy a remote site-testing facility to Dome A as part of the 2007/2008 International Polar Year activities (e.g., Lawrence et al. 2006b), the first major Antarctic optical astronomy telescope will probably be built on the permanently manned summit of Dome C.

1-4 Site testing at Dome C

Located at $75^{\circ}6'$ south, $123^{\circ}21'$ east, and an altitude of 3260 m, Dome C is the third highest place on the Antarctic Plateau. The French (Institut Polaire Français Paul Emile Victor; IPEV) and Italian (Programma Nazionale di Ricerche in Antartide; PNRA) Antarctic programs have operated a summertime scientific base, called Concordia, on Dome C since 1995 (Candidi & Lori 2003). Construction of a wintertime station was completed at the beginning of 2005, leading to the first manned winter season at Dome C. Preliminary site testing has been carried out at Dome C since 1995 (Valenziano & dall'Oglio 1999; Candidi & Lori 2003). Systematic measurements of the summertime (ConcordiAstro project; Aristidi et al. 2005b) and wintertime (AASTINO project; Storey et al. 2005)

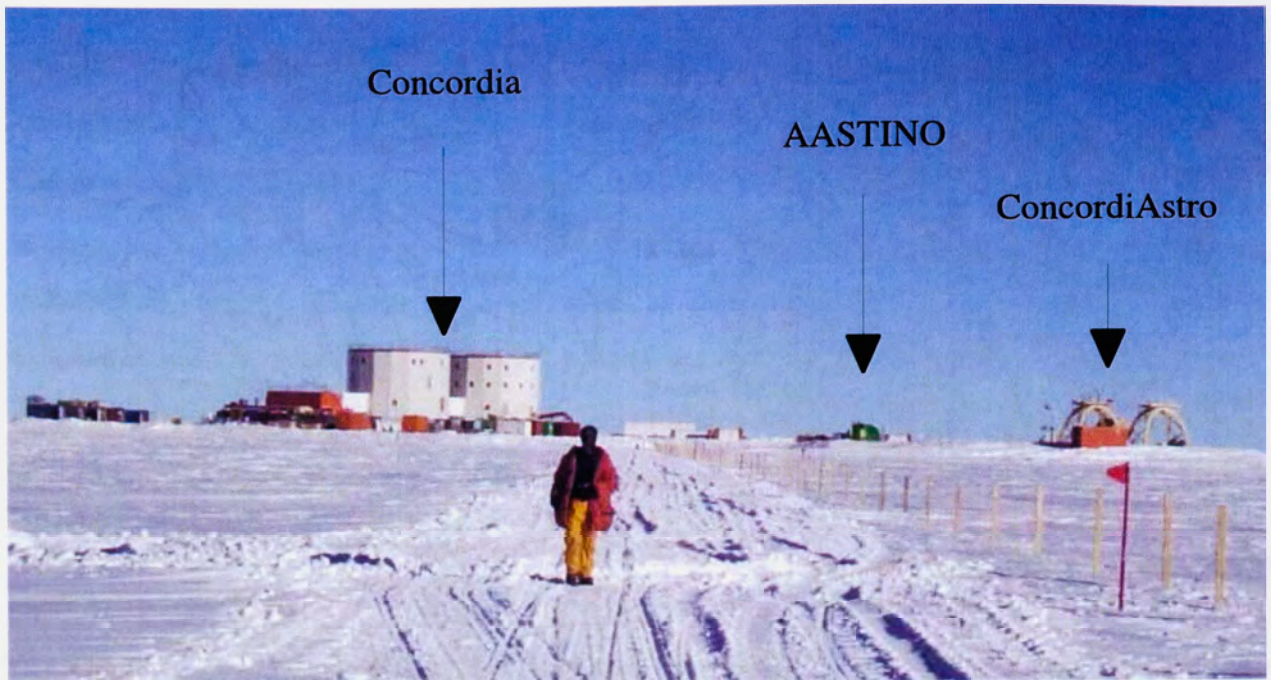


Figure 1.2. Image of the station at Dome C, Antarctica, showing the author in front of Concordia Station, the AASTINO and ConcordiAstro. Photograph courtesy of Jon Lawrence.

characteristics of the site began in 2001. The ConcordiAstro project also began winter measurements in 2005. Figure 1.2 shows a photograph of the station at Dome C. This thesis is part of the AASTINO site testing project.

The Automated Astrophysical Site Testing International Observatory (AASTINO) is a remote laboratory that operated at Dome C from January 2003 to February 2005, after which time the entire AASTINO system was shut-down. For full details on the AASTINO see Lawrence et al. (2003) and Lawrence et al. (2005); a brief summary of the AASTINO and instrument suite is supplied here.

The AASTINO is a completely self-contained laboratory that was designed to operate at Dome C before the station had a wintertime crew and power supply. From January 2003 to the end of 2004 the AASTINO was powered by solar panels (in the summer) and Stirling engines (in the summer and winter) with back-up batteries. From summer 2004/2005, the AASTINO power was supplied by the Concordia station power plant.

Control over the operation of the AASTINO was by the “Supervisor” computer. The Supervisor controlled the power and heat in the AASTINO as well as the operation of

various instruments and communications. Communications to the Supervisor from off-site were via the Iridium satellite network. The instruments that were operated from the AASTINO are listed below. See the associated references and the AASTINO website¹ for more details.

- **MASS** (Multi-Aperture Scintillation Sensor; see Lawrence et al. 2004 and Section 6-4.2): MASS monitors the scintillation of a single star to derive a low resolution profile of the turbulence in the atmosphere from 0.5 to 20 km above the surface. A MASS was installed in summer 2003/2004 and operated from 23 March to 16 May, 2004.
- **SODAR** (SOund Detection And Ranging; Travouillon et al. 2003a,b): A SODAR was one of the first instruments installed in the AASTINO. SODAR measures the echo strength of an acoustic pulse to derive the strength of temperature fluctuations in the atmosphere, the wind speed and wind direction. Profiles of each parameter are returned in 30 metre intervals from 30 to 900 m above the surface.
- **SUMMIT** (SUb-MilliMetre Tipper; Calisse et al. 2004) is a sub-millimetre radiometer for the measurement of the sky opacity at $350 \mu\text{m}$.
- **Nigel** (Kenyon et al. 2006a and Chapter 5) is a fibre-fed spectrograph for measurement of the spectrum of the twilight and nighttime sky. Nigel was installed at Dome C in summer 2004, but unfortunately no twilight or nighttime data were collected before the AASTINO was shut down in February 2005.
- A number of **Web Cameras** were situated in and on the AASTINO; these provided useful data on the conditions at the site such as cloud cover, wind, white-out and alien visitations. The web cameras were also used for monitoring the conditions of the other instruments for snow build up or icing.

Two robotic instruments were deployed to Dome C prior to the AASTINO:

- **ICECAM** (Ashley et al. 2005) is a CCD camera system that was used to monitor cloud cover by taking regular pictures of the sky over a 30° field of view. ICECAM was designed to work completely autonomously in air temperatures down to -80°C , powered by lithium thionyl chloride batteries.

¹The AASTINO project Web site: www.phys.unsw.edu.au/~mcba/aastino/

- **COBBER** (ClOud OBserBER; Dempsey et al. 2003) is a mid-infrared detector that monitors cloud cover by measuring the thermal emission from the atmosphere. COBBER was installed in summer 2001/2002 (as part of the ICECAM experiment); however, because of a wiring fault the instrument did not run successfully until the next summer season.

1-5 Thesis motivations

Previous to my thesis starting in 2004, Dome C already looked to be a very promising site for a range of wavelengths. The mean ground-level wind speed was known to be very slow, 2.9 m s^{-1} (Aristidi et al. 2005c), because of the extremely flat local topography. This wind speed is less than half that at most other observatories. The site is extremely cold. Combined with a very low precipitable water vapour (Valenziano & dall'Oglio 1999) this leads to exceptionally low sky backgrounds in the infrared (Walden et al. 2005) and the sub-millimetre (Calisse et al. 2004). Substantial improvements in atmospheric transmission were predicted at these wavelengths, opening up a number of new spectral windows that are inaccessible at non-Antarctic sites (Lawrence 2004). Cloud cover measurements in 2001 indicated the sky to be cloud-free for at least 74% of the time (Ashley et al. 2005). While the site looked very promising in terms of infrared wavelengths and beyond (e.g. Storey et al. 2003), a number of questions remained unanswered, especially in the “optical” region of the electromagnetic spectrum. In this thesis the optical region is considered to be between the atmospheric cut-off (around 320 nm) and 1 micron.

The atmospheric extinction is expected to be minimal at Dome C because of the high altitude and clean atmosphere. However, few measurements of the extinction in the Antarctic atmosphere have been made. In Chapter 2, the expected atmospheric conditions at Dome C are assessed, using models incorporating data from South Pole.

The high latitude of Dome C means that the sun spends a relatively small amount of time far below the horizon. This implies longer periods of astronomical twilight and less *optical* dark time than other sites, especially those close to the equator. In Chapter 3 the twilight sky brightness and the *quantity* of formal optical dark time are investigated. In Chapter 4 the *quality* of the dark time is assessed in terms of airglow, zodiacal light, integrated starlight, diffuse Galactic light, extra-galactic light, aurorae, moonlight and

artificial sources.

The conclusions drawn in Chapters 3 and 4 are based on models incorporating data from the South Pole and satellite based instruments. However, until the sky brightness at the site has been measured no firm conclusions can be made. The unique conditions of an Antarctic site introduce new aspects that would not normally be considered when assessing the sky brightness at a temperate site, such as ice reflection and aurorae. In Chapter 5, an instrument to measure the optical brightness, temporal characteristics, and spectrum of the twilight and nighttime sky is described.

The boundary layer of atmospheric turbulence was known to be close to the ground (Travouillon et al. 2003a) and the high altitude turbulence was expected to be weak. However, the high altitude turbulence was yet to be monitored during the winter. In Chapter 6 the first nighttime measurements of the strength of the turbulence as a function of altitude in the first 20 km of the atmosphere above Dome C are presented. The data derived from this experiment are evaluated in terms of the effects of phase fluctuations on image quality. Turbulence also introduces intensity fluctuations in the star light. This effect can be seen with the naked eye as the twinkling, or scintillation, of stars. Prior to the 2004 MASS measurements the winter time scintillation at Dome C had only been estimated from atmospheric models. In Chapter 7 the MASS measurements are interpreted in terms of the scintillation noise contribution to photometry and the atmospheric noise contribution to narrow-angle astrometry.

Final conclusions and a discussion of the future prospects for astronomy at Dome C are made in Chapter 8.

“Even more impressive than the clarity of some of the Antarctic days, is the atmospheric transparency of many of the Antarctic nights.”

Robert S. Dietz

Antarctic “Seeing” (1948)

Chapter 2

Atmospheric extinction

Dome C presents a very promising site for an astronomical observatory, as discussed in the introduction. Visually, the atmosphere appears to be very clear with minimal atmospheric extinction—the view from the 30 metre high tower at Dome C seems to stretch forever. Atmospheric extinction describes the absorption and scattering of light by molecules and aerosols in the atmosphere. While the atmospheric extinction at Dome C is theoretically expected to be minimal, few measurements have yet been taken. In this Chapter, the expected atmospheric conditions at Dome C are assessed, using models and data from South Pole. The atmospheric conditions at Mauna Kea, Hawaii are also assessed using data from Mauna Loa and Hilo in Hawaii; we selected Mauna Kea because it is the closest major observatory to the equator. The location and altitude of each site are listed in Table 2.1.

Atmospheric extinction is described in broad terms in Section 2-1. Each component contributing to atmospheric extinction is discussed in more detail in Sections 2-2 to 2-4. This chapter is an extension on work published in Kenyon & Storey (2006).

Table 2.1. Site parameters

Site	Latitude	Longitude	Altitude (m)
Dome C	75°06' S	123°06' E	3260
South Pole	90°00' S	...	2835
Mauna Kea	19°49' N	155°28' W	4205
Mauna Loa	19°53' N	155°57' W	3400

2-1 Atmospheric extinction

Atmospheric extinction causes the attenuation of light as it passes through the atmosphere. As light travels from the top of the atmosphere to the surface of the Earth it can be scattered, absorbed, or transmitted directly to the surface. Extinction collectively describes light scattering and absorption. Light can be scattered and absorbed in the atmosphere by gaseous molecules, and by aerosols—solid particles or liquid droplets that are suspended in the atmosphere. Scattering has two effects on astronomical observations: it increases the overall sky brightness and decreases the flux received from the object being observed. Atmospheric absorption reduces the amount of light reaching a telescope mirror, lowering the flux from both the sky background and the observed object. Light can also be reflected off the surface of the Earth back into the atmosphere. All processes of atmospheric scattering and absorption are strong functions of altitude, pressure, temperature, gas concentration and wavelength, and all, except for molecular scattering, are highly variable with location and time.

The attenuation of light by the atmosphere can be described by Beer's law,

$$I(\lambda) = I_0 e^{-\tau(\lambda)} \quad (2.1)$$

where I_0 is the flux of the astronomical object outside the atmosphere, $I(\lambda)$ is the attenuated flux received by the observer, λ is the wavelength of the light, and $\tau(\lambda)$ is the total wavelength-dependent optical thickness of the atmosphere. $\tau(\lambda)$ can be divided into the optical depths caused by molecular scattering τ_M^s and absorption (from water vapour τ_W^a , ozone τ_O^a and clouds τ_C^a), and aerosol scattering τ_A^s and absorption τ_A^a ,

$$\tau(\lambda) = \underbrace{\tau_M^s(\lambda) + \tau_W^a(\lambda) + \tau_O^a(\lambda) + \tau_C^a(\lambda)}_{\text{molecular component}} + \underbrace{\tau_A^s(\lambda) + \tau_A^a(\lambda)}_{\text{aerosol component}} \quad (2.2)$$

Each component is discussed separately below.

2-2 Molecular scattering

Molecular scattering was first described by Lord Rayleigh in 1871, and is commonly called “Rayleigh scattering”. The Rayleigh scattering optical depth (τ_M^s) is dependent on the molecular composition of the atmosphere—mainly nitrogen and oxygen, with small amounts of argon, carbon dioxide and other trace molecules. Rayleigh scattering occurs from molecules that are a lot smaller in size than the wavelength of light that is interacting with them and is therefore dependent on the wavelength, scaling as λ^{-4} . The Rayleigh optical depth is essentially constant between sites of similar altitude and atmospheric conditions, but does vary with pressure, temperature and carbon dioxide concentration. Dome C is almost a kilometre lower in altitude than Mauna Kea; in general an altitude difference of this extent would have a considerable impact on τ_M^s . However, the low pressure at Dome C (which is a consequence of the lower temperatures and hence thinner scale height of the atmosphere) results in a lower molecular density above the site than would be expected for a temperate site of similar altitude. Dome A is almost at the same altitude as Mauna Kea; however it has a lower atmospheric pressure, so a significant reduction in τ_M^s could be expected for Dome A.

Two methods for estimating τ_M^s are explained and applied to Dome C, Mauna Kea and Dome A.

2-2.1 Simple model

The first method is a simple model by Bodhaine et al. (1999); the calculations from that paper are summarised in this section. Bodhaine et al. (1999) estimate the Rayleigh optical depth using

$$\tau_M^s(\lambda) = \frac{\sigma_s P A}{m_a g} \quad (2.3)$$

where σ_s is the scattering cross section (m^2), P is the atmospheric pressure (Pa), A is Avogadro’s number, m_a is the average molecular weight of the atmosphere (kg mol^{-1}) and g is the local gravity. The average molecular weight and local gravity are estimated

from

$$m_a = (15.0556 \times 10^{-6} C_{\text{CO}_2} + 28.9595) \times 10^{-3} \quad (2.4)$$

and

$$\begin{aligned} g = & 9.806160 (1 - 2.6373 \times 10^{-3} \cos 2\phi + 5.9 \times 10^{-6} \cos^2 2\phi) \\ & - (3.085462 \times 10^{-6} + 2.27 \times 10^{-9} \cos 2\phi) z_c \\ & + (7.254 \times 10^{-13} + 1.0 \times 10^{-15} \cos 2\phi) z_c^2 + (1.517 \times 10^{-19} + 6 \times 10^{-22} \cos 2\phi) z_c^3 \end{aligned} \quad (2.5)$$

where C_{CO_2} is the concentration of carbon dioxide (parts per million), ϕ is the latitude, z_c is the effective mass-weighted altitude given by $z_c = 0.73737z + 5517.56$, and z is the altitude (m).

The scattering cross-section characterises the efficiency of the scatters based on the refractive index and wavelength, this is expressed as

$$\sigma_s(\lambda, z) = \frac{24\pi^3 (n^2 - 1)^2}{\lambda^4 N_s^2 (n^2 + 2)^2} F \quad (2.6)$$

where λ is the wavelength (m), N_{st} is the molecular density at 288.15 K and 1013.25 hPa (2.546889×10^{25} molecules m^{-3}) and n is the refractive index of air with carbon dioxide concentration C_{CO_2} , estimated from

$$n(\lambda, z) = [1 + 0.54 \times 10^{-6} (C_{\text{CO}_2} - 300)] [n_{300} - 1] + 1, \quad (2.7)$$

where n_{300} is the refractive index of air with 300 ppm concentration of CO_2 , given by

$$n_{300}(\lambda, z) = \left[8060.51 + \frac{2480990}{132.274 - \lambda^{-2} 10^{-12}} + \frac{17455.7}{39.32957 - \lambda^{-2} 10^{-12}} \right] \times 10^{-8} + 1. \quad (2.8)$$

Finally, in Equation 2.6, F is the depolarisation factor (otherwise known as $F(\text{air})$ or the King factor) that describes the effect of molecular anisotropy:

$$F = \frac{78.084 F_{\text{N}_2} + 20.946 F_{\text{O}_2} + 0.934 + C_{\text{CO}_2} \times 10^{-4} \times 1.15}{78.084 + 20.946 + 0.934 + C_{\text{CO}_2} \times 10^{-4}} \quad (2.9)$$

$$F_{\text{N}_2} = 1.034 + 3.17 \times 10^{-16} \lambda^{-2} \quad (2.10)$$

$$F_{\text{O}_2} = 1.096 + 1.385 \times 10^{-15} \lambda^{-2} + 1.448 \times 10^{-28} \lambda^{-4}. \quad (2.11)$$

Table 2.2. Data for the simple Rayleigh model. The average temperature (winter) and pressure at Dome C was obtained from an analysis of Automatic Weather Station (AWS) data (Valenziano & dall'Oglio 1999), and at Mauna Kea from the ESO Working Group (2003) report. The Dome A values are from AWS data, courtesy of the Polar Research Institute of China and the Australian Antarctic Division. The carbon dioxide concentration is for South Pole and Mauna Loa (Keeling & Whorf 2004).

Site	Latitude	Altitude (m)	Pressure (hPa)	Temperature (K)	CO ₂ concentration (ppm)
Dome C	75°06' S	3260	644	208	370 (South Pole)
Dome A	80°02' S	4084	569	210	370 (South Pole)
Mauna Kea	19°49' N	4205	614	275	375 (Mauna Loa)

2-2.1.1 Results

This model depends on the ground level pressure, altitude and carbon dioxide concentration, and the latitude of the site. Table 2.2 shows the values used to evaluate the model at each site. The carbon dioxide concentrations are for Mauna Loa and South Pole (Keeling & Whorf 2004).

The results of the calculation are shown in the first four columns of Table 2.3. Using this model we find a slightly higher molecular scattering optical depth at Dome C than at Mauna Kea. A lower τ_M^s was calculated for Dome A than the other sites.

2-2.2 Improved model

Tomasi et al. (2005) provide a different set of approximations for the Rayleigh optical depth; these are summarised below. Tomasi et al. (2005) note that simpler approximations do not properly take into account water vapour and carbon dioxide in the calculation of the refractive index, ignore the spectral dependence of the depolarisation factor, and do not take into account changes of the air composition with height.

The Rayleigh scattering optical depth is expressed as

$$\tau_M^s(\lambda) = \int_{z_0}^{z_\infty} N_s(z) \sigma_s(\lambda, z) dz \quad (2.12)$$

Table 2.3. Rayleigh optical depth at Dome C, Dome A and Mauna Kea calculated using two methods. The first method depends on the latitude of the site and the ground level pressure, altitude and carbon dioxide concentration. The second method takes into account altitude profiles of the water vapour partial pressure, air pressure, temperature and relative humidity.

Wavelength (nm)	τ_M^s First method			τ_M^s Second method		
	Dome C	Dome A	Mauna Kea	Dome C	Dome A	Mauna Kea
300	0.77	0.68	0.74	0.76	0.67	0.75
350	0.40	0.35	0.38	0.39	0.35	0.39
400	0.23	0.20	0.22	0.22	0.20	0.22
450	0.14	0.12	0.13	0.14	0.12	0.14
500	0.091	0.080	0.087	0.089	0.079	0.088
550	0.062	0.054	0.059	0.060	0.053	0.060
600	0.043	0.038	0.041	0.042	0.037	0.042

where $N_s(z)$ is the height-dependent number density of the molecules in the air. The molecular density is calculated by weighting the standard density at standard temperature and pressure by the temperature and pressure at the height z ,

$$N_s(z) = N_{st} \frac{P(z)}{P_s} \frac{T_s}{T(z)}, \quad (2.13)$$

where $P(z)$ and $P_s = 1013.25$ hPa are the total and standard air pressures, and $T(z)$ and $T_s = 288.15$ K are the air and standard temperatures. The scattering cross section is calculated using Equation 2.6; however, the refractive index n and the depolarisation factor F are now dependent on air pressure and temperature, water vapour partial pressure and CO₂ concentration. The refractive index is given by

$$n - 1 = \frac{\rho_a}{\rho_{axs}} (n_{axs} - 1) + \frac{\rho_w}{\rho_{ws}} (n_{ws} - 1) \quad (2.14)$$

$$n_{axs} - 1 = [1 + 0.534 \times 10^{-6} (C_{CO_2} - C_2)] \left[\frac{0.05792105}{238.0185 - \lambda^{-2} 10^{-12}} + \frac{1.67917 \times 10^{-3}}{57.362 - \lambda^{-2} 10^{-12}} \right] \quad (2.15)$$

$$n_{ws} - 1 = 1.022 \left(\frac{2.95235}{10^6} + \frac{2.6422}{\lambda^2 10^{20}} - \frac{3.2380}{\lambda^4 10^{34}} + \frac{4.028}{\lambda^6 10^{47}} \right) \quad (2.16)$$

where ρ_a and ρ_w are the density of dry air and water vapour at the site, and ρ_{axs} and ρ_{ws} are the same parameters for standard conditions. n_{axs} and n_{ws} are the refractive indices of dry air and water vapour under standard conditions. The wavelength is in metres.

The values of ρ_a , ρ_{axs} , ρ_w and ρ_{ws} (kg m^{-3}) are determined from

$$\rho_a = \frac{M_a}{R} \frac{P(z) - e(z)}{T(z)} \frac{1}{Z[P(z), T(z), X_w]} \quad (2.17)$$

$$\rho_{axs} = \frac{M_a}{R} \frac{P_s - e^*}{T_s} \frac{1}{Z[P_s, T_s, X_w]} \quad (2.18)$$

$$\rho_w = \frac{M_a}{R} \frac{f[P(z), T(z)] e(z)}{T(z)} \frac{1}{Z[P(z), T(z), X_w]} \left[1 - X_w [P(z), T(z)] \left(1 - \frac{M_w}{M_a} \right) \right] \quad (2.19)$$

$$\rho_{ws} = \frac{M_a}{R} \frac{f[P_s, T^*] e^*}{T^*} \frac{1}{Z[P_s, T^*, X_w]} \left[1 - X_w [P_s, T^*] \left(1 - \frac{M_w}{M_a} \right) \right]. \quad (2.20)$$

Here R is the gas constant, $T^* = 293.15$ K, $e^* = 1333$ Pa, $M_w = 0.018015$ is the molar mass of water vapour, and M_a is the molecular mass of dry air given by

$$M_a = 2.89635 \times 10^{-2} + 12.011 \times 10^{-9} (C_{\text{CO}_2} - C_1), \quad (2.21)$$

where $C_1 = 400$ ppm. Z is the compressibility of moist air calculated as

$$Z(P, T, X_w) = 1 - \frac{P}{T} \left[a_0 + a_1 (T - T_0) + a_2 (T - T_0)^2 + b_0 X_w + b_1 X_w (T - T_0) + c_0 X_w^2 + c_1 X_w^2 (T - T_0) + \left(\frac{P}{T} \right)^2 (d_0 + d_1 X_w^2) \right] \quad (2.22)$$

where $T_0 = 273.15$ K, $a_0 = 1.58123 \times 10^{-6} \text{ K Pa}^{-1}$, $a_1 = -2.9331 \times 10^{-8} \text{ Pa}^{-1}$, $a_2 = 1.1043 \times 10^{-10} \text{ K}^{-1} \text{ Pa}^{-1}$, $b_0 = 5.707 \times 10^{-6} \text{ K Pa}^{-1}$, $b_1 = -2.051 \times 10^{-8} \text{ Pa}^{-1}$, $c_0 = 1.9898 \times 10^{-4} \text{ K Pa}^{-1}$, $c_1 = -2.376 \times 10^{-6} \text{ Pa}^{-1}$, $d_0 = 1.83 \times 10^{-11} \text{ K}^2 \text{ Pa}^{-2}$, $d_1 = -7.65 \times 10^{-9} \text{ K}^2 \text{ Pa}^{-2}$.

In Equations 2.17-2.20 and 2.22

$$X_w(P, T) = \begin{cases} 0 & \text{for } \rho_a, \rho_{aws} \\ fhE(T)P^{-1} & \text{for } \rho_w, \rho_{ws} \end{cases} \quad (2.23)$$

where f is the enhancement factor of water vapour in air and $E(T)$ is the saturation vapour pressure of water vapour in air, given as

$$f(P, T) = 1.00062 + 3.14 \times 10^{-8} P + 5.6 \times 10^{-7} (T - 273.15)^2 \quad (2.24)$$

and

$$E(T) = \exp(1.2378847 \times 10^{-5} T^2 - 1.9121316 \times 10^{-2} T - 6343.1645 T^{-1}) \quad (2.25)$$

respectively. $F(\lambda, z)$ is calculated from

$$F = \frac{0.78084F_{\text{N}_2}(\lambda) + 0.20946F_{\text{O}_2}(\lambda) + 0.00934F_{\text{Ar}} + 10^{-6}\text{CO}_2F_{\text{CO}_2} + [e(z)/P(z)]F_{\text{H}_2\text{O}}}{0.999640 + 10^{-6}\text{CO}_2 + e(z)/P(z)} \quad (2.26)$$

where $F_{\text{N}_2}(\lambda) = 1.034 + 3.17 \times 10^{-16}\lambda^{-2}$, $F_{\text{O}_2}(\lambda) = 1.096 + 1.385 \times 10^{-15}\lambda^{-2} + 1.448 \times 10^{-28}\lambda^{-4}$, $F_{\text{Ar}} = 1.00$, $F_{\text{CO}_2} = 1.15$, $F_{\text{H}_2\text{O}} = 1.001$ and $e(z)$ is the water vapour pressure (Pa).

2-2.2.1 Results

To apply this model, profiles of the water vapour partial pressure, air pressure, temperature and relative humidity are required. A few temperature profiles have been measured above Dome C, however profiles of the other parameters have not been measured yet. The Earth System Research Laboratory of the National Oceanic and Atmospheric Administration (NOAA) have been using ozone and water vapour sondes to monitor the atmosphere above South Pole for a number of years. Included in the measurements are the pressure, temperature, relative humidity and water vapour pressure as a function of altitude; these data are accessible from the NOAA website¹. Profiles are also available for Hilo, Hawaii and a limited number are available for Mauna Kea. The calculations were carried out by limiting the profiles to above the altitudes of Dome C, Dome A and Mauna Kea. The few measured temperature profiles at Dome C show a good match to the South Pole measurements.

Figure 2.1 shows the profiles used at each site, and the resulting molecular density and optical depth. These results indicate that the optical depths at Mauna Kea and Dome C are virtually identical, so there is no disadvantage with the loss of altitude at Dome C compared with Mauna Kea. The optical depth at Dome A is considerably less, especially at shorter wavelengths. The two methods used to estimate the optical depths showed very similar results.

¹Global Monitoring Division, Earth System Research Laboratory, National Oceanic and Atmospheric Administration, on-line data available from <http://www.cmdl.noaa.gov/>.

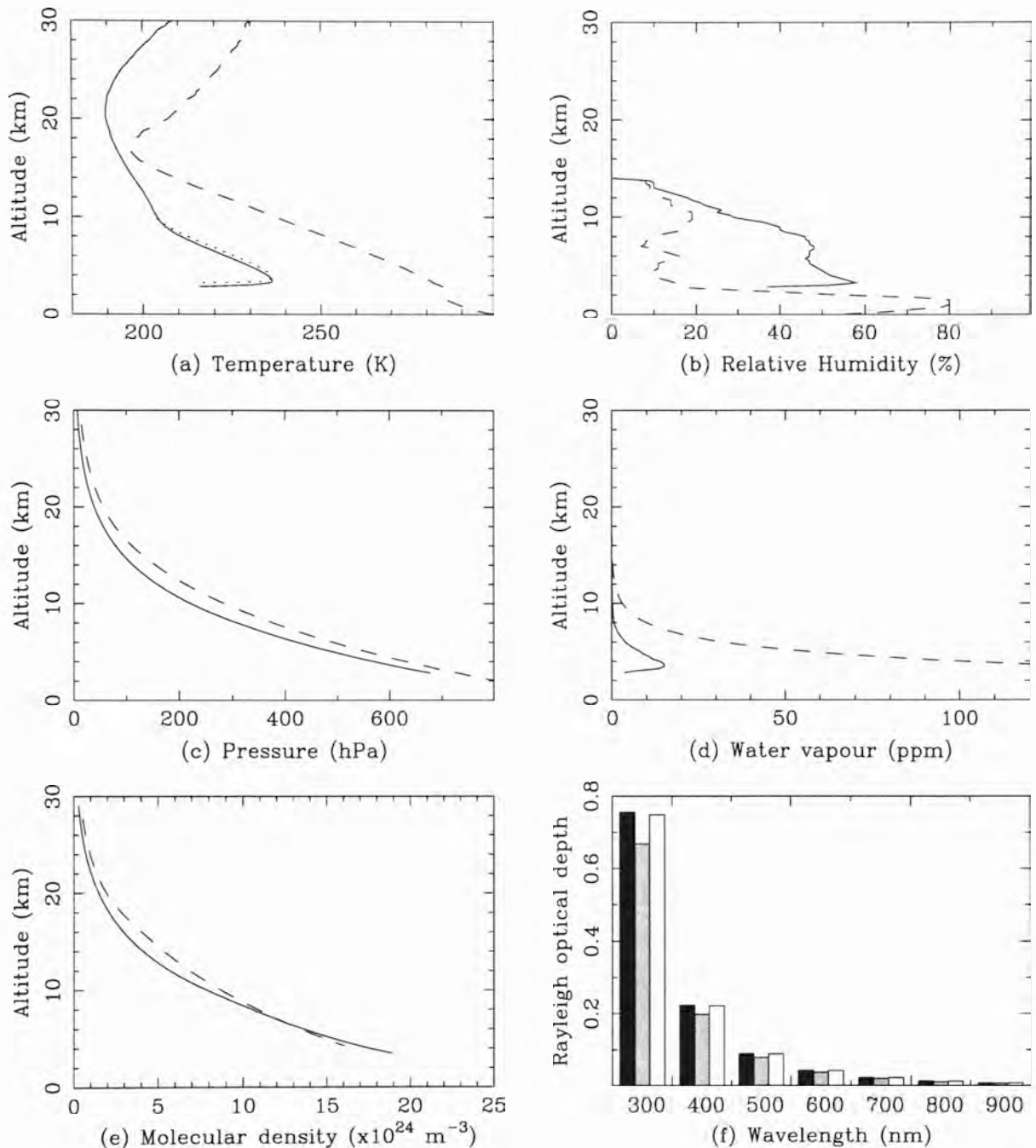


Figure 2.1. Altitude profiles of the average (a) temperature, (b) relative humidity, (c) pressure, (d) water vapour and (e) molecular density at South Pole (*solid*) and Hilo, Hawaii (*dashed*). The dotted line in plot (a) shows the average temperature profile measured at Dome C from 16 balloon launches between March 15th and August 1, 2005 (Agabi et al. 2006). Note that on the profile plots the altitude is plotted on the vertical axis and the dependent variable on the horizontal axis for easy visualisation. *Plot f*: calculated Rayleigh optical depth as a function of wavelength at Dome C (*black*), Dome A (*grey*) and Mauna Kea (*white*); see figure 2.2 for more detail in the 300–450 nm wavelength range.

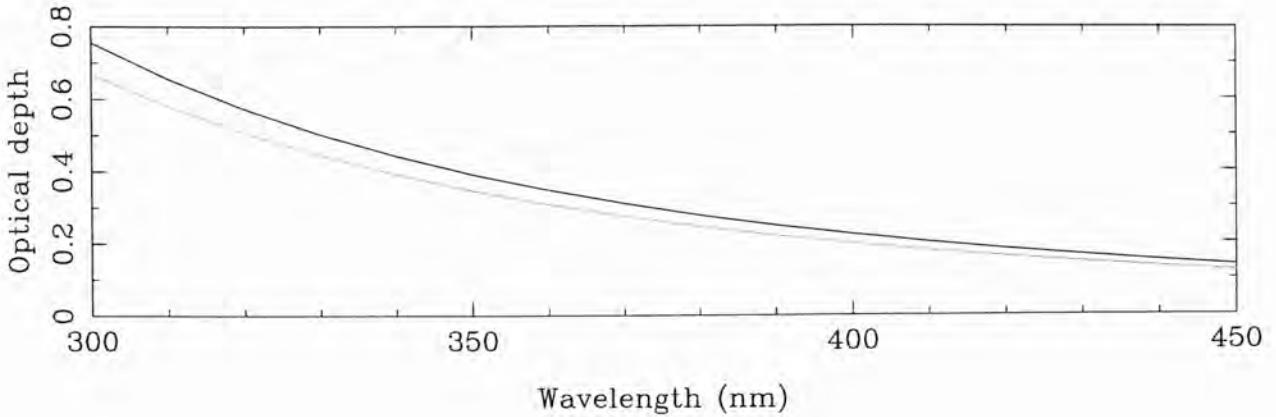


Figure 2.2. The calculated Rayleigh optical depth as a function of wavelength between 300 and 450 nm at Dome C (*black*) and Dome A (*grey*).

2-3 Molecular absorption

2-3.1 Water vapour and clouds

Water vapour is the primary absorber in the atmosphere for most wavelengths of light. The optical thicknesses for water vapour and clouds show complicated and highly variable changes in magnitude with wavelength and time. Figure 2.3 shows the precipitable water content of the atmosphere above Dome C in summer (Valenziano & dall'Oglio 1999), and South Pole, Mauna Kea and the Atacama desert in Chile, in summer and winter (Lane 1998). Valenziano & dall'Oglio (1999) note that the Dome C and South Pole summer measurements are similar and there is reason to believe the water vapour content over Dome C in winter will be similar to South Pole in winter. The water vapour content over Antarctica in winter is considerably less than at Mauna Kea and Atacama, implying less impact from the absorption of light by water vapour.

The optical depth caused by cloud cover at Dome C is expected to be at a minimum level because the skies over Dome C are cloud free for at least 74 (Ashley et al. 2005), and possibly up to 92 (Mosser & Aristidi 2007), per cent of the time (see Section 3-1 for further details).

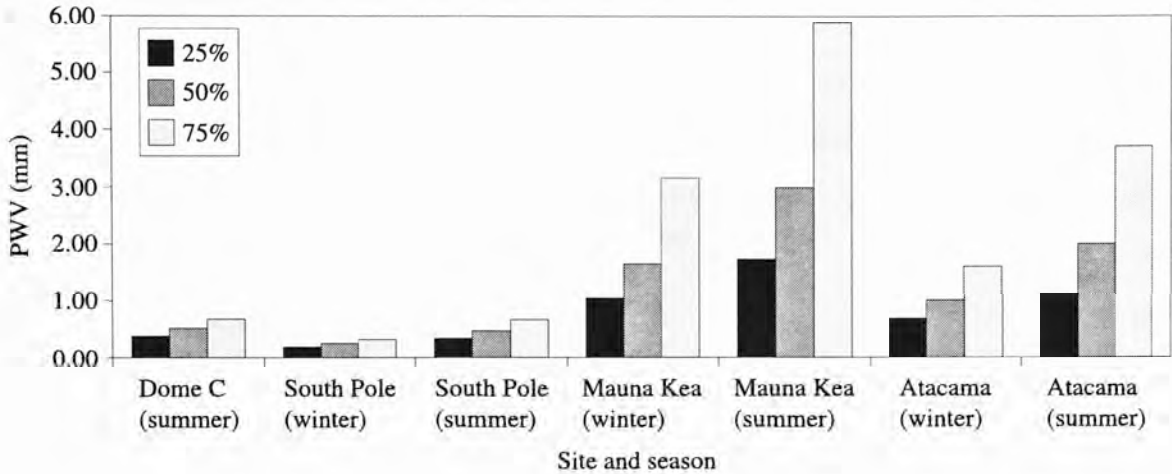


Figure 2.3. Quartile values of precipitable water vapour at Dome C, South Pole, Mauna Kea and Atacama. The values for Dome C were measured in for one month in summer 1997 and are comparable to the South Pole measurements in the same season. Data from Table 1 of Valenziano & dall’Oglio (1999) and Figure 2 of Lane (1998).

2-3.2 Ozone optical depth

The ozone optical depth is determined by the ozone concentration in the atmosphere. Figure 2.4 shows the average ozone content of the atmosphere (from 1996–2005) as a function of 5° latitudinal bins². In the polar regions the data only cover the summer months. For the southern polar regions this means measurements are only taken when the ozone hole is present and consequently the ozone content is at the lower level. The infamous “ozone hole” is unlikely to be of significant benefit to astronomers. From January until August the column density of ozone in the atmosphere above the southern regions is typically the same as at other sites around the world. It is only during the spring months that the ozone content falls to as low as 40% of its normal value. Unfortunately for astronomy, these low ozone values do not occur in the dark winter months, and so no benefit is expected for most astronomical programs. Furthermore, because the Hartley bands of ozone are heavily saturated, even a reduction in ozone column density by a factor of three (i.e., somewhat greater than is actually observed over the South Pole)

²Data compiled from the Total Ozone Mapping Spectrometer, Ozone Processing Team, NASA, on-line <http://toms.gsfc.nasa.gov/ozone/ozoneother.html>.

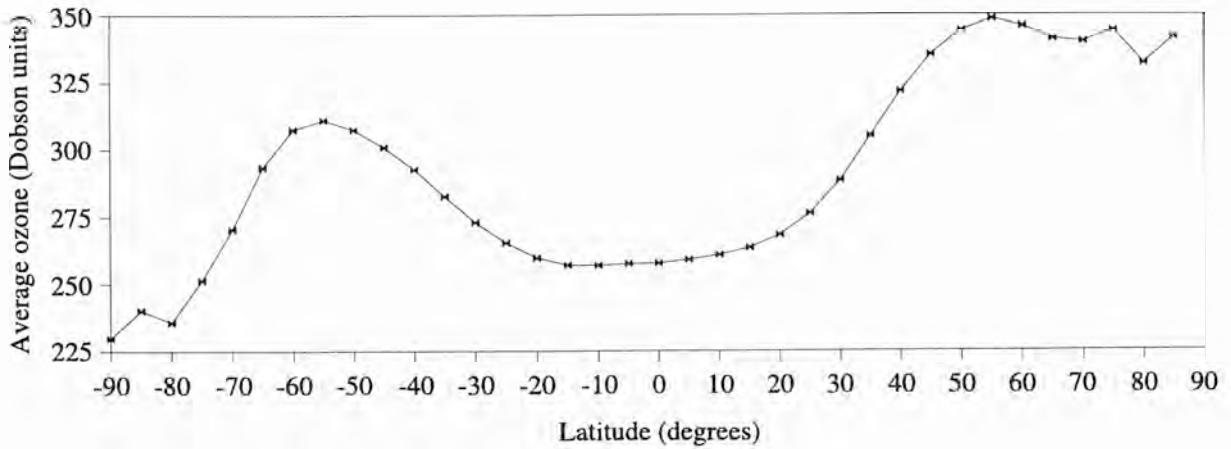


Figure 2.4. Average ozone content in the atmosphere in 5° latitudinal bins from 1996 – 2005. In the polar regions the data only cover the summer months, in particular at the latitude of Dome C (75°S) measurements are only made in January to March and September to December (see the text in Section 2-3.2 for the data source).

would shift the ultra-violet cutoff wavelength of the atmosphere by only about 5 nm (from a LOWTRAN simulation, courtesy of Jon Lawrence).

2-4 Aerosol scattering and absorption

Atmospheric aerosols come from assorted sources including dust from the ground, particles of sea salt, and pollution. Because of this large range of sources the aerosol optical depth varies with the geography of the site, the time and season, and the shape, size, chemical composition, concentration and complex refractive index of the aerosol particles. The complex refractive index of a particle is expressed as $m = n - ik$, where n is the real part (1.45–1.60) and k (0.001–0.1) the imaginary part; the bracketed ranges are typical values for most “dry” atmospheric aerosols (Coulson 1988). High humidity in the air can cause condensation to occur on aerosol particles, which changes the index of refraction, size and mean density of the particle. Most aerosols only absorb light weakly. However some particles such as carbon, are quite strong absorbers.

Aerosols promote both aerosol-to-aerosol and aerosol-to-molecule multiple scattering. Aerosols generally have a different scattering pattern to Rayleigh scattering. The aerosol

scattering cross-section is related to the wavelength of the scattered light by $\sigma_s \propto \lambda^{-\alpha}$, where α is known as the Angstrom exponent. α contains information about the size of the dominant aerosol particles, values close to zero indicate the dominant particles are larger than a few μm in diameter whereas sub-micrometre particles will have values around two (McComiskey et al. 2003). For the best astronomical sites the aerosol optical depth needs to be as small as possible.

2-4.1 Aerosols at Dome C

Dome C has a very clear atmosphere with no dust, so aerosol scattering is expected to be at a minimum level. The aerosol content of the atmosphere at Dome C was monitored during the 2003/2004 summer season (Six et al. 2005); however no night time aerosol measurements exist yet.

Six et al. (2005) monitored the atmosphere 1 km west of the summer station. A histogram of their results for the optical depth at 440 nm is shown in Figure 2.5. In clear-sky conditions they found on average $\tau_a(400 \text{ nm}) = 0.020 \pm 0.003$ and $\tau_a(870 \text{ nm}) = 0.007 \pm 0.003$, and interpolated a value of 0.016 at 500 nm. The average Angstrom coefficient was $\alpha = 1.65$, suggesting that small particles were dominant. In diamond dust³ conditions the optical depth increased to $\tau_a(440 \text{ nm}) = 0.025$ and $\tau_a(870 \text{ nm}) = 0.013$, and α decreased to 1.25 because of the larger ice crystals in the atmosphere. In comparison, Holben et al. (2001) find $\tau_a(500 \text{ nm}) = 0.020 \pm 0.008$ and $\alpha = 1.50 \pm 0.20$ from 1994–1999 at Mauna Loa.

The measurements by Six et al. (2005) only cover a small time period in the summer. Year-round measurements of the aerosol absorption and scattering coefficients have been taken at South Pole and a number of other sites around the world (including Mauna Loa, Hawaii) since 1974 (Bodhaine 1995, and references therein). At the South Pole $\beta_s(550 \text{ nm})$ is very low, varying between 1×10^{-7} and $4 \times 10^{-7} \text{ m}^{-1}$. The maximum values are seen in winter and are associated with long-range mid-tropospheric transport of sea salt from the coast. Scattering from polar stratospheric clouds may also contribute to the maximum seen in winter (Collins et al. 1993). In comparison, at Mauna Loa $\beta_s(550 \text{ nm})$ varies between $\beta_s = 6 \times 10^{-7}$ and $60 \times 10^{-7} \text{ m}^{-1}$, showing maximum values

³The expression “diamond dust” refers to tiny ice crystals in atmosphere.

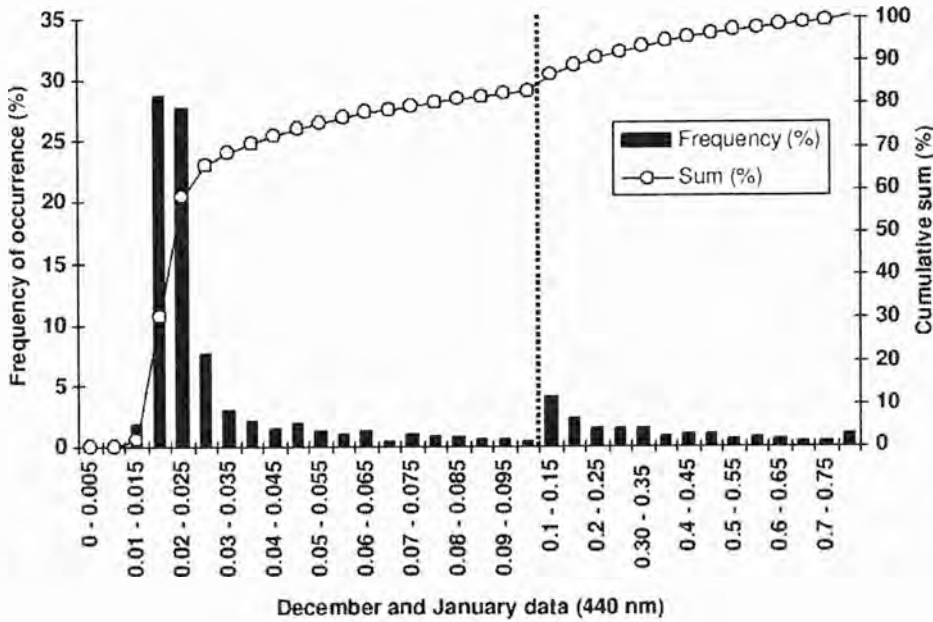


Figure 2.5. Histogram of the aerosol optical depth at 440 nm measured at Dome C in December 2003 and January 2004 (Figure 5 from Six et al. 2005). The dotted vertical line indicates a change of scale on the horizontal axis at $\tau_A = 0.1$.

in the winter and spring that are associated with dust transport.

The atmospheric absorption coefficient (related to the optical depth) is described by the imaginary part k of the refractive index of the atmospheric particles, such that

$$\beta_a(\lambda, z) = \frac{4\pi k}{\lambda}. \quad (2.27)$$

The aerosol absorption coefficient for light at 550 nm at South Pole varies between 2×10^{-10} and $5 \times 10^{-7} \text{ m}^{-1}$, significantly lower than at Mauna Loa (from 1×10^{-8} to $3 \times 10^{-7} \text{ m}^{-1}$) (Bodhaine 1995, and references therein).

2-5 Conclusions

Atmospheric extinction is caused by the scattering and absorption of light by molecules and aerosols. The only way to minimise the molecular contribution is to build a telescope at high altitude. Using two different models, it was shown that the molecular scattering at Dome C should be close to that at Mauna Kea. The molecular scattering at Dome A

will be less than at Mauna Kea, even though they are about the same altitude, because the air pressure at Dome A is less. Absorption by water vapour at Dome C should be less than at Mauna Kea because there is less water vapour in the atmosphere at Dome C. The ozone contribution is likely to be similar at both sites.

The aerosol contribution to atmospheric extinction is site-dependent. The aerosol optical depth measured at Dome C, over a short period of time, is slightly less than that at Mauna Kea. Year-round aerosol measurements at the South Pole show less aerosol scattering and absorption than at Mauna Loa. Dome C may have an even lower atmospheric aerosol content than South Pole because of its greater distance from the coast. Therefore, the scattering and absorption by aerosols is expected to be typically an order of magnitude less at Dome C than at Mauna Kea and the overall atmospheric extinction will be the minimum possible.

“Twilight drops her curtain down, and pins it with a star.”

Lucy Maud Montgomery (1874–1942)

Anne of Green Gables (1908)

Chapter 3

Optical twilight and formal dark-time

The thought of an Antarctic winter brings to mind a long, continuous, dark period. This is true at the South Pole, which experiences about 80 days of continuous astronomical dark-time. However, at lower latitude Antarctic sites the Sun spends more time close to the horizon, resulting in long periods of twilight. At Dome C, less formal optical astronomical dark-time is experienced compared to other sites, especially those close to the equator. The sky brightness at infrared wavelengths is not affected by twilight and the advantages offered by these longer wavelengths are well established (e.g., Storey et al. 2003).

In this Chapter, the amount of usable dark-time at Dome C is investigated. In Section 3-1 the concept of formal astronomical dark-time is explored and the effect of cloud cover on the available time is investigated.

Baldry & Bland-Hawthorn (2001) have suggested using a polarising filter on a telescope to reduce the scattered sunlight contribution to sky brightness during twilight, to achieve “dark-time” observing. At sites close to the equator this probably would not be worthwhile because twilight only lasts a few hours. However, the use of a filter during twilight in Antarctica could be very beneficial, as noted in that paper. For example, if dark-time conditions at Dome C could be achieved at a solar depression angle of 15° (in-

stead of requiring the “formal” depression angle of 18°), the available “dark” observing time would increase by 18%. Sections 3-2 to 3-5 look at the intensity and polarisation of twilight to evaluate the feasibility of using a polarising filter to reduce the twilight and increase the usable dark-time.

The majority of this chapter has been published in Kenyon & Storey (2006), see Appendix C-1.

3-1 Twilight, formal dark-time and cloud cover

Sunlight is the strongest contributor to the brightness of the sky. During the day the surface of the Earth is illuminated by *direct* sunlight and sunlight *scattered* by atmospheric molecules and particles. After sunset, the surface of the Earth is only illuminated by scattered sunlight; the direct component illuminates the atmosphere above the level of the Earth’s shadow. Over the course of twilight the scattered sunlight contribution to sky brightness decreases as higher and less dense levels of the atmosphere are illuminated (Rozenberg 1966). The total brightness (I_B) of the twilight sky can be separated into the contributions from light due to single (I_S) and multiple scattering (I_M), and from the overall night sky background (I_N),

$$I_B = I_S + I_M + I_N. \quad (3.1)$$

The night sky background (discussed further in Chapter 4) includes aurorae, airglow, zodiacal light, integrated starlight, diffuse Galactic light, integrated cosmic light and artificial light pollution.

In the absence of moonlight and artificial sources, scattered sunlight completely dominates the sky brightness until the Sun reaches a zenith angle of about 98° (Pavlov et al. 1995). For solar zenith angles greater than about 98° , multiple scattering accounts for essentially all of the sunlight contribution to sky brightness; this contribution is affected by the aerosol content in the atmosphere (Pavlov et al. 1995; Ugolnikov et al. 2004). Dome C has an exceptionally clear atmosphere with no dust, haze, smog or sand aerosols and therefore it is expected that the intensity of multiply scattered light will be at a minimum possible level. Paradoxically, the lack of aerosols will also decrease the attenuation of sunlight that grazes the Earth’s surface, with the result that at mid-twilight the inten-

sity just above the Earth's shadow could be brighter at some wavelengths than at sites with less clear skies. This has the effect of lowering the effective altitude of the so-called "twilight layer" (Ougolnikov 1999; Ougolnikov & Maslov 2003), creating an opportunity for enhanced scattering by the denser gas at those lower altitudes.

In the final part of twilight, the relative contribution of scattered sunlight to total sky brightness decreases sharply to a negligible level, marking the beginning of the night. In the V-band this occurs when the Sun is depressed 17–19° below the horizon; if there is a high amount of scattering in the atmosphere this can be extended to depressions of 20–23° (Rozenberg 1966). As discussed in Chapter 2, scattering in the atmosphere at Dome C is minimal and the onset of optical dark-time should occur at a relatively small solar depression angle. However, this cannot be quantified except by direct measurement or by detailed modelling using accurate atmospheric aerosol profiles.

A further effect that could brighten the Dome C sky is the high albedo¹ of the snow that covers the Antarctic plateau, which could increase the sky brightness by a small amount at sunset. However, this effect decreases with increasing solar zenith angle and is negligible once the Sun has set (Anderson & Lloyd 1990). During periods when the Moon is above the horizon the high albedo of the snow may also increase the sky brightness beyond that normally experienced during grey time.

Astronomical nighttime is formally defined to begin when the Sun reaches a depression angle of 18°. Figure 3.1 shows the solar elevation angle over the year at Dome C, South Pole and Mauna Kea. This figure shows that Dome C only experiences *almost* continual astronomical dark-time for a short period in the middle of the year, compared to South Pole which has a definite period of continual dark-time. Continuous 24 hour observations from Dome C would be possible for objects that can be observed with brighter skies. From a simple geometric calculation, Dome C has about 50% of the formal astronomical nighttime of Mauna Kea, as shown in Figure 3.2, with long periods of twilight.

The level of cloud cover at each site also needs to be taken into consideration when looking at the amount of dark-time available for optical observations. On the basis of 2001 data, Ashley et al. (2005) report the skies at Dome C to be cloud-less for 74% of the time, with the remaining 26% having more than 1/8 cloud cover. This is a tentative

¹The fraction of the incident light that is reflected from a surface.

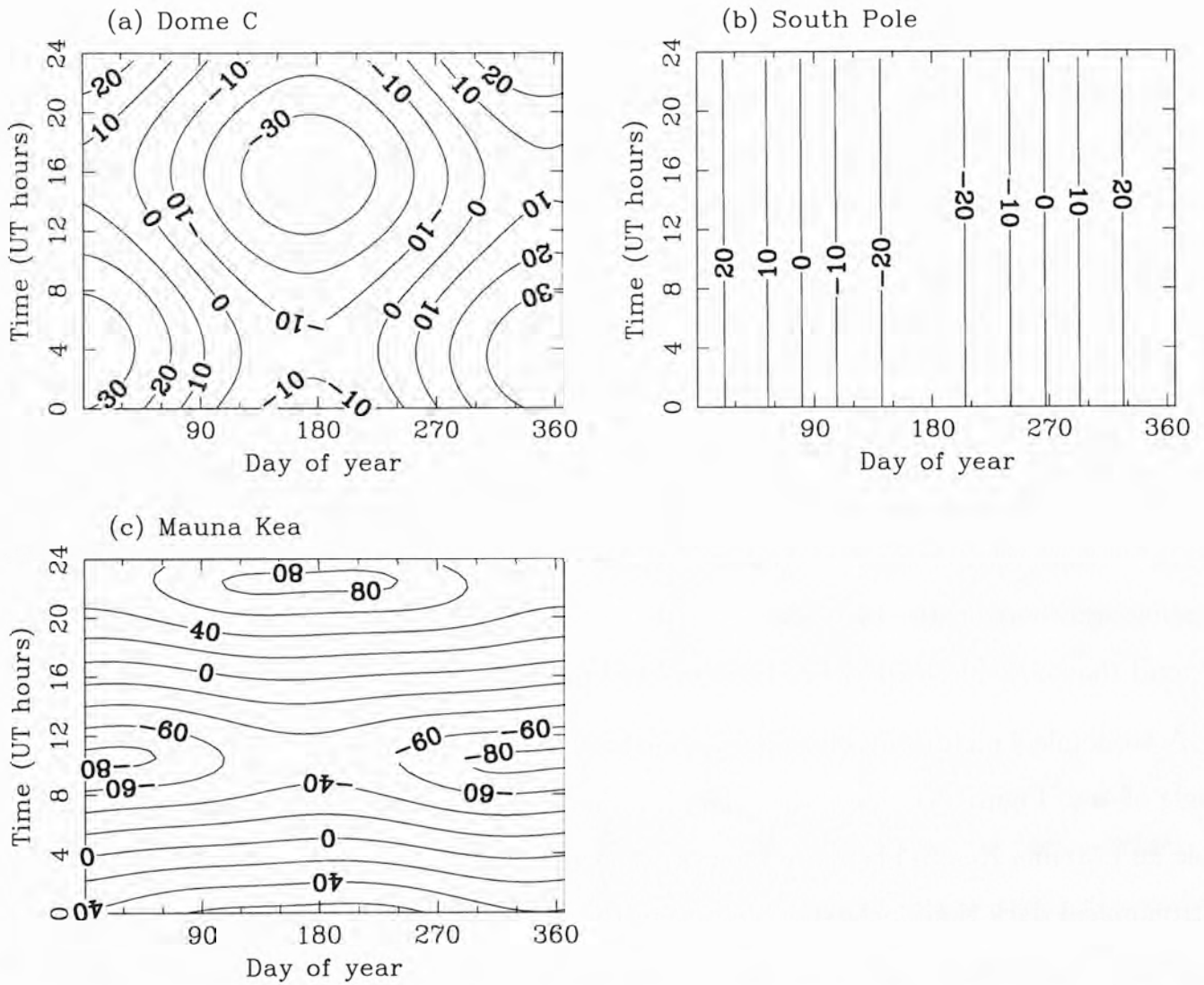


Figure 3.1. Contour maps of the solar elevation angle at (a) Dome C, (b) South Pole and (c) Mauna Kea over the course of one year, 2006.

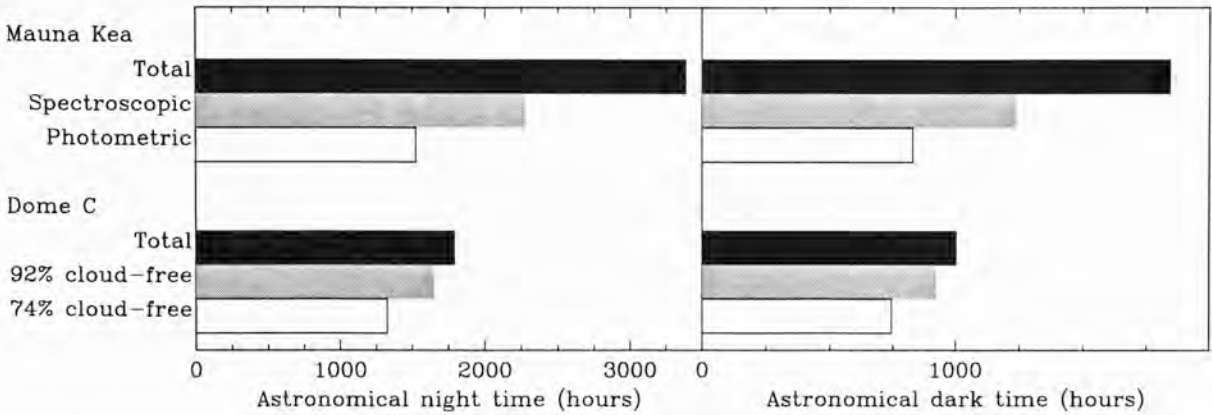


Figure 3.2. Comparison of the total available dark-time (*black*) and the available dark-time with cloud cover taken into account at Dome C and Mauna Kea. For Dome C the *white* and *grey* shading show the number of hours with 74% and 92% cloud free time. For Mauna Kea they show the number of photometric (*white*) and spectroscopic (*grey*) hours available (see the text for further details and references). The graphs on the left show the number of hours of formal astronomical nighttime (i.e., when the Sun is further than 18° below the horizon). The graphs on the right show the number of hours of astronomical dark-time (i.e., astronomical nighttime hours when the Moon is below the horizon or less than one quarter phase).

conclusion based on less than a full year of data from Dome C. Preliminary conclusions based on independent measurements in 2005 (Aristidi et al. 2005a) suggest that the percentage of cloud-free skies at Dome C may be as high as 96%; additional analysis of these data by Mosser & Aristidi (2007) found a metrological duty cycle of at least 92% at Dome C. In comparison, at Mauna Kea there are 45% photometric nights (no clouds) and 67% spectroscopic nights ($\frac{1}{4}$ – $\frac{1}{10}$ cloud cover) (ESO Working Group 2003, and references therein). Taking these percentages into account, the amount of usable dark-time at each site is calculated and shown in Figure 3.2.

If the more optimistic figures of Aristidi et al. (2005a) and Mosser & Aristidi (2007) are confirmed over subsequent years then Dome C will be seen to have a comparable number of usable, astronomically dark hours to Mauna Kea.

3-1.1 Sky coverage

In addition to the long twilight, high latitude sites suffer from reduced sky coverage because of the limited declination range of celestial objects that can be observed. To quantify this we use the fraction f of the total 4π steradians of the heavens that can be seen from a site of given latitude over a 24 hour period, that is

$$f = \frac{\sin N - \sin S}{2} \quad (3.2)$$

where N is the northernmost declination observable and S is the southernmost. We consider two cases: a zenith limit of 45° (1.4 airmasses), and a zenith limit of 60° (2 airmasses). Figure 3.3 shows the the declination range and f for these two cases as a function of latitude; the results for Dome C, South Pole, Mauna Kea and the Equator are summarised in Table 3.1. Mauna Kea has access to 81% of the sky at 2 airmasses or less, while at Dome C only 37% of the sky is similarly available.

In the case of a high-latitude southern site such as Dome C, this restricted sky coverage is mitigated somewhat by the accessibility of several key sources such as the Large (decl. = 69° S) and Small (decl. = 73° S) Magellanic Clouds and the Galactic Centre (decl. = 28° S). Such southern sources are of course favourably observed from Dome C. For example, although the Galactic Centre reaches comparable maximum elevations of 44° at Dome C and 41° at Mauna Kea, it is above 30° elevation for 1300 dark hours per year at Dome C, but only 660 dark hours per year at Mauna Kea. The advantages of a high-latitude southern site for the continuous monitoring of southern objects have already been discussed by a number of authors; such as Deeg et al. (2005). Another benefit offered by high latitude sites is the opportunity to observe object for long periods at almost constant zenith angle (and corresponding constant air mass).

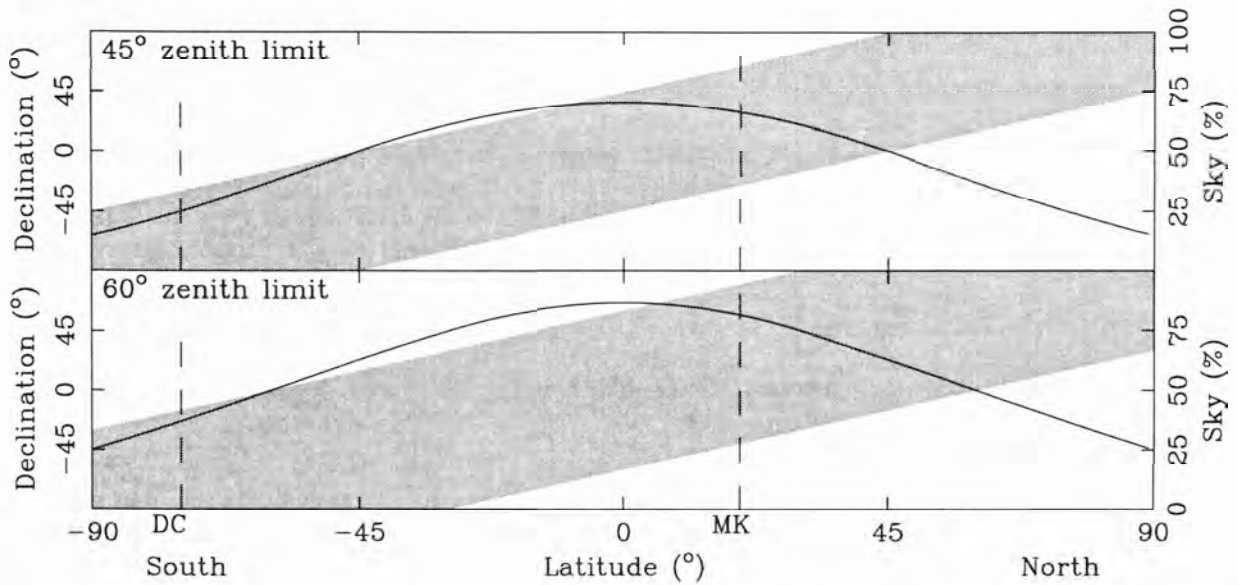


Figure 3.3. The observable sky as a function of latitude. The shaded regions show the declination range available (left axis). The solid lines show the percentage of the whole 4π steradians of the sky that is observable (right axis). The top plot shows the values for the 45° zenith limit and the bottom plot shows the range for the 60° zenith limit. The dashed lines show the latitudes of Dome C and Mauna Kea.

Table 3.1. The amount of sky observable from a site depends on the latitude of the site. This table shows the declination range and the percentage of the sky that is observable at each site for two zenith limits.

Site	45° Zenith limit		60° Zenith limit	
	Decl. Range	Sky percentage	Decl. Range	Sky percentage
Equator	$45^\circ\text{S} - 45^\circ\text{N}$	70 %	$60^\circ\text{S} - 60^\circ\text{N}$	86 %
Mauna Kea	$26^\circ\text{S} - 64^\circ\text{N}$	66 %	$41^\circ\text{S} - 79^\circ\text{N}$	81 %
Dome C	$90^\circ\text{S} - 30^\circ\text{S}$	25 %	$90^\circ\text{S} - 15^\circ\text{S}$	37 %
South Pole	$90^\circ\text{S} - 45^\circ\text{S}$	14 %	$90^\circ\text{S} - 30^\circ\text{S}$	25 %

3-2 Using a polariser to reduce sky background

The twilight sky brightness is a combination of singly and multiply scattered sunlight, and the background night sky illuminance, as summarised in Equation 3.1. When sunlight enters the atmosphere it is unpolarised. Sunlight becomes polarised in the Earth's atmosphere through scattering interactions with permanent (mainly oxygen and nitrogen) and variable atmospheric gases, and solid and liquid particles suspended in the atmosphere (aerosols, water, ice crystals). The degree of polarisation (P) quantifies the amount of polarised light as a fraction of the total light. The total degree of polarisation of twilight is given by:

$$P = \frac{I_S}{I_B} P_S + \frac{I_M}{I_B} P_M \quad (3.3)$$

where P_S and P_M are the degrees of polarisation of singly and multiply scattered light. The polarised component of the background night sky flux is assumed to be negligible with respect to that of the scattered sunlight.

The following derivation of the possible advantage of a polariser is summarised from Baldry & Bland-Hawthorn (2001). If a polariser is inserted in front of the receiver, the background flux received by the observer is reduced to

$$\begin{aligned} I'_B &= \tau [I_N + I_S (1 - P_S) + I_M (1 - P_M) + 2\gamma (P_M I_M + P_S I_M)] \\ &= \tau I_B [1 - P (1 + 2\gamma)] \end{aligned} \quad (3.4)$$

where τ is the transmission of the polariser with unpolarised light, γ is the extinction of the polariser ($\gamma \ll 1$) and P is the total polarisation as defined in Equation 3.3. A figure of merit, related to the observing efficiency for an instrument and telescope, is defined as

$$f = \frac{R^2}{t} = \frac{\epsilon I_O^2}{I_O + I_B} \quad (3.5)$$

where R is the signal to noise ratio, t is the integration time, ϵ is the efficiency of the telescope and instrument, and I_O is the object flux. If a polariser is inserted to reduce the background flux, this figure of merit is given by

$$f' \simeq \frac{\epsilon' (\tau I_O)^2}{\tau I_O + I'_B} = \frac{\epsilon' \tau I_O^2}{I_O + I_B [1 - P (1 + 2\gamma)]} \quad (3.6)$$

where ϵ' is the efficiency of the telescope and instrument with polarised light.

Using Equations 3.5 and 3.6, the gain in observing efficiency when using a polariser is given by

$$\frac{f'}{f} \simeq \tau \frac{\epsilon'}{\epsilon} \left[\frac{I_O + I_B}{I_O + I'_B} \right] = \tau \frac{\epsilon'}{\epsilon} \frac{I_O + I_B}{I_O + I_B [1 - P(1 + 2\gamma)]}. \quad (3.7)$$

A polariser will be beneficial whenever the gain is greater than unity. Assuming photon noise limited observations, a perfect polariser, no change in instrument response with polarisation, and setting $\gamma = 0$ and $\epsilon'/\epsilon = 1$, the sky must be polarised to

$$P > (1 - \tau) \frac{I_O + I_B}{I_B} \quad (3.8)$$

for the use of a polarising filter to be worthwhile. We consider two examples, in both cases setting $\tau = 0.48$.

1. For objects that are very dark compared to the sky background, a polarisation of $P > 52\%$ is required for this technique to be beneficial.
2. For a sky background of $20.5 \text{ mag arcsec}^{-2}$ and object of magnitude of $22 \text{ mag arcsec}^{-2}$, the polarisation must be greater than 65% for the use of a polariser to be beneficial.

Baldry & Bland-Hawthorn (2001) model the brightness of the sky at zenith during twilight, with and without the use of a polarising filter. In this model they assume the polarisation of twilight is always 85% , independent of the solar elevation angle. Although the polarisation of singly scattered light is probably always above 85% (for a clear atmosphere), the total polarisation depends on the relative intensity of the singly and multiply scattered light to the total sky intensity, as Equation 3.3 shows. In the next sections we look in some detail at the total polarisation of light in the atmosphere as a function of solar zenith angle and wavelength, to explore the benefit that might be gained by using a polariser on an Antarctic telescope.

3-3 The polarised sky

As a first step to evaluate the use of a polarising filter, the amount of polarised light in the sky is examined using a simple model for singly scattered sunlight. The polarisation

of sunlight singly scattered in a pure Rayleigh atmosphere can be described by (Coulson 1988):

$$P_S = \frac{P_S^{\text{MAX}} \sin^2 \alpha}{1 + \cos^2 \alpha} \quad (3.9)$$

$$\cos \alpha = \sin Z_{\odot} \sin Z \cos \phi + \cos Z_{\odot} \cos Z$$

where P_S^{MAX} is the maximum polarisation, Z_{\odot} and Z are the zenith angles of the Sun and observed sky point, and ϕ is the azimuth of the observed sky point from the solar meridian. In this model the atmosphere is considered to contain only permanent gases with no aerosols, clouds, water vapour or ionised particles; the scattering particles are assumed to be spherical; and the refractive index very close to unity.

We applied this model for solar zenith angles $Z_{\odot} = 90^\circ, 96^\circ, 102^\circ$ and 108° (i.e., from sunset to the end of astronomical twilight); Figure 3.4 shows the results. The light shading shows that a large section of the singly scattered sunlight perpendicular to the Sun is polarised to a high degree, whereas in the direction parallel to the Sun the polarisation rapidly drops off with zenith angle.

The degree of polarisation in the real atmosphere differs from this model because of non-isotropic molecular scattering, aerosol scattering and reflection from the Earth's surface (Coulson 1983). However, the *pattern* of polarisation across the sky will be close to the Rayleigh model. Molecular scattering is non-isotropic because atmospheric oxygen and nitrogen molecules are not spherical; this decreases the polarisation by about 3–5%. Aerosols promote depolarisation by encouraging aerosol-to-aerosol and aerosol-to-molecule multiple scattering. The depolarising effects of aerosols depend on the concentration, refractive index and size of the particles. The addition of aerosols will also increase the solar zenith angle at which maximum polarisation occurs, and will introduce a wavelength dependence.

The polarisation of sunlight can be further reduced by reflection from high level clouds and cloud forming particles. Pomozi et al. (2001) studied the effect of clouds on the polarisation of the sky compared to clear skies and found that although the degree of polarisation may decrease, the *pattern* of polarisation is the same if part of the atmosphere between the clouds and the Earth is directly illuminated by sunlight.

The degree of polarisation from single scattering is essentially independent of wavelength, however the scattering efficiency from atmospheric gases is proportional to λ^{-4}

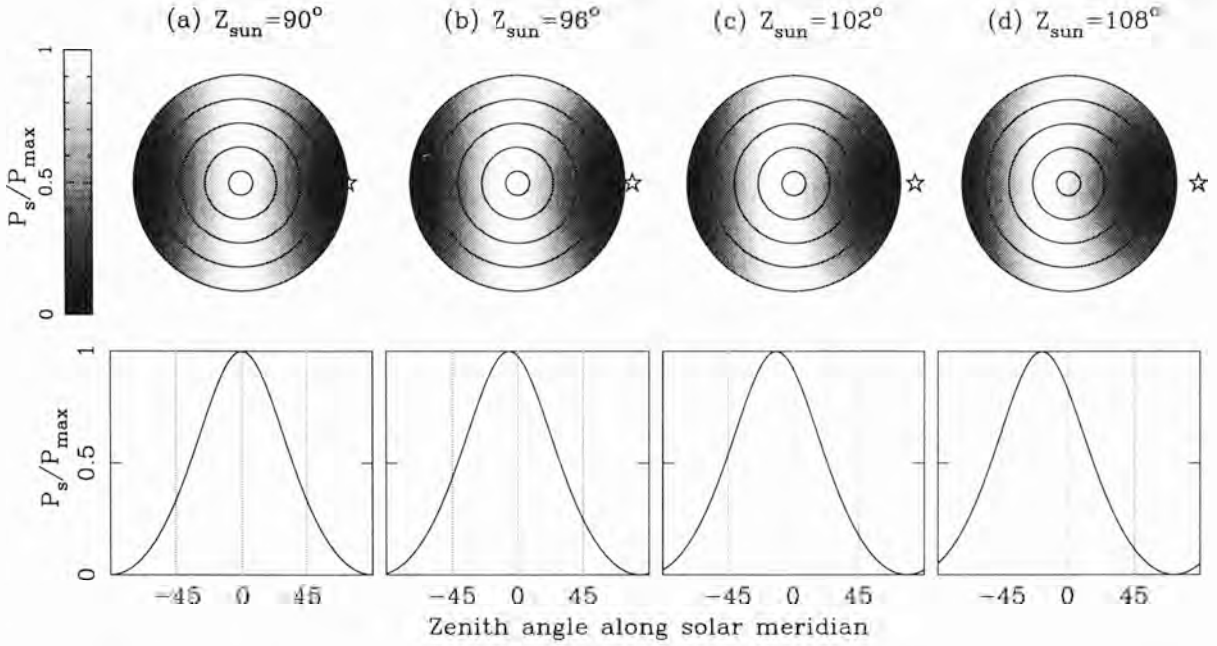


Figure 3.4. *Top:* Full sky plots of the degree of polarisation (P_s) as a fraction of the maximum polarisation (P_{\max}), using the Rayleigh model for solar zenith angles (a) 90° , (b) 96° , (c) 102° and (d) 108° (i.e., from sunset to the end of astronomical twilight). The circles indicate elevation angle and are spaced 20° apart, the outermost circle is the horizon. The position of the Sun is shown as a star in each plot. *Bottom:* a horizontal cut through each sky image.

(e.g., Coulson 1980), resulting in a wavelength dependence in I_S/I_B . Multiply scattered sunlight is polarised to a lesser degree than singly scattered light. In the Rayleigh model for single scattering the position of the maximum polarisation is always 90° from the Sun. The maximum polarisation point for multiple scattering should remain at zenith regardless of Z_\odot . The position of the maximum polarisation therefore gives an indication of the relative strength of primary and multiple scattering (Postylyakov et al. 2003). If the maximum polarisation occurs when the Sun is below the horizon, this indicates multiple scattering. Aerosol scattering will also change the maximum scattering angle.

The highest polarisation of light occurs when water vapour and aerosol concentrations are very low and the Rayleigh optical depth is as small as possible, suggesting that scattered sunlight at Dome C should, in general, be more highly polarised than at temperate or tropical sites.

3-4 Polarisation at the South Pole and effects of ice precipitation

At this stage no measurements of the polarisation of twilight at Dome C have been taken. However, Fitch & Coulson (1983) measured the polarisation of the sky at the South Pole during summer, under both clear sky conditions and conditions when ice crystals were evident.

A maximum polarisation at zenith of 80% was observed during clear sky conditions when the Sun was 10° above the horizon. Measurements taken on days with ice crystals in the atmosphere showed a decrease in polarisation of $\sim 6\%$ at 700 nm and of $< 1\%$ at 398 nm. In addition, the presence of ice crystals moved the position of the maximum polarisation away from the Sun by a few degrees. Further measurements taken when the Sun was on the horizon showed greater effects, with the maximum polarisation decreased by 10% at 398 nm and 45% at 872 nm compared to clear sky conditions. The effect of ice crystals is greater at longer wavelengths. The authors note that the data set is small and there may be ice crystal formation in the atmosphere when there are no visible clouds.

These results show that in the absence of ice crystals the atmosphere at South Pole is very clean and is very close to a “Rayleigh atmosphere”; that is, the only scatterers in the atmosphere are gaseous molecules. We expect that the atmosphere at Dome C will also closely resemble a Rayleigh atmosphere and therefore, at small solar depression angles, the scattered light will be highly polarised. The measurements by Fitch & Coulson (1983) were conducted when the Sun was on or above the horizon. In the next section the behaviour of the polarisation of twilight at various other high altitude, clean sites is analysed.

3-5 Polarisation measurements during twilight

During twilight the number of gas molecules and aerosol particles able to participate in scattering changes as different levels of the atmosphere are illuminated by solar radiation and the lower levels are shadowed by the Earth. The vertical concentration of molecules and aerosols changes with altitude, leading to changes in the polarisation and intensity of skylight as a function of solar angle and wavelength. Single scattering is confined to a

thin atmospheric layer; for $Z_{\odot} > 90^{\circ}$ the thickness of this layer does not depend on the solar zenith angle or the zenith distance of the observation (Ougolnikov 1999). However, the minimum altitude at which this layer begins slowly increases as the Sun sinks further and further below the horizon. Multiple scattering is confined to a thin atmospheric layer that is much closer to the Earth's surface than the single scattering layer (Ougolnikov 1999). For example, for $Z_{\odot} = 94^{\circ}$ the height of the single scattering layer is about 33 km and for multiple scattering the height of the layer is about 12 km (at $Z_{\odot} = 98^{\circ}$ these increase to 80 and 17 km respectively). The contribution of multiple scattering to the total background intensity can only be determined by computational modelling of the atmosphere coupled with intensity and polarisation measurements.

Measurements of the maximum polarisation at zenith during twilight can be used to determine the vertical profile of aerosols in the atmosphere (see, for example, Coulson 1980 and Ashburn 1952). In this section, various measurements of the twilight polarisation and intensity at various high altitude, clean sites are analysed and combined to form a general picture. The behaviour of the total degree of polarisation P as a function of solar zenith angle Z_{\odot} can be roughly divided into the three twilight regimes (civil, nautical and astronomical); the benefit of using a polariser in each regime is assessed. P also behaves somewhat differently for red $P(\text{red } \lambda)$ and blue $P(\text{blue } \lambda)$ wavelengths, with a division around $\lambda = 550$ nm. Note that $P(Z_{\odot})$ usually shows day-to-day variations at each site, probably caused by different weather conditions and vertical aerosol concentrations, and there is some overlap in the behaviour of $P(Z_{\odot})$ for the three twilight groups.

The typical behaviour of the degree of polarisation P as a function of solar zenith angle Z_{\odot} and wavelength λ is summarised in Table 3.2, which is derived from the work of Bondarenko (1964), Coulson (1980), Pavlov et al. (1995) and Postylyakov et al. (2003). Figure 3.5, from Pavlov et al. (1995), shows the typical variations of single, multiple and total polarisation as a function of solar zenith angle during twilight.

The $Z_{\odot} = 102\text{--}108^{\circ}$ regime is where one might have hoped to turn twilight into dark-time. For the use of a polariser to be worthwhile the sky must be polarised by at least 52%. However, between $Z_{\odot} = 102^{\circ}$ and 108° the overall polarisation at these sites drops from about 50% (depending on wavelength) to zero, and from $Z_{\odot} \sim 104^{\circ}$ the night illuminance accounts for more than 80% of the sky brightness, reaching 100%

Table 3.2. Summary of the typical behaviour of the degree of polarisation P in three twilight regimes. The first two rows for each regime describe the behaviour of blue and red wavelengths of light, the next row shows the dominant processes and the last row shows the maximum object brightness I_O (mag arcsec⁻²) at selected solar zenith angles (Z_{\odot}) for which a polariser will yield an advantage at 690 nm, based on the results of Pavlov et al. (1995). This table was compiled from Bondarenko (1964); Coulson (1980, 1988); Pavlov et al. (1995).

Civil twilight $Z_{\odot} = 90\text{--}96^{\circ}$	
P(blue λ)	The maximum polarisation occurs at a solar zenith angle of $\sim 92\text{--}94^{\circ}$, after which the polarisation decreases with increasing Z_{\odot} . The polarisation is wavelength dependent in this range.
P(red λ)	The maximum polarisation occurs at $Z_{\odot} \sim 90^{\circ}$ then $P(Z_{\odot})$ decreases. Occasionally a minimum in polarisation is seen at $Z_{\odot} = 94\text{--}95^{\circ}$. The polarisation is independent of wavelength.
Processes	Single scattering dominants over multiple and I_N is negligible.
Advantage	$Z \sim 90^{\circ}, I_O > 5.3$; $Z \sim 96^{\circ}, I_O > 9.9$
Nautical twilight $Z_{\odot} = 96\text{--}102^{\circ}$	
P(blue λ)	$P(Z_{\odot})$ decreases steeply to a flat or a minimum section between 98° and 102° .
P(red λ)	$P(Z_{\odot})$ decreases steadily. Occasional 2 nd maximum is observed, this is associated with aerosol layers.
Processes	Multiple scattering dominates over single, and $I_N \approx 0$ for $Z_{\odot} < 98^{\circ}$. In both wavelength ranges the polarisation is less than about 60%.
Advantage	$Z \sim 98^{\circ}, I_O > 14.3$; $Z \sim 100^{\circ}, I_O > 18.3$
Astronomical twilight $Z_{\odot} = 102\text{--}108^{\circ}$	
P(blue λ)	$P(Z_{\odot})$ decreases steeply then starts to flatten at $Z_{\odot} \sim 104^{\circ}$, reaching zero around $Z_{\odot} \sim 108^{\circ}$. Strongly λ dependent.
P(red λ)	$P(Z_{\odot})$ decreases steeply, reaching zero polarisation around 106° . Strongly λ dependent
Processes	Single scattering dominates over multiple for $Z_{\odot} > 104^{\circ}$ and the I_N dominates over the total scattered light. Aerosol scattering is important in this range. $P \lesssim 50\%$ for both wavelength ranges.
Advantage	No advantage in using a polariser.

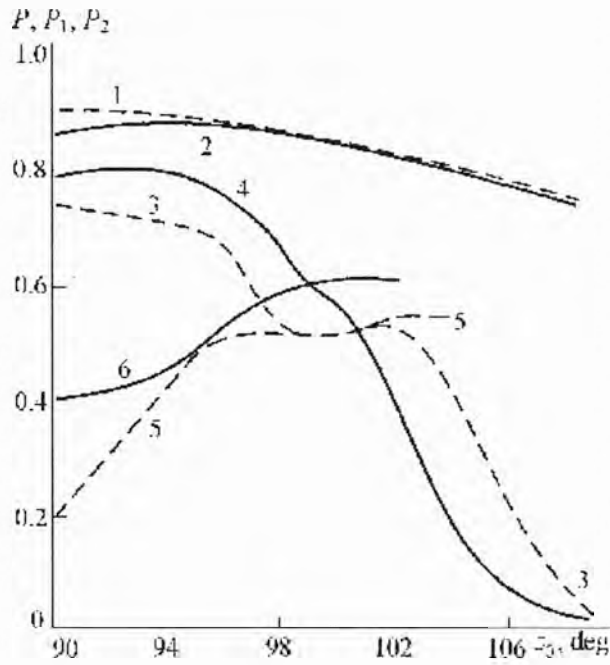


Figure 3.5. Polarisation as a function of solar zenith angle. Curves 1 and 2 are calculated for singly scattered light (P_S) in a clear atmosphere, curves 3 and 4 are averaged measurements of the total polarisation (P), and curves 5 and 6 are the calculated polarisation for multiply scattered light (P_M). The dashed lines are for polarisation at 480 nm and the solid lines are for 690 nm. (Plot is from Pavlov et al. 1995).

at the onset of night (Pavlov et al. 1995). Aerosol scattering plays an important role, causing depolarisation at certain wavelengths (i.e., when $2\pi r \sim \lambda$, where r is the particle size). The total polarisation at Dome C at these solar zenith angles is likely to be similar to the sites discussed because they are all at high altitude—therefore have small Rayleigh optical depths—and have clean atmospheres, with few aerosols. In addition all the measurements were taken on visibly clear days.

We conclude that there is likely to be no gain in using a polariser, in this regime. However, for observations of bright stars (for example, direct imaging of exoplanets around host stars of typical magnitudes $V = 11$) a high sky background can be tolerated. Using a polariser for this type of observation could be advantageous during those times when the Sun is 6° or further below the horizon. Of course if the light from the object itself is polarised then this method would have less benefit.

3-6 Conclusions

Most astronomical observations require very dark skies. We find that Dome C has a comparable number of cloud-free, formal astronomical dark hours to a more temperate site such as Mauna Kea. In the next Chapter the quality of this dark-time at Dome C is assessed. The fraction of sky observable at Dome C is considerably lower than at Mauna Kea; however some important southern objects are observable for longer at Dome C than Mauna Kea. The scattering at Dome C is expected to be close to the minimum possible. For this reason it is expected that astronomical nighttime will start when the Sun is closer to the horizon than at sites with high scattering. However, no firm conclusions can be made in this respect without detailed atmospheric modelling or measurements at the site. An instrument to measure the twilight and nighttime sky brightness is described in Chapter 5.

We assessed the use of polarising filters during twilight as a means to increase the amount of dark-time. We find that some advantage could be gained through the use of polarising filters in early evening twilight and late morning twilight; however, as the sky becomes darker, such filters are of less benefit.

“The summer day is closed—the sun is set:
Well they have done their office, those bright hours,
The latest of whose train goes softly out
In the red west.”

William Cullen Bryant (1794–1878)
An Evening Reverie (1842)

Chapter 4

Optical sky brightness

In Chapter 3 the twilight sky brightness and the *quantity* of formal optical dark time at Dome C were investigated; in this Chapter the *quality* of the dark time is assessed. The sky is never completely dark at optical wavelengths, even after the Sun has fully set. At any site the optical night sky is always brightened with airglow, zodiacal light, integrated starlight, diffuse Galactic light and extra-galactic light. Further brightening can be caused by scattered sunlight, auroræ, moonlight and artificial sources. A brief summary of the physical origins and dependencies of each of these contributions is presented in Table 4.1. Atmospheric scattering of the flux from each of these sources adds significantly to the sky brightness; for example, the contribution from zodiacal light can be increased by more than 15% by scattering and that from integrated starlight by 10–30% (Leinert et al. 1998). At the darkest sites the dark time sky background is on the order of 22.0–21.1 V mag arcsec⁻² at zenith (Leinert et al. 1998). The sky brightness at a particular site varies with solar activity, as first noted by Rayleigh (1928); for example, Walker (1988) records a change of at least 1 mag arcsec⁻² in sky brightness with solar activity at San Benito Mountain.

Dome C exhibits many characteristics that are extremely favourable to optical as-

Table 4.1. Contributions to the light of the night sky. Adapted from Roach & Gordon (1973).

Source	Physical Origin	Varies with
Scattered sunlight	Sunlight scattering from molecules and particles in the upper atmosphere	Ecliptic coordinates, season, location, aerosols
Moonlight	Sunlight reflected from the lunar surface, then scattered in the Earth's atmosphere	Lunar phase, position of the moon, aerosols
Aurora	Excitation of upper atmosphere atoms and molecules by energetic particles	Magnetic latitude, season, magnetic activity, solar activity
Airglow	Chemiluminescence of upper atmosphere atoms and molecules	Zenith angle, local time, latitude, season, solar activity, altitude, geomagnetic latitude
Zodiacal light	Sunlight scattered by interplanetary dust	Ecliptic coordinates
Integrated starlight ..	Unresolved stars in the Milky Way	Galactic coordinates
Diffuse galactic light .	Scattering of starlight by interstellar dust	Galactic coordinates
Integrated cosmic light	The universe	Galactic coordinates, cosmological red shift
Light pollution	Artificial lighting	Proximity to civilisation

tronomy; however, at this stage few measurements have been made of the brightness of the optical night sky. In the following sections each contribution to night sky brightness is considered and a comparison to Mauna Kea, Hawaii is presented. See Leinert et al. (1998) for a comprehensive discussion of diffuse night sky brightness, Patat (2003) for an in-depth survey of *UBVRI* night sky brightness at ESO-Paranal, and Benn & Ellison (1998) for a review of sky brightness measurements at La Palma. This chapter is an expansion of the work published by Kenyon & Storey (2006); see Appendix C-1.

4-1 Moonlight

Moonlight brightens the sky in much the same way as the Sun—by direct transmission and scattering. The sky brightness contribution caused by the Moon depends on its position and phase. Figures 4.1 and 4.2 show the elevation of the Sun and Moon, together with the phase of the Moon, for Dome C and Mauna Kea over the course of one year (2005). The darkest skies are when the Sun is far below the horizon and either the Moon is below the horizon or the phase of the Moon is close to new.

The 18 year lunar nodal cycle causes the Moon to cycle between declination ranges of $\pm 29^\circ$ and $\pm 18^\circ$. At Dome C, this results in the maximum elevation of the Moon cycling between about 33° and 43° over the 18 years. At sites closer to the equator, such as Mauna Kea, the Moon can always pass through the zenith, regardless of the lunar nodal cycle. Since the scattered moonlight contribution reaches a minimum level about 60° to 90° away from the Moon, a lower elevation angle is an advantage.

In the next section a model for moonlight scattering (Krisciunas & Schaefer 1991) is summarised and then applied to Dome C and Mauna Kea.

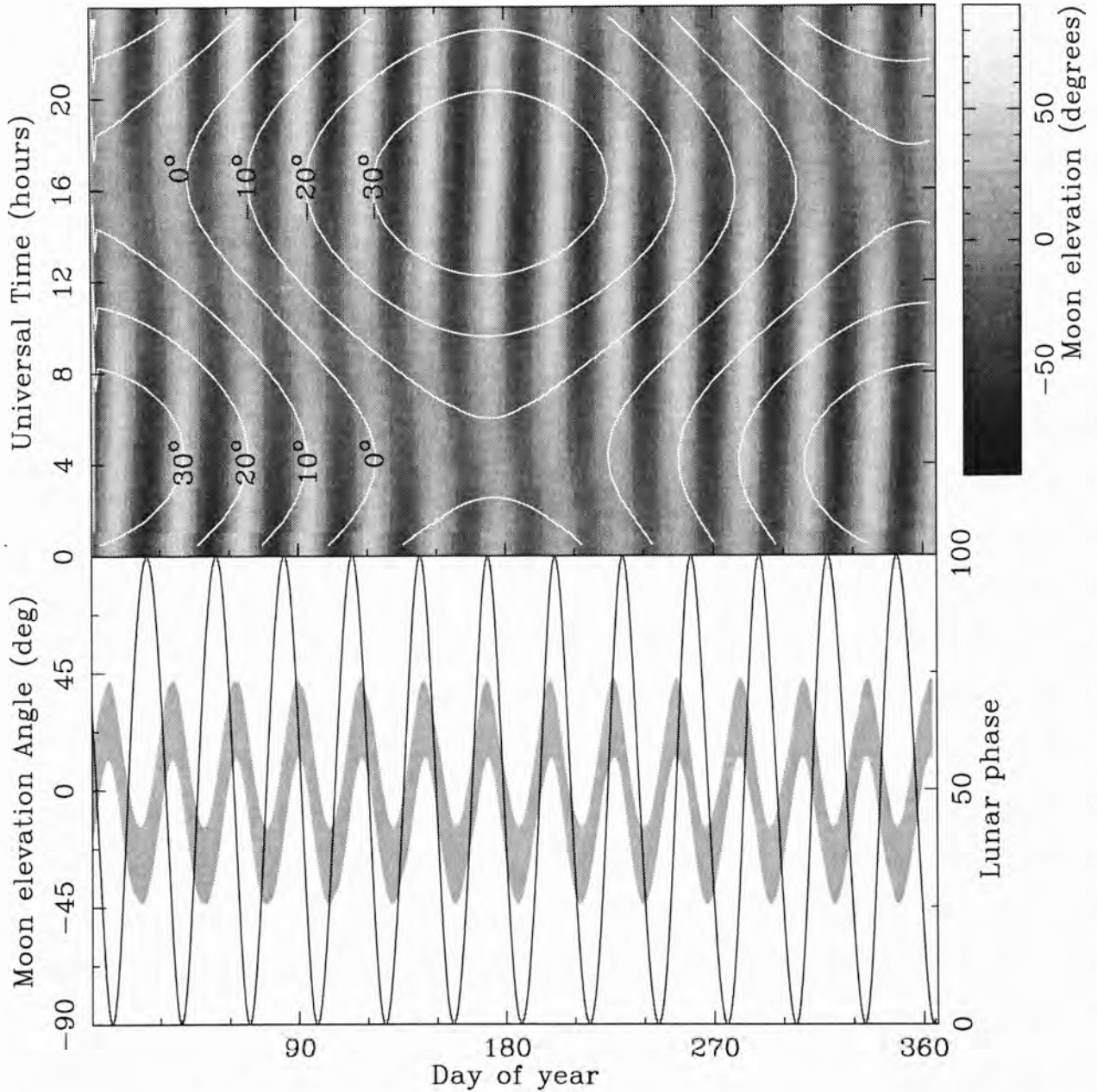


Figure 4.1. *Top:* solar and lunar elevation angles at Dome C over the course of one year (2005). The contours show the solar elevation angles and the grey scale shows the lunar elevation angles according to the scale to the right. The darkest skies are when the Sun is far below the horizon and either the Moon is below the horizon (dark shading) or the phase of the moon is close to new. *Bottom:* the lunar elevation angle (grey, left scale) and the lunar phase angle (black, right scale) over the same period.

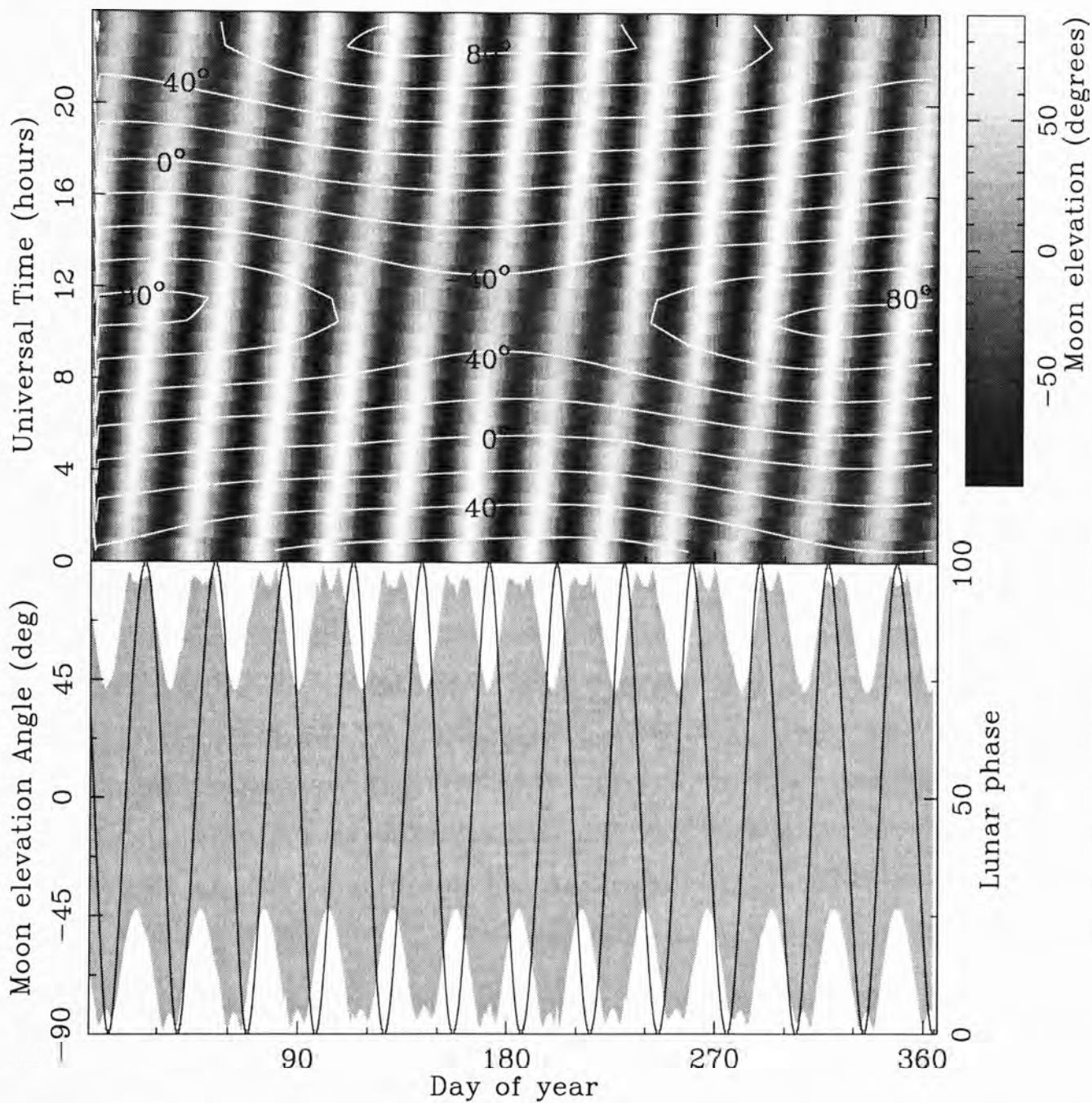


Figure 4.2. Solar and lunar elevation angles and lunar phase angle at Mauna Kea over the course of one year (2005). See the caption on Figure 4.1 for further details.

4-1.1 Model of the moonlight contribution to sky brightness

To quantify the effect of the different range of Moon elevation at Dome C and Mauna Kea, the scattered moonlight brightness was calculated using the model of Krisciunas & Schaefer (1991). In this model the scattered moonlight brightness is given by the following set of equations:

$$B_M = f(\rho)I^*10^{-0.4kX(Z_M)} \left(1 - 10^{-0.4kX(Z)}\right) \quad (4.1)$$

$$f(\rho) = f_A(\rho) + f_M(\rho) \quad (4.2)$$

$$f_A(\rho) = \begin{cases} 10^{6.15-\rho/40} & \text{for } 10^\circ < \rho < 80^\circ \\ 6.2 \times 10^7 \rho^{-2} & \text{for } \rho < 10^\circ \end{cases} \quad (4.3)$$

$$f_M(\rho) = 2.27 \times 10^5 (1.06 + \cos^2 \rho) \quad (4.4)$$

$$I^* = 10^{-0.4(m(\alpha)+16.57)} \quad (4.5)$$

$$m(\alpha) = -12.73 + 0.026 |\alpha| + 4 \times 10^{-9} \alpha^4 \quad (4.6)$$

$$X(Z) = (1 - 0.96 \sin^2 Z)^{-0.5} \quad (4.7)$$

$$X(Z_M) = (\cos Z_M + 0.025e^{-11 \cos Z_M})^{-1} \quad (4.8)$$

where $f(\rho)$ is the scattering phase function which incorporates models of the Rayleigh molecular (f_M) and aerosol (f_A) scattering as a function of the angular separation (ρ) of the Moon and sky position. I^* , m and α are the illuminance (footcandles), magnitude and phase angle (degrees) of the Moon; k is the local extinction coefficient; and $X(Z)$ and $X(Z_M)$ are the airmass of the sky position and Moon position as a function of the observed-sky (Z) and Moon (Z_M) zenith distances.

B_M is in units of nanoLamberts (nL) and can be related to magnitudes per square arc second using

$$B = 34.08 \exp(20.7233 - 0.92104V). \quad (4.9)$$

The change in V-band sky brightness caused by the Moon is expressed as

$$\Delta V = -2.5 \log \left(\frac{B_M + B_0}{B_0} \right) \quad (4.10)$$

where B_0 is the background sky brightness at zenith distance Z given as

$$B_0(Z) = B_{zen} 10^{-0.4k[X(Z)-1]} X(Z) \quad (4.11)$$

and B_{zen} is the sky brightness at zenith.

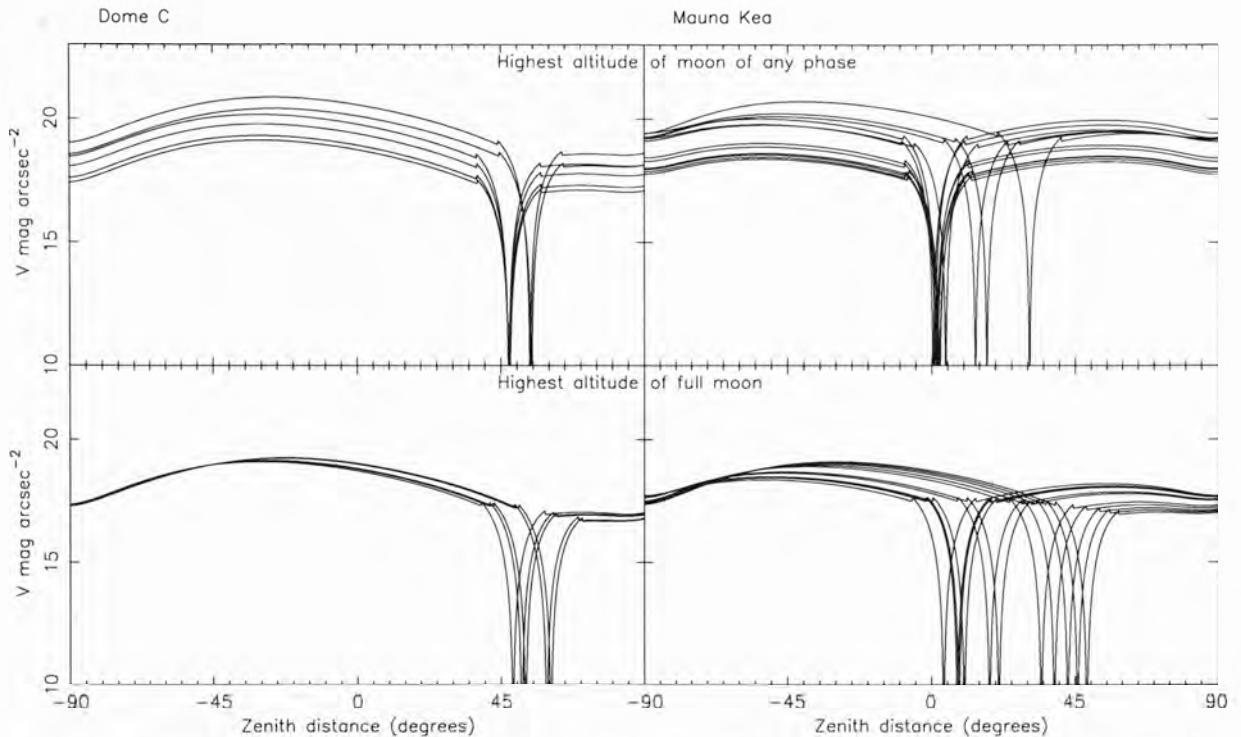


Figure 4.3. *Top:* scattered moonlight brightness as a function of zenith angle for the highest altitude of the Moon in each month (in 2005), regardless of phase. *Bottom:* scattered moonlight contribution when the *full* Moon reaches its highest altitude in each month. Each plot shows the moonlight contribution for a cross section of the sky that passes through the Moon and the zenith, for Dome C (*left*) and Mauna Kea (*right*). Each curve represents a different month.

4-1.2 Results

The lunar phase (from full to new and back) cycles over one month; for each month in 2005 the sky brightness was calculated when (1) the *full* Moon was at the highest elevation for that month and (2) the Moon was at the highest altitude, regardless of phase. In the calculation the extinction coefficient for both sites was set to the median value for Mauna Kea ($0.12 \text{ mag airmass}^{-1}$ at 550 nm).

A cross section of the sky, cutting through the position of the Moon and the zenith at those times, is plotted in Figure 4.3. The full-moon contribution at Dome C is less than that at Mauna Kea by several magnitudes at zenith, with little difference at the horizon. For the second case, excluding the sky close to the Moon, the contribution is also less

at Dome C than at Mauna Kea. As at all sites, this contribution reaches a minimum between 60° and 90° away from the Moon (Patat 2004). This advantage to Dome C is reduced to some extent by the fact that the fullness of the Moon and its maximum elevation are highly correlated (as seen in Figure 4.1) but only weakly so at Mauna Kea.

Averaged over the epoch 2005–2015, skies that would otherwise be dark are brightened at zenith by moonlight by a median value of $1.7 \text{ V mag arcsec}^{-2}$ at Dome C and $2.1 \text{ V mag arcsec}^{-2}$ at Mauna Kea.

4-2 Aurorae

Aurorae are the spectacular lights seen dancing across the skies in (mainly) polar regions. Aurorae result from the collisions of highly energetic solar particles with upper atmosphere atoms and molecules. These collisions excite the atoms and molecules to higher energy levels, from which they radiatively decay.

Aurorae are generally (though not exclusively) confined to annular regions $15\text{--}25$ degrees from the *geomagnetic* poles. The geomagnetic poles are the two positions where the theoretical magnetic dipole of the Earth intersects the surface. As shown in Figure 4.4 the geographic positions of the geomagnetic poles are not static and are recalculated each year. The size and position of the auroral oval also changes with solar activity; see the OVATION Web site¹ for plots of the size and position of the auroral oval from December 1983 to the present.

The particle collisions that cause aurorae typically occur $100\text{--}250$ km above the ground but can occur at altitudes anywhere between 80 and 1000 km. In the V-band the strongest auroral emission is from neutral oxygen at 557.7 nm; Table 4.2 shows the sources, wavelengths and typical intensities of some visible auroral emissions. Aurorae can vary rapidly in intensity and position across the sky during a night, and the long term intensity has a strong dependence on the 11 year sunspot cycle.

¹OVATION ([Auroral] Oval Variation, Assessment, Tracking, Intensity, and On-line Nowcasting) is a project of the Auroral Particles and Imagery Group and the John Hopkins University; see <http://sd-www.jhuapl.edu/Aurora/index.html>.

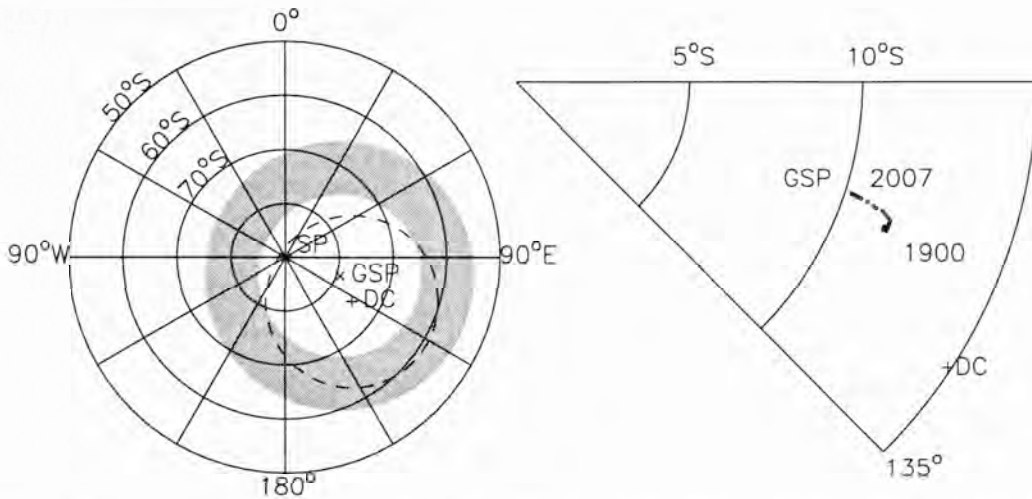


Figure 4.4. *Left:* Schematic of the typical southern auroral oval, showing the geographic South Pole (SP), Dome C (DC) and the position of the geomagnetic south pole (GSP) for the year 2005. The auroral oval is typically located 15–25° from the geomagnetic south pole (shown in grey shading). Aurorae at 250 km altitude will be above the horizon at Dome C only if they lie within the dotted line. *Right:* Positions of the geomagnetic south pole over 107 years (obtained from the Kyoto University Web page “World Data Center for Geomagnetism”, at <http://swdcwww.kugi.kyoto-u.ac.jp/poles/polesexp.html>).

4-2.1 Implications for Dome C

Dome C lies about 10° away from the inner edge of the typical auroral oval; aurorae are therefore expected to be low on the horizon and of low intensity. Figure 4.4 shows the geographic positions of Dome C, South Pole, the typical auroral oval and the geomagnetic south pole (for January 2005; 79.3°S, 108.5°E²). South Pole is located very close to the inner edge of the auroral oval and experiences considerable auroral activity.

Using the simple geometry shown Figure 4.5, the distance and elevation angle of aurorae, as viewed from Dome C, was calculated as a function of angular separation between Dome C and the aurorae. The calculation was carried out for aurorae occurring at 100 and 250 km above the Earth. The results are shown in Table 4.3. Aurorae at 100 km altitude will usually be below the horizon at Dome C; at 250 km altitude this occurs at 16° separation; the dotted circle in Figure 4.4 shows this range. The elevation

²Obtained from the National Geophysical Data Center Web page “Estimated Values of Magnetic Field Properties”, at <http://www.ngdc.noaa.gov/ngdc.html>.

Table 4.2. Typical auroral emissions in the visible, adapted from Dempsey et al. (2005).

Wavelength (nm)	Emitter	Typical intensity (kR)
391.4	$^1\text{N N}_2^+$ band	98.51
427.8	$^1\text{N N}_2^+$ band	30.0
557.7	[OI] line	100
630.0 – 636.4	[OI] line	2 – 100
687.3	M N_2^+ band	14.22
706.4	M N_2^+ band	10.50
731.9 – 733.0	[OII] line	0.4 – 100
777.4	[OI] line	9.6
785.3	M N_2^+ band	65.49
808.1	M N_2^+ band	38.91
823.3	M N_2^+ band	10.99
844.6	[OI] line	11.5
868.0	[NII] line	10.5

Note: $-1\text{R} = 1/(4\pi) \times 10^{10}$ photons $\text{m}^{-2} \text{s}^{-1} \text{sr}^{-1}$.

angle of typical aurorae seen from Dome C will be between the horizon and 7° elevation, and they will be between 1160 and 2000 km away. Sun-aligned quiet arcs will not decrease with increasing magnetic latitude in the same fashion as normal aurorae; however they are significantly less intense than the aurorae occurring within the auroral oval (Gary Burns, 2005, private communication).

Dempsey et al. (2005) used satellite measurements of the electron flux above Dome C to calculate the expected intensity of aurorae. They found in the V band the intensity of the auroral contribution to sky background was less than $22.7 \text{ mag arcsec}^{-2}$ for 50% of the wintertime during a solar maximum year and below $23.5 \text{ mag arcsec}^{-2}$ during solar minimum.

Aurorae are expected to have a minor impact on optical astronomy at Dome C, even without the use of narrow-band filters to remove the brightest emission lines. The contribution to sky brightness at Mauna Kea by aurorae is of course negligible.

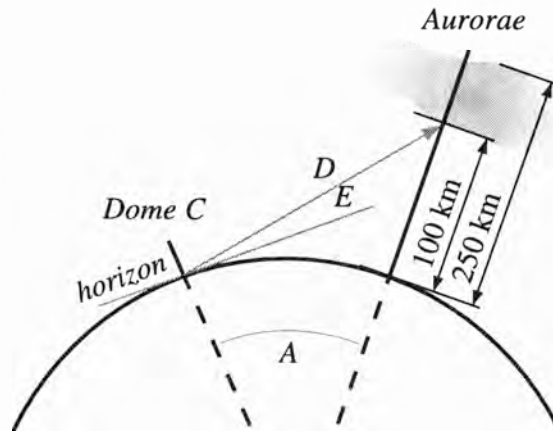


Figure 4.5. Schematic showing the geometry used to calculate the distance and elevation angle of typical aurorae as viewed from Dome C. In the figure, *A* is the angle between Dome C and position on Earth of the nadir of the aurorae, *E* is the elevation angle of the aurorae relative to the local horizon at Dome C and *D* is the distance to the aurorae.

Table 4.3. Position of aurorae as viewed from Dome C. The first column is the angular separation between the aurora and Dome C. From this the distance from the Dome C to the aurora and the elevation angle of the aurora at Dome C is calculated. See Figure 4.5 for the geometry.

Angular separation between aurora & Dome C (deg)	Aurora altitude: 100 km		Aurora altitude: 250 km	
	Distance (km)	Elevation (deg)	Distance (km)	Elevation (deg)
10	1130	0	1160	7
12	1350	-2	1380	4
14	1570	-3	1600	2
16	1790	-5	1830	0

4-3 Airglow

Airglow, at night, is the chemiluminescence of upper atmosphere molecules and atoms. This so-called “nightglow” includes a quasi-continuum from NO_2 and a number of discrete emission lines, the strongest by far from the hydroxyl radical. Nightglow is unpolarised and on a large scale increases from zenith to the horizon, as described by the van Rhijn function,

$$V = \left[1 - \left(\frac{R_0}{R_0 + h} \right)^2 \sin^2 z \right]^{-0.5} \quad (4.12)$$

where R_0 is the radius of the Earth, h is the height of the emitting atmospheric layer above the surface of the Earth and z is the zenith distance. On small spatial scales the nightglow emissions are uneven and blotchy across the sky. Nightglow emissions vary over short and long time scales.

4-3.1 Airglow reactions and emissions lines

Nightglow emissions are mainly from the thin mesospheric layer, centred at an altitude of 85–90 km. Nightglow includes a quasi-continuum from NO_2 and a number of discrete emission lines, primarily from atomic and molecular oxygen. The strongest emission in the visible is the 557.7 nm line of $\text{O}(^1\text{S})$ and at wavelengths longer than 600 nm the strongest emissions come from the hydroxyl radical (OH). Table 4.4 shows the wavelength, sources, typical intensities and chemical reactions for the formation of the most common visible airglow emissions.

The $\text{O}(^1\text{S})$ emission relies heavily on the concentration of atomic oxygen between 80 and 100 km (Yee et al. 1997). O_2^* and $\text{O}(^1\text{S})$ have very short lifetimes, but atomic oxygen above 100 km altitude has a long lifetime. The OH Meinel bands are primarily excited by a reaction between ozone and atomic hydrogen; the concentrations of O_3 and H depend on the atomic oxygen mixing ratio (Le Texier et al. 1987).

4-3.2 A reduction in airglow over Antarctica?

The emissions discussed above are produced photochemically through reactions involving atomic oxygen, atomic hydrogen and ozone. There have long been discussions that nightglow over Antarctica should decrease in winter because of a lack of atomic oxygen.

Table 4.4. Mesospheric nightglow emissions at zenith in the visible range. The first three columns are adapted from Roach & Gordon (1973); Leinert et al. (1998); McEwan & Phillips (1975) and references therein. The chemical reactions are sourced from McDade et al. (1986) [O₂, OI, NO₂], Yee et al. (1997, and references therein) [O₂ and OI] and Midya & Midya (1993) [Na].

Wavelength (nm)	Source	Typical intensity (R)	Comments	Reactions ^a
260–380	O ₂	0.5 Å ⁻¹	Herzberg bands	$O + O + N_2 \rightarrow O_2 (A^3\Sigma_u^+) + N_2$ $O_2 (A^3\Sigma_u^+) \rightarrow O_2 + h\nu$
391.4 etc	N ₂ ⁺	< 1		
500–650	NO ₂	250	Nightglow continuum	$NO + O \rightarrow NO_2 + h\nu$ or $NO + O + M \rightarrow NO_2^* + M$ $NO_2^* + M \rightarrow NO_2 + M$ $NO_2^* \rightarrow NO_2 + h\nu$
519.8, 520.1	N	1		
557.7	OI	250	Strongest visible emission	$O + O + M \rightarrow O_2^* + M$ $O_2^* + O \rightarrow O(^1S) + O_2$ $O(^1S) \rightarrow O(^1D) + h\nu$
589.0, 589.6	Na D	20–150	Strong seasonal variation	$Na + O_3 \rightarrow NaO^* + O_2$ $NaO^* + O \rightarrow Na(^2P) + O_2$ $Na(^2P) \rightarrow Na(^2S) + h\nu$
600–4500	OH	4500 k	Meinel bands from the transitions among the 9 lowest electronic levels	$O + O_2 + M \rightarrow O_3 + M$ $H + O_3 \rightarrow OH^* + O_2$ $OH^* \rightarrow OH + h\nu$
656.3	H	3		
761.9, 864.5	O ₂	1000	Atmospheric bands	$O + O + M \rightarrow O_2^* + M$ $O_2^* + O_2 \rightarrow O_2 (b^1\Sigma_g^+) + O_2$ $O_2 (b^1\Sigma_g^+) \rightarrow O_2 + h\nu$

^aIn all cases the species M is usually N₂.

However, atomic oxygen at about 100 km altitude has a long lifetime and is transported globally in the mesosphere and lower thermosphere via the two-cell meridional circulation from the equator to the poles (Garcia & Solomon 1985; Yee et al. 1997). Because of these efficient mechanisms that transport reactants from sunlit locations to the poles, there is no reason to expect a diminution in the chemiluminescence of species such as OH and O₂ during the long polar night. As discussed in the next section, this conclusion is supported by measurements.

4-3.3 Airglow measurements

Airglow measurements have been carried out all around the globe, both ground based and from satellites. A number of these measurements are selected and discussed in this section.

Continuous monitoring of the OH Meinel bands in the J-band with a Michelson interferometer has been carried out at the South Pole since January 1992, and the data are now publicly available (Sivjee et al. 2005). As expected, these data show very large hourly and nightly variations, with no diminution in average intensity as the winter progresses. Over a period somewhat less than a year, Phillips et al. (1999) observed a small reduction in OH emission at South Pole in 1995 relative to temperate sites, but this is more likely explained by the known highly variable nature of OH emission. Measurements of OH nightglow between 837.5 and 856.0 nm at Davis, Antarctica (68°35' S, 77°58' E) over seven years (Burns et al. 2002) show a barely significant seasonal variation in emission intensity, although there are large day-to-day variations (Gary Burns & John French, 2005, private communication). Zaragoza et al. (2001) measured the OH nightglow emissions in a narrow spectral band near 4.6 μm for just under one year. Using the Improved Stratospheric and Mesospheric Sounder on the UARS satellite they have almost full global coverage (80° N to 80° S). They find at high latitudes a springtime minimum in the OH emission $\sim 30\%$ below the global mean, although this is only for one year of data. During the Northern hemisphere winter solstice period their averaged measured intensities of OH nightglow at high and mid-latitudes are the same to within the errors. Therefore, we expect that the sky brightness in those bands (650 nm–4.6 μm) dominated by OH emission will be essentially identical at Dome C to that at all other

observatory sites, including Mauna Kea.

Models of the global tides in the thermosphere, ionosphere and mesosphere (Yee et al. 1997) predict an *increase* in 557.7 nm emission towards the poles, although more data are needed to confirm this model. Note, however, that this single strong line can be easily filtered from astronomical measurements. Figure 6 in Ratnam et al. (2004) shows the global volume emission rate of the O₂ atmospheric bands in four seasons; their results indicate no significant reduction in O₂ emission during the southern winter at high latitudes.

In general, we conclude that little difference in overall airglow emission between Antarctic and temperate sites should be expected.

4-4 Zodiacal light

Zodiacal light is sunlight scattered from the diffuse cloud of interplanetary dust that lies largely in the plane of the solar system. Zodiacal light is generally seen as a cone of light with its base at the horizon at the azimuth of the Sun. The cone is brightest at the base, decreasing in intensity towards the zenith, with a secondary maximum at the anti-solar point. The intensity of zodiacal light depends on the wavelength, observer position, and sky position. Zodiacal light is polarised, reaching a maximum polarisation of about 20% (Leinert et al. 1998).

Following Leinert et al. (1998), the expected zodiacal contribution to sky brightness at Dome C and Mauna Kea was calculated over one year. All correction factors in the model were set to unity; thus there is a possible variation in flux of up to 30%. A summary of the calculation is shown below, see Leinert et al. (1998) for details and look-up tables.

The visual zodiacal light brightness (I_{ZL}) can be estimated for a particular observer position, sky position and wavelength as

$$I_{ZL} = f_R I(\lambda - \lambda_{\odot}, \beta) f_{\infty} f_{SP} \quad (4.13)$$

where $I(\lambda - \lambda_{\odot}, \beta)$ is the visual intensity for a particular viewing direction, f_R is dependent on the heliocentric distance and varies by a few percent over the year, f_{∞} is dependent on wavelength and varies from unity by up to 20% in the wavelength range 350 nm to 800 nm, f_{SP} corrects for the position of the observer relative to the zodiacal

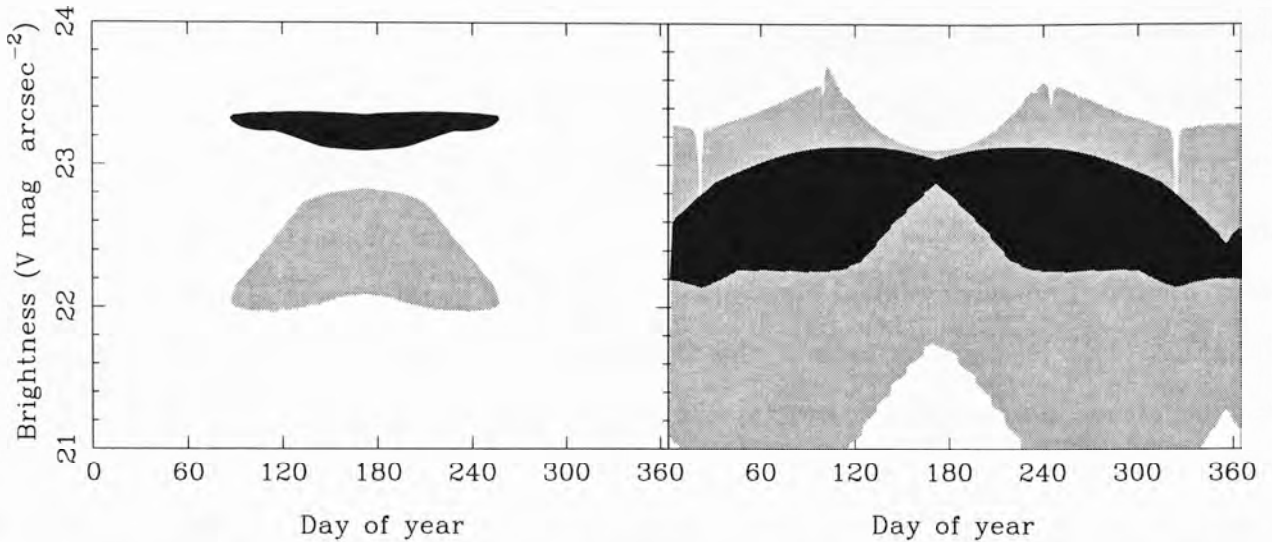


Figure 4.6. The range of zodiacal contribution to sky brightness ($V \text{ mag arcsec}^{-2}$) at Dome C (left) and Mauna Kea (right), over one year, for Sun elevations less than -18° . The black shading is for observations at zenith and the grey is for a zenith distance of 60° at the same azimuthal position as the Sun.

dust cloud and varies from unity by up to 10%.

4-4.1 Results

Limiting the calculations to astronomical nighttime, two cases were looked at: the zodiacal brightness at (1) the zenith and (2) at a zenith angle of 60° at the same azimuth as the Sun; the results are shown in Figure 4.6.

In the V-band, the model shows the zenith brightness of zodiacal light at Dome C is expected to be always *darker* than $23.1 \text{ mag arcsec}^{-2}$. This is because the ecliptic plane is always fairly low on the horizon. In comparison, at Mauna Kea the zodiacal sky brightness at zenith is expected to be always *brighter* than about $23.1 \text{ mag arcsec}^{-2}$, reaching a maximum contribution of about $22.1 \text{ mag arcsec}^{-2}$. For the second case, the zodiacal light at Dome C is always darker than about $22 \text{ mag arcsec}^{-2}$; at Mauna Kea it can get as bright as about $20.8 \text{ mag arcsec}^{-2}$.

This reduced contribution from zodiacal light at Dome C compared to Mauna Kea is a reflection of the fact that a different part of the sky passes overhead at Dome C than does at Mauna Kea.

4-5 Integrated starlight

Telescopes can only identify, as individual objects, those stars that are brighter than a certain magnitude. The integrated flux from all stars fainter than this magnitude contribute to the sky background. The limiting magnitude depends on the seeing and atmospheric extinction of the site, and the size of the telescope.

The excellent seeing (Lawrence et al. 2004 and Section 6-6) and expected low atmospheric extinction (Kenyon & Storey 2006 and Chapter 2) at Dome C will ensure that the limiting magnitude of even a small telescope will be sufficient to reduce the integrated unresolved starlight to negligible levels.

4-6 Diffuse Galactic light

Diffuse Galactic light is starlight that has been scattered off interstellar dust. Diffuse Galactic light is typically about $23.6 V \text{ mag arcsec}^{-2}$ at zenith (Roach & Gordon 1973); brighter towards the heart of the Milky Way where the concentrations of stars and dust are highest.

The Galactic plane is always close to the zenith at Dome C and this may result in a relatively higher contribution of diffuse Galactic light and integrated starlight, compared to lower latitude sites. At Dome C the galactic latitude of the zenith ranges between -10° to -40° , whereas at Mauna Kea the range is much larger: -40° to $+85^\circ$ with the galactic plane close to the horizon for some of the time. This contribution is rather smaller than other sources of sky brightness and, similarly to zodiacal light, depends on the celestial coordinates.

4-7 Integrated cosmic light

Integrated cosmic light is the red-shifted starlight from unresolved galaxies. No firm measurement exists for its exact value. Upper and lower limits have been measured and estimated from models, giving a range of about 25 to $30 \text{ mag arcsec}^{-2}$ at 550 nm (Leinert et al. 1998, and references therein).

The integrated cosmic light (red-shifted starlight from unresolved galaxies) contribu-

tion, at all sites, is very small in comparison to all other sources of sky brightness.

4-8 Light pollution

The night sky can be brightened considerably by light pollution from towns and cities. Light pollution is mainly from vapour lamps (Hg and Na emission lines) and a weak continuum from incandescent lamps (Benn & Ellison 1998). For example, Massey & Foltz (2000) found high pressure sodium street lamps to contribute about $0.2 \text{ mag arcsec}^{-2}$ to the sky brightness at Kitt Peak and Mount Hopkins in the USA.

Garstang (1989a) modelled the increase of the zenith sky brightness caused by light pollution at various sites. Garstang (1989b) further predicts the increase in light pollution at various sites over time. For example, Garstang (1989b) predicts the artificial sky brightness will increase the total sky brightness by between 0.04 and $0.53 \text{ mag arcsec}^{-2}$ at Mauna Kea by the year 2020. This estimate is based on projections of population increase and does not take into account changes in light sources and systems or unforeseen circumstances such as major tourist or housing developments nearby the sites, as noted in the paper. However, an expected increase in sky brightness of this size is not unreasonable; for example Massey & Foltz (2000) found sky brightness at Kitt Peak increased by $\sim 0.5 \text{ mag arcsec}^{-2}$ over 11 years, in the direction of the city of Tuscon. For further discussions of night sky brightness modelling and world maps of the artificial sky brightness see Cinzano et al. (2001) and Cinzano & Elvidge (2004) and references within.

The closest station to Dome C (Vostok at $78^{\circ}27'51''\text{S}$, $106^{\circ}51'57''\text{E}$) is 560 km away. The placement of external lighting at the Dome C station itself will be carefully considered in relation to astronomical observations. With proper planning there should continue to be no artificial light pollution at Dome C, while the light pollution at other sites is likely to increase.

4-9 Conclusions

As we saw in the previous chapter, Dome C has a comparable number of cloud-free, astronomically dark hours to a more temperate site such as Mauna Kea. Atmospheric scattering at Dome C should be close to the lowest anywhere on Earth, reducing the sky

brightness contributions from sunlight, moonlight and tropospheric scattering, and reducing the extinction throughout the optical. The moonlight contribution to sky brightness over the year is less than at lower latitude sites. Aurorae will rarely be more than 7° above the horizon and will typically be more than about 1160 km away; they will generally be unobservable. Zodiacal light is darker at the zenith and 60° from the zenith than at equatorial sites and will always be darker than $23.1 V \text{ mag arcsec}^{-2}$ at zenith. Airglow is essentially the same at all sites. The integrated starlight and diffuse galactic light will be slightly brighter at Dome C than at other sites because the galactic plane is always close to zenith. There is no artificial light pollution at Dome C; a condition that should persist indefinitely. Dome C thus appears to be an attractive site for optical as well as infrared astronomy.

“ ‘Scuse me while I kiss the sky”

Jimi Hendrix (1942–1970)

Purple Haze (1967)

Chapter 5

Nigel, monitoring the sky brightness at Dome C

The brightness of the night sky at an optical astronomical site is one of the principal factors that determine the quality and quantity of available observing time. In the previous two chapters, the optical sky brightness at Dome C was analysed using models, and data from the South Pole. However, until the sky brightness at the site has been measured no firm conclusions can be made.

Because of the high latitude of Dome C, the Sun spends a relatively small amount of time a long way below the horizon, resulting in long periods of twilight. The reduced aerosol content in the atmosphere above Antarctica, combined with the low density of the atmosphere, could result in astronomical nighttime starting at a smaller solar depression angle compared to other sites, increasing the available observing time. By monitoring the sky brightness during twilight and into the night, the solar elevation angle at which the sky ceases getting darker can be determined, and the maximum amount of dark-time can be measured. The unique conditions of an Antarctic site introduce new aspects that would not normally be considered when assessing the sky brightness at a temperate site, such as ice reflection and aurorae. The large surface of highly reflective ice around an Antarctic telescope could increase the sky brightness caused by scattered light, in particular moonlight scattered from the ice could considerably brighten the sky.

Broadband photometry of the sky can be used to measure the brightness; however, this includes artificial sources and strong natural airglow lines that could be eliminated or filtered during actual astronomical measurements. In particular, at polar sites broadband photometry would also include auroral lines that could be filtered from observations. Ideally, one would also take absolute spectrography of the sky; this allows individual spectral contributions to the sky brightness to be extracted; the overall background sky brightness in various bands can then be derived. Sky brightness assessments need to be carried out over long periods of time because various contributions, for example airglow and aurora, are known to vary in intensity both over very short time scales, and longer periods such as the 11 year solar cycle.

Previous to 2005, the optical sky brightness above Dome C had not been monitored during the winter. Nigel is a fibre-fed spectrograph that was deployed to Dome C for the measurement of the optical brightness, temporal characteristics, and spectrum of the twilight and nighttime sky. Nigel was installed in the AASTINO at Dome C in November 2004, and operated until 13 February 2005, at which time the entire AASTINO system was shut down. Unfortunately this means that the darkest sky recorded was when the Sun was barely below the horizon.

The design and control of Nigel are described in Sections 5-1 and 5-2. Nigel is designed to operate at a remote observatory; since it is not desirable to take expensive calibration standards into the field, alternative inexpensive methods for wavelength (Section 5-3) and flux (Section 5-4) calibration were explored. In Section 5-6 the future plans for Nigel are discussed. The majority of this chapter has been published in Kenyon et al. (2006a), see Appendix C-3.

5-1 Instrument description

Nigel is a fibre-fed UV/visible grating spectrograph with a thermoelectrically cooled 256×1024 pixel CCD camera, designed to measure the twilight and night sky brightness from 250 to 900 nm. Nigel was developed from the Antarctic Fibre Optic Spectrograph (AFOS; Boccas et al. 1998) which operated at the South Pole from 2002 to 2003 (Dempsey et al. 2004).

Nigel has six optical fibres that collect light from three directions in the sky and direct

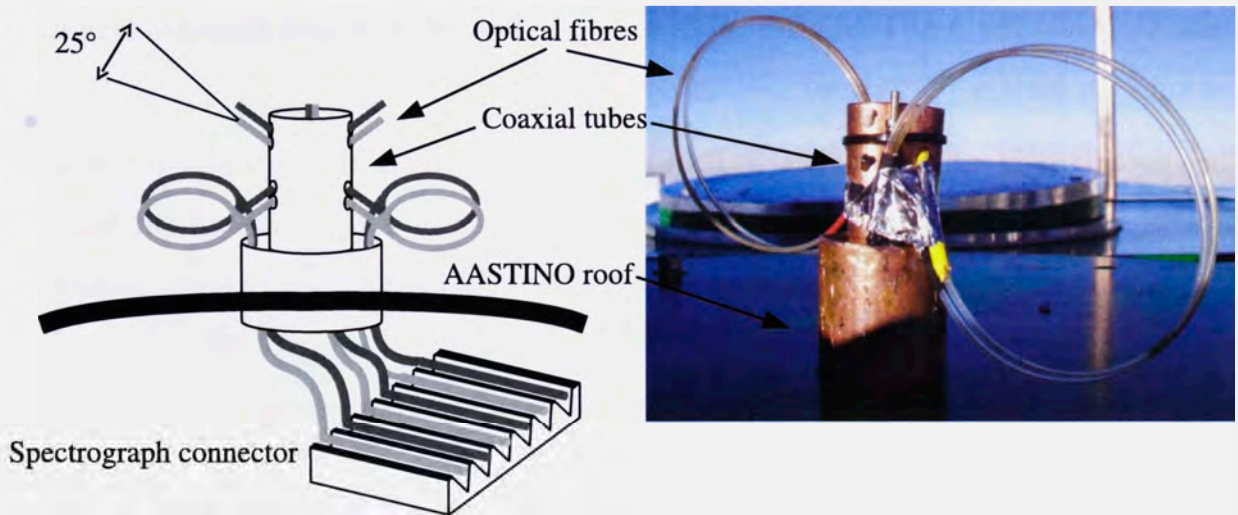


Figure 5.1. Schematic and photograph showing the set-up of Nigel’s fibres. Three pairs of optical fibres (with one blue and one red wavelength optimised fibre) are held in a coaxial copper tube on the roof of the AASTINO; each pair of fibres points in a different direction. On the spectrograph end the fibres are held parallel in a brass V-groove connector.

it into a spectrograph; the resulting image is recorded on a CCD. The spectrograph, CCD and control computer were located inside the AASTINO and the fibres fed outside through a roof port (Figure 5.1 shows a schematic and photograph of the fibre set-up). Nigel is designed to operate in the wavelength range 250–900 nm; to ensure good efficiency over the whole spectral range two sets of fibres were used, optimised in red and blue wavelength ranges. Both sets of fibres were supplied by Ceramoptec (WF100/132P and UV100/110) and have a standard numerical aperture of 0.22 ± 0.02 with a core diameter of $100 \mu\text{m}$. The numerical aperture corresponds to an f -ratio of $f/2.2$; each fibre thus sees a field of view of 25° on the sky. The six fibres are paired into blue and red optimised combinations; each pair was pointed in a different direction, one towards the zenith and the other two pairs elevated to 30° and pointed in northerly and southerly directions.

The “sky” end of each fibre is held in an SMA connector, with a coaxial copper tube to hold the fibres in place on the top of the AASTINO. The tube can be electrically heated to prevent ice build up near the fibres. Each fibre is threaded into Teflon tubing for protection; Teflon was chosen as it remains flexible at the cold temperatures experienced

at Dome C. Inside the AASTINO the tubes were bundled together and threaded into a rubber tube for further protection.

The spectrograph end of the fibres is held in a brass connector that is machined with six parallel, evenly spaced V-grooves. Each fibre was glued into a groove and cut flush with the edge of the connector; the fibre ends were hand-polished by Jon Everett (School of Physics, University of New South Wales). The resulting linear array of fibres forms a pseudo-slit to the spectrograph, with the spectrum from each fibre separated by about 20 pixels on the CCD.

A commercial spectrometer (Jobin Yvon model CP200) was used; the characteristics of the spectrograph are shown in Table 5.1. Figure 5.2 shows a schematic of the light path in the spectrograph. The grating is concave holographic and produces a linear dispersion that varies from 24.6 nm/mm in the blue to 25.7 nm/mm in the red. With the 100 μm fibres, the resulting resolution is 2.5 nm full width half maximum. The 1024 \times 256 pixel CCD camera was an Andor unit supplied by Oriel Instruments (model Instaspec IV, open electrode), cooled by a single air-cooled Peltier stage. The images from the CCD are saved in the FITS file format. Figure 5.3 shows a CCD image taken with Nigel; each horizontal line corresponds to the spectrum from one fibre, and the wavelength decreases to the right.

5-2 Control and communication

Ultimate control over the operation of Nigel was by the “Supervisor” computer in the AASTINO. The Supervisor controlled the power and heat in the AASTINO as well as the operation of various instruments and communications. Communications to the Supervisor from off-site were via the Iridium satellite network. Nigel has a separate PC104 computer to control the CCD; the two computers were connected via Ethernet and communicate using the ERIC software package (Ashley et al. 1996).

The observing sequence of Nigel was controlled by a Perl script (`run_nigel`) on the Supervisor computer; this script was started each day by a crontab file. `run_nigel` turns on the power to Nigel’s computer and carries out a continuous observing loop for 23 hours. At the end of this period the CCD cooling system is turned off, the log file for the day is saved and moved to the data directory, and the computer is turned off. This

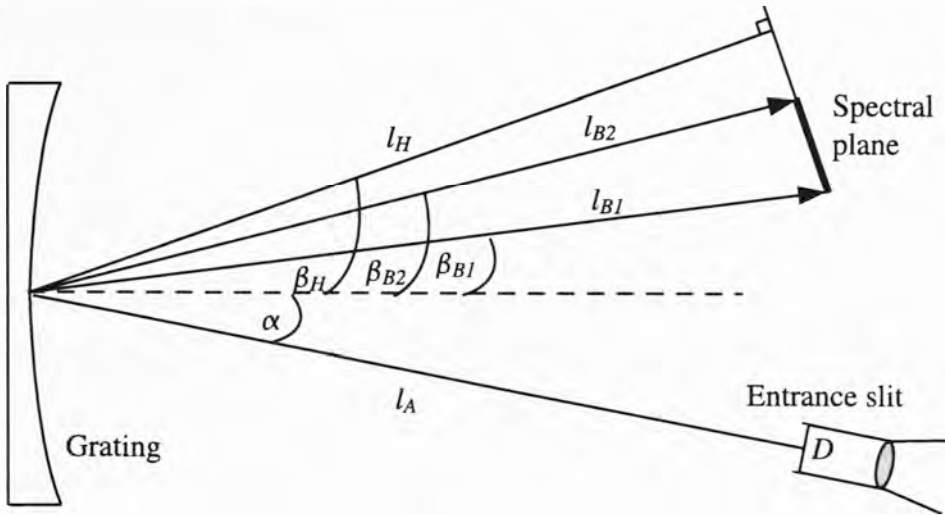


Figure 5.2. Light path in the spectrograph used in Nigel, see Table 5.1 for an explanation of the symbols and the values.

Table 5.1. Characteristics of the fibre and spectrograph used in Nigel

Fibre acceptance angle (ψ)	12.7°
Fibre diameter (D)	100 μm
Grating groove density	200 grooves mm^{-1}
Length of spectrum	25 mm
Length of entrance arm (l_A)	191.721 mm
Angle of incidence (α)	-3.942°
Length from grating to spectral plane (l_H)	181.075 mm
Angle between the grating and spectral plane (β_H)	25°
Diffraction order (K)	1
Entrance dispersion	260.2 $\text{\AA} \text{mm}^{-1}$
Angle of diffraction (β_B)	6.127° at 190 nm 13.458° at 820 nm
Flat field dispersion ($d\lambda/dx$)	24.58 $\text{nm} \text{mm}^{-1}$ at 190 nm 25.78 $\text{nm} \text{mm}^{-1}$ at 820 nm
Exit arm length (l_B)	191.36 mm at 190 nm 184.36 mm at 820 nm
Pixel size (x)	27 μm
CCD gain (G)	48 $e^- \text{DN}^{-1}$

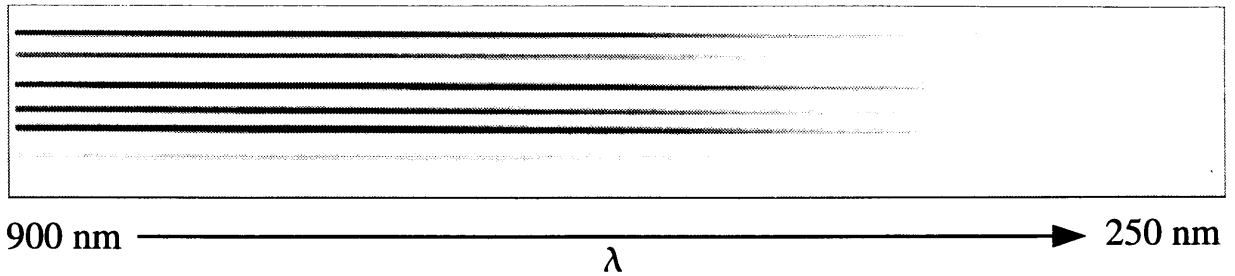


Figure 5.3. Raw CCD image taken with Nigel. Each horizontal line corresponds to the spectrum from one fibre; wavelength decreases to the right.

script controls the frequency and the exposure time of each exposure, these depend on the azimuth and altitude of the Sun and Moon, and the phase of the Moon. Every six minutes the position of the Sun and Moon are found from a look-up table. If the Sun is in the field of view of a pair of fibres no exposure is taken; exposures are taken every 15 minutes if the Moon is in the field and the lunar phase is more than half-full, otherwise the CCD is exposed every three hours. The number of exposures taken with Nigel was limited solely by the storage capacity available on the Supervisor; each compressed FITS file is about 125 KByte. The Sun or Moon was considered to be within the field of view of one of the fibres if the elevation angle was between 15° and 45° , and the azimuth angle was in the range $295^\circ \leq \text{Azi} \leq 355^\circ$ or $135^\circ \leq \text{Azi} \leq 185^\circ$. The exposure time was set depending on whether the altitude of the Sun is above 10° , below -5° or between these two values.

If `run_nigel` determines that the CCD is to be exposed then a shell script (`nigel.sh`) is started. This script communicates and controls the CCD computer. The shell script connects to the CCD computer and sets the time to match that of the supervisor. The CCD was then cooled if the temperature in the AASTINO was higher than -27°C ; the readout area of the CCD was set to 10–1024 by 48–218 pixels (covering the area of the CCD used by the fibres). The CCD is exposed and the FITS file is moved to the supervisor computer, compressed, and renamed with the time of the start of the observation.

5-3 Wavelength Calibration

The wavelength scale of the spectrograph was calibrated using a domestic fluorescent light tube. This method is an easy and inexpensive way to calibrate the instrument in a remote location. The tube of a fluorescent light contains a rare gas (usually Argon) and a small amount of mercury. The tube is coated on the inside with phosphor; typically a combination of three rare earth phosphors are used to cover the visible spectrum (Srivastava & Sommerer 1998; Dejneka et al. 2003). In the red, green and blue colour ranges the compounds often used are:

- Red— $\text{Y}_2\text{O}_3:\text{Eu}^{3+}$
- Green— $\text{CeMgAl}_{11}\text{O}_{19}:\text{Tb}^{3+}$; $\text{LaPO}_4:\text{Ce}^{3+},\text{Tb}^{3+}$ or $\text{GdMgB}_5\text{O}_{10}:\text{Ce}^{3+},\text{Tb}^{3+}$
- Blue— $\text{BaMgAl}_{10}\text{O}_{17}:\text{Eu}^{2+}$ or $(\text{Sr},\text{Ba},\text{Ca})_5(\text{PO}_4)_3:\text{Eu}^{2+}$

Tables 5.2 and 5.3 show the typical emission wavelengths and transitions for Europium IV (Eu^{3+}) and Terbium IV (Tb^{3+}), respectively. Table 5.4 shows the most intense visible emission lines of Mercury I (Hg). Using these tables, the emission lines in a typical fluorescent light spectrum, recorded by Nigel, were identified; Table 5.5 and Figure 5.4a show the nominal wavelengths and probable identifications of each fluorescent peak used for wavelength calibration.

Additional wavelength calibration is possible from known Fraunhofer absorption lines in daytime sky spectra, and airglow emission features during twilight and night time. Figure 5.4b shows a daytime sky spectrum recorded with Nigel; the Fraunhofer calibration lines are marked on this spectrum; see Table 5.6 for the line identifications. Table 5.7 shows several twilight airglow emission wavelengths and typical intensities that could also be used for calibration.

Table 5.2. Europium IV transitions and wavelengths.

Transition	Wavelength (nm)	References	Transition	Wavelength (nm)	References
${}^5D_0 \rightarrow {}^7F_1$	587.7	1	${}^5D_0 \rightarrow {}^7F_3$	630.5	2
	590.51	2		630	1, 2
	590	3		650	3
	591.28	2		653.3	2
${}^5D_0 \rightarrow {}^7F_2$	596.45	2	${}^5D_0 \rightarrow {}^7F_4$	657	2
	593	1		700	3
	599	1	${}^5D_0 \rightarrow {}^7F_5$	710.6	2
	611	1, 4			
	609.7	2			
	614	3			

References: [1] Satoh et al. (2005), [2] Konigstein (1964), [3] Wang & Yan (2005) and [4] Ofelt (1963)

Table 5.3. Terbium IV transitions and wavelengths.

Transition	Wavelength (nm)	References	Transition	Wavelength (nm)	References
${}^5D_4 \rightarrow {}^7F_6$	484	1	${}^5D_4 \rightarrow {}^7F_4$	583	1
	489	2, 4, 5		584	2
	490	3		587	3
${}^5D_4 \rightarrow {}^7F_5$	542	1, 5	${}^5D_4 \rightarrow {}^7F_3$	618	1
	544	2		621	2
	544	3		622	3
		625		6	

References: [1] Hussain et al. (2002), [2] Ng et al. (2000), [3] Wang & Yan (2005), [4] Dejneka et al. (2003), [5] Ofelt (1963), [6] Thompson et al. (1977)

Table 5.4. The most intense Mercury transitions in the visible range (NIST 2006).

Transition	Wavelength (nm)	Relative intensity	Transition	Wavelength (nm)	Relative intensity
$^3P_2 \rightarrow ^3D_3$	302.1504	300	$^3P_0 \rightarrow ^3S_1$	404.6565	1800
$^3P_1 \rightarrow ^3D_2$	312.5674	400	$^1P_1 \rightarrow ^3D_2$	433.9220	250
$^3P_1 \rightarrow ^3D_1$	313.1555	320	$^1P_1 \rightarrow ^1D_2$	434.7506	400
$^3P_1 \rightarrow ^1D_2$	313.1844	320	$^3P_1 \rightarrow ^3S_1$	435.8335	4000
$^3P_2 \rightarrow ^3D_3$	365.0158	2800	$^3P_2 \rightarrow ^3S_1$	546.0750	1100
$^3P_2 \rightarrow ^3D_2$	365.4840	300	$^1P_1 \rightarrow ^3D_2$	576.9610	240
$^3P_2 \rightarrow ^1D_2$	366.3284	240	$^1P_1 \rightarrow ^1D_2$	579.0670	280

Table 5.5. Probable identification of phosphor emission lines in a spectrum of a fluorescent tube. The peak labels correspond to Figure 5.4a.

Peak label	Nominal wavelength (nm)	Probable identification	Peak label	Nominal wavelength (nm)	Probable identification
a	405	Hg I $^3P_0 \rightarrow ^3S_1$	i	625	Tb IV $^5D_4 \rightarrow ^7F_3$
b	436	Hg I $^3P_1 \rightarrow ^3S_1$	j	631	Eu IV $^5D_0 \rightarrow ^7F_3$
c	488	Tb IV $^5D_4 \rightarrow ^7F_6$	k	651	Eu IV $^5D_0 \rightarrow ^7F_3$
d	544	Tb IV $^5D_4 \rightarrow ^7F_5$	l	662	?
	546	Hg I $^3P_2 \rightarrow ^3S_1$	m	688	Eu IV $^5D_0 \rightarrow ^7F_4$
e	588	Eu IV $^5D_0 \rightarrow ^7F_1$	n	694	Eu IV $^5D_0 \rightarrow ^7F_4$
f	593	Eu IV $^5D_0 \rightarrow ^7F_2$	o	711	Eu IV $^5D_0 \rightarrow ^7F_5$
g	599	Eu IV $^5D_0 \rightarrow ^7F_2$	p	742	Eu IV $^5D_0 \rightarrow ^7F_5$
h	611	Eu IV $^5D_0 \rightarrow ^7F_2$	q	809	Eu IV $^5D_0 \rightarrow ^7F_6$

Table 5.6. Fraunhofer lines in the visible, the data is from a Web site Sterner (2006) which draws the information from Delbouille et al. (1973).

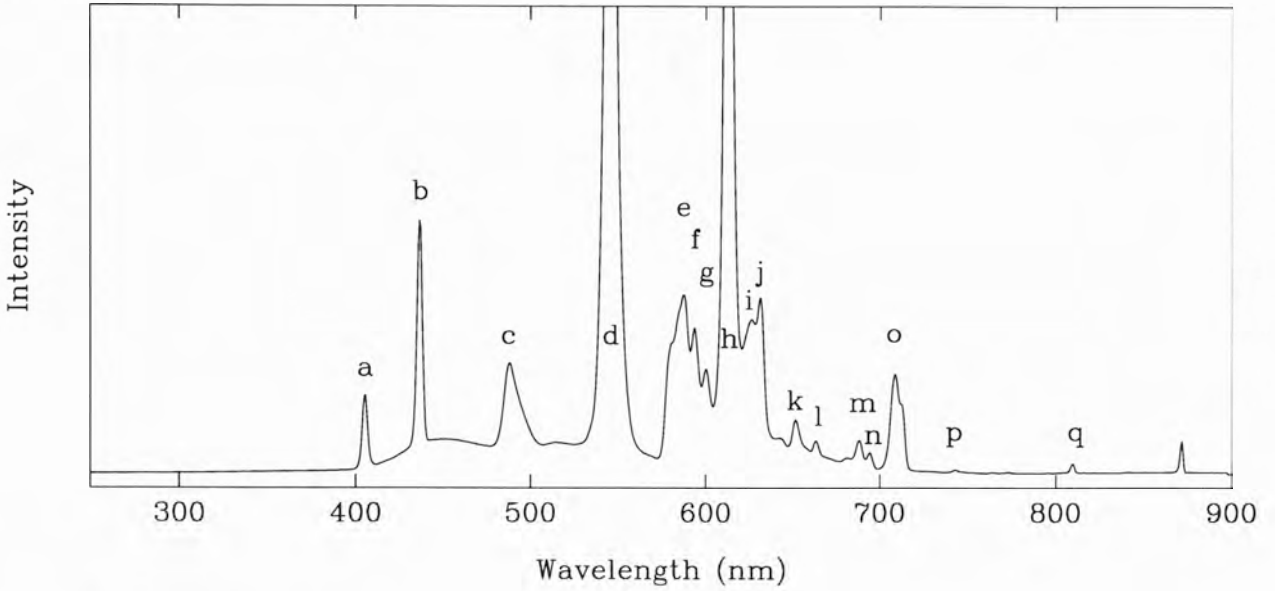
Designation	Species	Wavelength (nm)	Designation	Species	Wavelength (nm)
A band ...	O ₂	759.4–762.1	F	H β	486.1342
B band ...	O ₂	686.7–688.4	d	Fe I	466.8
C	H	656.2808	e	Fe I	438.3557
a band	O ₂	627.6–628.7	f	H γ	434.0475
D1	Na I	589.5940	G	Ca/Fe	430.8
D2	Na I	588.9973	g	Ca I	422.6740
E	Fe I	526.9550	h	H δ	410.1748
b1	Mg I	518.3619	H	Ca II	396.8492
b2	Mg I	517.2698	K	Ca II	393.3682
c	Fe	495.7613			

Table 5.7. Twilight glow emission features (McEwan & Phillips 1975).

Wavelength (nm)	Source	Intensity (R)	Wavelength (nm)	Source	Intensity (R)
388.9	He	1	557.7	O	400
391.4 etc .	N ₂ ⁺	200–500	589.3	Na	1–4 k
393.3	Ca ⁺	≤ 100	630, 636.4	O	1k
396.8	Ca ⁺	≤ 100	670.8	Li	10–1000
436.8	O	1	769.9	K	40
520.0	N	10	1083.0	He	3k

Note: 1R = $1/(4\pi) \times 10^{10}$ photons m⁻² s⁻¹ sr⁻¹.

(a) Fluorescent tube spectrum



(b) Day time sky spectrum

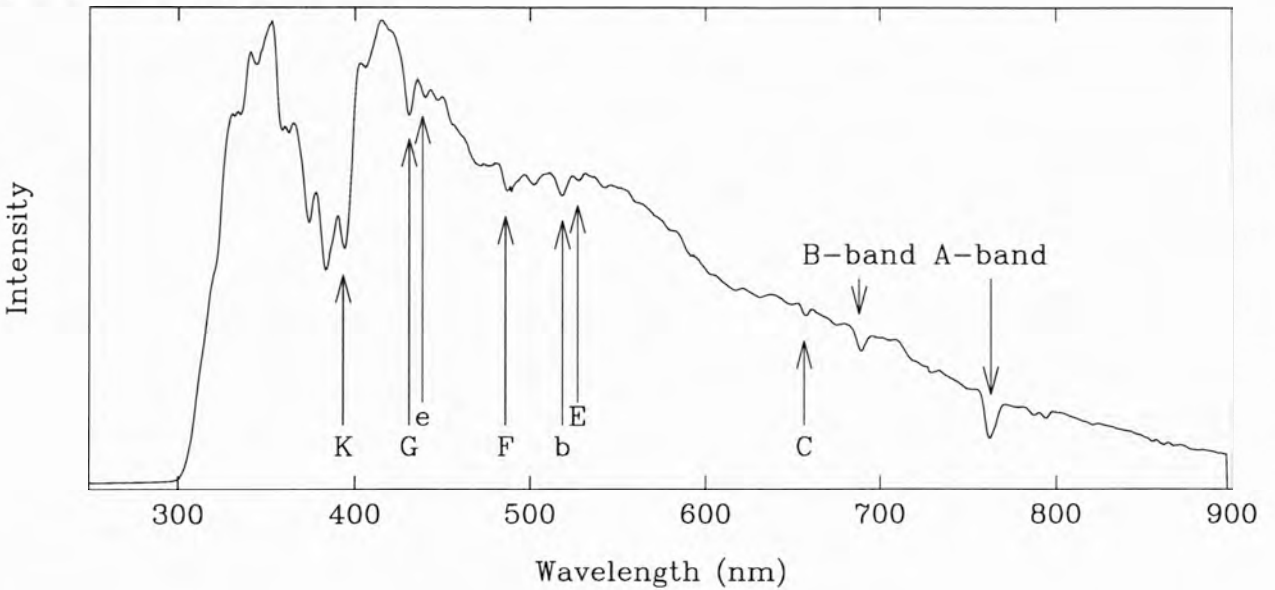


Figure 5.4. Spectra of (a) a compact fluorescent tube and (b) the daytime sky showing the calibration wavelengths, see Tables 5.5 and 5.6 for line identifications.

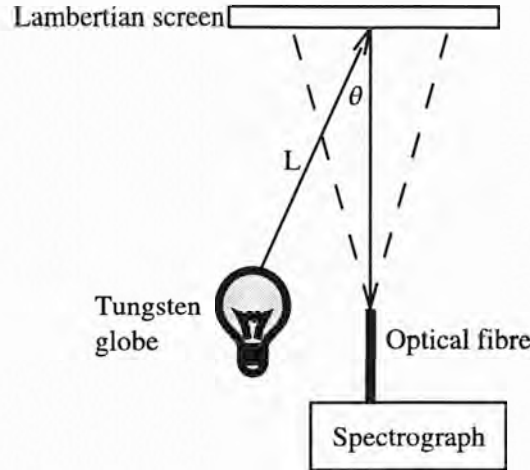


Figure 5.5. Absolute flux calibration using a tungsten bulb; the light from a tungsten globe is reflected from a Lambertian surface and directed via an optical fibre to the spectrograph.

5-4 Flux calibration

To achieve an absolute flux calibration of Nigel, a method using light from a tungsten bulb reflected off a diffuse white surface was explored (Harang & Kosch 2003; Kosch et al. 2003; Harang 2004). We also planned to use lunar spectra to check the flux calibration during the year, as the Moon would pass through the field of view of all but the zenith-pointing fibres on several occasions.

The idea behind the first method is to illuminate a Lambertian surface¹ with a tungsten globe and observe the reflected light with the spectrograph (see Figure 5.5). The spectral luminance [photons $\text{s}^{-1}\text{m}^{-2}\text{sr}^{-1}(\text{m}^{-1})$] of the Lambertian surface can be calculated from

$$B(\lambda, T) = a_f E(\lambda, T) \alpha(\lambda) \frac{1}{4\pi^2 L^2} \cos \theta, \quad (5.1)$$

where λ is the wavelength; T , a_f and $E(\lambda, T)$ are the temperature, area and spectral emittance of the tungsten filament; $\alpha(\lambda)$ is the albedo of the surface; L is the distance between the filament and the surface; and θ is the angle between the filament and the normal to the Lambertian surface. This method is summarised below, for full details see Harang & Kosch (2003) and Kosch et al. (2003).

¹The luminance of a Lambertian surface is the same at all viewing angles.

The effective surface area of the filament is calculated from

$$a_f = \frac{VI}{\epsilon(T)\sigma T^4} \quad (5.2)$$

where V and I are the voltage across and the current through the filament, $\epsilon(T)$ is the total emissivity of tungsten at temperature T , and σ is the Stefan-Boltzmann constant. In the temperature range $1200 < T < 2500$ K, $\epsilon(T)$ is calculated from an empirical relationship

$$\epsilon_m(T) = -5.0 \times 10^{-8}T^2 + 3.11 \times 10^{-4}T - 0.161. \quad (5.3)$$

The temperature of the bulb is estimated from the known temperature-resistivity relationship for tungsten. First, the room temperature resistivity, is calculated using an empirical relationship, valid in the temperature range $200 < T < 400$ K,

$$\rho_0 = 1.25 \times 10^{-6}T_0^2 + 0.0236T_0 - 1.57. \quad (5.4)$$

The resistivity at temperature T is calculated using the relationship

$$\rho(T) = \frac{\rho_0 V}{R_0 I} \quad (5.5)$$

where R_0 is the resistance in the filament at room temperature. The bulb temperature is now found by solving

$$\rho(T) = 1.79 \times 10^{-6}T^2 + 0.0264T - 3.25 \quad (5.6)$$

for T (this expression holds for $1200 < T < 2500$ K).

The spectral emittance of the Lambertian surface is calculated from

$$E(\lambda, T) = \epsilon(\lambda, T) \frac{2\pi c}{\lambda^4} \frac{1}{e^{hc/\lambda kT} - 1} \quad (5.7)$$

where $\epsilon(\lambda, T)$ is the tungsten emissivity, h is the Plank constant, c is the speed of light, and k is the Boltzmann constant. The tungsten emissivity at a particular wavelength and temperature is interpolated from the values in Table 5.8.

5-4.1 Theoretical sensitivity

The count rate on a CCD pixel (DN s^{-1} ; here DN stands for data numbers) is given by

$$N_{DN} = I_R S \quad (5.8)$$

Table 5.8. Emissivity of tungsten as a function of temperature and wavelength (Lide & Frederikse 1996).

Wavelength (nm)	Temperature (K)						
	1600	1800	2000	2200	2400	2600	2800
250	0.45	0.44	0.44	0.43	0.42	0.42	0.41
300	0.48	0.48	0.47	0.47	0.47	0.46	0.46
350	0.48	0.48	0.47	0.47	0.47	0.46	0.46
400	0.48	0.48	0.47	0.47	0.47	0.46	0.46
500	0.47	0.47	0.46	0.46	0.46	0.45	0.45
600	0.46	0.45	0.45	0.45	0.44	0.44	0.43
700	0.44	0.44	0.44	0.43	0.43	0.42	0.42
800	0.43	0.43	0.42	0.42	0.41	0.40	0.40
900	0.41	0.41	0.40	0.40	0.39	0.39	0.38
1000	0.39	0.39	0.38	0.38	0.37	0.37	0.37

where I_R is brightness of source (R nm^{-1}), related to Equation 5.1 by $B_{ph,\lambda} = I_R 10^{10}/(4\pi)$. The sensitivity of the Nigel instrument ($\text{DN R}^{-1} \text{ s}^{-1} \text{ nm}$) is given by,

$$S = \frac{10^{10}}{4\pi} Q(\lambda) \tau(\lambda) \frac{1}{G} \cdot A \cdot \Omega \cdot D \cdot P \quad (5.9)$$

where $Q(\lambda)$ is quantum efficiency of the CCD ($e^- \text{ph}^{-1}$), $\tau(\lambda)$ is the optical efficiency of the spectrograph, G is the CCD gain ($e^- \text{DN}^{-1}$), A is the surface area of the end of the fibre (m^2), Ω is the solid angle of the sky that the fibre ‘sees’ (sr), d is the dispersion in nm/mm , and P is the pixel size (mm).

The theoretical sensitivity of the system was calculated using the CCD quantum efficiency and the spectrograph efficiency supplied by the manufacturers. Figure 5.6 shows the CCD and spectrograph efficiencies, and the theoretical sensitivity of the system as a function of wavelength.

5-4.2 Measured sensitivity

Calibration images were taken while Nigel was at Dome C, using a 25 W tungsten globe. Because of the large wavelength range, light from wavelengths between 245 and 450 nm

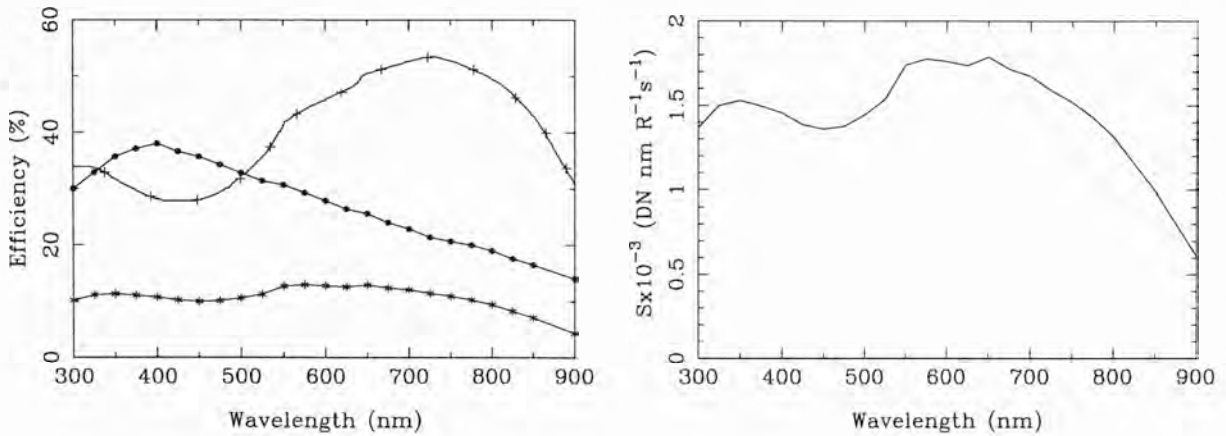


Figure 5.6. *Left:* manufacturer’s data on the CCD quantum efficiency (*crosses*), spectrograph efficiency (*dots*), and combined CCD and spectrograph efficiency (*stars*) as a function of wavelength. *Right:* theoretical sensitivity of Nigel, calculated using Equation 5.9.

will pass through the grating in the second order and contaminate the wavelength range 490–900 nm. To account for this, calibration images were taken with and without a 515 nm long-pass glass filter in front of the fibres. Figures 5.7a and 5.7b show the response of the system to the illuminated Lambertian screen, unfiltered and filtered, respectively. There is considerable difference between response of each fibre; the “worst” fibre only collects about 5% of the flux that the “best” fibre receives. This is probably because of poor coupling efficiency between the fibre ends and the grating, possibly a result of the polishing technique, or the fibre ends could have been damaged in transit.

Figures 5.7c and 5.7d show the response of each fibre with the intensity axis zoomed in to show the behaviour at short wavelengths. Even in the filtered case, the intensity does not drop to zero at shorter wavelengths but has a pedestal of about 2.7 DN s^{-1} . This is probably caused by scattering within the spectrometer. On average this pedestal accounts for about $(0.1\text{--}2) \times 10^{-4}$ of the total flux recorded in a fibre, close to the expected stray light rejection ratio, 10^{-4} , of the spectrometer.

The expected output from the tungsten globe was calculated using Equation 5.1. After removing the scattered light contribution from the measured spectra, the ratio between the measured response and the tungsten spectrum was calculated (i.e., the sensitivity, see Figures 5.7e and 5.7f). Also plotted is the theoretical sensitivity that was calculated

in Section 5-4.1. The system sensitivity obtained for the “best” fibre agrees reasonably well both in shape and in absolute terms with the expected transmission at wavelengths longer than about 500 nm. However, the absolute transmission of the other fibres is considerably less, as discussed earlier.

As shown in Figure 5.7e, this technique of flux calibration becomes unreliable at short wavelengths. This is because the flux radiated from the bulb is too weak and the response becomes dominated by scattered light; in addition, the glass bulb absorbs some UV light (Harang 2004).

Figures 5.7g and h show the measured transmission of each fibre, divided by the transmission through the best fibre. Each ratio is fairly constant, showing that as a means of calibrating the relative transmission between each fibre, this method is quite useful.

5-5 Conclusions on calibration methods

The wavelength calibration using the fluorescent tube was successful, and easy to carry out in a remote location. This calibration can be checked during the year using twilight and airglow emission lines.

The incandescent bulb method can potentially be used for absolute flux calibration at visible and near infrared wavelengths. Some care needs to be taken when using this method, including careful measurement of the albedo of the Lambertian surface, ensuring that all the fibres are exposed equally to the luminous surface, and eliminating background light. This technique could be improved by using a hotter filament in conjunction with a short-pass filter, although at very short wavelengths absorption of UV by the glass bulb becomes a problem. If delicate calibration standards cannot be taken into the field with the instrument, careful calibration could be carried out in a laboratory and this method could be used to check the calibrations in the field. Coupled with the wavelength calibration using a fluorescent bulb, this incandescent bulb method is a cheap and easy way to test the calibration.

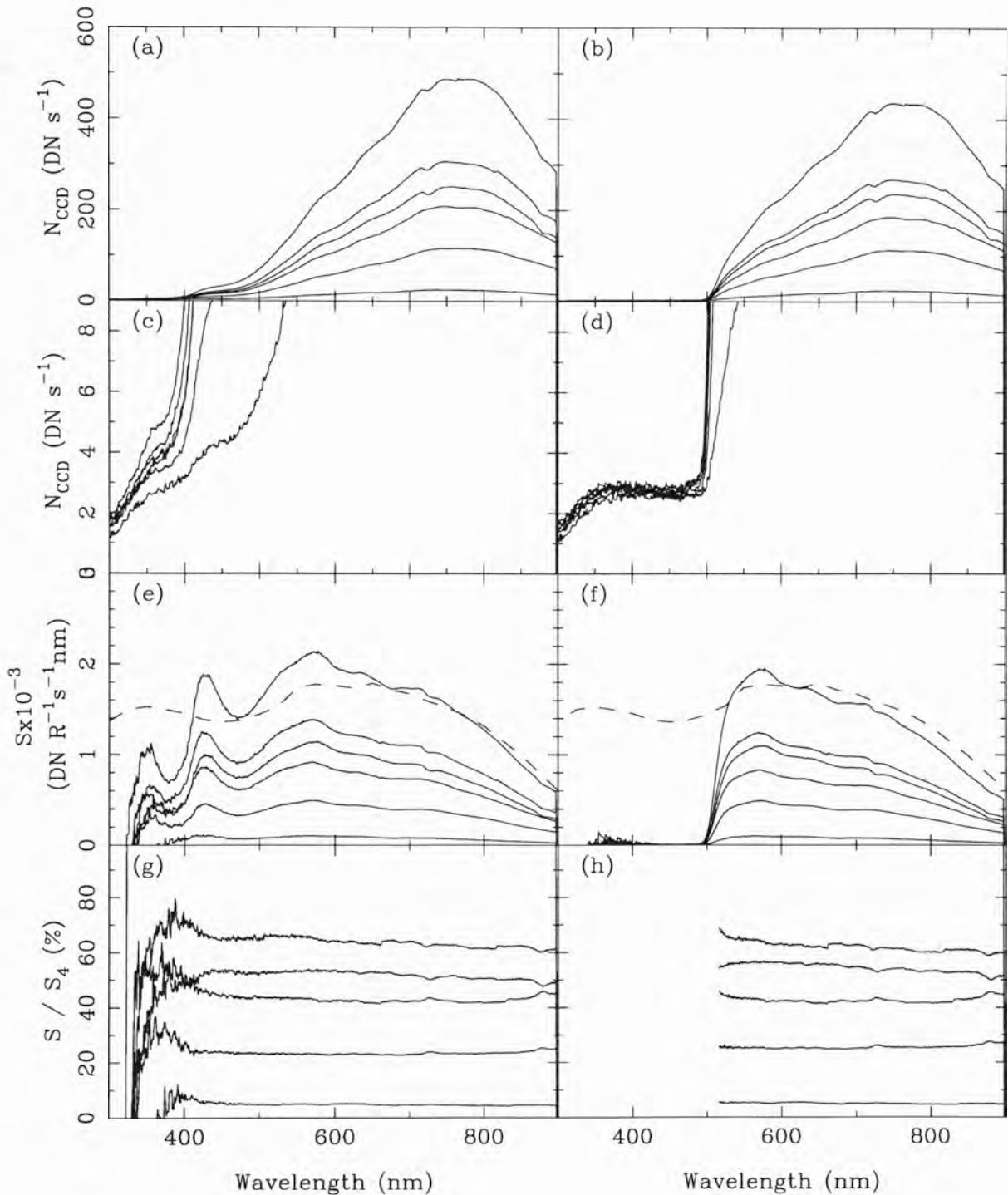


Figure 5.7. (a) The measured counts on the CCD for each fibre as a function of wavelength, for an exposure of the Lambertian screen, and (b) with a 515 nm long-pass filter in front of the fibres. Plots (c) and (d) are the same with the intensity axis zoomed in. Plots (e) and (f) show the measured sensitivity of the system, for the unfiltered and filtered set-ups, respectively. Also shown (*dashed*) is the theoretical sensitivity. Plots (g) and (h) show the measured sensitivity of each fibre relative to the “best” fibre. In all cases the top three fibres are those optimised for receiving the longer wavelengths.

5-6 Discussion and Nigel's plans for the future

Spectra measured by Nigel will be useful for measuring the overall sky brightness, and the contributions from individual airglow and aurora emission lines. Twilight spectra from Nigel could potentially be used to probe the aerosol content of the atmosphere as a function of the altitude of the Sun; these data could be compared to similar measurements at ESO-Paranal (Patat et al. 2006). Periods of cloud cover may also be identified using the spectra from Nigel because cloud will attenuate the light and change the spectrum, particularly in the early parts of twilight.

The large field of view (25°) of Nigel will mean that at times when the Galactic plane is passing through the field, the contribution from starlight will be comparatively large; each measurement needs to be carefully analysed according to what part of the sky is being observed. In this respect Nigel is an ideal companion instrument to the Gattini-Sky Background (Gattini-SBC) and Gattini-All Sky cameras (Moore et al. 2006a), currently in operation at Dome C. The Gattini-SBC is designed to measure the optical sky brightness between the stars in a 6° by 4° field centred on the South Pole. Gattini-SBC will also pick up auroral events; combination of these data with spectra from Nigel would allow these auroral events to be identified.

Nigel was removed from Dome C during the summer 2005/2006 season and returned to Sydney. The instrument will be upgraded and sent to either Dome C or Dome A for the 2008 winter. Before redeployment the fibres and connectors will be upgraded, and an in-line long-pass filter will be included on each of the red fibres to eliminate second order contamination from the shorter wavelengths. If the instrument is deployed to Dome A, it will need to be completely autonomous and may need to include a system to test the calibration throughout the year. Dome C is now manned all year around and the calibration could be regularly checked by the winter-over person in charge of the site-testing experiments.

‘Turbulence is the most important unsolved problem of classical physics.’

Richard Feynman (1918–1988)

Chapter 6

Atmospheric turbulence in Antarctica

The light from a star, or other astronomical object, is distorted as it passes through the turbulent atmosphere of the Earth. This distortion places limits on the resolution and sensitivity of ground-based optical telescopes. Astronomical telescopes should be located at sites where the atmosphere is calm and stable, and the turbulence is weak. The measurement of turbulence is a key part of every site-testing campaign.

In Section 6-1, the concept of turbulent flow in a fluid is introduced. The theory and statistical description of atmospheric turbulence are outlined in Section 6-2, and various parameterisations (including seeing, isoplanatic angle, and coherence time) are introduced. The first winter-time measurements of the strength of the turbulence as a function of altitude above Dome C were conducted in 2004; this experiment is described in Section 6-4. The data derived from this experiment are discussed in Section 6-5, and are compared to data measured with similar instruments at Cerro Tololo and Cerro Pachón in Chile. In Section 6-6, the turbulence measurements are interpreted in terms of the seeing, isoplanatic angle and coherence time.

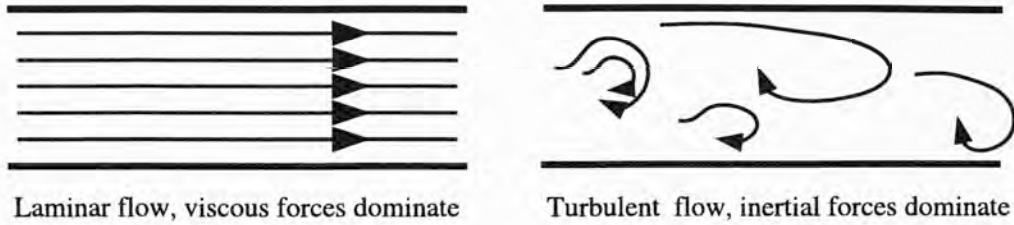


Figure 6.1. Schematic illustrating laminar and turbulent flow in a pipe. Laminar flow (*left*) occurs when the viscous forces dominate; the flow is smooth and steady. Turbulent flow (*right*) occurs when the inertial forces dominate; in a turbulent flow, eddies randomly form and swirl around.

6-1 Turbulent flow in fluids

We are surrounded by fluids that are in turbulent flows; for example, water spurting from a fire hose or smoke billowing from a chimney. A fluid is a liquid, gas or plasma that has the ability to deform, or flow, under an applied shear stress. Fluids are composed of discrete particles that interact with each other; however, the fluid as a whole is considered to be continuous and properties such as velocity, pressure, temperature and density are assumed to vary continuously. For example, water flowing from a tap is considered as a continuous stream rather than a series of individual molecules.

Two forces are at work in a fluid: viscous forces and inertial forces. The viscous force is related to the fluid viscosity (μ); the inertial force—the resistance of the fluid to change of motion—is related to the fluid density (ρ). The smooth and steady flow that occurs when the viscous forces dominate is called *laminar* flow. An example of this flow occurs when you slowly turn on a tap, the flow is streamlined and smooth. As the tap is turned on further the speed of the flow increases; although the average motion of the flow continues in one direction, the flow pattern becomes unsteady and chaotic, never repeating itself. In this type of flow the inertial forces dominate; this is called *turbulent* flow. Figure 6.1 illustrates laminar and turbulent flow in a pipe. The Reynold's number, Re , is used to characterise the flow conditions as laminar or turbulent; Re is simply the ratio of the inertial to the viscous forces and is defined geometrically as,

$$Re = \frac{\rho v L}{\mu} = \frac{v L}{\nu} \quad (6.1)$$

where ν is the kinematic fluid viscosity ($\nu = \mu/\rho$), v is the magnitude of the average

velocity of the flow, and L is the characteristic length of the flow. Turbulence occurs when Re exceeds a certain critical value. In the laminar flow illustrated in Figure 6.1, L is the diameter of the pipe.

In a turbulent flow, eddies of all different sizes form, these swirl around randomly with an overall motion in the direction of the flow. The largest scale of turbulent motion is labelled the *outer scale* (L_0); these large eddies break down into smaller eddies and these in turn break down into even smaller eddies. At a certain small scale (the inner scale, l_0) the viscous forces will dominate and the kinetic energy in these eddies dissipates into heat. This processes was summed up in verse by Richardson (1922)

“Big whorls have little whorls,
Which feed on their velocity,
And little whorls have lesser whorls,
And so on to viscosity.”

In 1941, Andrei Kolmogorov translated this notion of cascades, for eddies in the scale range $l_0 < L < L_0$, into a mathematical description. This paper was first published in Russian (Kolmogorov 1941), an English translation was published in 1991 (Kolmogorov 1991).

6-2 Optical turbulence

In the context of astronomy, turbulence refers to optical turbulence created in the atmosphere. The theory of optical turbulence was developed by Kolmogorov (1941) and Tatarski (1961). An excellent review of turbulence theory and its application to astronomy is presented by Roddier (1981). This next section draws largely on those three papers.

Two ingredients are required for the formation of optical turbulence in the atmosphere: a temperature gradient and wind shear. A simplified view of the formation of optical turbulence is illustrated in Figure 6.2. In this view, we consider two horizontal layers of the atmosphere that are at different temperature and have different water vapour concentration. As wind blows through these layers, the warmer and cooler air are mechanically mixed. If these layers are not completely mixed then cells of different

temperature, humidity and refractive index form—the refractive index of air is a function of the air temperature and water vapour concentration. These turbulent cells distort the light from a star as it passes through the atmosphere; see Figure 6.3 for an illustration of this process. The light from a star enters the atmosphere as a plane undistorted wavefront. Turbulent cells introduce phase changes in the wavefront; as the wave propagates towards the Earth these cells act as positive or negative “lenses” changing the wavefront curvature and introducing intensity fluctuations in the wavefront as well—this is sometimes described as a “speckle pattern”. The effect of these phase and intensity fluctuations can be seen on an image taken through a telescope. With a small aperture telescope the image is seen to randomly move around. With a larger aperture, the image will be blurred.

In the simplified view of turbulence formation we considered two horizontal layers of the atmosphere at different temperature; in the real atmosphere the temperature change with altitude is continuous, and optical turbulence formation is associated with rapid changes of temperature with altitude. A typical temperature profile is shown in Figure 6.3b; a rapid change in temperature with altitude usually occurs in the region of the tropopause. Strong optical turbulence is usually confined to several thin layers in the atmosphere. In an astronomical context atmospheric turbulence is usually divided into three regimes:

Telescope and dome turbulence: telescope and dome turbulence is usually related to temperature gradients inside the dome itself, and temperature gradients between the inside and outside of the dome. These gradients can usually be overcome by equalising internal and external temperatures; for example, by opening side panels on the dome to let air flow through.

Surface layer turbulence: surface layer turbulence is caused by the lower atmosphere interacting with the surface of the Earth. Wind shear is caused as the wind interacts with the local terrain (e.g., mountains and oceans) and man-made structures (e.g., nearby buildings). Temperature gradients are formed in this layer by the diurnal cycle of solar heating of the ground.

Free atmosphere turbulence. The free atmosphere turbulence is associated with wind shears (for example, caused by strong jet-stream winds), and convection in the

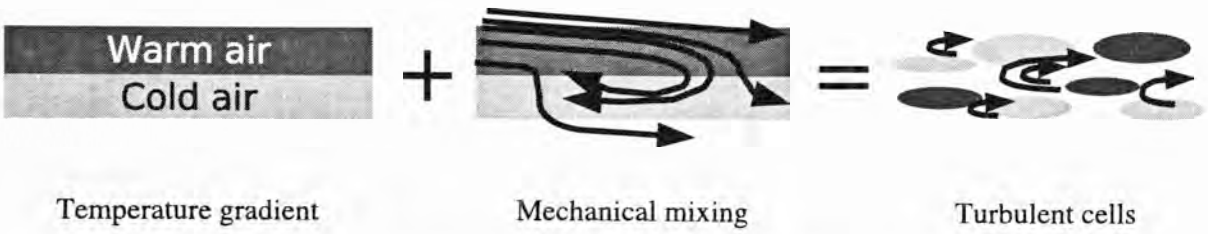


Figure 6.2. The formation of optical turbulence (adapted from Figure 2 of Lloyd 2004). Consider two horizontal layers in the atmosphere that are at different temperatures; as wind blows through these layers the warmer and cooler air is mixed. If the layers are not completely mixed then cells of varying temperature and humidity, and consequently refractive index, form. These cells randomly move around but have an overall average movement in the direction of the wind.

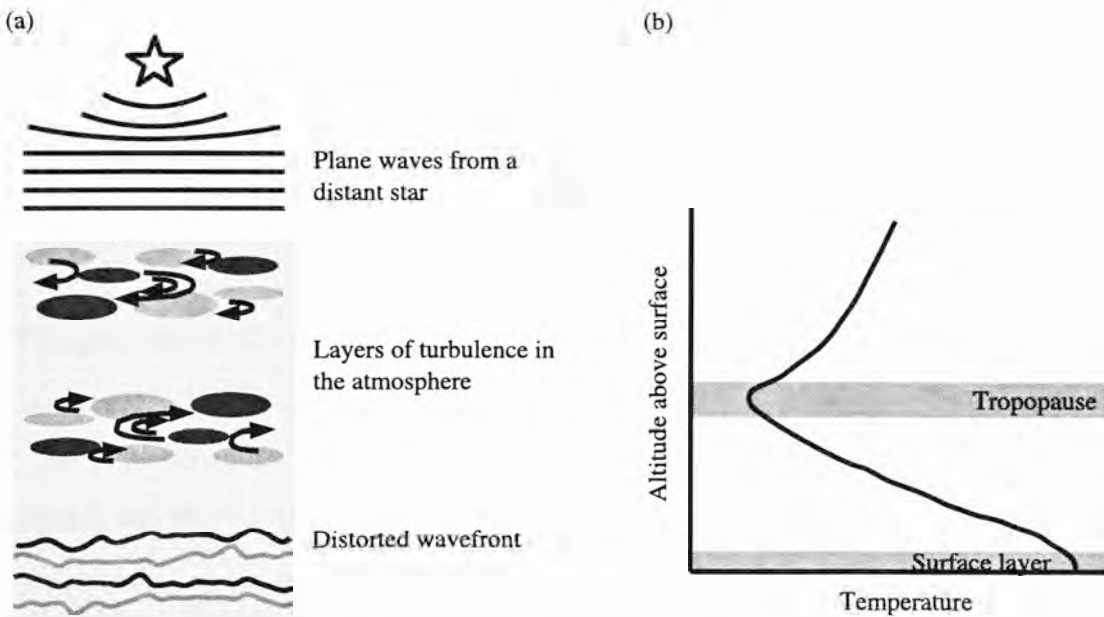


Figure 6.3. (a) A plane wave from a star is distorted by layers of turbulence in the Earth’s atmosphere, resulting in phase and intensity variations in the image. (b) A typical temperature profile in the atmosphere; strong turbulence is usually generated in the surface and tropopause layers. Note that in a profile plot the altitude is normally plotted on the vertical axis (even though it is the independent variable) to make visualisation easier.

tropopause.

6-2.1 Statistical description of turbulence

As discussed in the previous section, the light from an astronomical object is distorted by refractive index fluctuations in the atmosphere and these are related to temperature fluctuations. In the following section, the various parameters used to describe turbulence are defined, following Kolmogorov (1941); Tatarski (1961); Roddier (1981); Roddier et al. (1982a,b). To describe statistically the fluctuations in some parameter f we use a structure function—the mean square difference in the value of f at two points separated in space by distance r ; this is expressed as

$$D_f(r) = \left\langle (f(x) - f(x+r))^2 \right\rangle. \quad (6.2)$$

In the Kolmogorov theory of turbulence this structure function can be expressed as a power law,

$$D_f(r) = Br^{2/3} \quad (6.3)$$

where B quantifies the strength of the fluctuations. Temperature fluctuations in a turbulent flow are characterised by the structure function

$$D_T(r) = \left\langle (\Theta(x) - \Theta(x+r))^2 \right\rangle = C_T^2 r^{2/3} \quad (6.4)$$

where $\Theta = T - \langle T \rangle$ is the covariance of temperature fluctuations and C_T^2 is the temperature structure constant. A similar expression can be derived for humidity fluctuations $c = C - \langle C \rangle$ where C is the concentration of water vapour in the atmosphere. Fluctuations in the refractive index N of air are related to the temperature and humidity fluctuations by

$$n = N - \langle N \rangle = \frac{\delta N}{\delta T} \Theta + \frac{\delta N}{\delta C} c. \quad (6.5)$$

The variance of these fluctuations is given by

$$\langle n^2 \rangle = \left(\frac{\delta N}{\delta T} \right)^2 \langle \Theta^2 \rangle + 2 \frac{\delta N}{\delta T} \frac{\delta N}{\delta C} \langle \Theta c \rangle + \left(\frac{\delta N}{\delta C} \right)^2 \langle c^2 \rangle. \quad (6.6)$$

The last two terms are negligible for most astronomical observations (Roddier 1981, and references therein), so the refractive index fluctuations can be expressed as $n = (\delta N/\delta T)/\Theta$ and the structure function of n then also follows a power law,

$$D_N(r) = C_N^2 r^{2/3} \quad (6.7)$$

where C_N^2 is the refractive index structure constant, quantifying the strength of the optical turbulence. C_T^2 and C_N^2 , at height h , are related by

$$C_N^2(h) = \left(80 \times 10^{-6} \frac{P(h)}{T(h)^2}\right)^2 C_T^2(h), \quad (6.8)$$

where P and T are the pressure (mbar) and temperature of the atmosphere.

A wavefront in the atmosphere that is located at height h and horizontal position vector \mathbf{x} can be described by its complex amplitude (Roddiier 1981),

$$\Psi_h(\mathbf{x}) = e^{\chi_h(\mathbf{x}) + i\psi_h(\mathbf{x})}, \quad (6.9)$$

where χ_h is the logarithm of the amplitude and ψ_h is the phase of the wave. The wave structure function has the form (Fried 1966)

$$\begin{aligned} D(r) &= D_\chi(r) + D_\psi(r) \\ &= \left\langle |\chi(x) - \chi(x+r)|^2 \right\rangle + \left\langle |\psi(x) - \psi(x+r)|^2 \right\rangle, \end{aligned} \quad (6.10)$$

where D_χ and D_ψ describe the phase and intensity fluctuations in the wavefront. The wave structure function can be expressed as (Fried 1966)

$$D(r) = \mathcal{A}r^{5/3} = 6.88 \left(\frac{r}{r_0}\right)^{5/3}, \quad (6.11)$$

where \mathcal{A} quantifies fluctuations in the wavefront. Fried (1965) finds

$$\mathcal{A} = 2.91 \left(\frac{2\pi}{\lambda}\right)^2 \sec \gamma \int_{\text{prop path}} C_N^2(h) dh, \quad (6.12)$$

where γ is the zenith angle. The Fried parameter r_0 (m) is defined as

$$r_0 \simeq \left(\frac{6.88}{\mathcal{A}}\right)^{3/5} = \left[0.423 \left(\frac{2\pi}{\lambda}\right)^2 \sec \gamma \int C_N^2(h) dh\right]^{-3/5}. \quad (6.13)$$

The angular resolution, ϕ , of a telescope is given by

$$\phi = \begin{cases} 1.22\lambda D^{-1} & D < r_0 \\ 1.27\lambda r_0^{-1} & D > r_0 \end{cases} \quad (6.14)$$

where D is the diameter of the telescope. The light from a point source, such as a star, is diffracted as it enters the aperture of a telescope. When $D < r_0$, the resulting image will be limited by diffraction and will appear as an Airy disk; see Figure 6.4a. When $D > r_0$,

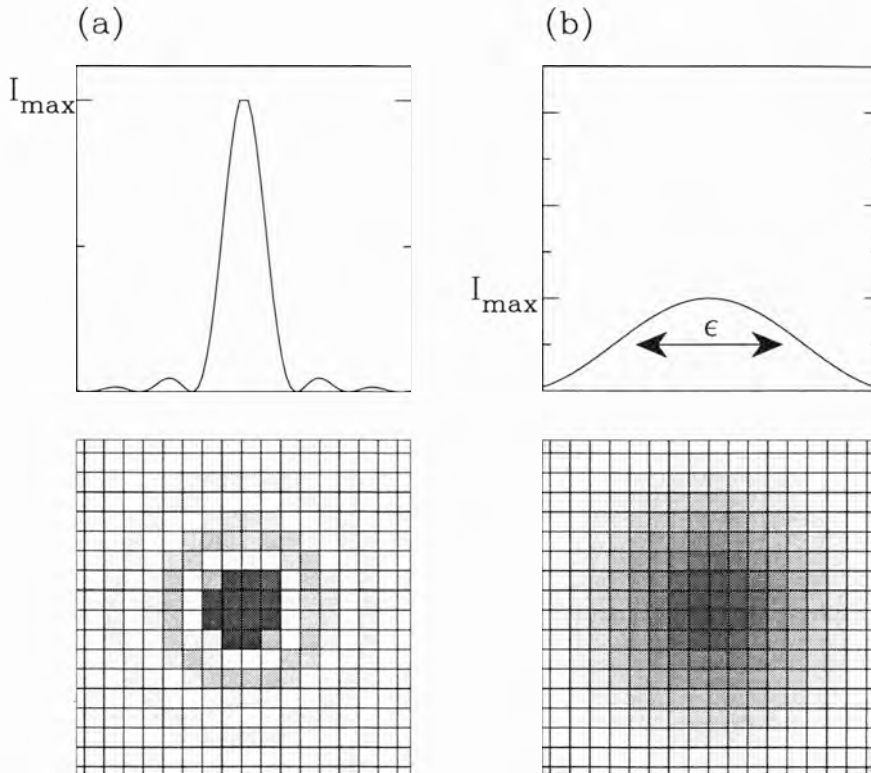


Figure 6.4. If the diameter (D) of a telescope is less than the Fried parameter (r_0) then the resulting image will be diffraction limited and the point spread function (PSF) will be an Airy disk; (a) shows the PSF and pixelated image for diffraction limited conditions. In turbulence-limited conditions ($D > r_0$) the PSF is broadened to a “seeing disk” as shown in (b); the full width at half maximum of this disk is called the *seeing* (ϵ).

phase perturbations in the atmosphere will broaden the image into a “seeing disk”; see Figure 6.4b. The full-width at half maximum of the seeing disk is called the *seeing* (ϵ); seeing is related to r_0 by $\epsilon = 0.98\lambda r_0^{-1}$ and can be calculated from the turbulence profile by

$$\epsilon = 5.307\lambda^{-1/5}(\sec \gamma)^{3/5} \left[\int C_N^2(h)dh \right]^{3/5} \quad (6.15)$$

where γ is the zenith distance.

The Fried parameter is also numerically equal to the largest size telescope aperture that will give diffraction-limited images. r_0 is typically in the range 10 to 20 cm for mid-latitude observatory sites. However, the diameter of modern optical telescopes is around 4 to 8 m, clearly larger than the typical Fried parameter. With the advent of extremely large telescopes the aperture sizes will be even larger, perhaps 20 to 100 m. Adaptive optics (AO) systems are installed on many telescopes to correct for some of the

effects of turbulence, thus increasing the resolution. AO systems operate by measuring the atmospheric distortion in a wavefront and then using deformable mirrors to correct the distortion. Most astronomical target objects are too faint for a fast and accurate measurement of the wavefront distortion, so a bright natural star or artificial reference star is used. Natural “guide” stars can be used if they are within the same coherent patch in the sky as the target object; i.e., the target and reference beam both pass through the same turbulence. The larger this “isoplanatic patch”, the more chance there is of finding a suitable reference star nearby the target object. If there is no natural reference beam close-by to the target, a strong laser beam can be used as an artificial reference; however, this adds another complexity to the system. A natural guide star is still needed for tip-tilt correction when using a laser guide star; however, this star can be fainter than that needed for full correction. The angular size of the isoplanatic patch, the isoplanatic angle (θ_0), for adaptive optics is related to the C_N^2 profile by (Roddier et al. 1982b)

$$\theta_0 = \left(\frac{\lambda}{2\pi} \right)^{6/5} \left[2.91 \sec \gamma \int h^{5/3} C_N^2(h) dh \right]^{-3/5}. \quad (6.16)$$

The atmospheric turbulence above a telescope continuously changes, remaining coherent for only a few milli-seconds. The deformable mirror in the AO system has to keep up with these fast changes; a fast coherence time means a more complex system is required. The coherence time for adaptive optics, τ_0 , is calculated using (Roddier et al. 1982a)

$$\tau_0 = \left(\frac{\lambda}{2\pi} \right)^{6/5} \left[2.91 \sec \gamma \int v^{5/3}(h) C_N^2(h) dh \right]^{-3/5} \quad (6.17)$$

where $v(h)$ is the wind speed profile. Formally θ_0 and τ_0 are the angle and time over which the coherence area for wavefront perturbations decays by $1/e$ (Roddier et al. 1982a,b). By measuring the turbulence C_N^2 profile in the atmosphere we can describe the optical turbulence at a particular site using these parameters.

6-3 Turbulence measurements in Antarctica

The excellent optical conditions in Antarctica have been recognised for many years. For example, following a ship voyage to the Antarctic waters, Diets (1948) comments:

“Even more impressive than the clarity of some of the Antarctic days, is the atmospheric transparency of many of the Antarctic nights... Stars shine

brilliantly and can be seen down almost as far as the horizon. Most surprising is the fact that the stars shine with a bright steady light and do not twinkle. All of this adds up to excellent “seeing”—probably unsurpassed anyway in the world.”

Diets was observing the effect of weak atmospheric scintillation, i.e., the stars are seen not to twinkle. He used the expression “seeing” to refer to the clear atmospheric conditions, rather than the formal astronomical meaning related to phase fluctuations.

In the early 1990’s, Gillingham (1991, 1992) suggested that, above a thin boundary layer, the atmospheric turbulence on the Antarctic plateau would generally be very weak. This was confirmed by the first measurements at the South Pole by Marks et al. (1999). These showed that most turbulence is found close to the surface, in this case confined to a 220 m thick layer, with very weak turbulence at high altitudes. In comparison, at most temperate sites the turbulence is strong, not only in the surface layer, but also in the tropopause and above, caused by the interactions of the jet stream with temperature gradients in the tropopause.

The atmospheric turbulence at Dome C has now been studied with five different instruments: an acoustic radar or SODAR (SOund Detection And Ranging), a Multi-Aperture Scintillation Sensor (MASS), a Differential Image-Motion Monitor (DIMM), a Single Star Scidar (SSS), and microthermal sensors. SODAR emits sound pulses into the air and derives the strength of the atmospheric turbulence as a function of height from the intensity and delay time of the reflected sound. MASS uses the scintillation from a single star to provide a low resolution profile of the atmosphere. DIMM observes the relative motion of two images of the same star viewed through two sub-apertures of a small telescope; from this, the integrated atmospheric seeing is derived. SSS monitors the scintillation from a single star to measure the turbulence and wind profile in the atmosphere. Microthermal sensors, carried aloft on a weather balloon, make in-situ measurements of the temperature fluctuations of the air as a function of height, usually up to about 20 km.

SODAR measurements in the early months of 2003 by Travouillon (2005) showed that, as expected, the surface turbulent layer at Dome C was much thinner than at South Pole. Summer-time measurements using a DIMM in 2003/2004 and 2004/2005 showed a median seeing and isoplanatic angle of 0.54” and 6.8”, respectively; the lowest seeing

recorded was $0.08''$ (Aristidi et al. 2005b). The upper atmosphere winter-time turbulence profile was first monitored in 2004 with a MASS; this experiment is discussed below.

6-4 Measuring the night time turbulence profile at Dome C

The distribution of turbulence in the atmosphere, not just the integrated seeing, is very important for assessing an astronomical site. A SODAR was used at Dome C from 2003 to 2005 to monitor the turbulence profile from 30 m to 900 m above the ground in 30 m intervals. In 2004, a MASS was installed to simultaneously measure the turbulence from 0.5 km to 20 km above the surface. The MASS instrument operated from 23 March to 16 May for up to 17.5 hours a day, depending on the elevation of the Sun; the SODAR was in operation from 1 February to 4 May of 2004. The data from this time period are analysed in detail in the sections below and have been reported in Lawrence et al. (2004) and Kenyon et al. (2006b) in terms of seeing and scintillation, respectively.

6-4.1 Dome C SODAR

The SODAR instrument used at Dome C is described in detail in Travouillon et al. 2003a,b and Travouillon 2004. In brief, the SODAR operates by emitting a pulsed acoustic signal into the atmosphere and listening for a return signal. The signal is partially reflected from turbulent layers; the intensity of the returned signal C_{T0}^2 , for this instrument, is related to the temperature fluctuation constant C_T^2 of the atmosphere by $C_T = 1.43 \times 10^6 C_{T0} + 5.4 \times 10^6$. When the echo strength is not strong enough (i.e., $C_T^2 \approx 0$) then we only obtain an upper limit on the strength of the turbulence. C_T^2 is converted to the refractive index fluctuation constant C_N^2 using Equation 6.8. Profiles of the wind speed and direction are also extracted from the SODAR signal. The turbulence is averaged over 30 minute intervals.

6-4.2 MASS

MASS gives the vertical turbulence profile of the atmosphere above a site using the scintillation information from a single star (Tokovinin & Kornilov 2002; Kornilov et al. 2003b). As light from a star propagates through the atmosphere it passes through cells

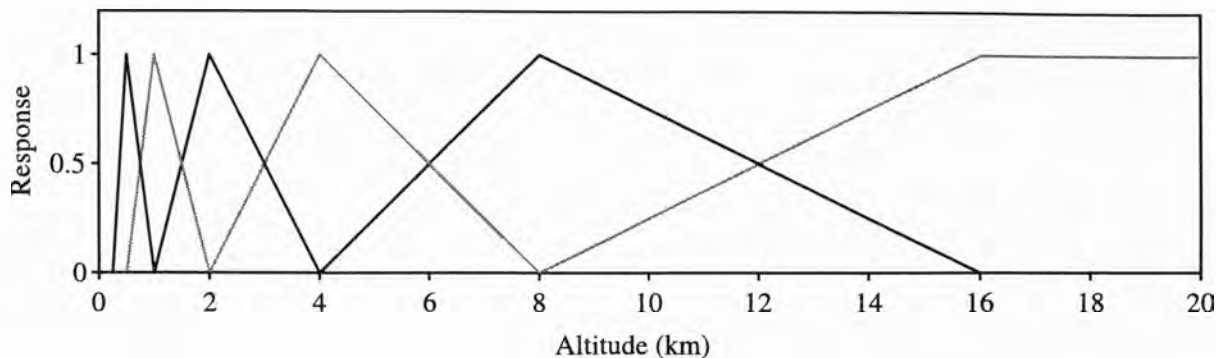


Figure 6.5. Ideal MASS response function for a single turbulence layer at each altitude (0.5, 1, 2, 4, 8 and 16 km) with resolution $\Delta h/h$ (Tokovinin et al. 2003b).

of turbulence. These cells introduce phase perturbations in the wavefront, resulting in phase (seeing) and intensity (scintillation) modulations at the telescope. The spatial distribution of the scintillation pattern is related to the altitude of the turbulent layers by $r_F = (\lambda h)^{1/2}$; hence it is possible to restore the turbulence profile as a function of height above the ground from the scintillation pattern.

MASS measures the light flux from a star through four concentric apertures (diameters 2, 3.7, 7.0 and 13 cm). The smallest aperture collects data on turbulence lower in the atmosphere and the largest on turbulence in the higher layers (Tokovinin et al. 2003b). The flux from each aperture is directed onto a photomultiplier tube in photon-counting mode. The algorithm to restore the turbulence profile from the photon counts is described in Tokovinin et al. (2003b). Briefly, the raw photon counts are used to calculate four normal and six differential scintillation indices. There is a linear relation between the scintillation indices and the height and strength of the turbulence layers; this relationship is derived in two ways:

1. A linear matrix is solved to find the intensity J_l (see Equation 6.18) of six turbulent layers at *fixed* altitudes of 0.5, 1, 2, 4, 8, and 16 km above ground level, with resolution of $\Delta h/h = 0.5$ (Figure 6.5 shows the ideal MASS response function).
2. The matrix is solved to find the strength, J_l , and height of three *floating* turbulent layers on a higher resolution altitude grid; this method is useful to locate dominant turbulent layers.

The intensity of a layer, J_l ($\text{m}^{1/3}$), is the integral of the refractive index structure constant $C_N^2(h)$ over the layer width (Tokovinin et al. 2003b),

$$J_l = \int_{\text{layer}} C_N^2(h)W(h)dh, \quad (6.18)$$

where $W(h)$ is the response function of the MASS. Atmospheric seeing (in arcseconds) at 500 nm is related to the turbulence intensity at each altitude l by (Tokovinin et al. 2003a)

$$\epsilon_l = \left(\frac{J_l}{6.8 \times 10^{-13}} \right)^{3/5}. \quad (6.19)$$

The spectral filter in MASS passes wavelengths from 400 to 550 nm with a full-width at half maximum bandwidth of 100 nm (Tokovinin et al. 2003b).

The raw MASS data for each night are saved into a time-stamped file. Each line in the file starts with a letter identifying the data it contains, for more details see the MASS user Guide (Kornilov et al. 2003a).

6-4.3 Dome C MASS

The MASS unit that was used in the AASTINO at Dome C is described in detail in Lawrence et al. (2004). The installation of the Dome C MASS unit was modified from the typical set-up that is used at temperate sites because of the unusual conditions of the site; in particular, the extremely cold temperature and the remote location—Dome C was unmanned during winter until 2005. The installation of the MASS instrument in the AASTINO is shown in Figure 6.6. Starlight comes through a window on the top of the AASTINO and is reflected from a gimbal-mounted siderostat mirror to a fold mirror, and then into the 85 mm refracting telescope. The telescope is fixed pointing towards the zenith. From the telescope, 5% of the light is directed via a beamsplitter to a CCD camera, used for star tracking. The remaining 95% is reflected into the MASS instrument. A second CCD camera points towards the window to monitor icing.

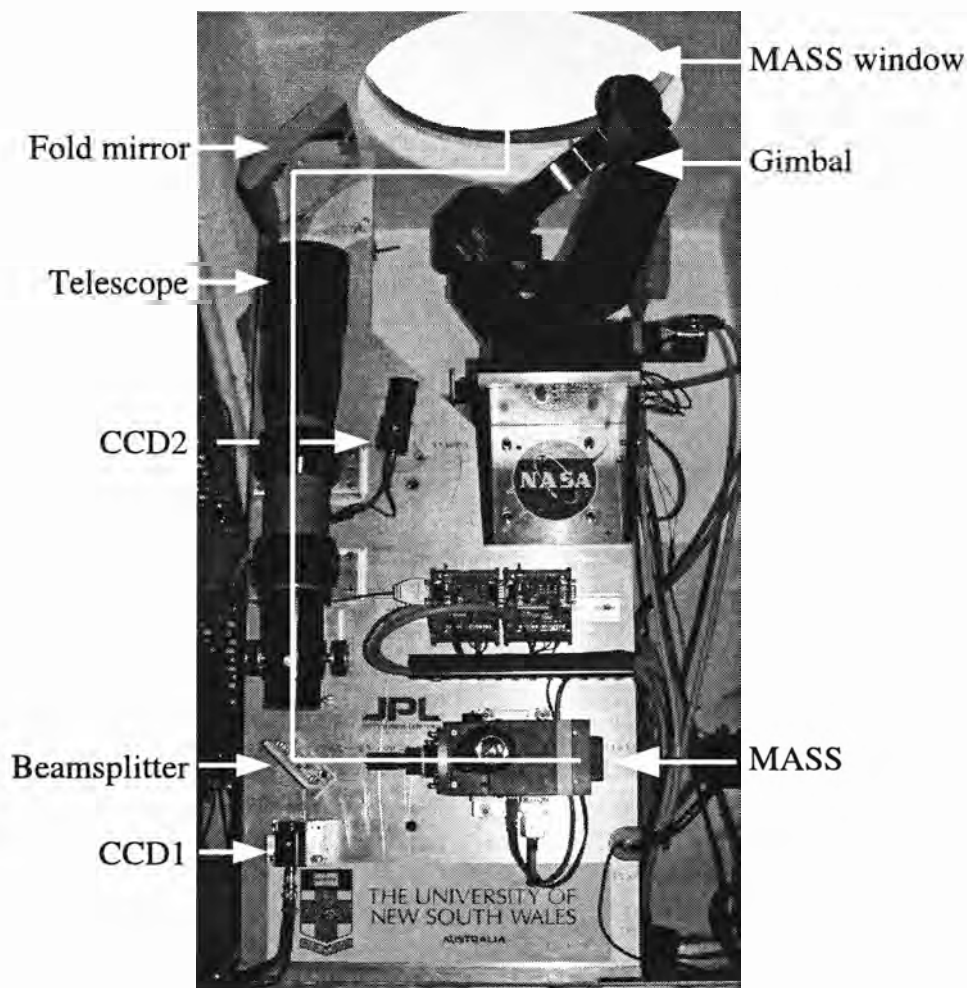


Figure 6.6. MASS installation in the AASTINO showing the light path (*white*) through the window, reflected from the gimbal and fold mirror to the telescope. The majority of the light from the telescope is reflected from a beamsplitter into the MASS instrument; the remainder is transmitted to a camera (CCD1) used to check the star position in the telescope. A second camera (CCD2) is used to monitor the window for icing. (Figure from Lawrence et al. 2005).

6-4.4 MASS data filtering

Over the eight weeks that the MASS operated at Dome C, 11 532 turbulence profiles were extracted spread over 51 nights (“night” is used to mean the period within 24 hr when the Sun is farther than 10° below the horizon). These data were filtered according to a number of criteria (listed below); histograms of each of these parameters are shown in Figures 6.7 and 6.8. After filtering, 1850 profiles over 26 nights remained for further analysis.

Filtering criteria:

1. The flux in channel D (the largest aperture) must be above a certain value. This helps to eliminate data where the star is not properly centred and when the flux is attenuated by cloud, diamond dust, or ice on the window. Three stars were used for scintillation measurements at Dome C. Figure 6.7 shows the flux measurements for each star and the corresponding flux limits (100 counts/ms for α Trianguli, and 200 counts/ms for β Crucis and β Carinae). A large amount of data did not meet this criterion because either the window was covered by ice, or there were ice crystals in the atmosphere. Figure 6.9 shows the flux measurement in channel D on three days with different weather conditions.
2. The uncertainty in the flux measurement in channel D must be less than 0.003 (i.e., $\delta F_D < 0.003$). The parameter δF_D shows slow flux variations and is used to eliminate data affected by guiding errors; see Figure 6.8a.
3. The ratio between the background and star flux in channel D must be less than 0.03 (i.e., $B_D/F_D < 0.03$). This criterion eliminates data where the background flux is too high, or when the flux is diminished by cloud or ice or because the star is not centred; see Figure 6.8b.
4. The ratio between the flux in channels C and D must be in the range $0.7 < F_C/F_D < 0.9$. The flux ratio, F_C/F_D , serves to control the aperture vignetting by the entrance window, which was sometimes covered by snow or frost; see Figure 6.8c.
5. The final criterion is $\chi^2 < 100$, where χ^2 is a measure of the fit quality.

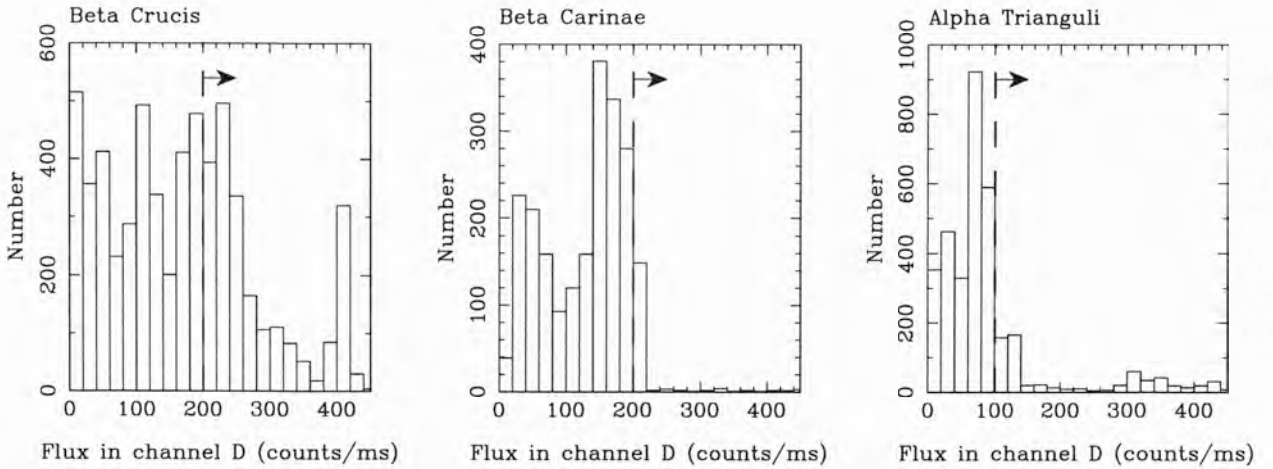


Figure 6.7. Histograms of the flux recorded in channel D for *alpha* Trianguli, *beta* Carinae and *beta* Crucis; the *dashed* line in each plot shows the flux cut-off limit for each star and the arrows show the direction of “good” data.

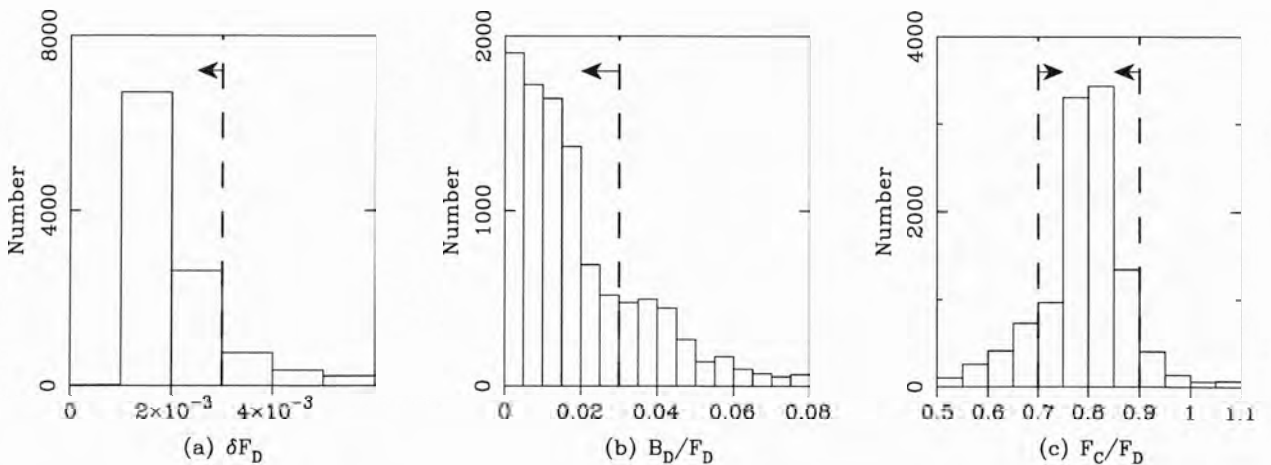


Figure 6.8. Histograms of (a) the uncertainty (δF_D) in the channel D flux measurement, (b) the ratio of the background (B_D) to star flux (F_D) in channel D , and (c) the ratio of flux in channel C to D . The *dashed* line in each plot shows the cut-off limit for each filtering criteria (see text) and the arrows show the direction of “good” data.

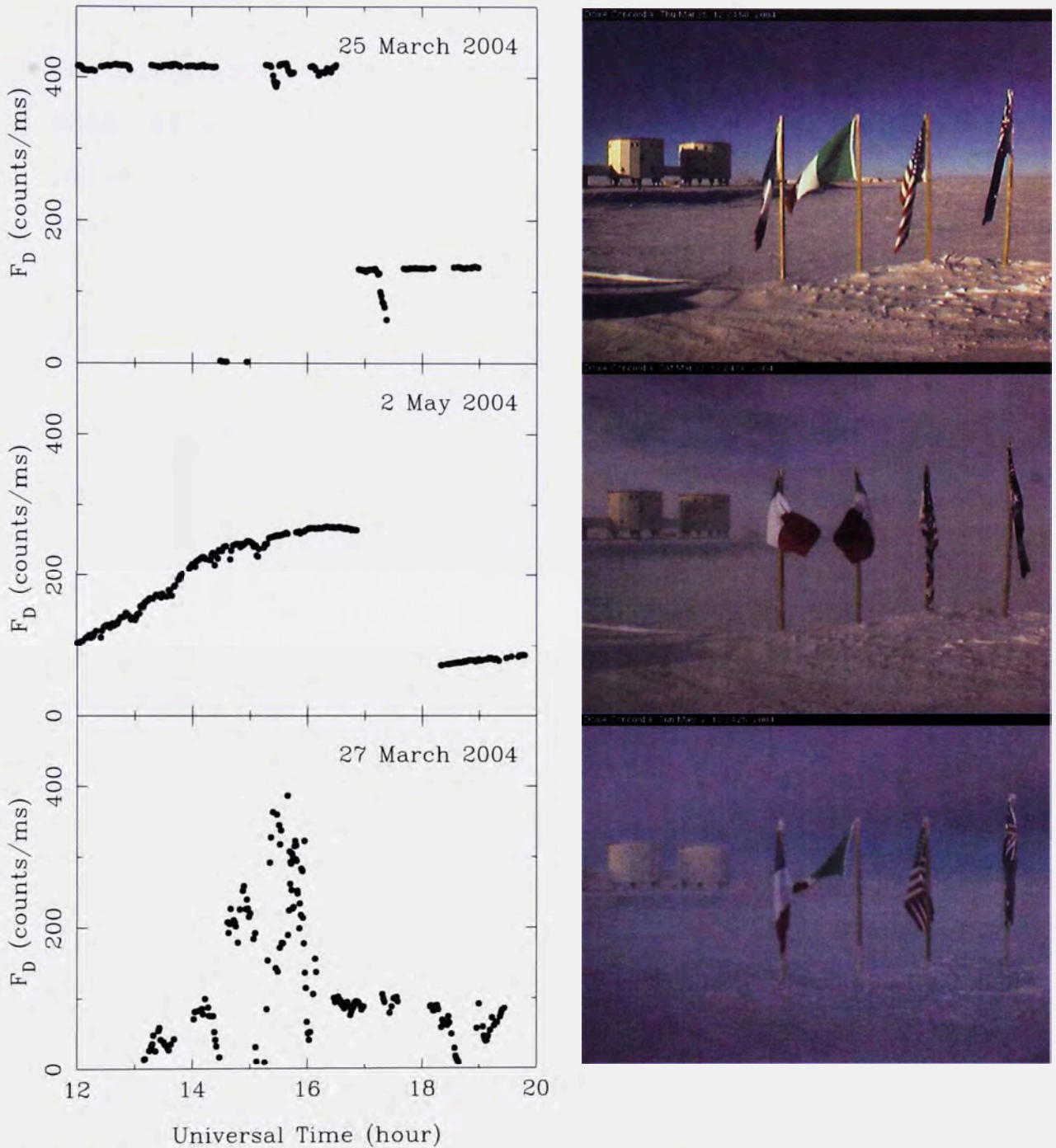


Figure 6.9. The stellar flux received by the MASS is attenuated if the star is not centred in the telescope, or by weather conditions such as ice on the window, diamond dust in the atmosphere and clouds. The flux that was recorded through the largest aperture of MASS, on three nights, is shown on the left; the images on the right show the weather conditions on each day. The large step in the flux at about 17:00 corresponds to a change in the star being observed. The weather was very clear on 25 March, resulting in steady flux measurements; on the other two days the flux was attenuated by the weather conditions.

6-4.5 Combining SODAR and MASS data

To cover the whole atmosphere (from 30 m to 20 km) the SODAR and MASS data were combined; the SODAR data were limited to the measurements below 500 m. The MASS measurements are recorded every few minutes whereas the SODAR data are recorded in 30 minutes blocks; each MASS measurement was matched to the nearest 30 minute SODAR measurement. The total seeing and isoplanatic angle were summed using

$$\epsilon_{total} = \left[\epsilon_{mass}^{5/3} + \epsilon_{sodar}^{5/3} \right]^{3/5} \quad (6.20)$$

and

$$\theta_{total} = \left[\theta_{mass}^{-5/3} + \theta_{sodar}^{-5/3} \right]^{-3/5}. \quad (6.21)$$

6-5 Turbulence profiles

6-5.1 Lower atmosphere turbulence profiles

Low-altitude turbulence profiles are used to detect the strength and height of the surface layer turbulence; a telescope can be built above the surface layer if the turbulence is confined close to the ground. Temperature gradients form in the surface layer when the Sun heats the surface of the Earth. Low-altitude turbulence profiles, measured with SODAR in 2004, are displayed in Figure 6.10; the data are expressed in terms of C_T^2 in height intervals of 30 m. The SODAR was run almost continuously between 1 February and 4 May, and was restarted again on 22 November. Also shown in Figure 6.10 is the altitude range of the Sun over the same time periods as the SODAR measurements.

Dome C experiences surface heating during the summer months because the Sun is always above the horizon. A boundary turbulence layer is formed during these months, rising to about 200 m above the surface (see February and December in Figure 6.10). As the Sun steadily drops toward and below the horizon, the boundary layer becomes lower in height and weaker in strength until it completely disappears below the detection height (30 m) of the SODAR. In April and May random patches of turbulence were measured, but on the whole the turbulence is below the sensitivity limit of the SODAR and we can only get an upper limit on the strength of the turbulence. This effect is discussed in more detail in Travouillon (2004).

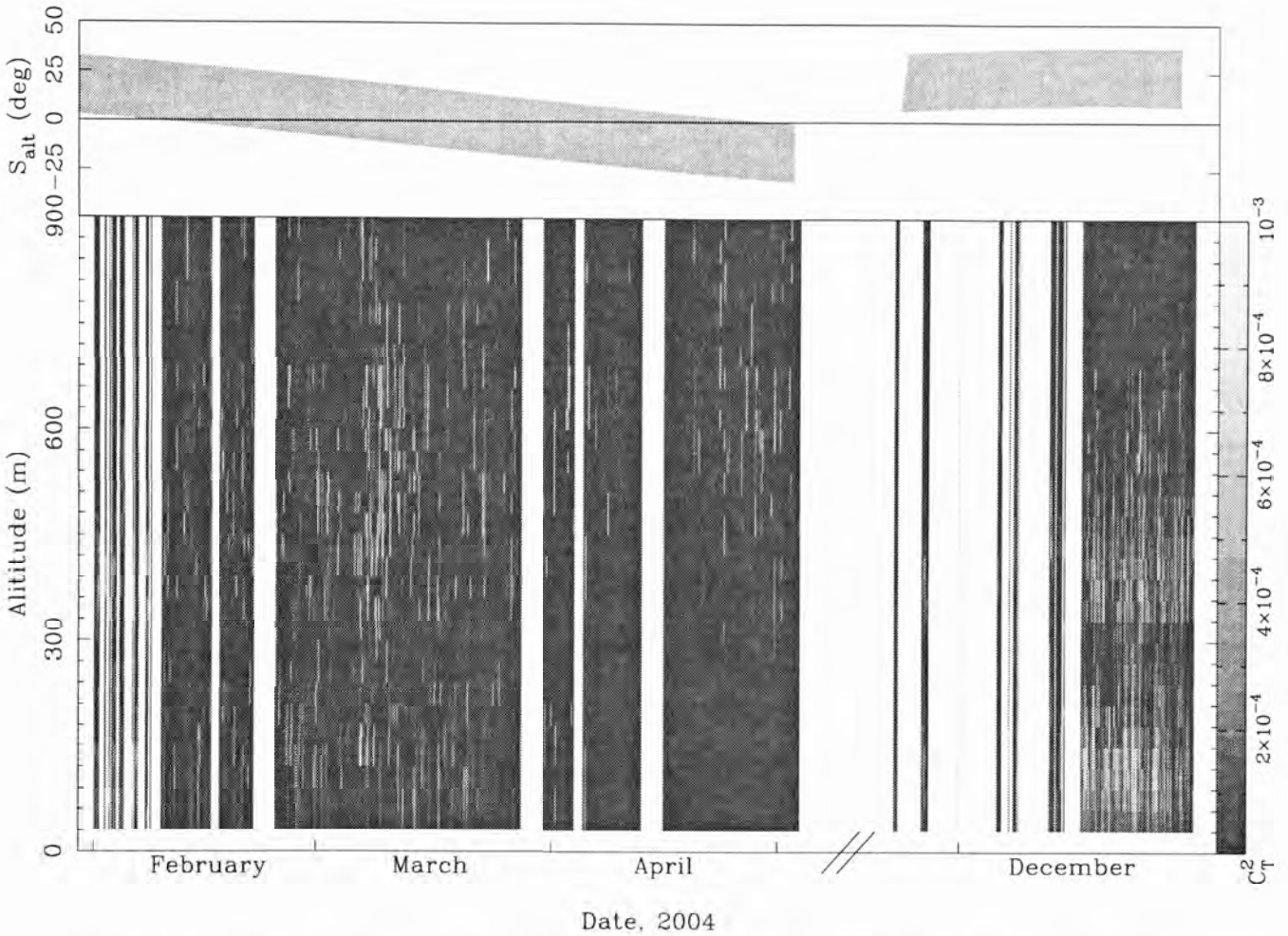


Figure 6.10. *Top:* the grey shading shows the altitude range of the Sun during 2004. *Bottom:* colour-intensity diagram of the turbulence in the lower atmosphere at Dome C in 2004, measured using a SODAR. The colour level indicates the intensity of C_T^2 according to the scale on the right, the darkest colour corresponds to the detection limit of the SODAR; the vertical axis indicates the height of each level above the ground. The horizontal axis shows the date of each measurement; note there is a break in the scale at the beginning of May.

6-5.2 Upper atmosphere turbulence profiles

The MASS profiles measured at Dome C in 2004 are displayed in Figure 6.11; Figures B.1 to B.13 in Appendix B show daily plots of the turbulence profiles. At Dome C the strongest turbulence occurs in the lowest MASS layer (centred at 0.5 km); the turbulence in the layers at 1 km and 16 km is very weak compared to the other layers. Strong turbulence tends to occur in short “bursts” of a few minutes to about an hour; for example, see the profiles for 24 and 25 March (Figure B.1 on page 142). On a number of days the turbulence over the entire atmosphere was very weak (e.g., 1 April on page 145). The only day that had very strong turbulence, in comparison to the average, was 14 May (page 153); the turbulence was very strong in the layers centred at 0.5, 4 and 8 km, with very little turbulence in the other layers.

The floating restoration method of the MASS instrument gives the altitudes (selected from a higher resolution grid) of the three most intense levels of turbulence in the atmosphere for each measurement (rather than for six fixed layers; see Section 6-4.2 for further details). Figure 6.12 shows a histogram of the number of times a profile at a particular altitude was extracted, as a fraction of the total number of profiles. This plot gives an indication of the heights in the atmosphere of the dominant turbulence layers; in this case broad peaks occur at 1.6 km, 2.5 km, and 9.9 km, and sharp spikes occur at 0.5 km in the lowest level and 20.0 km in the highest level. The sharp spike at 0.5 km is expected because strong turbulence is usually found close to the Earth’s surface.

MASS instruments are operated at a number of other sites around the world. To provide a comparison to the Dome C results, the publicly available MASS data¹ from the Cerro Tololo and Cerro Pachón observatories in Chile are also included (see Table 6.1 for information on each data set). The profiles for Cerro Pachón have been discussed and modelled by Tokovinin & Travouillon (2006).

Figure 6.13 shows the cumulative probability that the integrated turbulence for each height is less than the given J_l , for the three sites. Cerro Tololo has the lowest turbulence in the 0.5 km layer. At 1 km the turbulence at Dome C is so low that, for most of the time, it cannot be reliably measured with MASS. Dome C has a slightly higher probability of

¹Obtained from the National Optical Astronomy Observatory web page “Sites Data Access,” at <http://139.229.11.21/>

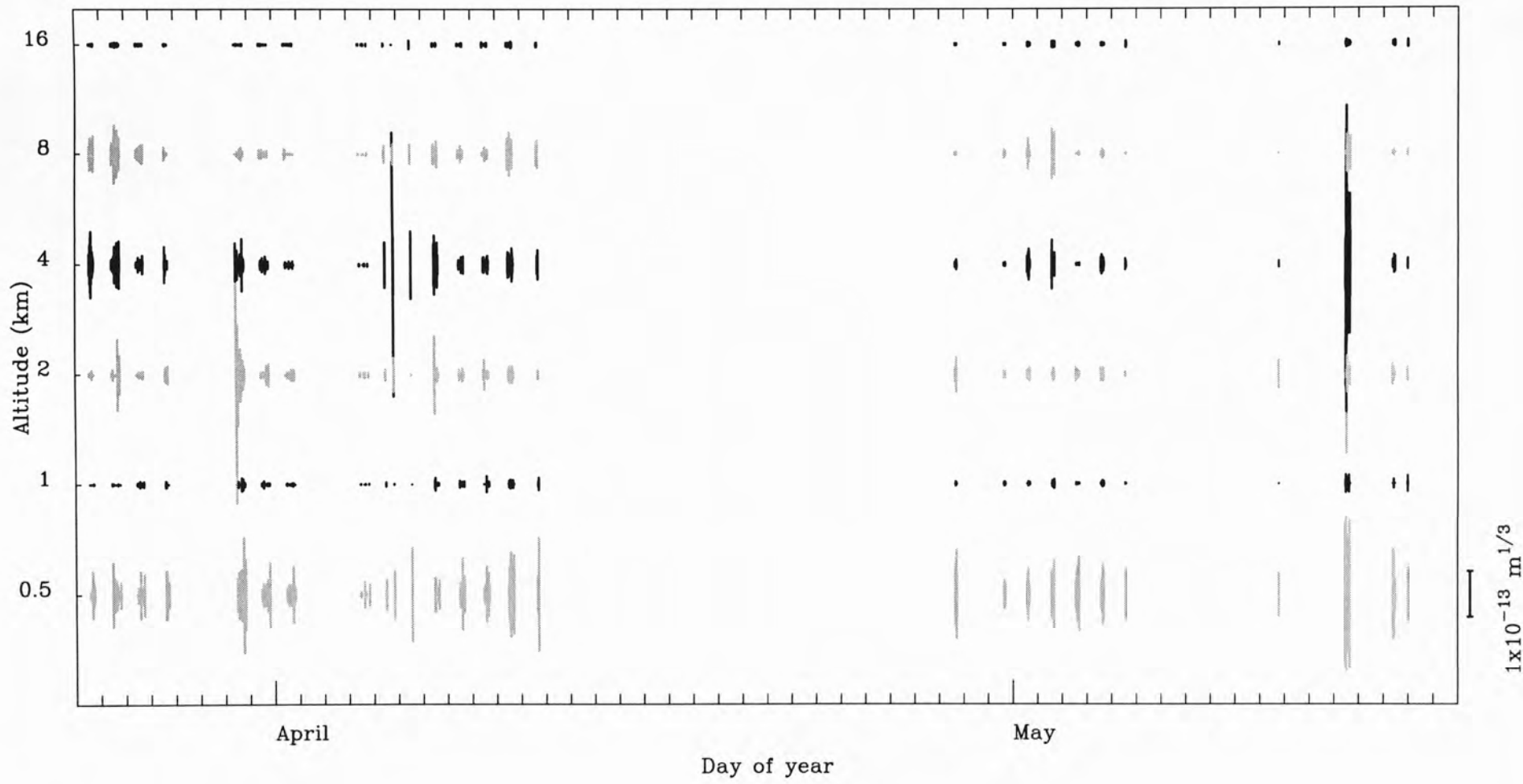


Figure 6.11. Integrated turbulence profiles measured by the MASS at Dome C in 2004. Each line gives the turbulence strength J_l at a particular height, according to the scale on the right.

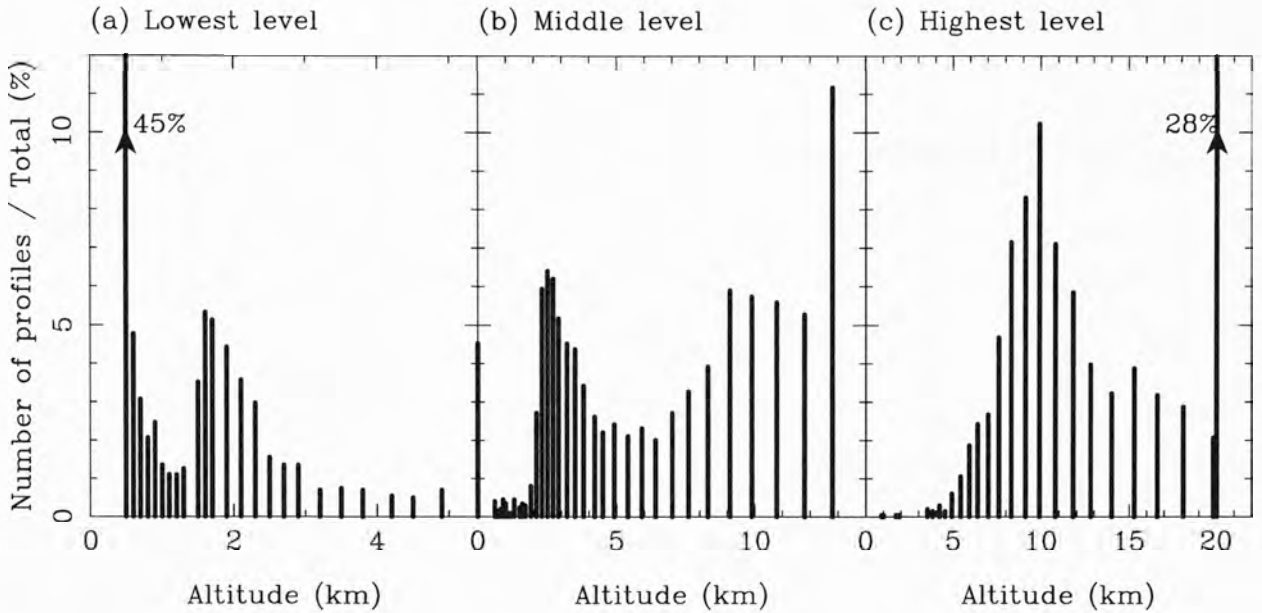


Figure 6.12. In the *floating* layer reduction method of MASS, the height of the three layers with the strongest turbulence are extracted from a grid of altitudes. This plot shows the number of times a layer was extracted at each altitude as a fraction of the total number of layers.

Table 6.1. Data sets for each site. The last two columns show the total number of nights for which useful data were extracted, and the number of useful profiles that were extracted. In the case of Dome C “night” is used to mean the period within 24 hours when the Sun is further than 10° below the horizon.

Site	Location	Altitude (m)	Date range	Number of	
				Nights	Profiles
Dome C	123°21' E 75°06' S	3260	23 Mar 04–16 May 04	26	1850
Cerro Tololo	70°48' W 30°09' S	2215	19 Mar 03–26 Aug 06	613	110394
Cerro Pachón	70°44' W 30°14' S	2215	9 Jan 03–30 Jan 06	293	39819

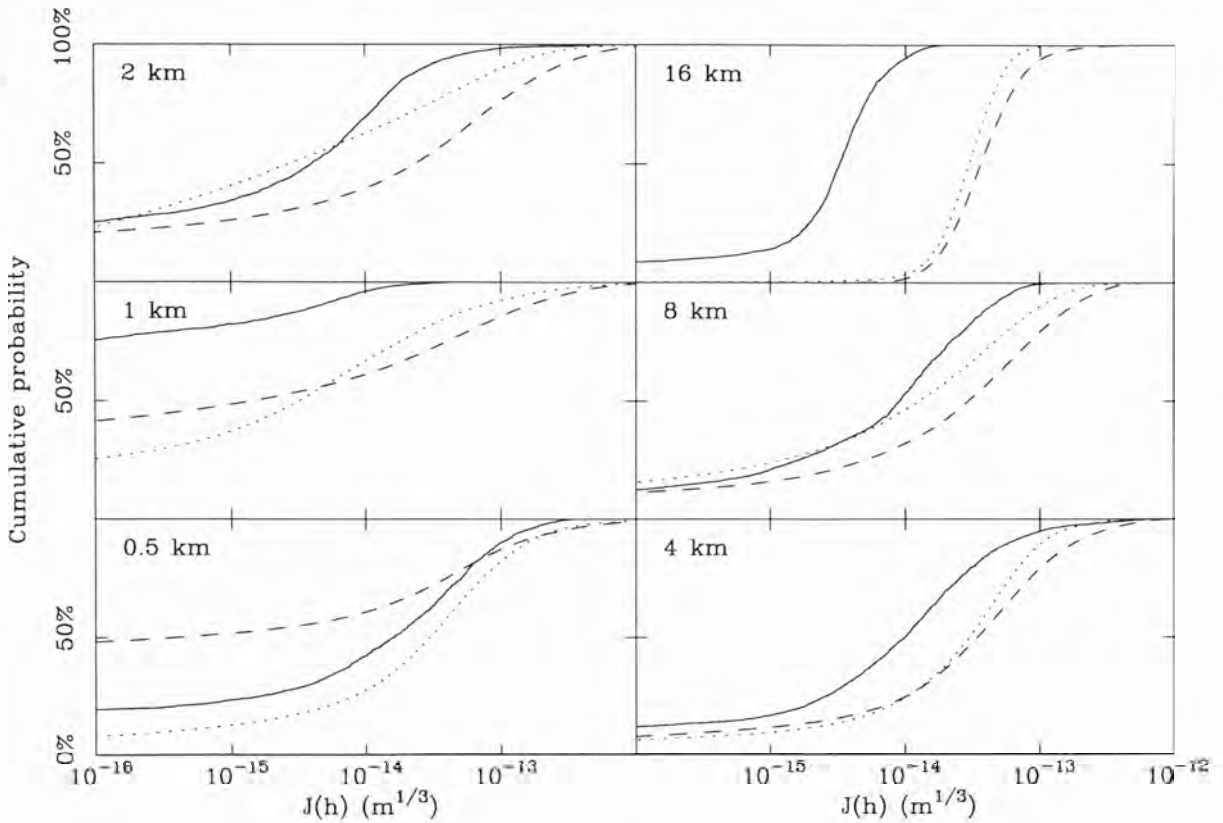


Figure 6.13. Cumulative probabilities that the integrated turbulence for each height (above the surface) is less than the given J_l for Dome C (*solid*), Cerro Tololo (*dashed*) and Cerro Pachón (*dotted*). The large fraction of very low J_l values for the 0.5 km and 1 km layers is an artifact of the MASS profile restoration method in situations when these layers do not dominate.

weaker turbulence in the 4 and 8 km layers. However, the most significant difference between the sites is in the 16 km layer; at Dome C the integrated turbulence in this high-altitude layer is *always less* than the median values at Cerro Tololo and Cerro Pachón.

The Cerro Tololo and Cerro Pachón sites are only 10 km apart and have a 400 m altitude difference. Hence, we expect identical high-altitude turbulence for those sites. The differences seen in Figure 6.13 reflect mostly different seasonal coverage of the data sets (more winter-spring data for Cerro Tololo) coupled to the systematic seasonal trends in high-altitude turbulence. Similar caution is warranted for the Dome C data that cover only 25 nights.

Table 6.2. Isoplanatic angle and coherence time (above 500 m) at Dome C, Cerro Tololo and Cerro Pachón taken from the MASS data files.

Site	Median		Average	
	θ_0 (arcsec)	τ_0 (ms)	θ_0 (arcsec)	τ_0 (ms)
Dome C	5.4	7.1	5.8	8.9
Cerro Tololo	1.8	2.0	1.9	2.8
Cerro Pachón	2.0	2.6	2.1	3.3

6-6 Seeing, isoplanatic angle and coherence time

After applying the filters (Section 6-4.4) on the Dome C MASS data, an average seeing above 500 m of $\epsilon_{500} = 0.32 \pm 0.16''$ was derived; the median seeing is $0.28''$. Histograms of the seeing, isoplanatic angle and atmospheric time constant are shown in Figure 6.14. The average isoplanatic angle and atmospheric time constant (above 500 m) are $5.8 \pm 2.6''$ and 8.8 ± 7.7 ms, respectively. Table 6.2 compares these atmospheric parameters at Dome C with those at the Chilean sites.

Combining the MASS and SODAR data gave an average and median seeing above 30 m of $\epsilon_{30} = 0.30 \pm 12''$ and $0.28''$, respectively. The seeing above 30 m (ϵ_{30}) was measured to be less than the seeing above 500 m (ϵ_{500}) because ϵ_{30} covers a smaller time period; the SODAR and MASS were only operated simultaneously between 23 March and 4 May, whereas the MASS measurements were taken up until the 16 May. Some of the strongest upper atmosphere turbulence was recorded in this excluded period (5–16 May). Balloon microthermal measurements in winter 2005 (Agabi et al. 2006) confirmed these results showing a median seeing of $0.36'' \pm 0.19''$ at a height of 30 m. They also showed the existence of an intense turbulent boundary layer, finding a median seeing of $1.9''$ from ground level, with 87% of the total atmospheric turbulence confined to the first 36 m of atmosphere. The seeing, isoplanatic angle and coherence time at Dome C are compared to other sites around the world in Table 6.3.

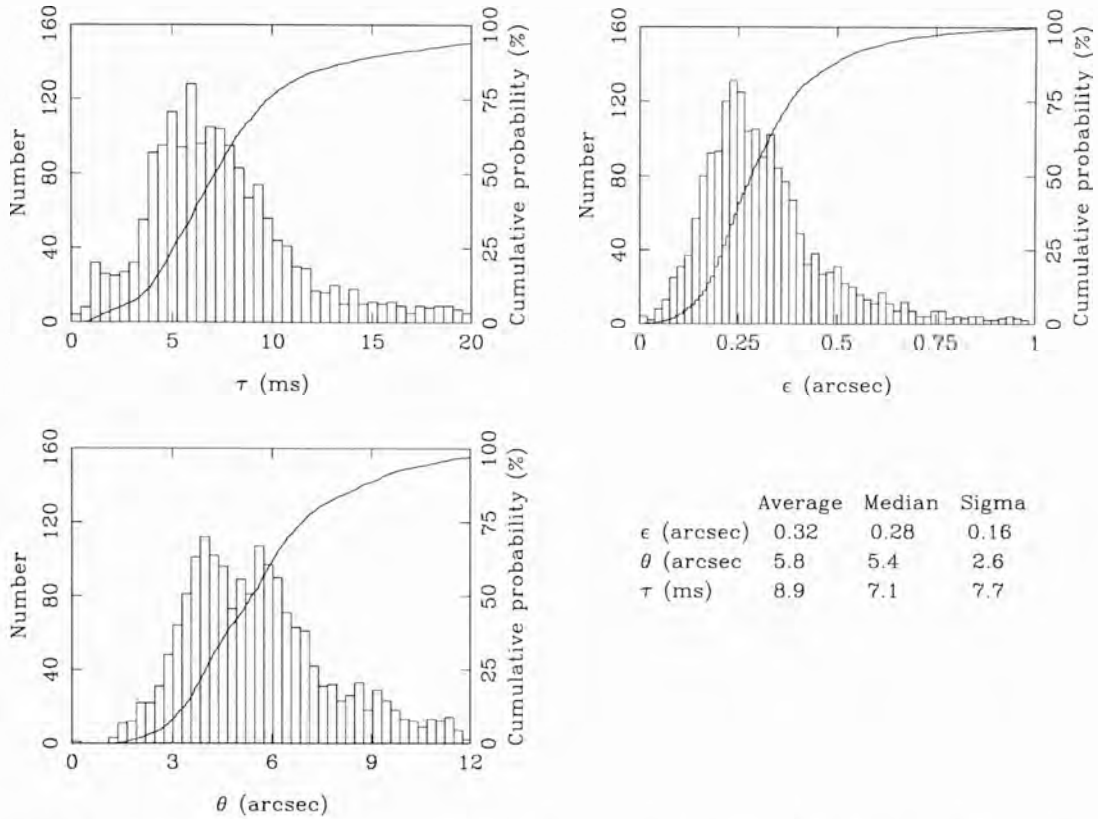


Figure 6.14. Histograms of the atmospheric time constant (*top left*), seeing (*top right*) and isoplanatic angle (*bottom left*) from the MASS measurements at Dome C. Also shown (*bottom right*) is the average, median and standard deviation of each parameter.

Table 6.3. Comparison of seeing, isoplanatic angle and coherence time at various sites. The values for Dome C show ϵ_0 above 30 m and the θ_0 and τ_0 above 500 m. Values for the other sites are from Lawrence et al. (2004, and references therein).

Site	Site Elev. (m)	ϵ_0 (arcsec)	θ_0 (arcsec)	τ_0 (ms)
Dome C, Antarctica	3260	0.30	5.0	8.8
Mauna Kea, USA	4208	0.5–0.7	1.9	2.7
San Pedro Mártir, Mexico	2830	0.71	1.6	6.5
La Palma, Canary Islands	2327	0.76	1.3	6.6
Cerro Paranal, Chile	2635	0.80	2.6	3.3
South Pole, Antarctica	2835	1.8	3.2	1.6

6-7 Discussion

Atmospheric turbulence distorts the light from astronomical objects. We are in a new era of extremely large telescope design, and the search is on to find sites on the Earth with the weakest atmospheric turbulence. Antarctica offers unique atmospheric conditions, with a very thin boundary layer and almost non-existent upper atmosphere turbulence compared to temperate sites. Dome C offers an improvement in seeing of 1.6–4 compared to current astronomical sites and the isoplanatic angle and coherence time are far larger than any other current astronomical site in the world.

We note that the data presented here cover only very limited time periods. The MASS data cover 26 days from 23 March to 16 May, 2004, and the results reported by Agabi et al. (2006) used only 16 balloon launches between 1 March and 23 August. Some additional data have been taken at Dome C using balloons and a Single Star Scidar (Vernin et al. 2006), but have not yet been published. Further measurements, extending over several years, are needed to fully characterise the site.

“Twinkle, twinkle, little star,
How I wonder what you are!
Up above the world so high,
Like a diamond in the sky.”

Jane Taylor (1783–1824)

The Star (1806)

Chapter 7

Atmospheric scintillation

In the previous chapter, the atmospheric turbulence at Dome C was evaluated in terms of the effects of phase fluctuations on image quality. Turbulence also introduces intensity fluctuations in the star light. This effect can be seen with the naked eye as the twinkling, or scintillation, of stars. Scintillation is an important factor in measurements requiring high-precision photometry (e.g., extrasolar planet detection) and astrometry, and of objects with very fast intensity changes (e.g., asteroseismology; Heasley et al. 1996; Fossat 2005). Dome C is a favourable site for high precision astrometry and photometry because the upper atmosphere turbulence, and hence the atmospheric scintillation, is very weak. Prior to the MASS measurements the winter time scintillation at Dome C had only been estimated from atmospheric models (e.g., Swain et al. 2003).

In Section 7-1, the theory of atmospheric scintillation is outlined and the scintillation index is introduced. In Sections 7-2 and 7-3, the scintillation noise contribution to photometry and the atmospheric noise contribution to narrow-angle astrometry are introduced. The photometric and astrometric noise at Dome C, Cerro Tololo and Cerro Pachón are calculated in Sections 7-6 and 7-5. Calculations of this type ideally require simultaneous turbulence and wind profiles; since the wind speed profile at each site was

not measured at the same time as the turbulence profiles, two alternative approaches were taken to estimate the wind speed profiles. Initially, fixed wind profiles were used for each site; these results have been published in Kenyon et al. 2006b (see Appendix C-2). As an extension, wind profiles were extracted from a global meteorological database and the results were reanalysed. In Section 7-7, the correlation between the turbulence and wind shear at each MASS altitude is examined.

7-1 Scintillation

As illustrated in Figure 7.1, light from a star, or other astronomical object, enters the Earth's atmosphere as a plane wave. Turbulent cells in the atmosphere introduce pure phase distortions in the wavefront. In the geometric optics approximation these phase perturbations act as positive or negative lenses as the wave propagates through the atmosphere, changing the wavefront curvature and producing amplitude modulations—sometime described as a “speckle pattern” on an image. The size of the most effective atmospheric “lenses” is governed by diffraction to be of the order of the Fresnel radius,

$$r_F \approx (\lambda h)^{1/2}, \quad (7.1)$$

where λ is the wavelength of light and h is the height of the dominant turbulence layer. For example, for $h = 10$ km and $\lambda = 500$ nm, $r_F = 7$ cm.

Scintillation describes the *intensity* modulation of light by the atmosphere. The scintillation index (σ_I^2) is used as a measure of the amount of intensity modulation caused by the atmosphere. It is defined (for small intensity fluctuations) as the variance of $\Delta I / \langle I \rangle$ where I is the intensity of light from a star. Dravins et al. (1997a,b, 1998) present detailed discussions of stellar scintillation, including statistical distributions, temporal properties, dependence on wavelength and effects for different telescope apertures.

In the weak-scintillation regime, $\sigma_I^2 \ll 1$, the effects of all turbulence layers are additive and the scintillation index is related to the refractive index structure constant ($C_N^2(h)$) by (Roddier 1981; Krause-Polstorff et al. 1993)

$$\sigma_I^2 = \int_0^\infty C_N^2(h) W(h) dh. \quad (7.2)$$

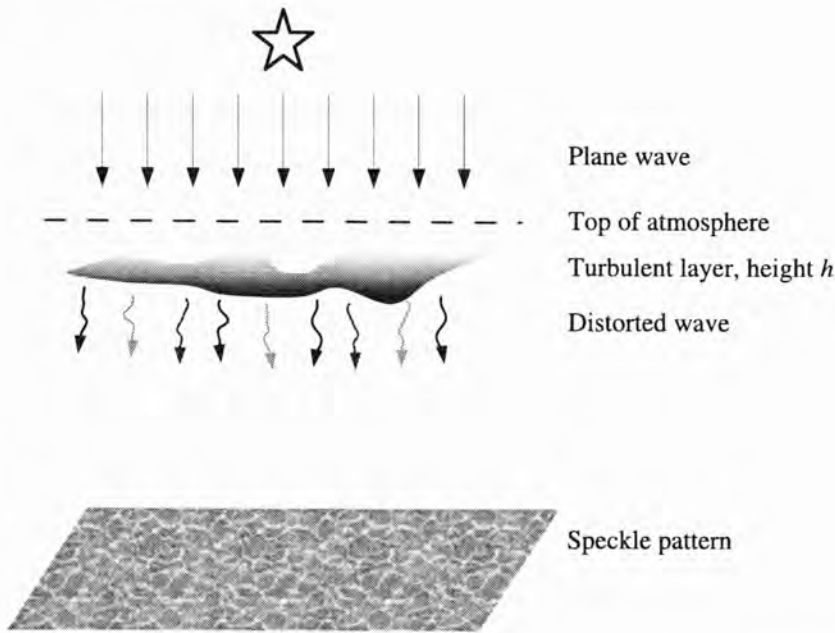


Figure 7.1. A schematic illustrating the formation of atmospheric scintillation. A plane wave from a star enters the atmosphere and passes through a turbulent layer, distorting the phase of the wavefront. These phase distortions propagate through the atmosphere and give rise to intensity distortions that result in a speckle pattern on the receiver.

where the weighting function $W(h)$ is given by

$$W(h) = 16\pi^2 0.033 \left(\frac{2\pi}{\lambda}\right)^2 \int_0^\infty |A(fD)|^2 f^{-8/3} \sin^2\left(\frac{\lambda h f^2}{4\pi}\right) df. \quad (7.3)$$

Here, h is the height above the observatory, λ is the wavelength, f is the spatial frequency, D is the diameter of the aperture, and $|A(fD)|^2$ is an aperture filter function. The weighing function given above is valid for monochromatic light and has to be modified for wide-band radiation. The aperture function for a circular aperture is defined as

$$A(fD) = \frac{2J_1(fD/2)}{fD/2} \quad (7.4)$$

where J_1 is the Bessel function of the first kind of the order of one.

The scintillation index calculation can be simplified by looking at particular cases of telescope size and integration times; three cases are shown below. The first two cases hold for short integration times and the last for long integration times.

7-1.1 Scintillation index for a very small aperture

This case holds when the diameter of the telescope is very much smaller than the Fresnel size (i.e., $D \ll r_F$); for this reason the aperture function A is set to unity. To simplify Equation 7.3, a new variable [$w = (\lambda h f^2)/(4\pi)$] is introduced such that

$$W(h) = 16\pi^2 0.033 h^{5/6} \left(\frac{2\pi}{\lambda}\right)^{7/6} 2^{-11/6} \int_0^\infty w^{-11/6} \sin^2 w dw \quad (7.5)$$

and

$$\sigma_I^2 = 12.5 \lambda^{-7/6} \int_0^\infty C_N^2(h) h^{5/6} dh \int_0^\infty w^{-11/6} \sin^2 w dw. \quad (7.6)$$

The last integral is solved numerically to give

$$\sigma_I^2 = 19.12 \lambda^{-7/6} \int_0^\infty C_N^2(h) h^{5/6} dh. \quad (7.7)$$

7-1.2 Scintillation index for a large aperture

For a large aperture telescope, $D \gg r_F$, the aperture cut-off is small enough that the approximation

$$\sin^2 \left(\frac{\lambda h f^2}{4\pi} \right) \approx \left(\frac{\lambda h f^2}{4\pi} \right)^2$$

can be used in Equation 7.3, such that

$$W(h) = 4\pi^2 0.033 h^2 \int_0^\infty |A(fD)|^2 f^{4/3} df. \quad (7.8)$$

Substituting in the expression for a circular aperture (Equation 7.4) and introducing a new variable ($a = fD/2$), gives

$$\begin{aligned} W(h) &= 16 \times 0.033 \pi^2 h^2 \left(\frac{2}{D}\right)^{7/3} \int_0^\infty [J_1(a)]^2 a^{-2/3} da \\ &\approx 17.3 h^2 D^{-7/3} \end{aligned} \quad (7.9)$$

with the integral over a solved numerically. Finally the scintillation index is

$$\sigma_I^2 = 17.3 D^{-7/3} \int_0^\infty C_N^2(h) h^2 dh. \quad (7.10)$$

Large apertures effectively average small-scale intensity fluctuations, so that only atmospheric lenses of the order of the aperture diameter contribute to the flux modulation. In this case, geometric optics applies and the scintillation becomes independent of both the wavelength and the spectral bandwidth.

7-1.3 Scintillation index for a long integration time and large aperture

The above two expressions for σ_I^2 are for very short exposure times. For exposure times that are longer than the time taken for a scintillation pattern to cross the telescope aperture (i.e., $t > (\pi D)/V_\perp$, where D is the telescope diameter and V_\perp is the speed of the turbulence layer normal to the plane of the telescope), the scintillation index can be calculated from (Dravins et al. 1998)

$$\sigma_I^2(t) = \int_0^\infty P(\nu) \text{sinc}^2(\pi\nu t) d\nu. \quad (7.11)$$

Here, ν (s^{-1}) is the temporal frequency and $P(\nu)$ is the temporal power spectrum. Following Tatarski (1961) and Yura & McKinley (1983), $P(\nu)$ is given by

$$P(\nu) \approx 8.27k^{2/3} \int_0^\infty \frac{C_N^2(h)h^{4/3}}{V_\perp(h)} Q(h) dh, \quad (7.12)$$

at zenith, where k is the wavenumber ($k = 2\pi/\lambda$) and the weighting function (Q) for a circular aperture is expressed as

$$Q(h) = \int_0^\infty \left[\frac{2J_1 \left(R(k/L)^{1/2} \sqrt{x^2 + \frac{\nu^2}{v_0^2(h)}} \right)}{R(k/L)^{1/2} \sqrt{x^2 + \frac{\nu^2}{v_0^2(h)}}} \right]^2 \left[x^2 + \frac{\nu^2}{v_0^2(h)} \right]^{-11/6} \sin^2 \left[x^2 + \frac{\nu^2}{v_0^2(h)} \right] dx. \quad (7.13)$$

Here, R is the radius of the telescope, $x = f(h/k)^{1/2}$ and $v_0 = V_\perp h^{1/2} (2\pi k)^{-1/2}$. For a long integration time Equation 7.11 can be simplified to (Dravins et al. 1998)

$$\sigma_I^2(t) = \frac{P(0)}{2t}. \quad (7.14)$$

Using this simplification and setting $\nu = 0$, Equation 7.13 is now

$$Q(h) = \int_0^\infty \left[\frac{2J_1 (R(k/h)^{1/2} x)}{R(k/h)^{1/2} x} \right]^2 x^{-11/3} \sin^2 [x^2] dx. \quad (7.15)$$

In the large aperture case, $D \gg r_F$, the sine in the equation above can be replaced by its argument giving

$$Q(h) = \int_0^\infty \left[\frac{2J_1 (R(k/h)^{1/2} x)}{R(k/h)^{1/2} x} \right]^2 x^{-11/3} x^4 dx \quad (7.16)$$

$$= \frac{4h}{R^2 k} \int_0^\infty x^{-5/3} \left[J_1 (R(k/h)^{1/2} x) \right]^2 dx. \quad (7.17)$$

Introducing a new variable, $y = R(k/L)^{1/2} x$, then gives

$$Q(h) = 4 \left(\frac{L}{R^2 k} \right)^{2/3} \int_0^\infty y^{-5/3} [J_1(y)]^2 dy. \quad (7.18)$$

By the solving the integration numerically we calculate,

$$Q(h) \approx 2.58 \left(\frac{h}{kD^2} \right)^{2/3} \quad (7.19)$$

in terms of the telescope diameter. Substituting this into Equation 7.12 gives,

$$P(0) \approx 21.3D^{-4/3} \int_0^\infty \frac{C_N^2(h)h^2}{V_\perp(h)} dh. \quad (7.20)$$

Finally the scintillation index is

$$\sigma_I^2 = 10.7t^{-1}D^{-4/3} \int_0^\infty \frac{C_N^2(h)h^2}{V_\perp(h)} dh. \quad (7.21)$$

7-2 Photometric noise

For a particular set of turbulence measurements the photometric noise caused by atmospheric scintillation can be expressed as

$$\sigma_I = \begin{cases} S_1 & D \ll r_F, t \ll (\pi D)/V_\perp \\ S_2 D^{-7/6} & D \gg r_F, t \ll (\pi D)/V_\perp \\ S_3 D^{-2/3} t^{-1/2} & D \gg r_F, t \gg (\pi D)/V_\perp \end{cases} \quad (7.22)$$

where

$$S_1 = \left[19.12\lambda^{-7/6} \int_0^\infty C_N^2(h)h^{5/6} dh \right]^{1/2} \quad (7.23)$$

$$S_2 = \left[17.3 \int_0^\infty C_N^2(h)h^2 dh \right]^{1/2} \quad (7.24)$$

$$S_3 = \left[10.7 \int_0^\infty \frac{C_N^2(h)h^2}{V_\perp(h)} dh \right]^{1/2} \quad (7.25)$$

The above expressions are for observations at the zenith; for other zenith angles (γ) replace h by $h/\cos \gamma$, i.e.,

$$S_1 = (\cos \gamma)^{-11/3} \left[19.12\lambda^{-7/6} \int_0^\infty C_N^2(h)\gamma h^{5/6} dh \right]^{1/2} \quad (7.26)$$

$$S_2 = (\cos \gamma)^{-3/2} \left[17.3 \int_0^\infty C_N^2(h)h^2 dh \right]^{1/2} \quad (7.27)$$

$$S_3 = (\cos \gamma)^{-3/2} \left[10.7 \int_0^\infty \frac{C_N^2(h)h^2}{V_\perp(h)} dh \right]^{1/2} \quad (7.28)$$

The photometric noise can be expressed in magnitudes using $\sigma_{I,\text{mag}} = 2.5 \log(\sigma_I + 1)$. In these three cases the photometric noise is dominated by the high-altitude turbulence, more so in the case of large apertures because of the h^2 weighting. It is the large-aperture case that is generally of more relevance to astronomical photometry.

7-3 Astrometric precision

Differential astrometric measurements require simultaneous observations of the target and reference object; this can be achieved using a single dish telescope or an interferometer. In the latter case, each telescope in the interferometer has a dual feed to direct the beam from each star to the beam combiner (Shao & Colavita 1992). On combination of the beams, a fringe pattern is produced if the difference between the optical path lengths from each arm of the interferometer to the beam combiner is within $\lambda^2/\Delta\lambda$, where $\Delta\lambda$ is the optical bandwidth of the interferometer (Lane & Muterspaugh 2004). The difference between the fringe positions of the two stars is measured. Phase referencing can be used to improve the limiting magnitude of the interferometer if the target star and reference object are within the isoplanatic patch (Shao & Colavita 1992).

Uncertainties in astrometric position measurements arise from instrumental effects (photon noise, systematics) and atmospheric effects associated with temporal incoherence and anisoplanatism. See Shao & Colavita (1992); Sozzetti (2005) and Lane & Muterspaugh (2004) for further details of instrumental effects; here we focus on the atmospheric effects.

The variance in an astrometric position measurement caused by anisoplanatism (assuming a Kolmogorov turbulence spectrum) is described by Shao & Colavita (1992) as

$$\sigma_{\text{atm}}^2 \approx 5.25t^{-1} \begin{cases} \theta^2 B^{-4/3} \int_0^\infty \frac{C_N^2(h)h^2}{V(h)} dh & \text{Case 1} \\ \theta^{2/3} \int_0^\infty \frac{C_N^2(h)h^{2/3}}{V(h)} dh & \text{Case 2,} \end{cases} \quad (7.29)$$

where t is the integration time, θ is the angular separation between two stars, $C_N^2(h)$ and $V(h)$ are the vertical turbulence and wind profiles, h is the height above the site, and B is the baseline or diameter of the entrance pupil. These formulae are only approximate, but the exact coefficient is not needed for the purpose of site inter-comparison. Case 1 applies to interferometry when the integration time $t \gg B/\bar{V}$ and $\theta\bar{h} \ll B$; where \bar{h} and

\bar{V} are the turbulence-weighted effective atmospheric height and wind speed. Because of the h^2 weighting, σ_{atm} in this regime is very sensitive to high-altitude turbulence. Case 2 is applicable to single dish astrometry and is independent of the size of the telescope when $\theta\bar{h} \gg B$ and $t \gg \theta\bar{h}/\bar{V}$.

For a particular set of turbulence and wind profiles, the error σ_{atm} (arcseconds) can be expressed as

$$\sigma_{\text{atm}} = \begin{cases} C_1 t^{-1/2} \theta B^{-2/3} & \text{Case 1} \\ C_2 t^{-1/2} \theta^{1/3} & \text{Case 2,} \end{cases} \quad (7.30)$$

where

$$C_1 = 472\,000 \left[\int_0^\infty \frac{C_N^2(h) h^2}{V(h)} dh \right]^{1/2} \quad (7.31)$$

and

$$C_2 = 472\,000 \left[\int_0^\infty \frac{C_N^2(h) h^{2/3}}{V(h)} dh \right]^{1/2}. \quad (7.32)$$

Note that the expression for C_1 contains the same combination of atmospheric parameters as the expression for the photometric error S_3 . This is not a coincidence, as both narrow-angle astrometry and large-aperture photometry are affected by the same physical phenomenon—large-scale curvature fluctuations of wavefronts. Hence, scintillation in large apertures contains information on the potential accuracy of narrow-angle astrometry at a given site.

Using long baseline techniques, Lane & Muterspaugh (2004) have achieved an astrometric measurement precision of $\approx 9 \mu\text{arcsec}$ for a 70 minute integration using a 110 m baseline on a $0.25''$ binary system.

7-4 Wind profiles

The photometric error for long integration times (Equation 7.25) and the astrometric errors (Equations 7.31 and 7.32) depend not only on the turbulence profile but also on the wind speed profile. As these quantities are likely correlated, the correct way to estimate the errors requires simultaneous data on wind and turbulence. Two approaches were taken to estimate the wind speed profiles. Initially, a simplified approach was adopted using fixed wind profiles (Section 7-5). As an extension, wind profiles were retrieved

from the NCEP/NCAR¹ Reanalysis Project (Kalnay et al. 1996) global meteorological database, and the data were reanalysed (Section 7-6).

Owing to the strong h^2 weighting, the astrometric and photometric errors are almost entirely determined by the highest MASS layer at 16 km. Hence, the adopted wind speed in this layer critically influences the results.

7-5 Results using fixed wind profiles

The wind speed profiles for Cerro Pachón and Cerro Tololo were modelled using a constant ground layer speed, V_g , plus a Gaussian function to represent the jet stream contribution (Greenwood 1977)

$$V(h) = V_g + V_t \exp \left[- \left(\frac{h - H}{T} \right)^2 \right], \quad (7.33)$$

where h is the altitude above the observatory. The parameters were set to $V_g = 8 \text{ m s}^{-1}$, $V_t = 30 \text{ m s}^{-1}$, $H = 8 \text{ km}$ and $T = 4 \text{ km}$ by comparing the model to the Cerro Pachón wind profiles in Avila et al. (2000, 2001).

The summer wind speed profile at Dome C also shows a Gaussian peak at the somewhat lower tropopause layer ($\sim 5 \text{ km}$), and fairly constant wind speed at other elevations (see Figure 4 of Aristidi et al. 2005c). The winter wind speed profile is different, showing an increase in stratospheric wind speeds and no peak at the tropopause. So far only three profiles of the winter wind speed have been published (Agabi et al. 2006). Figure 7.2 shows the average winter (Agabi et al. 2006) and summer (Aristidi et al. 2005c) time wind profiles at Dome C, the winter-time wind profile was used in this work.

¹This is a joint project between the National Centres for Environmental Prediction (NCEP) and the National Center of Atmospheric Research (NCAR).

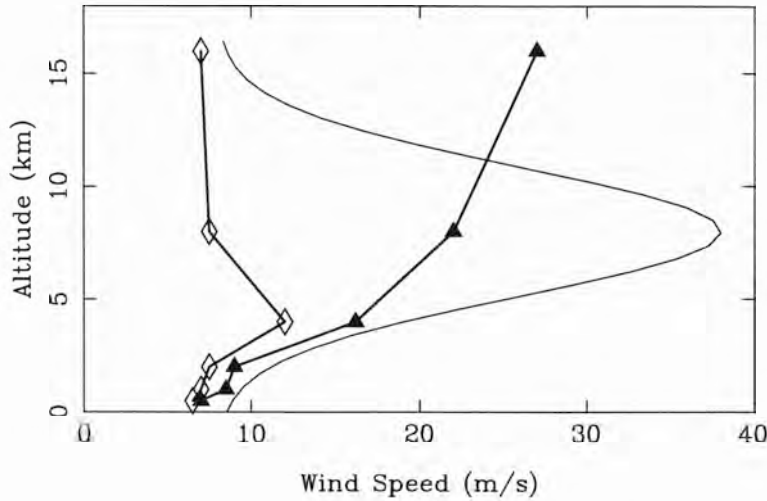


Figure 7.2. Average wind speeds profiles at Dome C in the winter (*triangles*; Agabi et al. 2006) and summer (*diamonds*; Aristidi et al. 2005c), and a model of the wind profile at Cerro Tololo and Cerro Pachón (*line*).

7-5.1 Photometry

The scintillation noise was calculated for the three regimes discussed in Section 7-2, using the turbulence profiles from the three sites. Figure 7.3 shows the cumulative probabilities for S_1 , S_2 and S_3 . The scintillation noise is calculated at wavelength 500 nm using profiles from 500 m above the surface.

For short time scales, the median scintillation noise at Dome C is a factor of ~ 2 less than at Cerro Tololo and Cerro Pachón, in the small aperture regime. For larger apertures the gain is slightly higher, ~ 2.4 , because of the weaker high altitude turbulence at Dome C. As an example, for a 4 m diameter telescope, the median values of the scintillation noise at each site are: 1.2 mmag (Dome C), 3.2 mmag (Cerro Tololo) and 2.8 mmag (Cerro Pachón).

The more relevant figure is the scintillation noise for long exposure times. Based on the results using fixed wind profiles, Dome C offers a potential gain of about 3.6 in photometric precision compared to Cerro Tololo and Cerro Pachón. From these results the median photometric error expected on a 4 m telescope for a 60 s integration is: $\sim 53 \mu\text{mag}$ at Dome C; $\sim 200 \mu\text{mag}$ at Cerro Tololo, and $\sim 180 \mu\text{mag}$ at Cerro Pachón. For a 300 s integration on a 2 m telescope Chadid et al. (2005) estimate the scintillation noise at Dome C to be 12–20 ppm (i.e., 13–22 μmag).

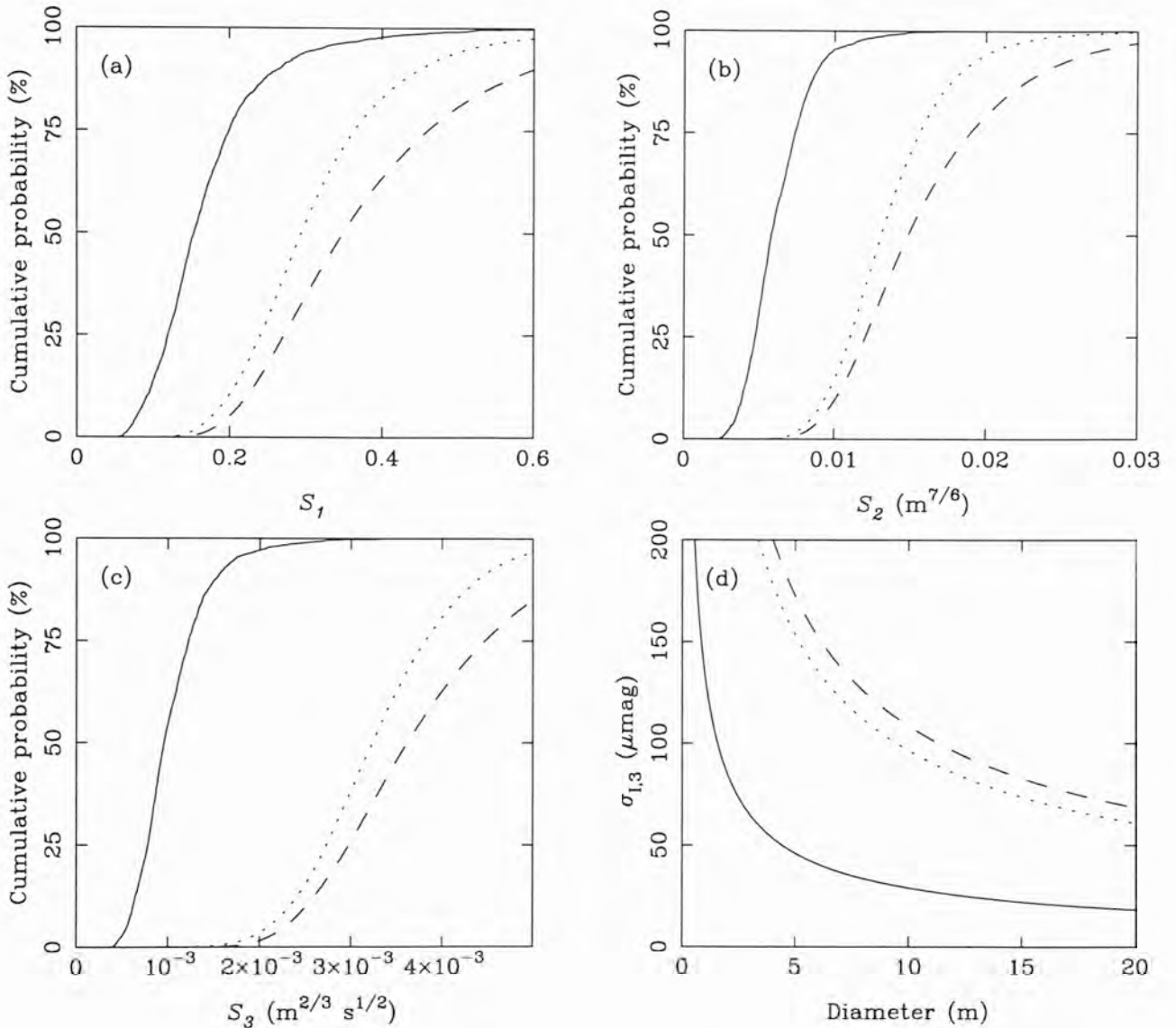


Figure 7.3. Cumulative probabilities of the constants (a) S_1 , (b) S_2 ($\text{m}^{7/6}$) and (c) S_3 ($\text{m}^{2/3}\text{s}^{1/2}$) for Dome C (*solid*), Cerro Tololo (*dashed*) and Cerro Pachón (*dotted*). The scintillation noise σ_I is the standard deviation of $\Delta I/I$ where I is the stellar flux, and is equal to: S_1 for $D \ll r_F$; $S_2 D^{-7/6}$ for $D \gg r_F$, and $S_3 D^{-2/3} t^{-1/2}$ for $D \gg r_F$ and $t \gg (\pi D)/V_\perp$, where D is the telescope diameter, r_F is radius of the Fresnel zone and t is the integration time. Plot (d) shows the median photometric error at each site for a 60 s integration time as a function of telescope diameter.

As a comparison, Dravins et al. (1998) measured $P(\nu)$ at La Palma using various small apertures. From their results they extrapolate $P(0) = 5 \times 10^{-6}$ s for a 4 m aperture at zenith, which gives $\sigma_I = 220 \mu\text{mag}$ for a 60 s integration, similar to the typical values for Cerro Tololo and Cerro Pachón. Our results are also consistent with those measured at Kitt Peak and Mauna Kea by Gilliland et al. (1993). Figure 7.3d shows the median photometric error at each site for a 60 s exposure time as function of telescope diameter, illustrating the benefits of even a small telescope at the Antarctic site.

7-5.2 Astrometry

The constants C_1 and C_2 (Equations 7.31 and 7.32) were calculated for each site; cumulative probabilities are shown in Figures 7.4a and 7.4b. The median astrometric error σ_{atm} at Dome C is ~ 3.5 times less than the median values at Cerro Tololo and Cerro Pachón. The median σ_{atm} for each site is plotted in Figure 7.4c as a function of angular separation for a 10 m baseline and 1 h integration time. In Figure 7.4d, σ_{atm} at Dome C is plotted for several baselines, as a function of separation angle θ for an integration time of 1 h. This last figure illustrates the extreme advantage in placing a long-baseline interferometer at Dome C, implying an achievable accuracy of a few microarcseconds.

The advantage of Dome C for narrow-angle astrometry over mid-latitude sites is even larger than its advantage in the fast scintillation. This difference is related to the adopted wind speed at 16 km altitude (27 m s^{-1} and 8.5 m s^{-1} for Dome C and the Chilean sites, respectively). Using the mean Dome C winter wind speed we calculated a median C_1 value of $140 \text{ arcsec rad}^{-1} \text{ m}^{2/3} \text{ s}^{1/2}$; decreasing the 16 km wind speed to 7 m s^{-1} gave a median C_1 value of $200 \text{ arcsec rad}^{-1} \text{ m}^{2/3} \text{ s}^{1/2}$, still well below the median values at Cerro Tololo and Cerro Pachón. As an additional check (conducted by A. Tokovinin), C_1 was computed from a set of six balloon profiles of C_N^2 and wind speed measured at Cerro Pachón in October 1998 (see Avila et al. 2000 and Avila et al. 2001 for the discussion of these data). The C_1 values range from 380 to $660 \text{ arcsec rad}^{-1} \text{ m}^2 \text{ s}^{1/2}$, with a median of 480. This is close to the median value for Cerro Pachón given in Figure 4. Shao & Colavita (1992) calculate C_1 at Mauna Kea to be $300 \text{ arcsec rad}^{-1} \text{ m}^2 \text{ s}^{1/2}$, using the results from two short observing campaigns.

The fringe phase of an interferometric measurement must be determined within the at-

Table 7.1. Isoplanatic angle (ϵ_0) and coherence time (τ_0) for adaptive optics at Dome C, Cerro Tololo and Cerro Pachón from the MASS data files.

Site	θ_0 (median) (arcsec)	θ_0 (average) (arcsec)	τ_0 (median) (ms)	τ_0 (average) (ms)
Dome C	5.4	5.8	7.1	8.9
Cerro Tololo	1.8	1.9	2.0	2.8
Cerro Pachón	2.0	2.1	2.6	3.3

mospheric coherence time. Table 7.1 shows the median coherence time τ_0 and isoplanatic angle θ_0 at each site at 500 nm. The median coherence time at Dome C, measured with MASS, is 7.1 ms at $\lambda = 500$ nm. Using the measured turbulence profiles and assumed wind profile at Dome C we calculated $\tau_0 = 9.4$ ms at $\lambda = 500$ nm.

Phase referencing during the measurement (Shao & Colavita 1992) increases the usable integration time, with the condition that the target and reference objects are within the same isoplanatic patch. The median isoplanatic angle at Dome C is ~ 3 times larger than at the two Chilean site, allowing much wider fields to be used for phase referencing.

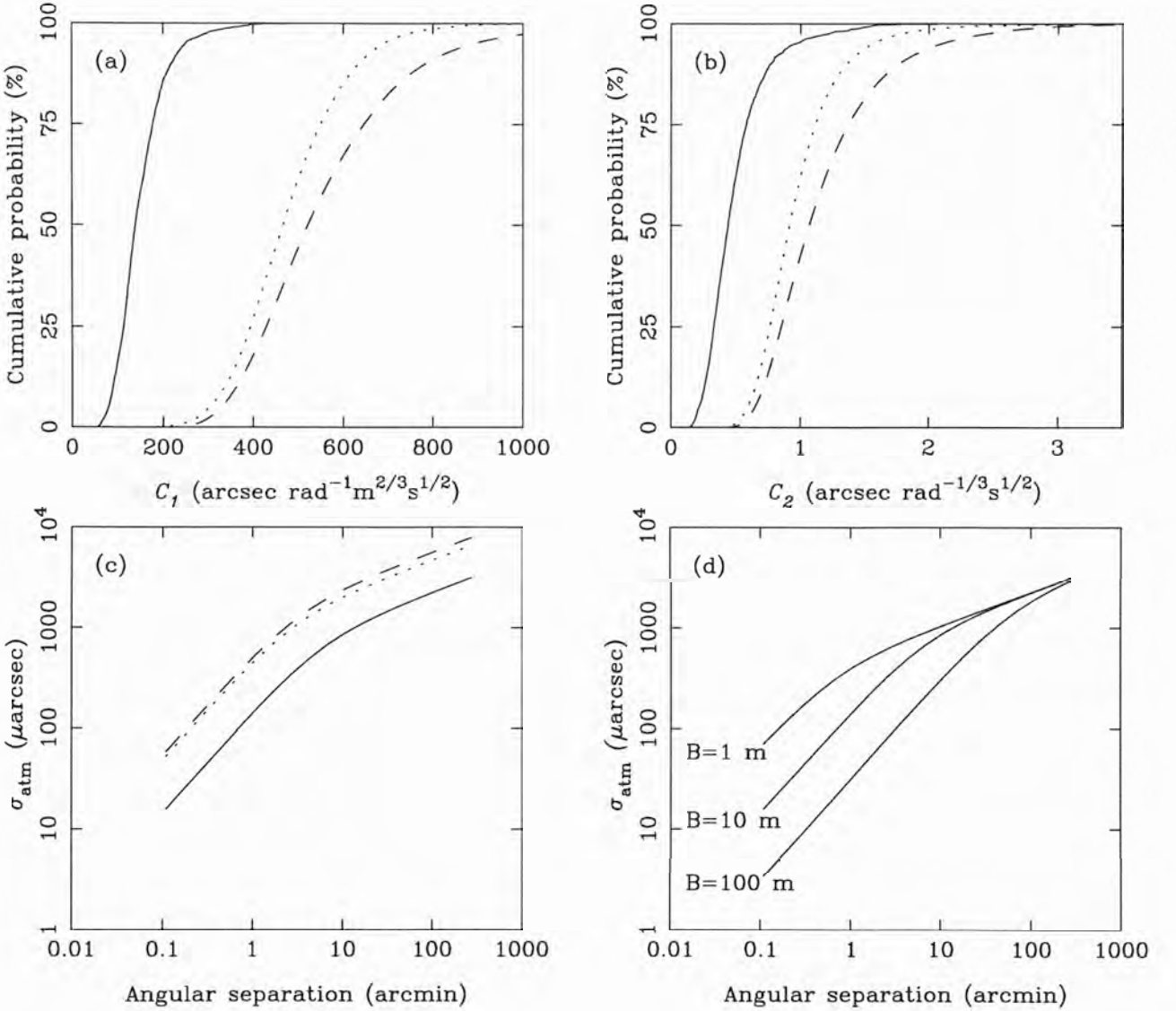


Figure 7.4. Plots (a) and (b) show the cumulative probabilities that the constants C_1 and C_2 are less than the value given, for Dome C (*solid*), Cerro Tololo (*dashed*) and Cerro Pachón (*dotted*). The astrometric error σ_{atm} (arcsecond) is equal to: $C_1 t^{-1/2} \theta B^{-2/3}$ for $t \gg B/\bar{V}$ and $\theta \bar{h} \ll B$, and $C_2 t^{-1/2} \theta^{1/3}$ for $t \gg \theta \bar{h}/\bar{V}$ and $\theta \bar{h} \gg B$. Here, t is the integration time, B is the baseline length, \bar{h} and \bar{V} are the turbulence-weighted effective atmospheric height and wind speed, and θ is the stellar separation. Plot (c): The median error σ_{atm} at each site as a function of angular separation with an integration time of 1 h and baseline of 10 m. Plot (d): the median error σ_{atm} for three baseline lengths at Dome C, with an integration time of 1 h.

7-6 Results using dynamic wind profiles

As an extension on the initial analysis that used fixed wind speed profiles, wind data were taken from the NCEP/NCAR Reanalysis website² for Dome C and Cerro Tololo in the time periods shown in Table 6.1 (on page 104 in the previous chapter). The reanalysis project (Kalnay et al. 1996) uses historical data to model various parameters in the atmosphere from 1948 to the present. The use of re-analysis databases for site evaluation is becoming more common: for example, Geissler & Masciadri (2006) use data from the European Center for Medium-Range Weather Forecasts (ECWMF) re-analysis database to characterise the meteorological conditions above Dome C in terms of the wind speed and direction, pressure, and absolute and potential temperature.

Data on the u -wind (zonal) and v -wind (meridional) speeds as a function of 17 pressure levels were extracted from the database at the grid points (30° S, 70° W) for Cerro Tololo and ($72^\circ.5$ S, 123° E) for Dome C. The u -wind is the wind component parallel to the direction of the local latitude, positive values indicate the wind is blowing from the west. The v -wind is the component along the local meridian and is positive for southerlies. The u -wind and v -wind data were combined to give the magnitude and direction of the wind at each pressure level. The pressure levels were converted to geopotential height using a separate file. The time is given in 6 hour intervals as the number of hours since 1 January 0001 00:00:0.0. This was converted to universal time for matching with the MASS data.

Figure 7.5 shows the wind speed and direction as a function of altitude, extracted from the database for Dome C (23 March–20 May 2004). For the first half of the time period the wind speed was fairly constant over the entire altitude range. Following this, the wind speed started to increase in the higher altitude ranges, as expected during the Antarctic winter. The wind direction is fairly consistently from the North ($0^\circ/360^\circ$) with occasional bursts from the South.

For each MASS measurement the nearest wind measurement in time was matched, then for each MASS altitude the wind speed and direction were extracted in two ways (Figure 7.6 illustrates these two methods):

²The NCEP/NCAR Reanalysis Project at the NOAA/ESRL Physical Sciences Division website <http://www.cdc.noaa.gov/cdc/reanalysis/reanalysis.shtml>

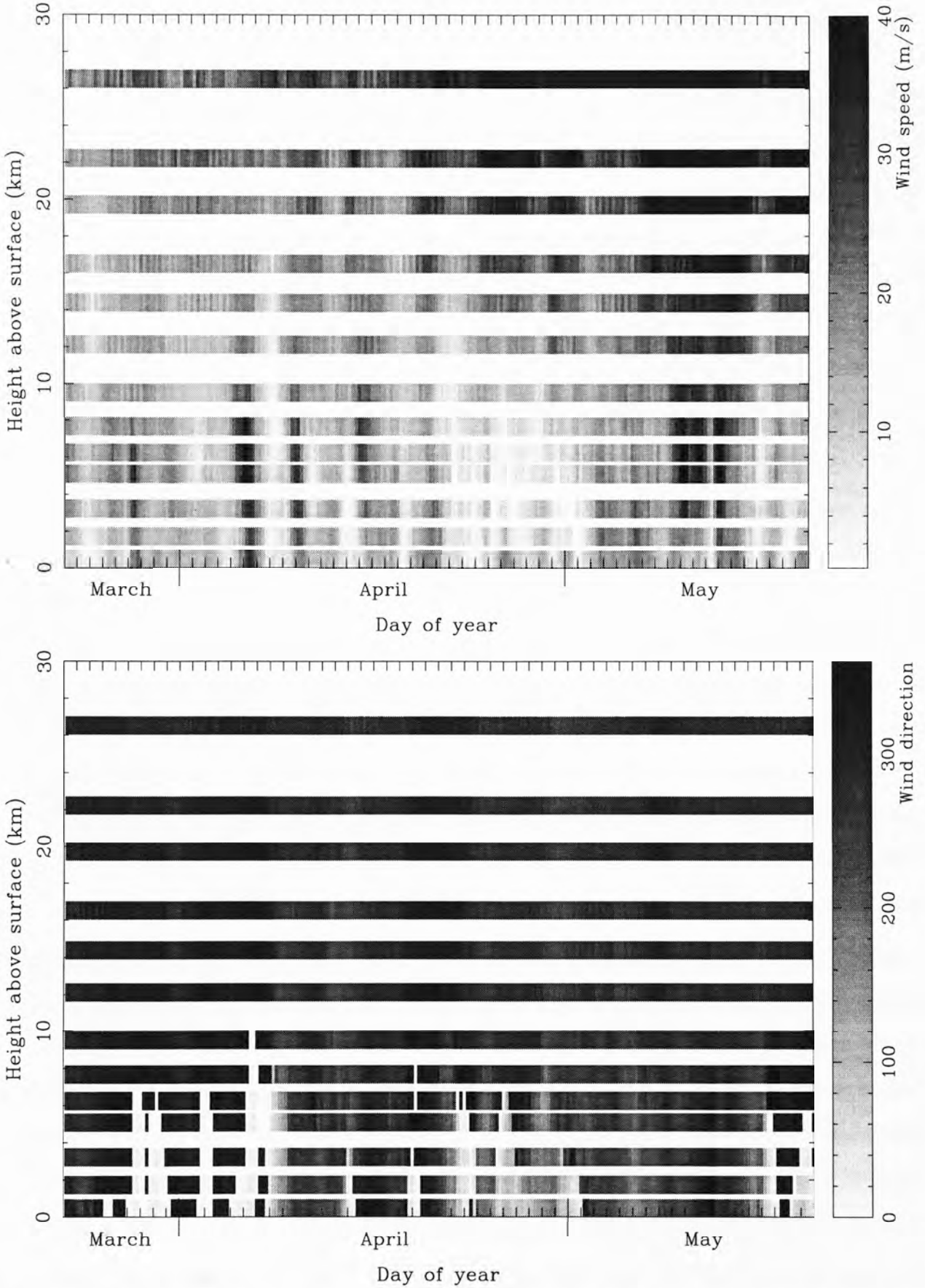


Figure 7.5. Wind speed (*top*) and direction (*bottom*) as a function of height above for Dome C from 23 March to 20 May 2004. Data from the NCEP/NCAR reanalysis project, see the text for details.

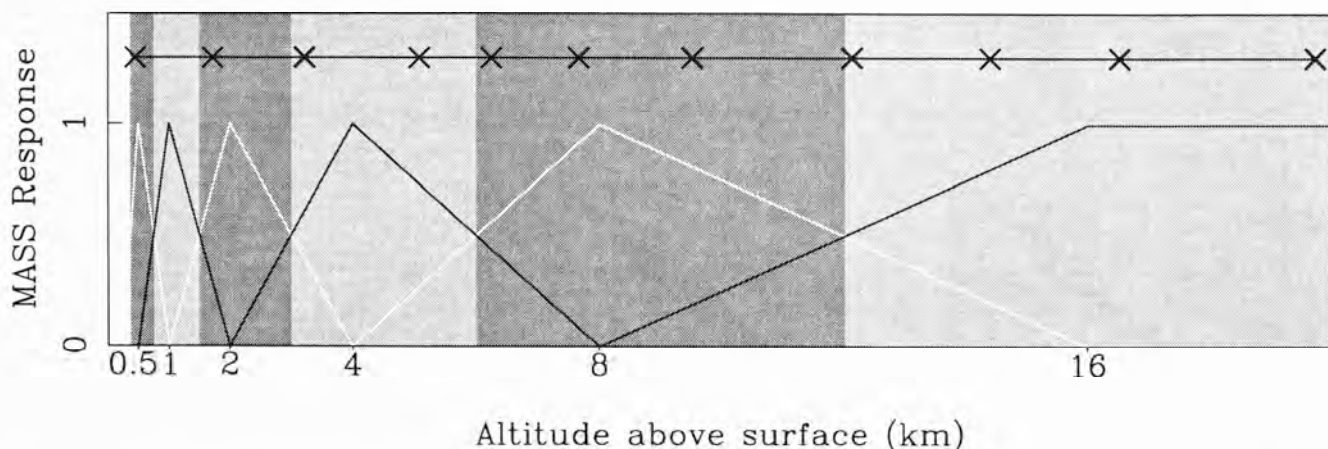
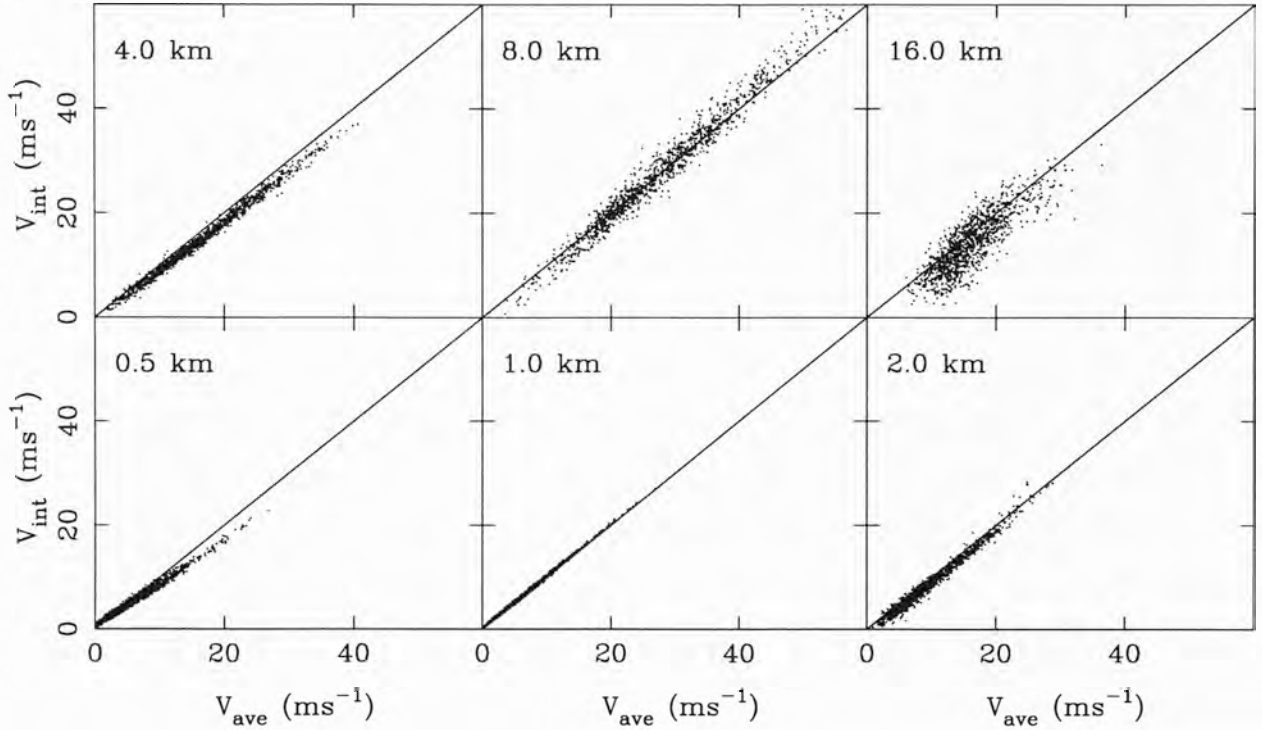


Figure 7.6. Schematic showing how the wind speeds were chosen for each MASS altitude. The triangular lines show the ideal MASS response function at each MASS altitude; the *crosses* show the altitudes of the wind speeds from the NCAR database. The wind speed at each MASS level was extracted by: (1) averaging the wind speeds at altitudes encompassed by the top-half of the MASS response function (*grey shading*) (V_{ave}); (2) interpolating between the two wind altitudes closest to the MASS altitude (V_{int}).

1. The wind speed and direction at the MASS altitude (e.g., 8 km) was *interpolated* ($V_{int}(h)$), from the two closest wind altitudes.
2. The wind speeds and directions from all altitudes encompassed by the top-half (0.5–1.0) of the MASS response function at a particular level were *averaged* ($V_{ave}(h)$). For example, for the 8 km MASS layer the wind speeds at altitudes between 6 km and 12 km were averaged.

The $V_{int}(h)$ and $V_{ave}(h)$ wind speeds derived from the database are compared in Figure 7.7; for some MASS levels V_{int} returns a smaller wind speed than V_{ave} .

(a) Cerro Tololo



(b) Dome C

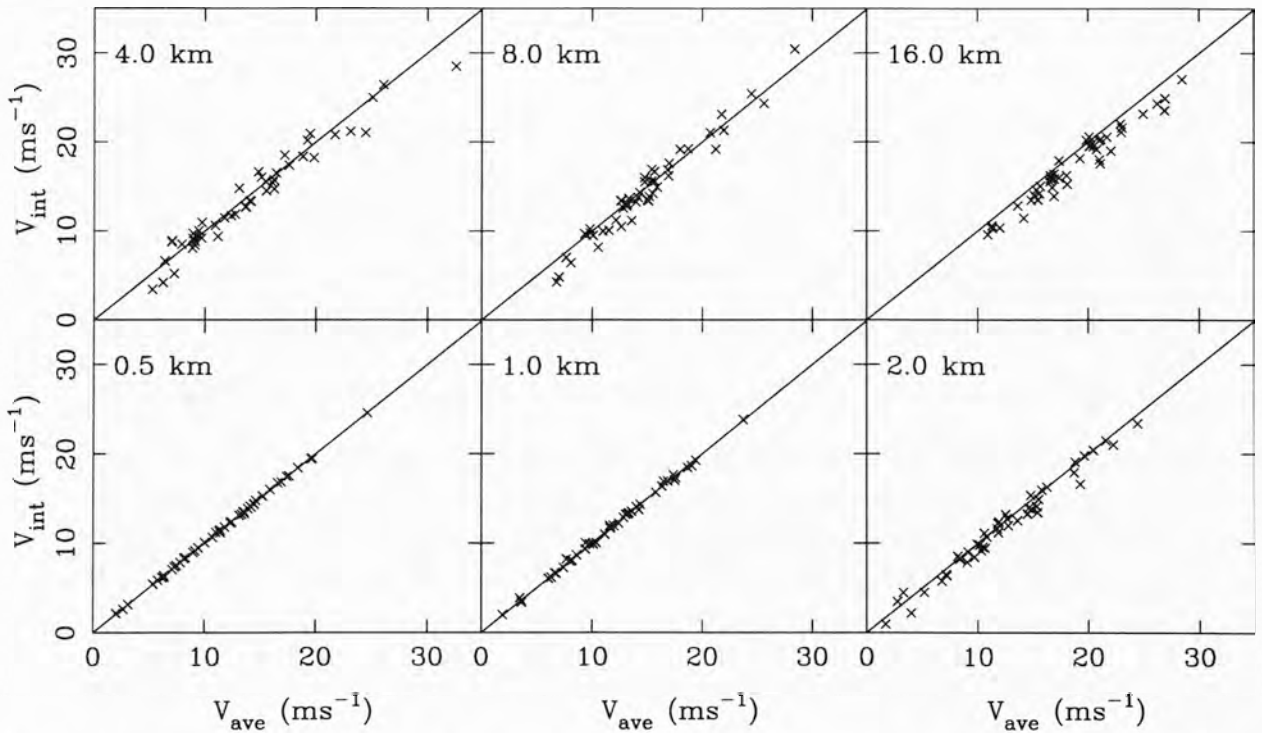


Figure 7.7. Comparison of the two wind speed extraction methods for each MASS layer at Cerro Tololo (a) and Dome C (b). The line in each plot shows the one-to-one relationship.

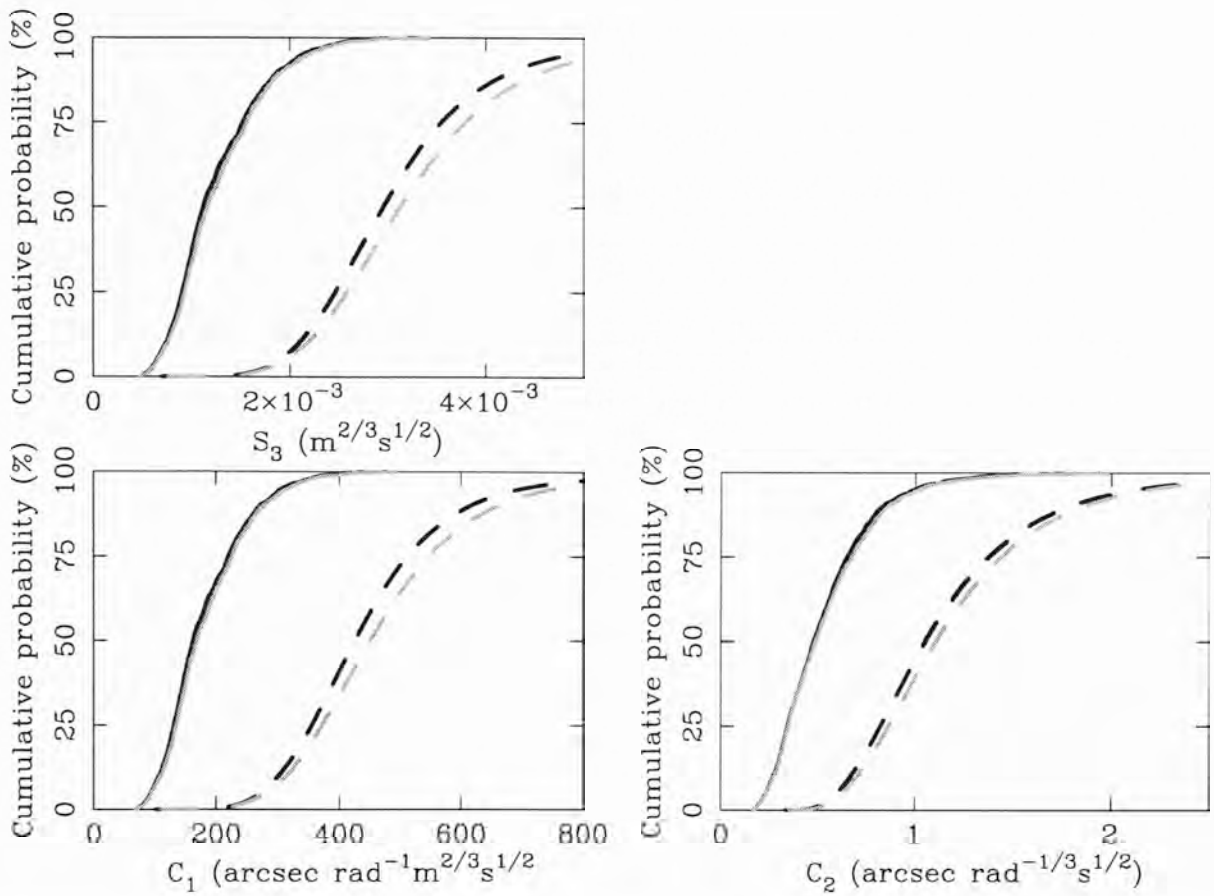


Figure 7.8. C_1 , C_2 and S_3 calculated using the MASS turbulence data and the NCEP/NCAR wind speeds for Dome C (*solid*) and Cerro Tololo (*dashed*). Calculations using the average wind speed are shown in *black* and those using the interpolated wind speeds are showing in *grey* (see the text for further details).

7-6.1 Photometry and astrometry reanalysed

The wind speed dependent photometric and astrometric uncertainties (i.e., C_1 , C_2 and S_3) at Dome C and Cerro Tololo were recalculated using the averaged and interpolated wind speeds from the NCEP/NCAR database. The results are shown in Figure 7.8. The two methods produced similar results at Dome C. However, for Cerro Tololo using the interpolated wind speeds resulted in slightly higher values.

Tables 7.2 and 7.3 show the average astrometric and photometric results using the three types of wind profile. At Dome C the average and interpolated results for C_1 were both larger than those using the fixed profile; the opposite case occurred for Cerro Tololo. The results for C_2 and S_3 were very close for all three methods.

Table 7.2. Average results for astrometric errors using three types of wind profiles: fixed wind profiles, and averaged and interpolated wind data from the NCEP database.

Site	Wind profile	C_1	C_2
		(as $\text{rad}^{-1}\text{m}^{-2/3}\text{s}^{1/2}$)	(as $\text{rad}^{-1/3}\text{s}^{1/2}$)
Dome C	Fixed	150 ± 60	0.50 ± 0.25
	Average	180 ± 67	0.53 ± 0.25
	Interpolated	185 ± 68	0.54 ± 0.26
Cerro Tololo	Fixed	560 ± 180	1.2 ± 0.5
	Average	450 ± 140	1.2 ± 0.5
	Interpolated	475 ± 150	1.2 ± 0.5
Cerro Pachón	Fixed	480 ± 120	0.98 ± 0.33

Table 7.3. Average results for photometric errors using three types of wind profiles: fixed wind profiles, and averaged and interpolated wind data from the NCEP database.

Site	Wind profile	S_1	S_2	S_3
			($\times 10^{-2}\text{m}^{7/6}$)	($\times 10^{-3}\text{m}^{2/3}\text{s}^{1/2}$)
Dome C	Fixed	0.17 ± 0.08	0.62 ± 0.21	1.0 ± 0.4
	Average	1.2 ± 0.5
	Interpolated	1.3 ± 0.5
Cerro Tololo	Fixed	0.38 ± 0.16	1.6 ± 0.6	3.9 ± 0.1
	Average	3.1 ± 1.0
	Interpolated	3.3 ± 1.0
Cerro Pachón	Fixed	0.31 ± 0.11	1.4 ± 0.4	3.3 ± 0.8

7-7 Correlation between wind shear and turbulence

Turbulence and wind shear are known to be related. This relationship is examined for Dome C using the wind speeds extracted from the NCEP/NCAR database. The sample size at Dome C is small and unlikely to show any statistically significant correlation so we also examine the larger sample from Cerro Tololo.

Wind shear is the change in wind speed over height, expressed as

$$W = \frac{\Delta V}{\Delta h} = \frac{V(h_2) - V(h_1)}{h_2 - h_1} \quad (7.34)$$

where $V(h_1)$ and $V(h_2)$ are the wind speeds at altitudes h_1 and h_2 . As Figure 7.6 shows, the NCEP/NCAR database supplies the wind speeds at certain altitudes. For each MASS layer the wind shear was calculated between each wind speed encompassed by the whole ideal MASS response function; for example, for 4 km MASS layer at Dome C the wind is recorded at 3.2, 5.1, 6.3 and 7.6 km, so three wind shears were calculated. For each MASS profile at Dome C the closest set of wind data was matched in time, and then the altitudes were matched as just outlined.

Figures 7.9 and 7.10 show the seeing contribution (derived from the Dome C MASS data) at each MASS level as a function of the wind shear (derived from the NCEP/NCAR database). The seeing contribution at each MASS layer was calculated using Equation 6.19. To examine correlations between the seeing contribution and the wind shear, the seeing corresponding to the wind shears within a series of bins were averaged. These averages are also shown on the figures. The formation of optical turbulence requires a vertical temperature gradient as well as wind shear. We have not taken temperature gradients into account in this study, therefore we expect to see a correlation but not a perfect one. Figures 7.11 and 7.12 show the average data for Cerro Tololo; individual points are not shown because they are too dense.

At Dome C there is a possible correlation between the turbulence and wind shear in the following MASS layers: 8.0 km layer [$V(5.1)$ and $V(6.2)$], 16.0 km [$V(19.7)$ and $V(22.2)$]. The bracketed values after each MASS height show the altitudes between which the wind shear was calculated. Strong correlations are seen for all MASS layers at Cerro Tololo, as expected for the larger sample.

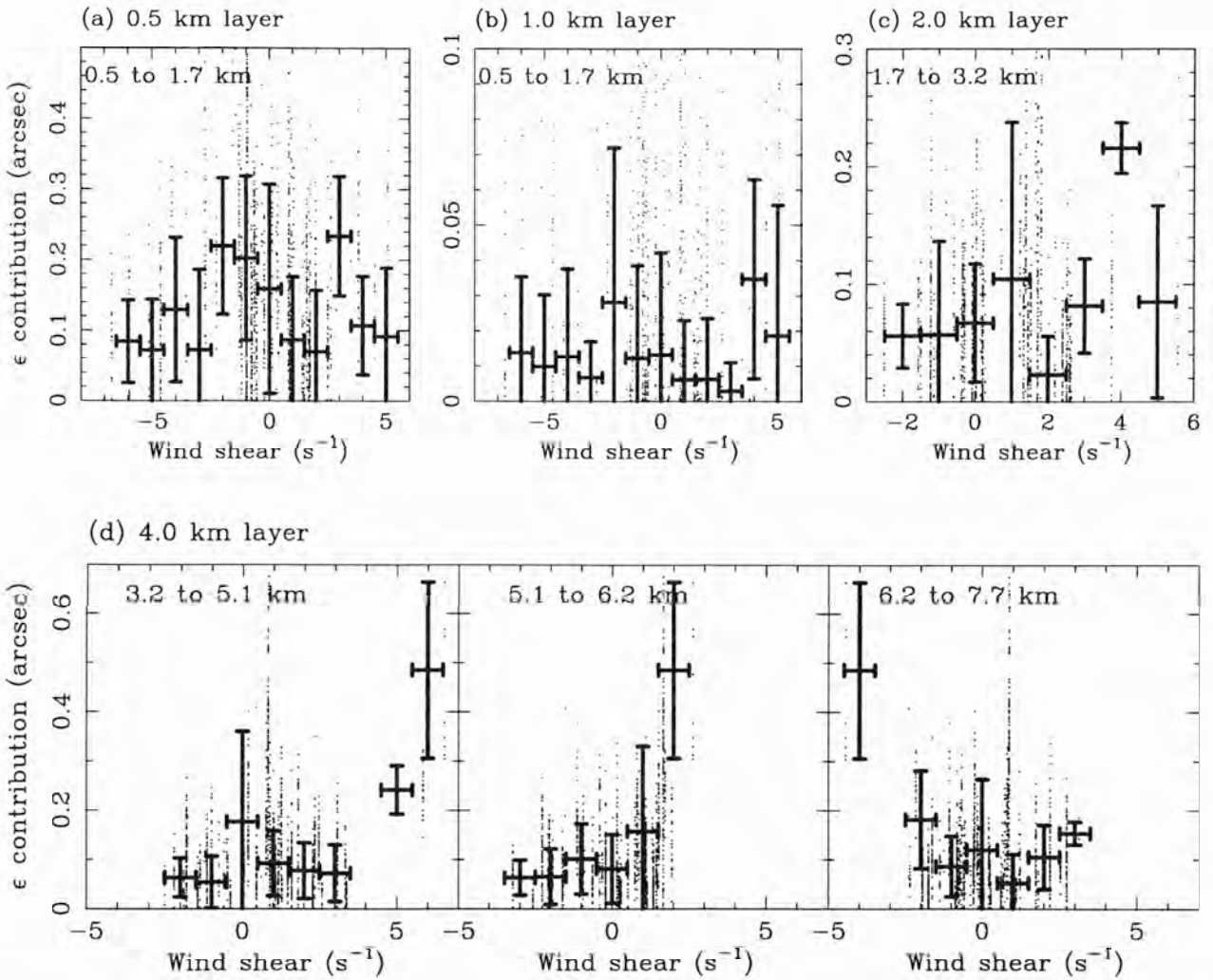


Figure 7.9. The seeing (ϵ) contribution (derived from the MASS data) in the (a) 0.5 km, (b) 1 km, (c) 2 km and (d) 4 km MASS layers at Dome C as a function of the wind shear (derived from the NCEP/NCAR database). For each MASS measurement the wind shear ($\Delta V/\Delta h$) was calculated using wind speeds extracted from the NCEP/NCAR database, matched closest in time and altitude range. The altitudes of the wind speeds used for each wind shear calculation are shown in each plot. The wind shears were divided into a series of bins and the seeing contribution corresponding to the wind shear points within each bin were averaged, these points are shown as crosses on the plots. The horizontal bars shown the width of each wind shear bin and the vertical bars shown the standard deviation on the average seeing contribution.

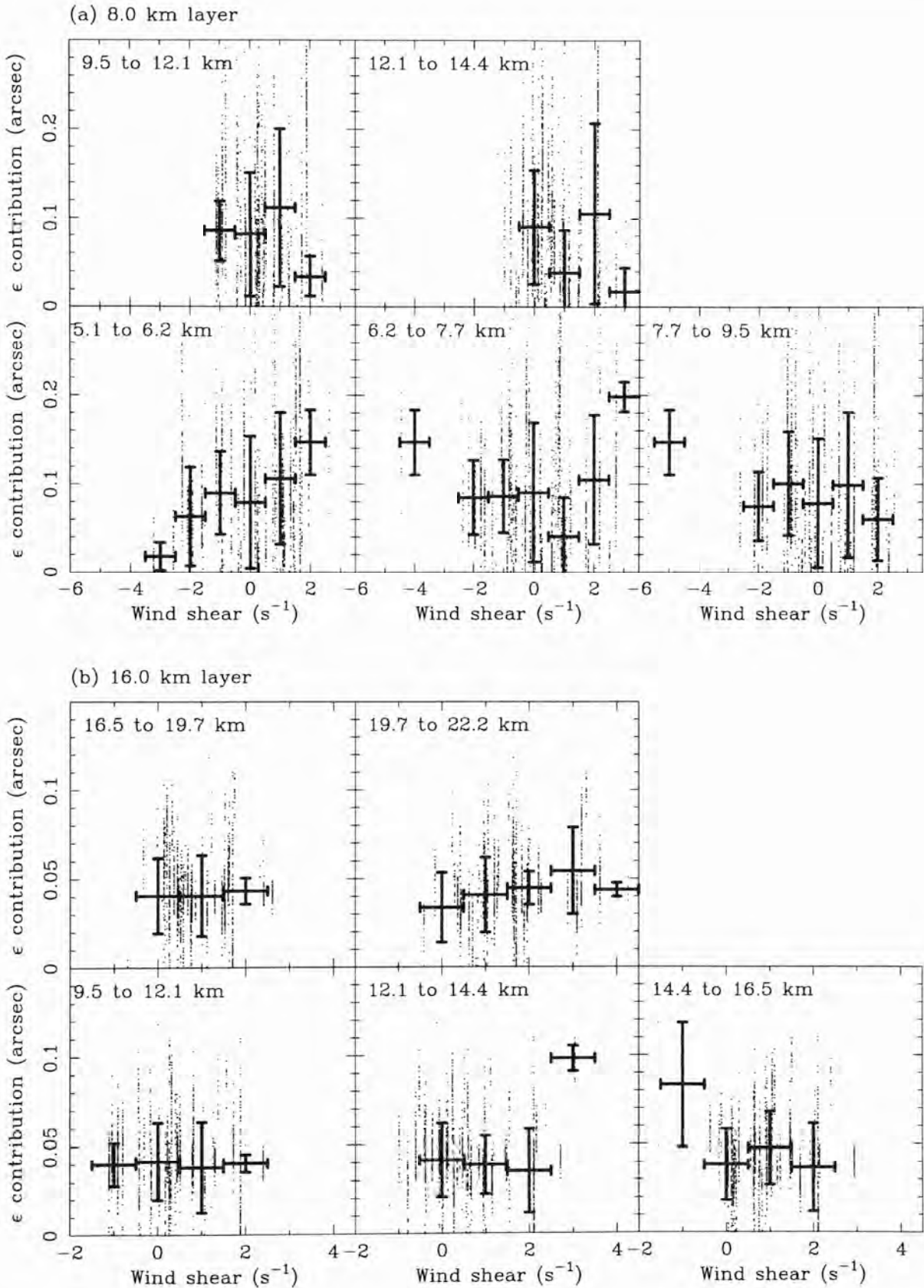


Figure 7.10. The seeing contribution (derived from the MASS data) in the (a) 8 km and (b) 16 km MASS layers at Dome C as a function of the wind shear (derived from the NCEP/NCAR database). See the caption of Figure 7.9 for further details.

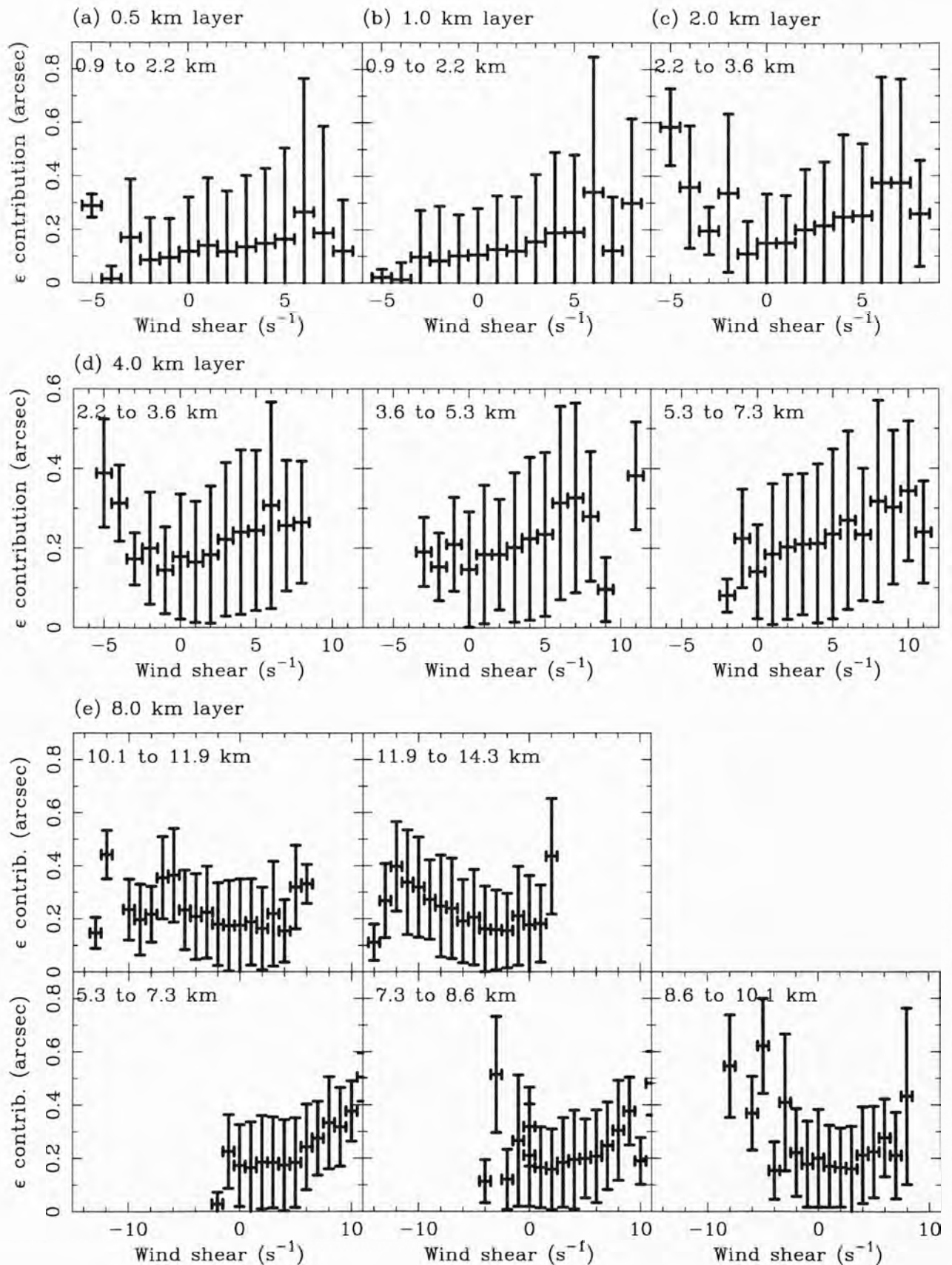


Figure 7.11. The seeing (ϵ) contribution (derived from the MASS data) in the (a) 0.5 km, (b) 1 km, (c) 2 km, (d) 4 km and (d) 8 km MASS layers at Cerro Tololo as a function of the wind shear (derived from the NCEP/NCAR database). See the caption of Figure 7.9 for further details.

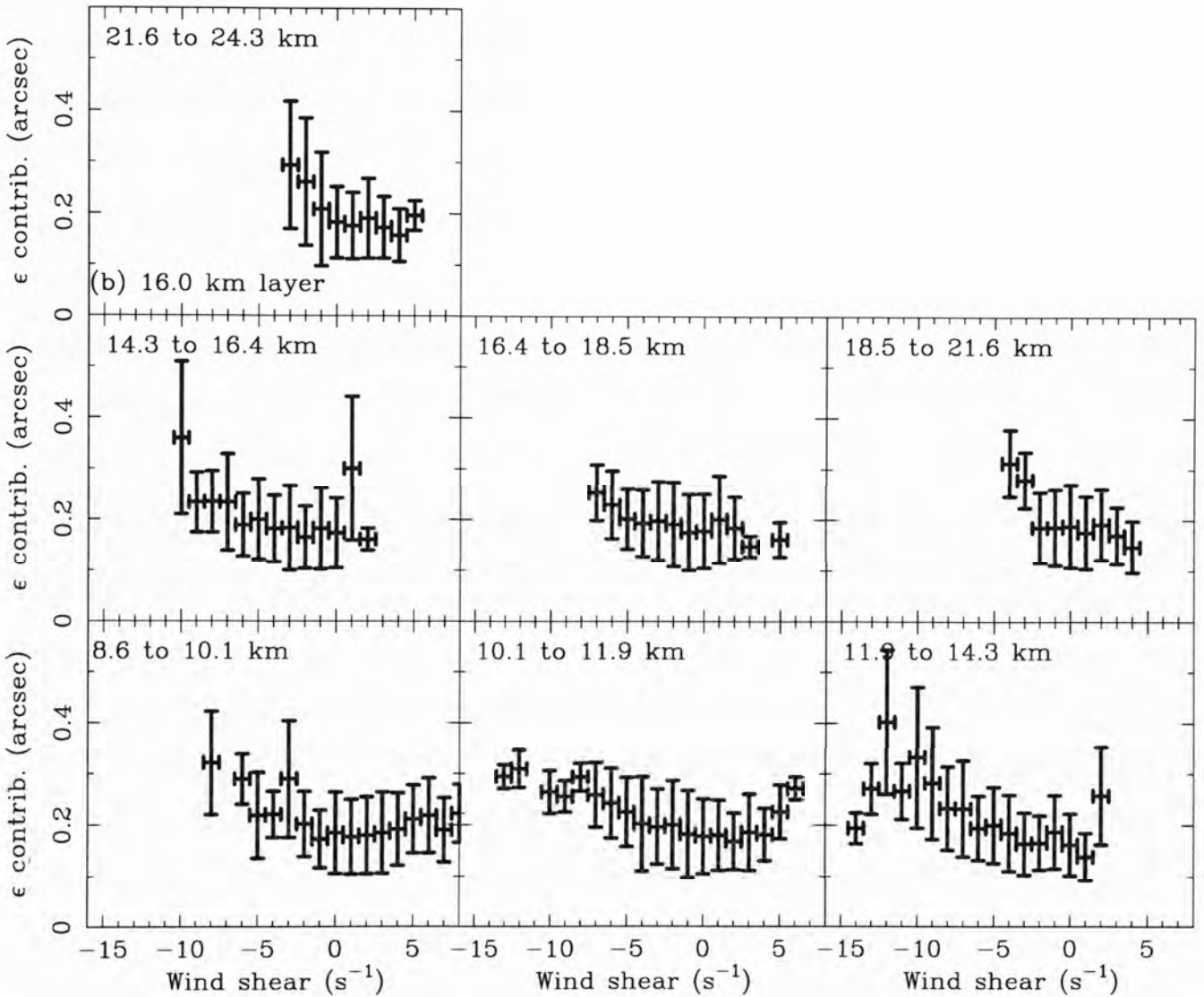


Figure 7.12. The seeing (ϵ) contribution (derived from the MASS data) in the (16 km MASS layer at Cerro Tololo as a function of the wind shear (derived from the NCEP/NCAR database). See the caption of Figure 7.9 for further details.

7-8 Conclusions

The scintillation noise at Dome C for fast exposures is typically a factor 1.9–2.6 times lower than at Cerro Tololo and Cerro Pachón, leading to a corresponding reduction in this ultimate limit for high precision photometry. The “small aperture” scintillation index becomes important for adaptive optics when the distance between the actuators approaches the Fresnel zone size r_F , and shadow patterns start becoming resolved (Masciadri et al. 2004). Adaptive optics will also benefit from the long coherence time and large isoplanatic angle at Dome C.

For longer exposures, σ_I at Dome C is typically 3.4–3.8 times less than at Cerro Tololo and Cerro Pachón. For a 60 second integration on a 4 m telescope, the median photometric error is $\sim 53 \mu\text{mag}$ at Dome C. This parameter is important for exoplanet transit measurements because the change in flux caused by a transiting planet is related to the planet R_p and star R_s radii by $\Delta F/F = (R_p/R_s)^2$. For example, for a Jupiter size planet transiting a Sun size star, $\Delta F/F = 0.01$; for an Earth size planet this ratio is 0.0001. The lower scintillation noise at Dome C will allow for the transits of smaller planets to be detected than at the Chilean sites.

The atmospheric contribution to the positional error in a differential astrometric measurement using a long baseline interferometer at Dome C is always less than the median values at Cerro Tololo and Cerro Pachón. Very narrow angle differential astrometry using long baseline interferometry at Dome C (Lloyd et al. 2002, 2003) would benefit a number of science programs, including extra-solar planet searches and orbit determination and the measurement of micro-lensing events (see, for example, Swain et al. 2003 and Sozzetti 2005).

Based on the expected low astrometric error at Dome C, a number of interferometric projects have already been proposed. These include the Antarctic Planet Interferometer (API; Swain et al. 2004), the Kiloparsec Explorer for Optical Planet Search (KEOPS; Vakili et al. 2004) and the Antarctic L-band Astrophysics Discovery Demonstrator for Interferometric Nulling (ALADDIN; Coudé du Foresto et al. 2006).

“For most programs, any loss in mental speed is amply compensated by the superior observing conditions.”

Morrison et al. (1973)

Evaluation of Mauna Kea, Hawaii as an observatory site

Chapter 8

Conclusions

Dome C, Antarctica, is potentially one of the best locations on the Earth to locate a telescope. The characteristics of an ideal astronomical site were outlined in the introduction; Dome C possesses many of these. Dome C is a high altitude site (3260 m), the atmosphere is dry, there is little precipitation, no lightning and few clouds. The surface wind speed is very slow and there is very little seismic activity. Concordia station at Dome C can be accessed during the summer months by small aircraft and large tractor traverses and has had a year-round crew since the austral summer of 2004/2005. This thesis has contributed to further understanding the atmospheric extinction, sky brightness and optical turbulence at Dome C; the main conclusions are summarised below.

Dome C has a similar number of cloud-free, astronomically dark hours compared to a more temperate site. The fraction of observable sky at Dome C is considerably lower than at temperate sites; however, many southern objects can be observed for longer. The overall atmospheric extinction at Dome C is expected to be close to the lowest anywhere on Earth because of the high altitude, low water vapour concentration, infrequent clouds and low aerosol concentration.

The contributions from moonlight and zodiacal light to sky brightness are less than at lower latitude sites. Aurorae will rarely be more than 7° above the horizon and will typically be more than about 1160 km away; they will generally be unobservable. Airglow

will be essentially the same as at other sites, while the integrated starlight and diffuse galactic light will be slightly brighter at Dome C. There is no artificial-light pollution at Dome C, a condition that should continue indefinitely. However, at this stage few measurements have been made of the brightness of the optical night sky.

An instrument, called Nigel, was designed to measure the twilight and night sky brightness at Dome C from 250 nm to 900 nm. Nigel did not collect any twilight or nighttime data at Dome C; however, the instrument will be upgraded and sent to either Dome C or Dome A for the 2008 winter.

The first winter-time turbulence profiles of the atmosphere above Dome C are presented here. Using a MASS and SODAR, these measurements give a low resolution altitude profile of the turbulence in the atmosphere from 30 m to 20 km above the surface. The accumulated effect of turbulence was evaluated showing a median seeing of 0.28'' above 30 m, and a median isoplanatic angle and coherence time of 5.4'' and 7.1 ms, respectively, above 500 m. Dome C was found to have significantly less turbulence, especially in the upper atmosphere, than two Chilean sites. The scintillation noise at Dome C for fast exposures is typically a factor 1.9–2.6 times lower than at Cerro Tololo and Cerro Pachón, leading to a corresponding reduction in this ultimate limit for high-precision photometry. The “small aperture” scintillation index becomes important for adaptive optics when the distance between the actuators approaches the Fresnel zone size and shadow patterns start becoming resolved (Masciadri et al. 2004). Adaptive optics will also benefit from the long coherence time and large isoplanatic angle at Dome C.

For longer exposures, the scintillation noise at Dome C is typically 3.4–3.8 times less than at Cerro Tololo and Cerro Pachón. The atmospheric contribution to the positional error in a differential astrometric measurement at Dome C is always less than the median values at Cerro Tololo and Cerro Pachón. However, the conclusions obtained here using the MASS data only cover a small sample and remain provisional until more measurements are made.

Site-testing of an astronomical site needs to be carried out over a number of years. The results described in this thesis are very encouraging for the future of astronomy at Dome C, providing strong motivation for further measurements.

Turbulence monitoring will continue as part of the ConcordiAstro project, using a

Differential Image Motion Monitor (DIMM), balloon-borne micro-thermals, and a Single Star Scidar (Agabi et al. 2006; Vernin et al. 2006). Sonic anemometers, similar to those described in Skidmore et al. (2006), have been installed on a 30 m high tower to monitor the turbulence close to the ground (Tony Travouillon, private communication). A Surface-layer NOn Doppler Acoustic Radar (SNODAR; Lawrence et al. 2006a) is due to be deployed to Dome C in the 2007/8 austral summer to monitor the turbulence in the first 10–50 m above the surface. The MASS and SUMMIT from the AASTINO project may also be sent back to Dome C. The atmospheric aerosol optical depth and the thin cloud variability will be monitored from 2009 using LIDAR (LIght Detection And Ranging), Sun and Star Photometers and in-situ measurements, as part of the TAVERN project (quantification of Tropospheric Aerosol and thin clouds Variability over the East Antarctic Plateau, including Radiation budget; Herber et al. 2006). The precipitable water vapour at $20 \mu\text{m}$ will be monitored with IRMA (Infrared Radiometer for Millimeter Astronomy; Phillips et al. 2006) and the Gattini cameras will continue to monitor the sky brightness (Moore et al. 2006a).

Based on the expected excellent conditions at Dome C a number of projects have already been proposed. Nulling interferometry (Swain et al. 2003) and astrometric differential interferometry (Lloyd et al. 2002, 2003) will benefit from the weaker high altitude turbulence and long coherence time. Interferometry projects include the Antarctic Planet Interferometer (API; Swain et al. 2004), the Kiloparsec Explorer for Optical Planet Search (KEOPS; Vakili et al. 2004), and the Antarctic L-band Astrophysics Discovery Demonstrator for Interferometric Nulling (ALADDIN; Coudé du Foresto et al. 2006). Many science programs would benefit from such facilities, these include exoplanet detection and orbit determination, and the measurement of micro-lensing events (e.g., Lloyd et al. 2002).

The high precision achievable in photometry will be an advantage for asteroseismology, helioseismology and stellar pulsation projects at Dome C; for example, see Briguglio et al. (2005); Chadid et al. (2005). The excellent photometric precision and long observing times will also benefit the Permanent All Sky Survey (PASS; Deeg et al. 2005) proposed for Dome C.

A 2 metre “path-finder” telescope is proposed for Dome C (PILOT—a Pathfinder for an International Large Optical Telescope). Several science programs that could use this

telescope are outlined in Burton et al. (2005). These include planetary studies, investigations within the Milky Way, and larger-scale universe observations. Following PILOT, more ambitious projects are proposed such as the 8.4 m Large Antarctic Plateau Clear-Aperture Telescope (LAPCAT; Storey et al. 2006) and a second 21 m Giant Magellan Telescope (Angel et al. 2004).

The future for astronomy at Dome C is bright, and represents an exciting new opportunity for the international community.

Appendix A

Acronyms

AAD Australian Antarctic Division

AASTINO Automated Astrophysical Site Testing International Observatory

AASTO Automated Astrophysical Site Testing Observatory

ALADDIN Antarctic L-band Astrophysics Discovery Demonstrator for Interferometric Nulling

AO Adaptive Optics

API Antarctic Planet Interferometer

CCD Charge Coupled Device

DIMM Differential Image Motion Monitor

IPEV Institut Polaire Français Paul Emile Victor

IRMA Infrared Radiometer for Millimeter Astronomy

KEOPS Kiloparsec Explorer for Optical Planet Search

LAPCAT Large Antarctic Plateau Clear-Aperture Telescope

LIDAR Light Detection And Ranging

MASS Multi-Aperture Scintillation Sensor

PASS Permanent All Sky Survey

PILOT Pathfinder for an International Large Optical Telescope

PNRA Programma Nazionale di Ricerche in Antartide

SNODAR Surface-layer NOn Doppler Acoustic Radar

SODAR SOund Detection And Ranging

SSS Single Star Scidar

TAVERN Quantification of Tropospheric Aerosol and thin clouds Variability over the
East Antarctic Plateau, including Radiation budget

UNSW University of New South Wales

Appendix B

Daily turbulence profiles at Dome C

This appendix shows individual daily plots of the turbulence profile measured by MASS at Dome C.

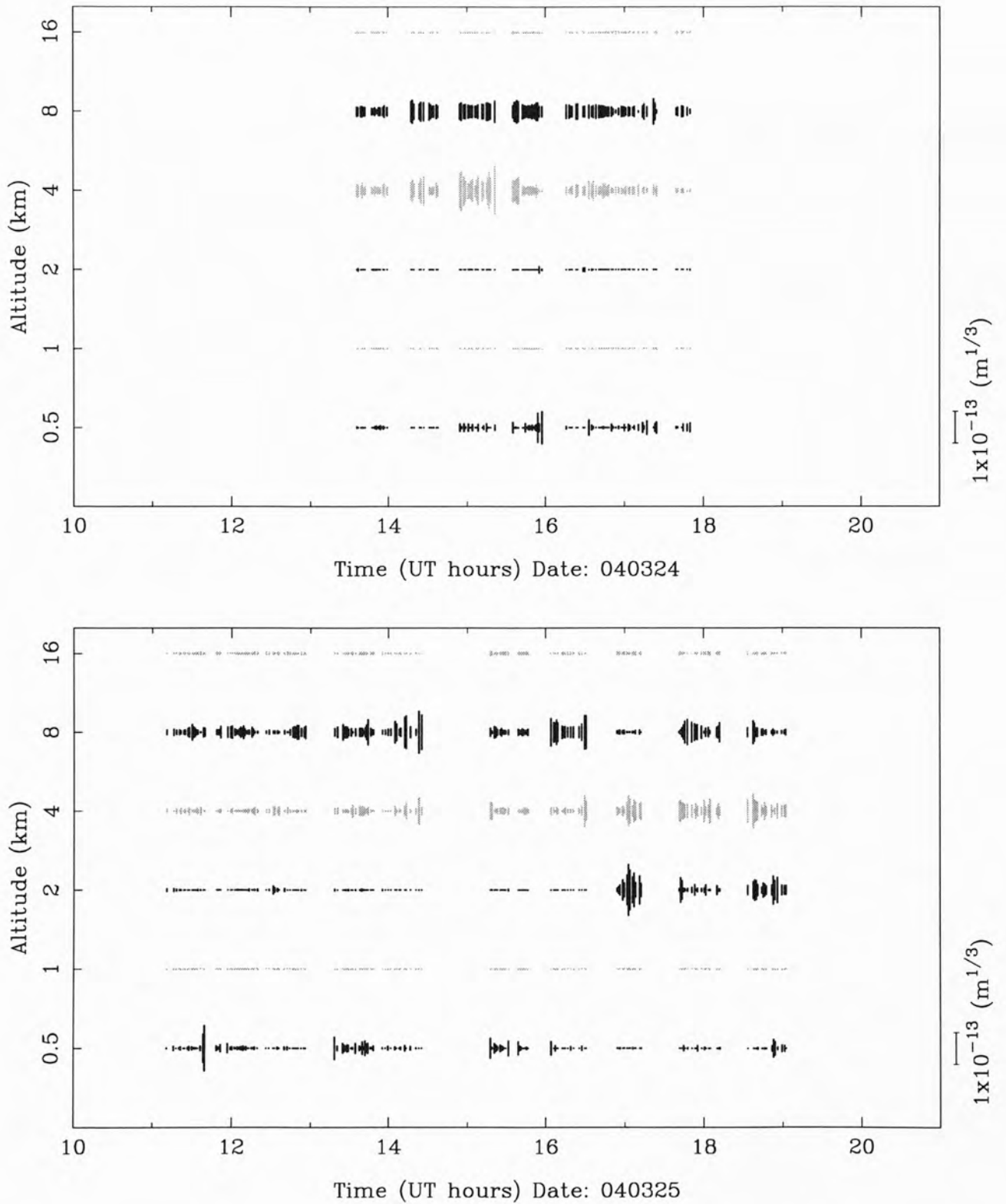


Figure B.1. MASS integrated turbulence profiles as a function of time for 24 March 2004 and 25 March 2004.

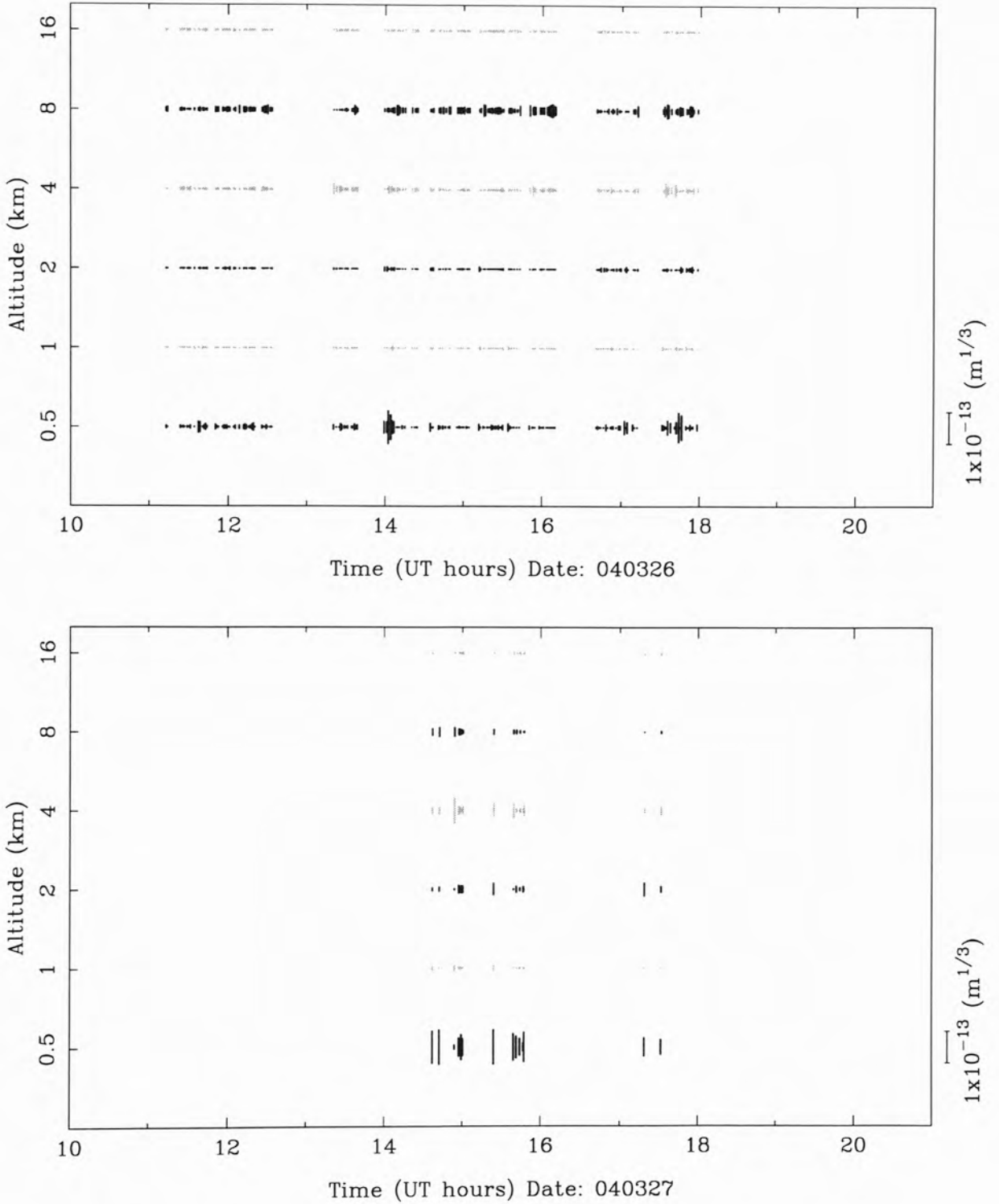


Figure B.2. MASS integrated turbulence profiles as a function of time for 26 March 2004 and 27 March 2004.

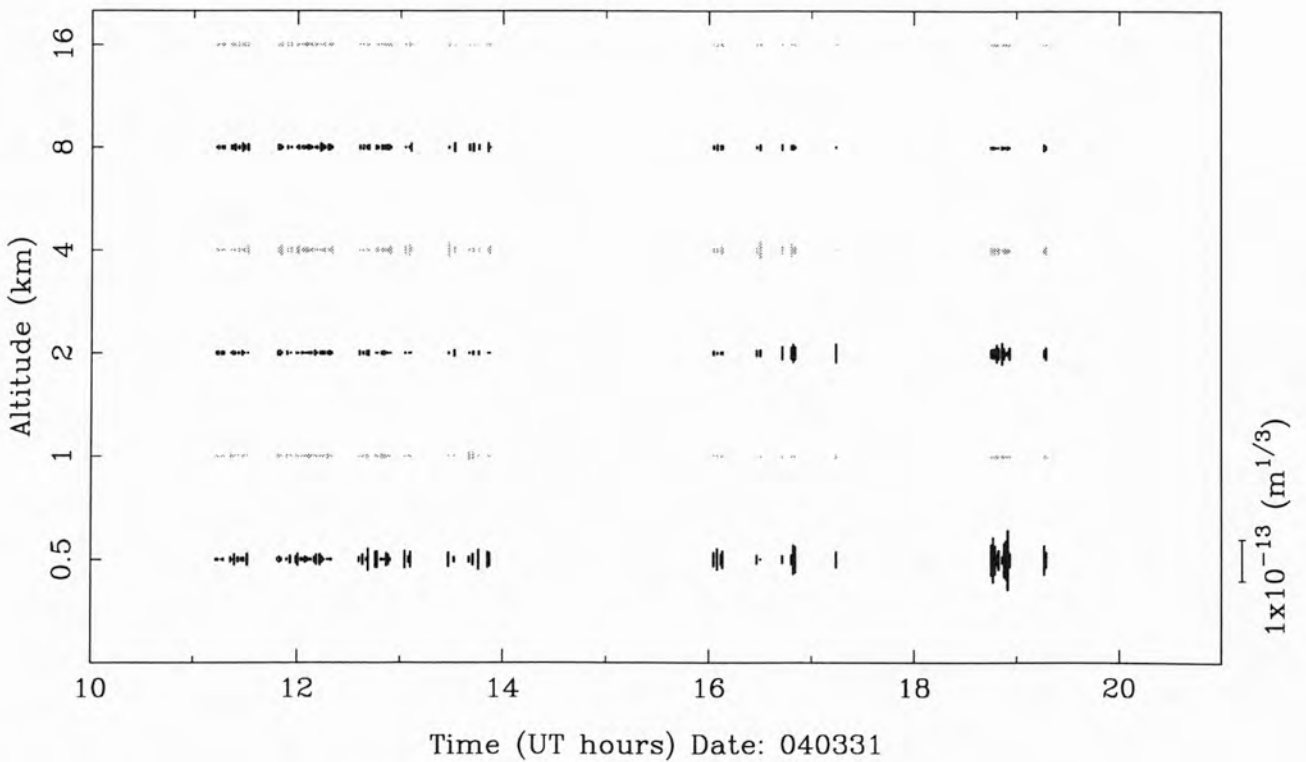
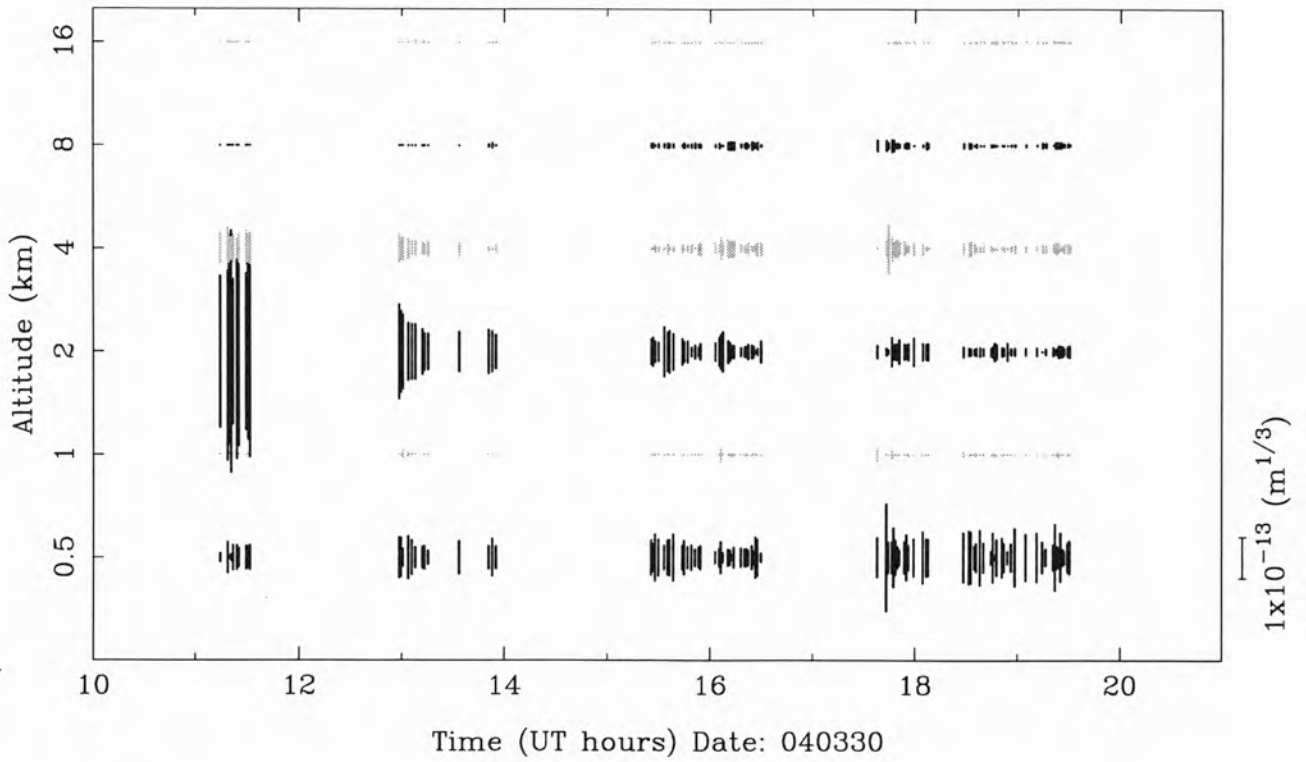


Figure B.3. MASS integrated turbulence profiles as a function of time for 30 March 2004 and 31 March 2004.

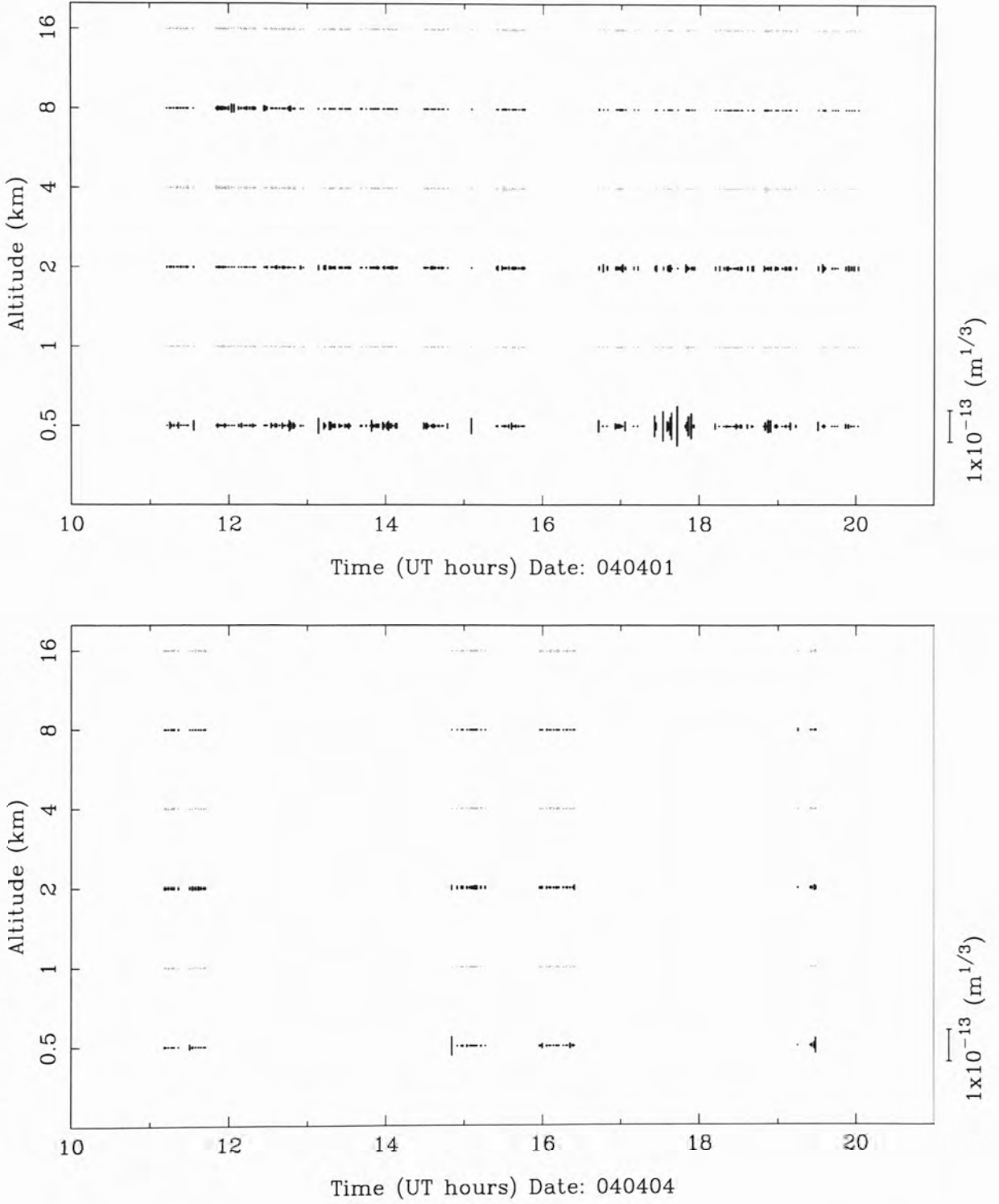


Figure B.4. MASS integrated turbulence profiles as a function of time for 1 April 2004 and 4 April 2004.

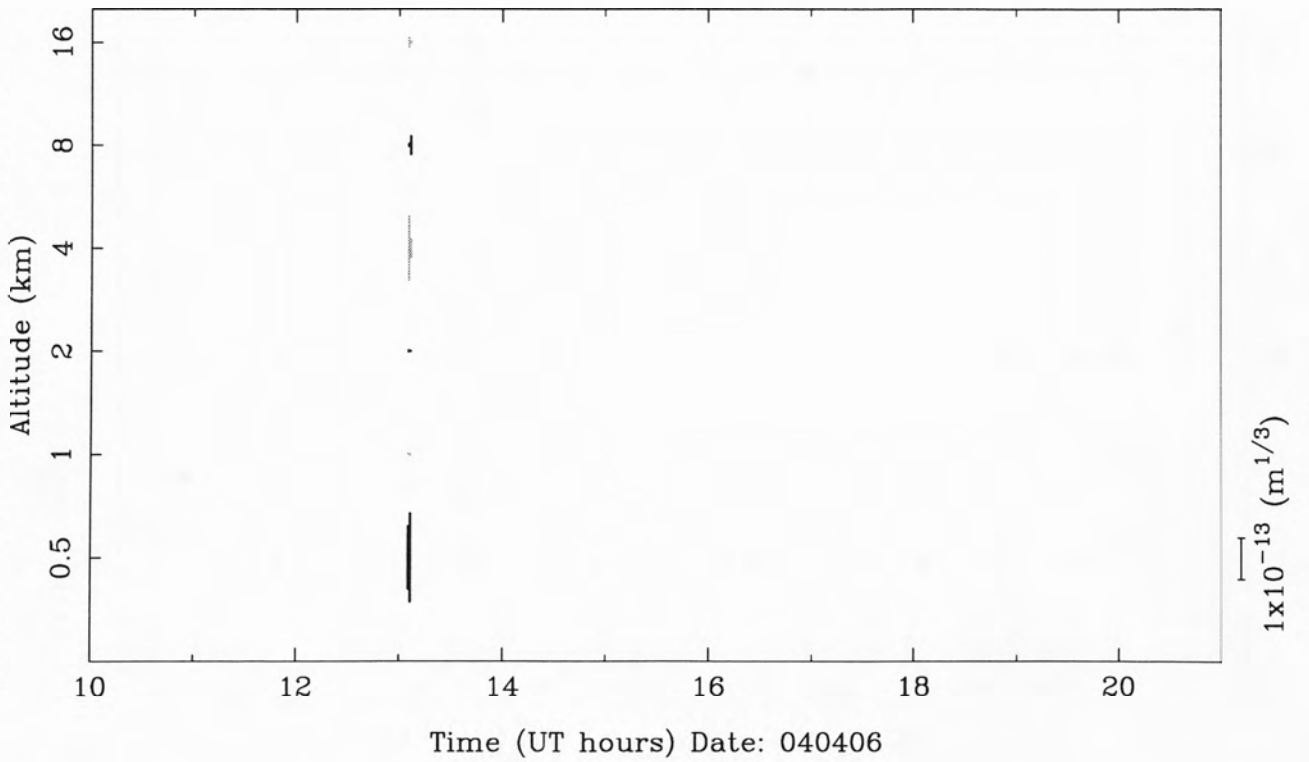
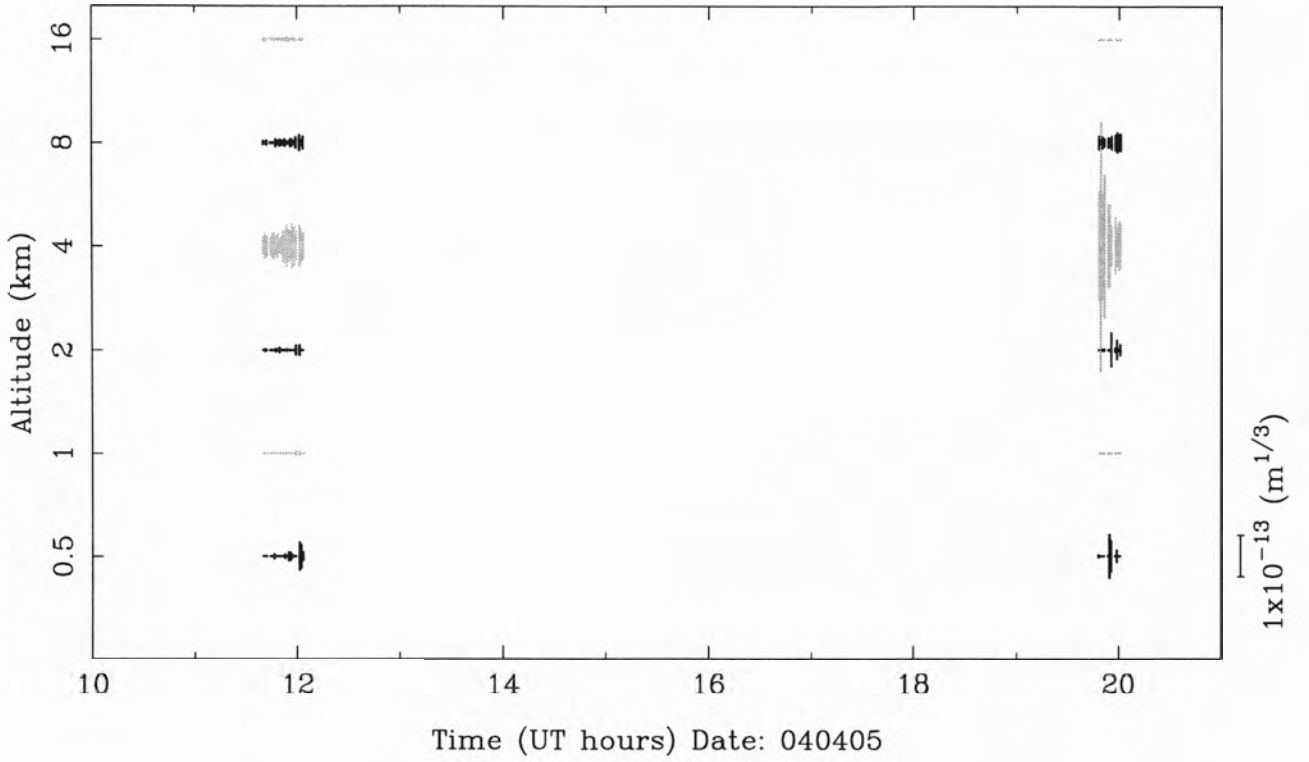


Figure B.5. MASS integrated turbulence profiles as a function of time for 5 April 2004 and 6 April 2004.

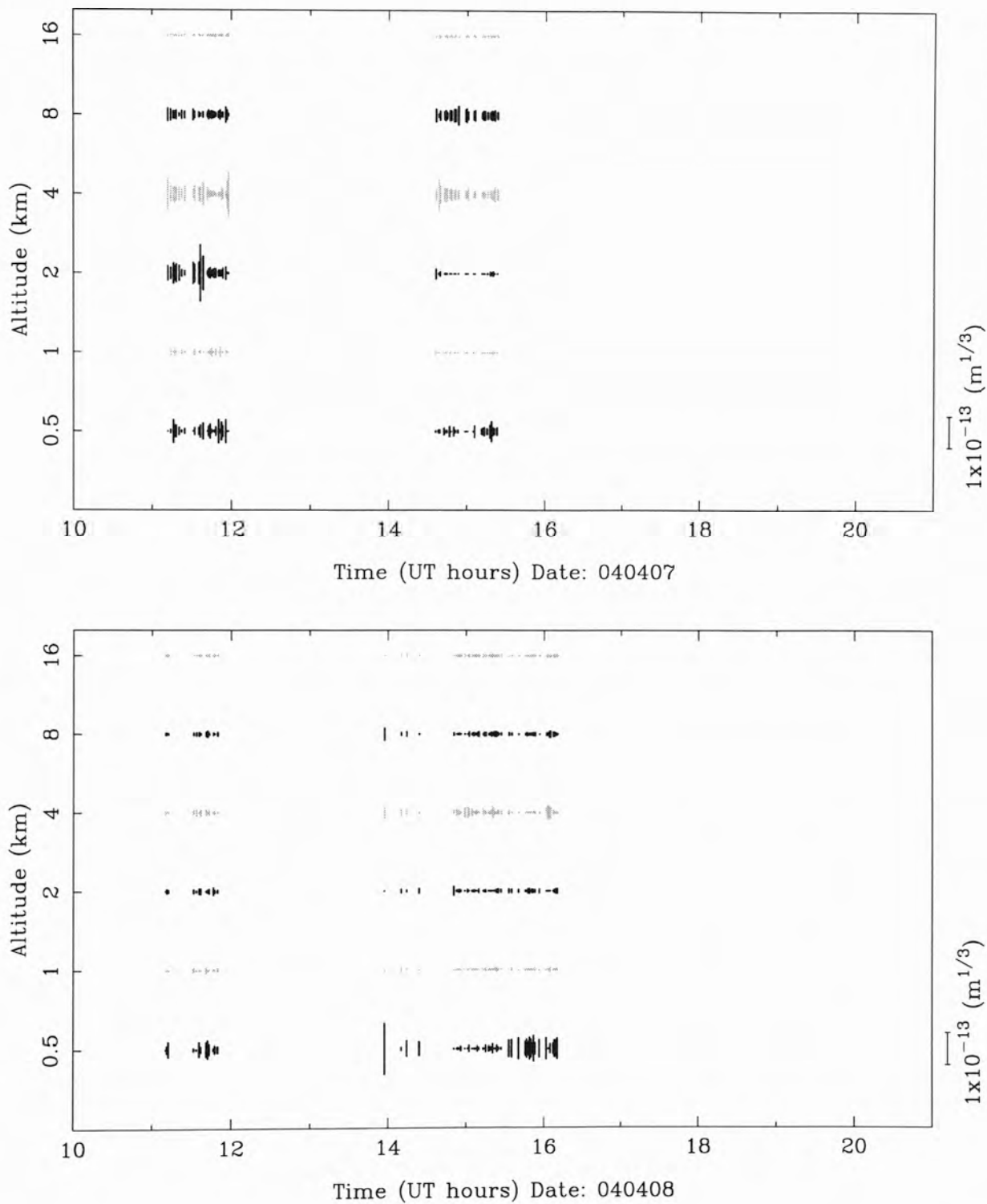


Figure B.6. MASS integrated turbulence profiles as a function of time for 7 April 2004 and 8 April 2004.

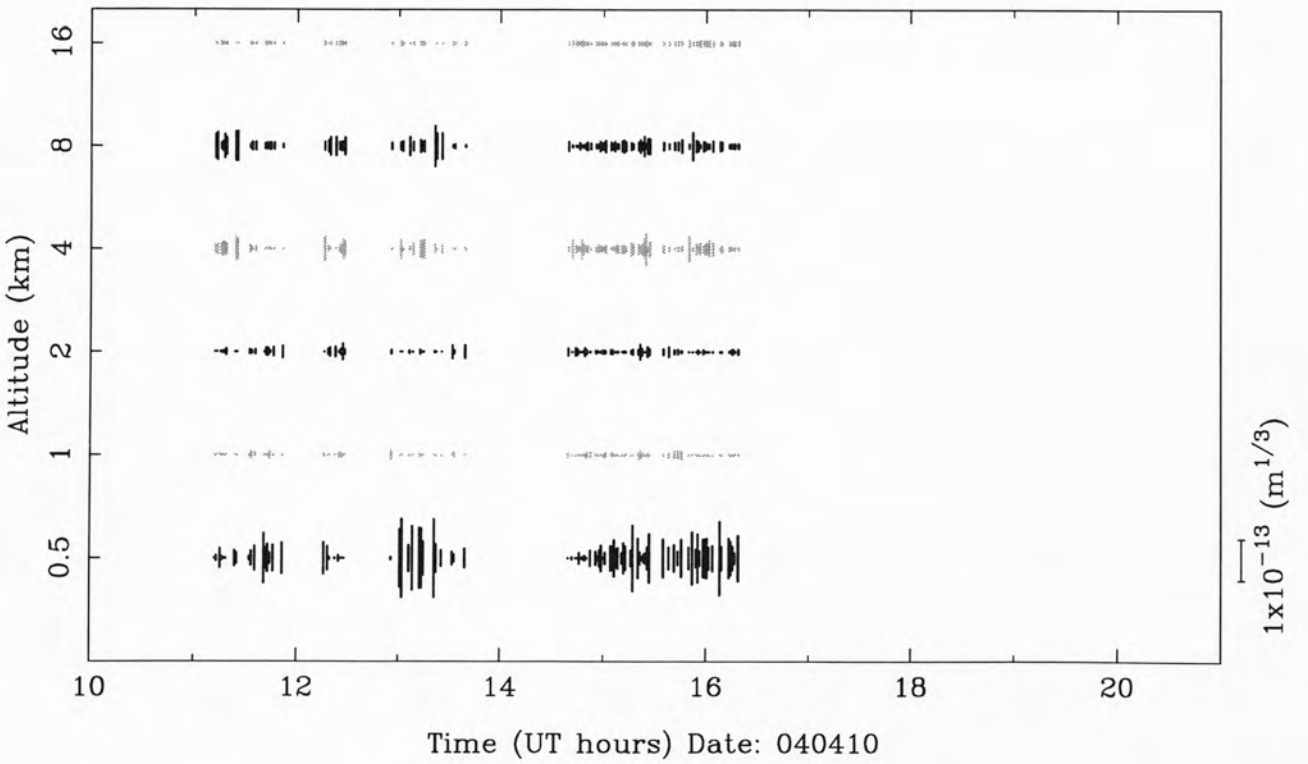
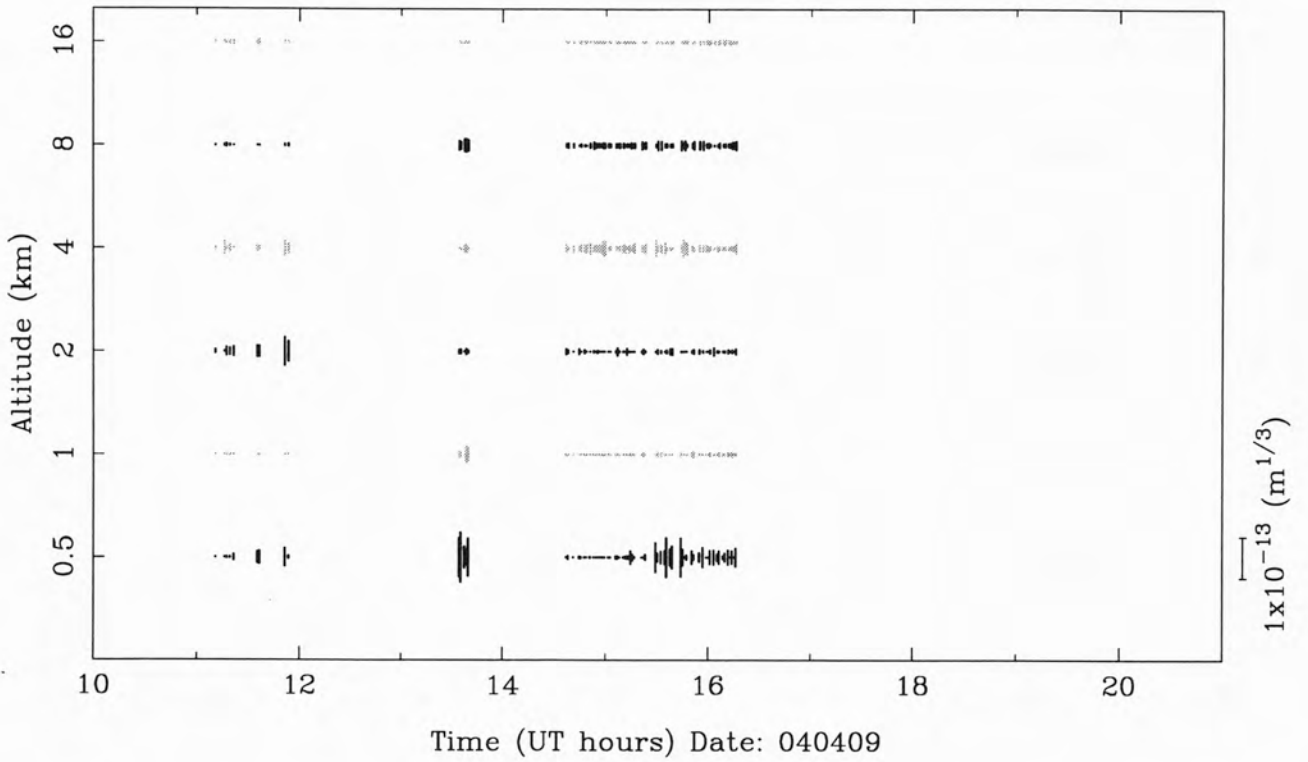


Figure B.7. MASS integrated turbulence profiles as a function of time for 9 April 2004 and 10 April 2004.

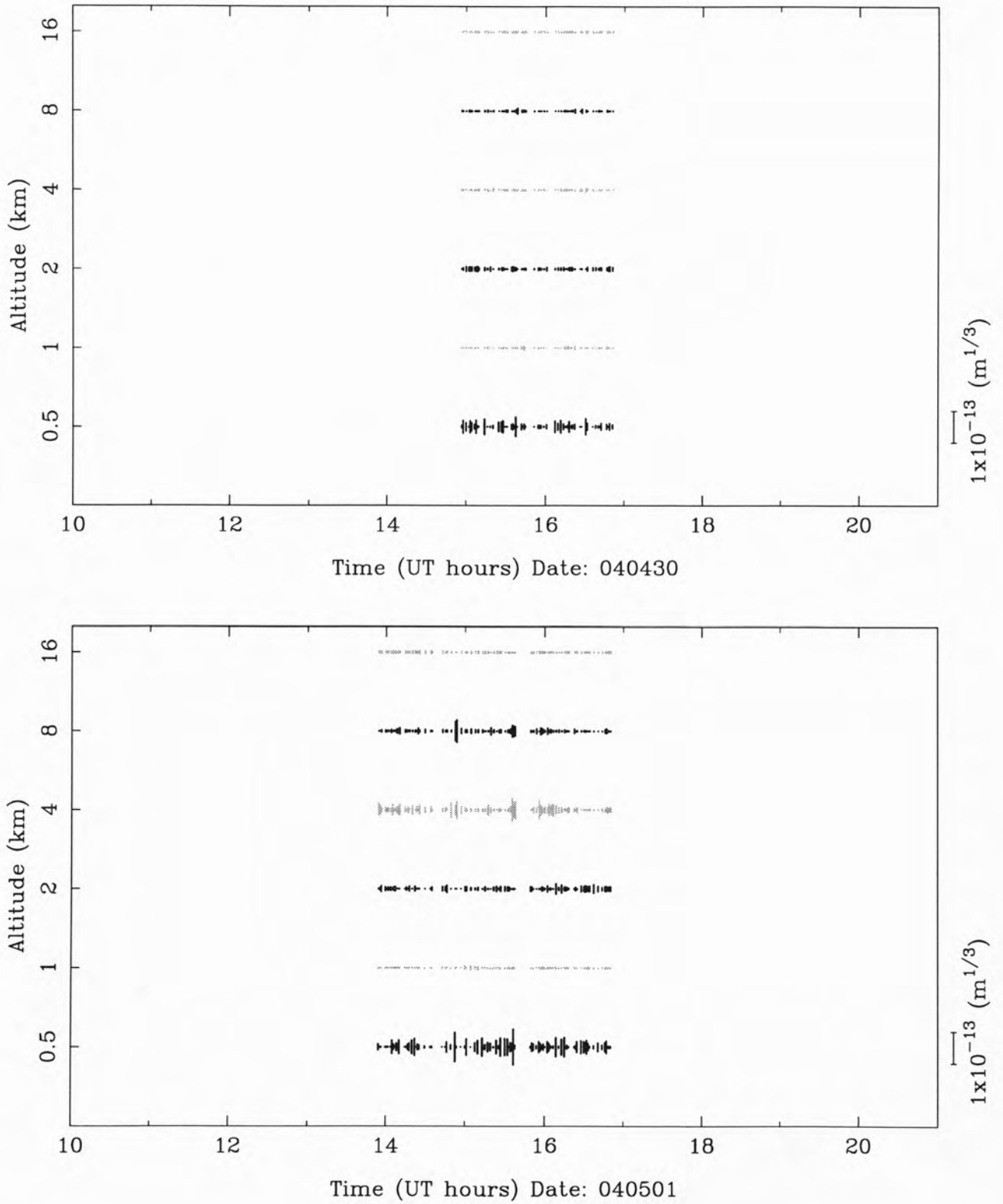


Figure B.9. MASS integrated turbulence profiles as a function of time for 30 April 2004 and 1 May 2004.

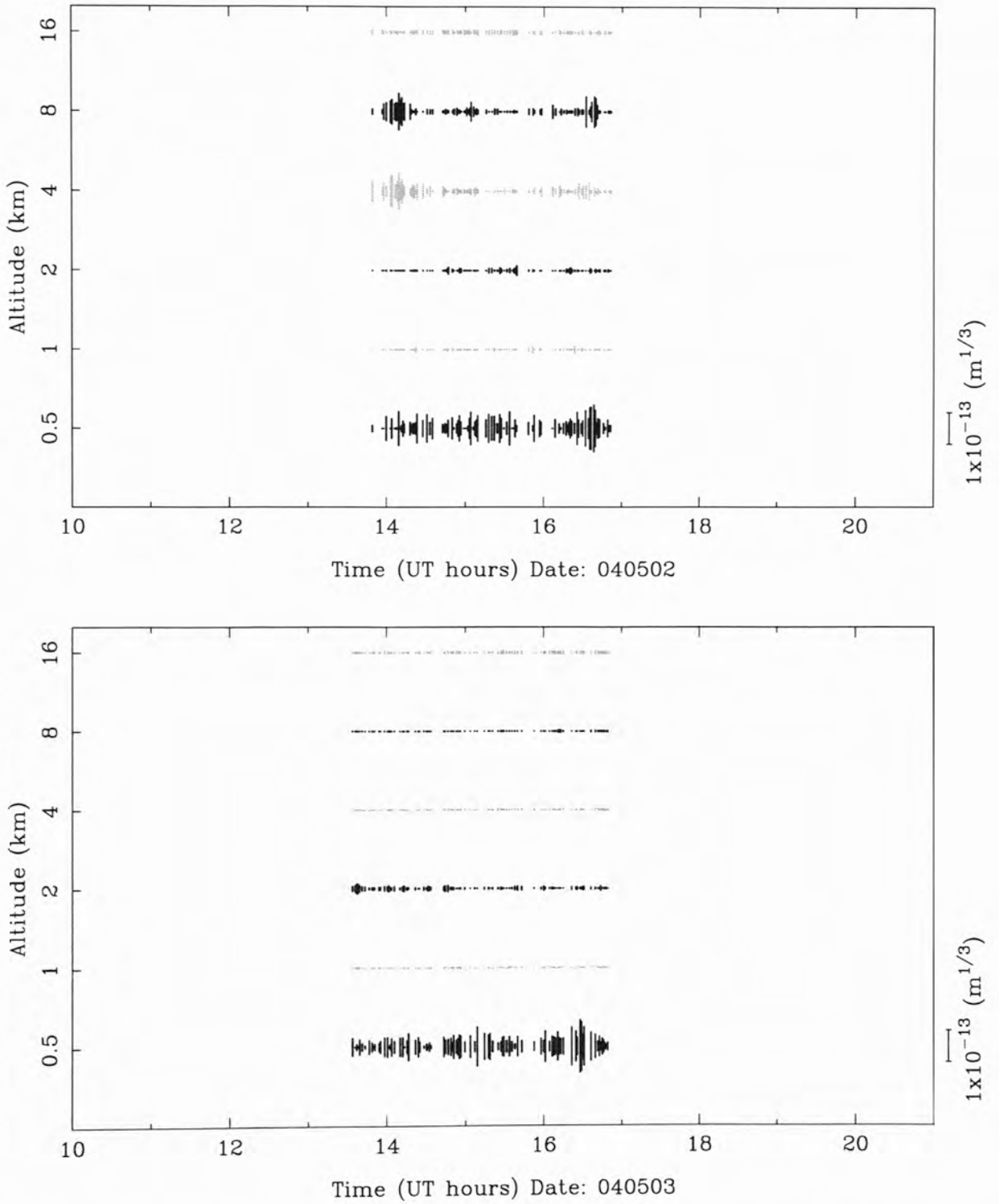


Figure B.10. MASS integrated turbulence profiles as a function of time for 2 May 2004 and 3 May 2004.

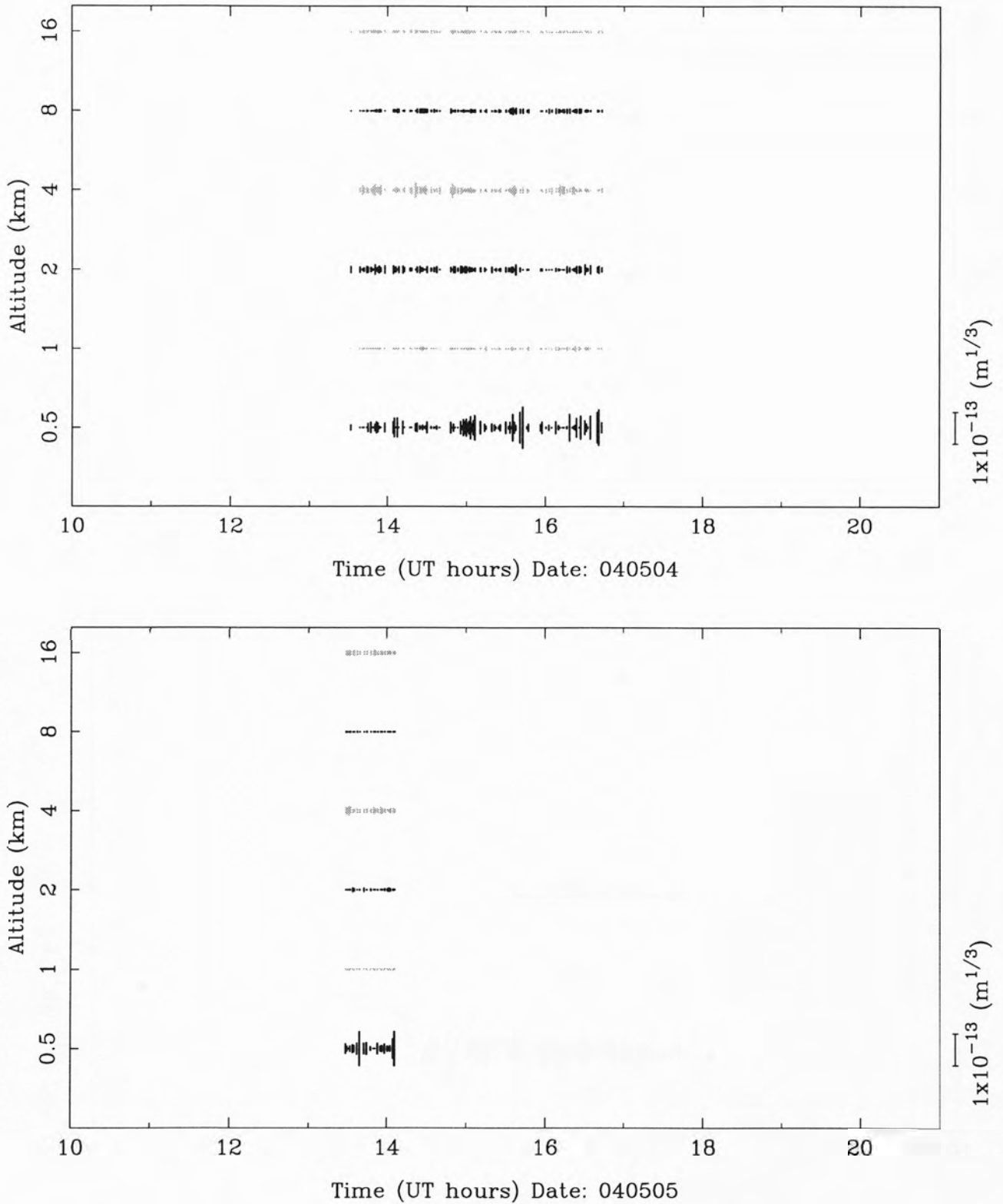


Figure B.11. MASS integrated turbulence profiles as a function of time for 4 May 2004 and 5 May 2004.

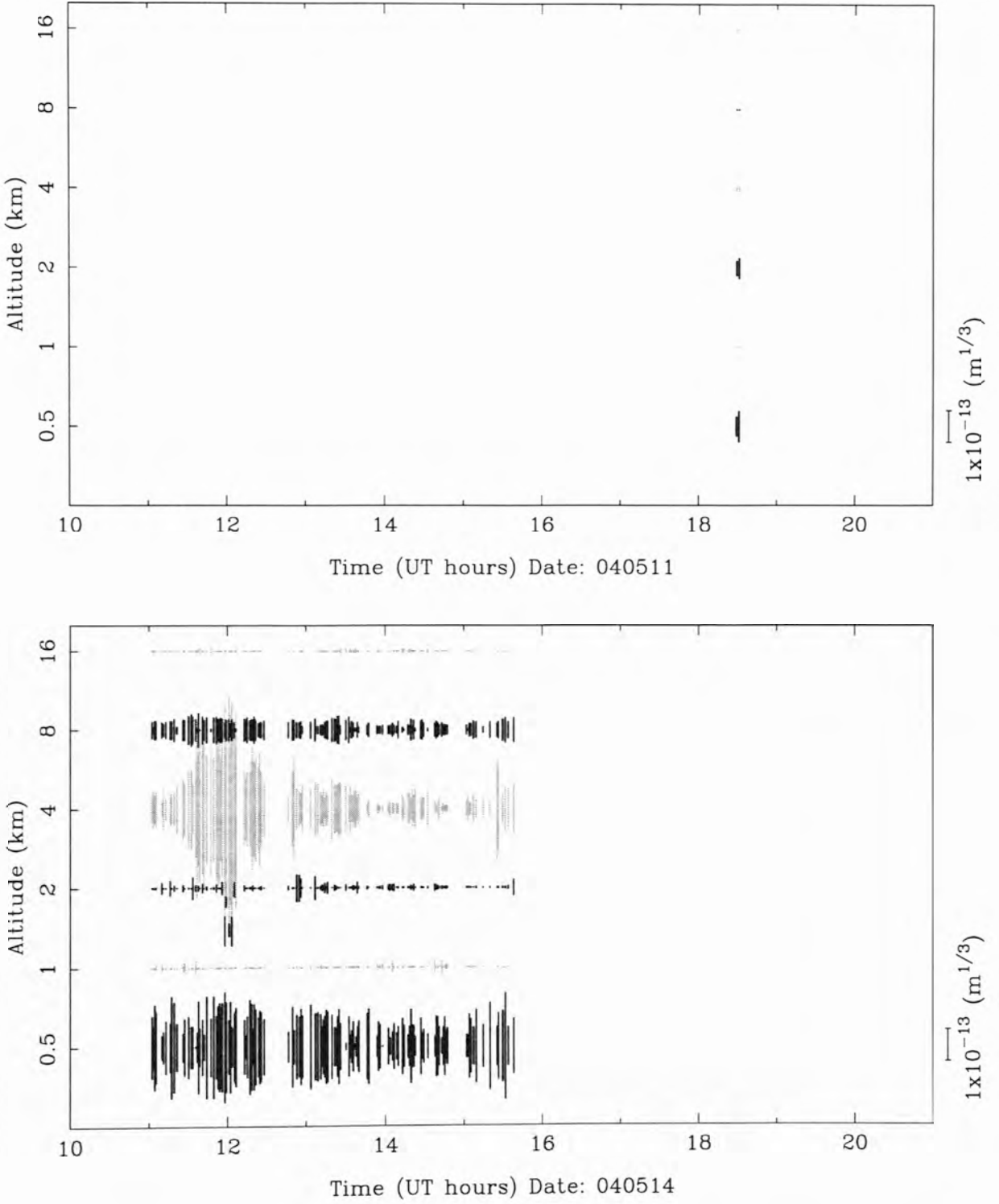


Figure B.12. MASS integrated turbulence profiles as a function of time for 11 May 2004 and 14 May 2004.

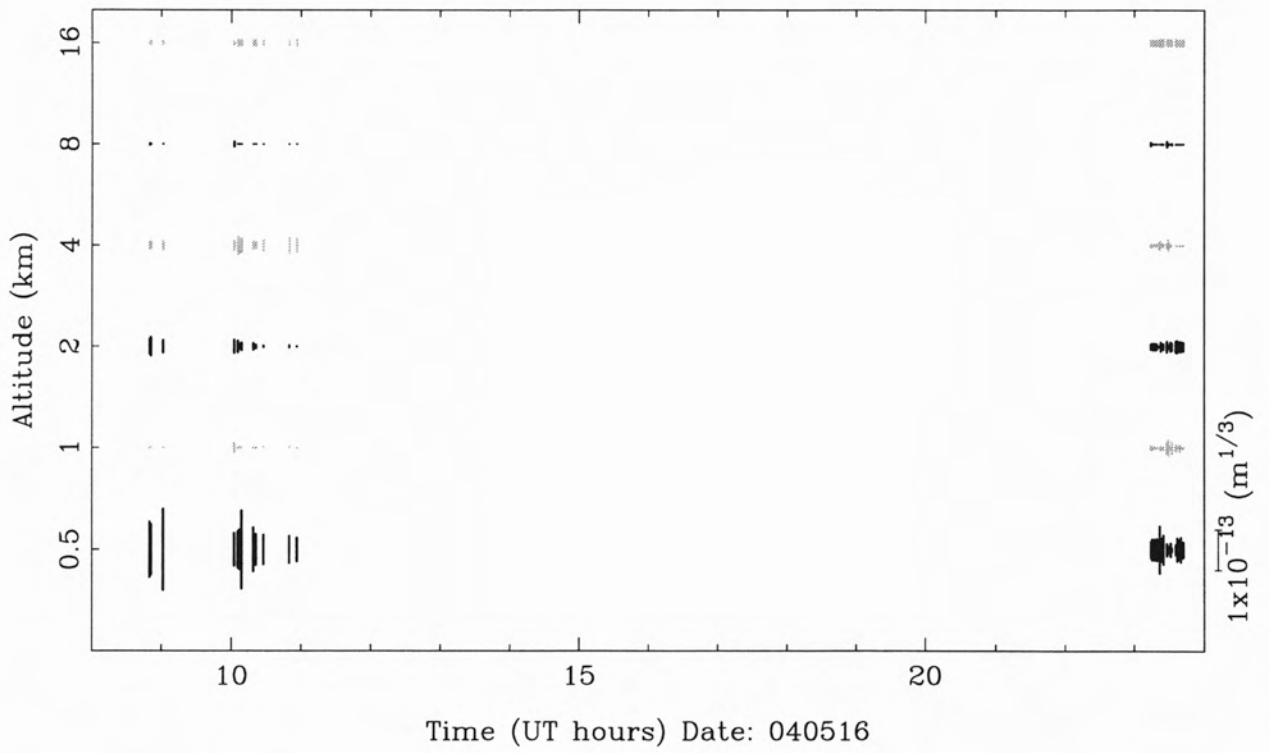


Figure B.13. MASS integrated turbulence profiles as a function of time for 16 May 2004.

Appendix C

Published papers

The following papers are included in their published form,

- **A review of the optical sky brightness and extinction at Dome C, Antarctica**, 2006, S. L. Kenyon and J. W. V. Storey, Publications of the Astronomical Society of the Pacific, **118**, 489–502. Appendix C-1.
- **Atmospheric scintillation at Dome C, Antarctica: implications for photometry and astrometry**, 2006, S.L. Kenyon, J.S. Lawrence, M.C.B. Ashley, J.W.V. Storey, A. Tokovinin and E. Fossat, Publications of the Astronomical Society of the Pacific, **118**, 924-932. Appendix C-2
- **Nigel and the optical sky brightness at Dome C, Antarctica**, 2006, S.L. Kenyon, M.C.B. Ashley, J. Everett, J.S. Lawrence and J.W.V. Storey, Proceedings of the SPIE, **6267**, 62671M. Appendix C-3.

Additional papers that I co-authored during the thesis are:

- **Ground-layer turbulence profiling using a lunar SHABAR**, 2006, A.M. Moore, E. Aristidi, M.C.B. Ashley, M. Busso, M. Candidi, J. Everett, S.L. Kenyon, J.S. Lawrence, D. Luong-Van, A. Phillips, B. Le Roux, R. Ragazzoni, P. Salinari, J.W.V. Storey, M. Taylor, G. Tosti and T. Travouillon, Proceedings of the SPIE, **6269**, 62695U
- **The Gattini cameras for optical sky brightness measurements in Antarctica**, 2006, A.M. Moore, E. Aristidi, M.C.B. Ashley, M. Busso, M. Candidi, J.

Everett, S. L. Kenyon, J. S. Lawrence, D. Luong-Van, A. Phillips, B. Le Roux, R. Ragazzoni, P. Salinari, J. W. V. Storey, M. Taylor, G. Tosti and T. Travouillon, Proceedings of the SPIE, **6267**, 62671N

- **Site testing Dome A, Antarctica**, 2006, J. S. Lawrence, M. C. B. Ashley, M. G. Burton, X. Cui, J. R. Everett, B. T. Indermuehle, S. L. Kenyon, D. Luong-Van, A. M. Moore, J. W. V. Storey, A. Tokovinin, T. Travouillon, C. Pennypacker, L. Wang and D. York, Proceedings of the SPIE, **6267**, 62671L
- **A robotic instrument for measuring high altitude atmospheric turbulence from Dome C, Antarctica**, 2004, J. S. Lawrence., M. C. B. Ashley., S. L. Kenyon, J. W. V. Storey, A. Tokovinin, J. P. Lloyd, and M. R. Swain, Proceedings of the SPIE, **5489**, 174

C-1 A review of the optical sky brightness and extinction at Dome C

PUBLICATIONS OF THE ASTRONOMICAL SOCIETY OF THE PACIFIC, 118:489–502, 2006 March
 © 2006, The Astronomical Society of the Pacific. All rights reserved. Printed in U.S.A.

A Review of Optical Sky Brightness and Extinction at Dome C, Antarctica

S. L. KENYON AND J. W. V. STOREY

School of Physics, University of New South Wales, Sydney 2052, Australia; suzanne@phys.unsw.edu.au, j.storey@unsw.edu.au

Received 2005 September 29; accepted 2005 November 16; published 2006 March 21

ABSTRACT. The recent discovery of exceptional seeing conditions at Dome C, Antarctica, raises the possibility of constructing an optical observatory there with unique capabilities. However, little is known from an astronomer's perspective about the optical sky brightness and extinction at Antarctic sites. We review the contributions to sky brightness at high-latitude sites and calculate the amount of usable dark time at Dome C. We also explore the implications of the limited sky coverage of high-latitude sites and review optical extinction data from the South Pole. Finally, we examine the proposal of Baldry & Bland-Hawthorn to extend the amount of usable dark time through the use of polarizing filters.

1. INTRODUCTION

Dome C, Antarctica, is one of the most promising new sites for optical, infrared, and submillimeter astronomy. Located at 75°6' south, 123°21' east, and an altitude of 3250 m, Dome C is the third highest point on the Antarctic Plateau. The French (Institut Paul Emile Victor) and Italian (Programma Nazionale di Ricerche in Antartide) Antarctic programs have operated a summertime scientific base on Dome C since 1995 (Candidi & Lori 2003). Construction of a wintertime station was completed at the beginning of 2005, leading to the first manned winter season at Dome C. Preliminary site testing has been carried out at Dome C since 1995 (Valenziano & dall'Oglio 1999; Candidi & Lori 2003), and systematic measurements of the summertime (Aristidi et al. 2005b) and wintertime (Storey et al. 2005) characteristics of the site began in 2001. The results, summarized below, indicate very favorable conditions for astronomy.

The local topography of Dome C is extremely flat, resulting in a mean ground-level wind speed of 2.9 m s⁻¹ (Aristidi et al. 2005a), less than half that at most other observatories. Wintertime measurements of the turbulence in the atmosphere above Dome C (with MASS [multiaperture scintillation sensors] and a SODAR [sound detection and ranging]) indicate that above a thin surface layer, the atmosphere is extremely stable. From above 30 m, a median seeing of 0".27 is observed during the winter, with seeing below 0".15 for 25% of the time (Lawrence et al. 2004). In comparison, the median seeing at the best midlatitude sites is between 0".5 and 1".0. Agabi et al. (2006) measure the wintertime seeing from the ground level to be 1".9 ± 0".5 and attribute this to a thin but intense layer of surface turbulence. From above this layer, which they estimate to be 36 m, the exceptionally good seeing observed by Lawrence et al. (2004) is confirmed. In addition, summertime site testing with a differential image motion monitor (DIMM)

(i.e., while the Sun is continuously above the horizon) shows a remarkable median seeing of 0".54 (Aristidi et al. 2005b).

The cloud cover is very low, with cloud-free skies observed at least 74% of the time (Ashley et al. 2005). In addition, the site is extremely cold, and the atmosphere has very low precipitable water vapor in comparison to other sites (Valenziano & dall'Oglio 1999), leading to exceptionally low sky backgrounds in the infrared (Walden et al. 2005) and the submillimeter (Calisse et al. 2004). Substantial improvements in atmospheric transmission are predicted at these wavelengths, and a number of new spectral windows are opened up that are inaccessible at non-Antarctic sites (Lawrence 2004).

Despite these attractions, the high latitude of Dome C means that the Sun spends a relatively small amount of time far below the horizon. This implies longer periods of astronomical twilight and less *optical* dark time than other sites, especially those close to the equator. Thus, although the advantages offered by Antarctica at infrared wavelengths and beyond (where sky brightness is unaffected by twilight, moonlight, and aurorae) are well established (e.g., Storey et al. 2003), it remains to be seen whether the amount of usable dark time at Dome C is sufficient to allow observers to take effective advantage of the seeing conditions in the optical.

In addition to the long twilight, high-latitude sites suffer from reduced sky coverage. The fraction f of the total 4π sr of the heavens that can be seen from a site of given latitude over a 24 hr period is

$$f = \frac{1}{2}(\sin N - \sin S), \quad (1)$$

where N is the northernmost declination observable and S is the southernmost. We consider two cases: a zenith limit of 45° (1.4 air masses) and a zenith limit of 60° (2 air masses). As seen in Table 1, Mauna Kea has access to 81% of the sky at

490 KENYON & STOREY

TABLE 1
OBSERVABLE SKY

SITE	45° ZENITH LIMIT		60° ZENITH LIMIT	
	Decl. Range	Percentage of Sky	Decl. Range	Percentage of Sky
Equator	45° south–45° north	70	60° south–60° north	86
Mauna Kea	26° south–64° north	66	41° south–79° north	81
Dome C	90° south–30° south	25	90° south–15° south	37
North or South Pole	90° north/south–45° north/south	14	90° north/south–30° north/south	25

2 air masses or less, while at Dome C only 37% of the sky is similarly available.

In the case of a high-latitude southern site such as Dome C, this restricted sky coverage is mitigated somewhat by the accessibility of several key sources, such as the LMC (decl. = 69° south) and SMC (decl. = 73° south) and the Galactic center (decl. = 28° south). Such southern sources are of course favorably observed from Dome C. For example, although the Galactic center reaches comparable maximum elevations of 44° at Dome C and 41° at Mauna Kea, it is above 30° elevation for 1300 dark hours per year at Dome C, but only 660 dark hours per year at Mauna Kea. The advantages of a high-latitude southern site for the continuous monitoring of southern objects have already been discussed by a number of authors; for example, Deeg et al. (2005).

In § 2, we assess the amount of *usable* dark time at Dome C and examine the various contributions to optical sky brightness. The causes of atmospheric extinction are discussed in § 3. Baldry & Bland-Hawthorn (2001) have suggested using a polarizing filter to reduce twilight contributions to sky background. In § 4 we examine the polarization of scattered sunlight over the course of twilight to evaluate the feasibility of this idea.

2. OPTICAL SKY BRIGHTNESS

The night sky is never completely dark at any site. The darkest optical skies on Earth are on the order of 22.0–21.1 mag arcsec⁻² in *V* at zenith (Leinert et al. 1998). See Leinert et al. (1998) for a comprehensive discussion of diffuse night-sky brightness, Patat (2003) for an in-depth survey of *UBVRI* night-sky brightness at ESO-Paranal, and Benn & Ellison (1998) for a review of sky brightness measurements at La Palma.

On a moonless night, long after the Sun has set, the sky is brightened by aurorae, airglow, zodiacal light, integrated starlight, diffuse Galactic light, extragalactic light, and artificial sources (see Table 2). As first noted by Rayleigh (1928), the sky brightness at a particular site varies with solar activity; for example, Walker (1988) recorded a change of at least 1 mag arcsec⁻² in sky brightness with solar activity. Atmospheric scattering of the flux from each of these sources adds significantly to the sky brightness; for example, the contribution from zodiacal light can be increased by more than 15% by scattering, and that from integrated starlight by 10%–30% (Leinert et al. 1998). During twilight, the scattered sunlight usually makes

the dominant contribution to the overall sky brightness, while the flux from direct and scattered moonlight adds a further strong contribution when the Moon is above the horizon. The best dark conditions occur at a site with minimal atmospheric scattering.

In this section, we discuss each source of sky brightness at Dome C and provide a comparison to Mauna Kea, Hawaii, which we select because it is the closest major observatory to the equator.

2.1. Scattered Sunlight and Usable Dark Time

Sunlight is the strongest contributor to the brightness of the sky. During the day, the surface of the Earth is illuminated by *direct* sunlight and by sunlight that is *scattered* by atmospheric molecules and particles. After sunset, the surface of the Earth is only illuminated by scattered sunlight; the direct component illuminates the atmosphere above the level of the Earth's shadow. Over the course of twilight, the scattered sunlight contribution to sky brightness decreases as higher and less dense levels of the atmosphere are illuminated (Rozenberg 1966). In the absence of moonlight and artificial sources, scattered sunlight completely dominates the sky brightness until the Sun reaches a zenith angle of about 98° (Pavlov et al. 1995). The relative contribution of scattered sunlight to total sky brightness then decreases sharply to a negligible level, and nighttime starts. In the *V* band, this occurs when the Sun is depressed 17°–19° below the horizon; if there is a high amount of scattering in the atmosphere, this can be extended to depressions of 20°–23° (Rozenberg 1966). Astronomical nighttime is usually considered to begin when the Sun is more than 18° below the horizon.

For solar zenith angles greater than about 98°, multiple scattering accounts for essentially all of the sunlight contribution to sky brightness; this contribution is affected by the aerosol content in the atmosphere (Pavlov et al. 1995; Ugolnikov et al. 2004). Dome C has an exceptionally clear atmosphere, with no dust, haze, smog, or sand aerosols (see § 3 for a discussion of scattering at Dome C), and therefore it is expected that the intensity of multiply scattered light will be at the lowest possible level. Paradoxically, the lack of aerosols will, however, decrease the attenuation of sunlight that grazes the Earth, with the result that at midtwilight the intensity just above the Earth's shadow could be brighter at some wavelengths than at sites with less clear skies. This has the effect of lowering the ef-

TABLE 2
CONTRIBUTIONS TO THE LIGHT OF THE NIGHT SKY

Source	Function of Dependence	Physical Origin
Scattered sunlight	Ecliptic coordinates, season, location, aerosols	Sunlight scattering from molecules and particles in the upper atmosphere
Moonlight	Lunar phase, position of the Moon, aerosols	Sunlight reflected from the lunar surface, then scattered in the atmosphere
Aurora	Magnetic latitude, season, magnetic activity, solar activity	Excitation of upper atmosphere atoms and molecules by energetic particles
Airglow	Zenith angle, local time, latitude, season, solar activity, altitude, geomagnetic latitude	Chemiluminescence of upper atmosphere atoms and molecules
Zodiacal light	Ecliptic coordinates	Sunlight scattered by interplanetary dust
Integrated starlight	Galactic coordinates	Unresolved stars in the Milky Way
Diffuse Galactic light	Galactic coordinates	Scattering of starlight by interstellar dust
Integrated cosmic light	Galactic coordinates, cosmological redshift	The universe
Light pollution	Proximity to civilization	Artificial lighting

NOTE.—From Roach & Gordon 1973.

fective altitude of the so-called twilight layer (Ougolnikov 1999; Ougolnikov & Maslov 2003), creating an opportunity for enhanced scattering by the denser gas at those lower altitudes. A further effect that could brighten the Dome C sky is the high albedo of the snow that covers the Antarctic plateau, which will increase the sky brightness by a small amount at sunset. However, this effect decreases with increasing solar zenith angles and is negligible once the Sun has set (Anderson & Lloyd 1990). During periods when the Moon is above the horizon, the high albedo of the snow may also increase the sky brightness beyond that normally experienced during gray time.

From the above discussion, it is clear that the twilight sky

brightness at Dome C and the solar depression angle at which nighttime commences cannot be calculated in a straightforward manner. Both parameters can only be quantified by direct measurement or by detailed modeling using accurate atmospheric aerosol profiles.

Using the formal definition above, Dome C has less astronomical nighttime than lower latitude sites, with long periods of twilight. From a simple geometric calculation, Dome C has about 50% of the astronomical nighttime of Mauna Kea, as shown in Figure 1. The cloudiness of each site also needs to be taken into consideration when looking at the amount of dark time available for optical observations. On the basis of 2001

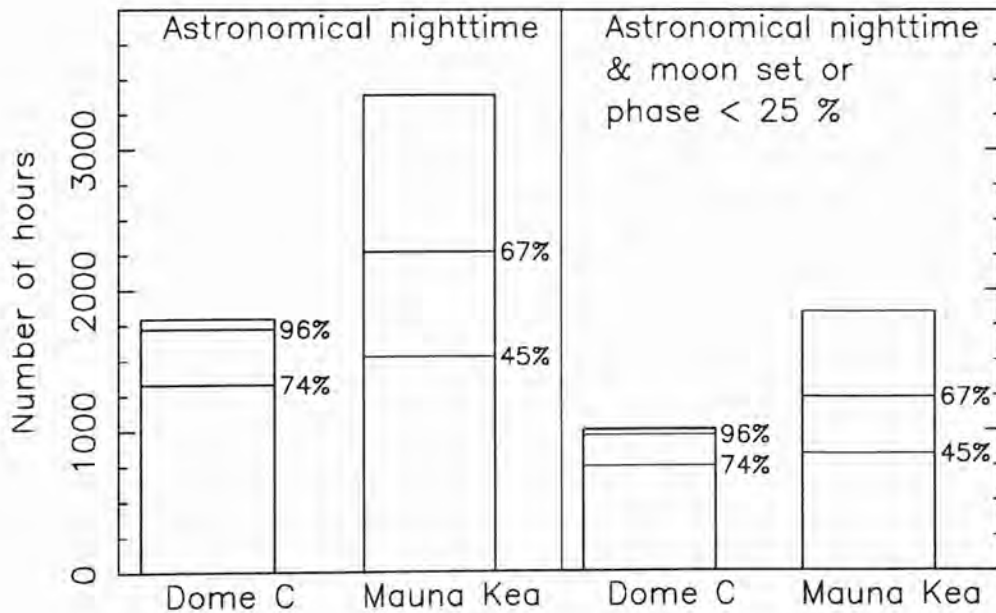


FIG. 1.—Comparison of the available dark time and cloud statistics (see text) at Dome C and Mauna Kea. *Left*: Number of hours of formal astronomical nighttime (i.e., when the Sun is more than 18° below the horizon). *Right*: Number of hours of astronomical nighttime when the Moon is below the horizon or less than 1/4 phase. The percentage bars indicate the usable dark time once cloud cover is taken into account.

492 KENYON & STOREY

data, Ashley et al. (2005) report the skies at Dome C to be cloudless 74% of the time, with the remaining 26% having more than $\frac{1}{8}$ cloud cover. While this is a tentative conclusion based on less than a full year of data from Dome C, new independent measurements in 2005 (Aristidi et al. 2006) suggest that the percentage of cloud-free skies at Dome C may be as high as 96%. In comparison, Ortolani (2003 and references therein) report 45% photometric nights (no clouds) and 67% spectroscopic nights ($\frac{1}{4}$ – $\frac{1}{10}$ cloud cover) at Mauna Kea. These percentages are also displayed in Figure 1.

If the more optimistic figure of Aristidi et al. (2006) is confirmed, Dome C will be seen to have a similar number of usable, astronomically dark hours as compared to Mauna Kea.

2.2. Moonlight

The sky brightness contribution caused by the Moon depends on its position and phase. Moonlight illuminates the surface of the Earth both directly and by scattering, in a similar fashion to sunlight. Figure 2 shows the elevation of the Sun (contours) and Moon (gray scale), together with the phase of the Moon, for Dome C and Mauna Kea over the course of 1 year (2005). The darkest skies are when the Sun is far below the horizon and either the Moon is below the horizon (dark shading) or the phase of the Moon is close to new. The 18.6 yr lunar nodal cycle changes the declination range of the Moon; this ranges between $\pm 29^\circ$ and $\pm 18^\circ$. At Dome C, the Moon reaches a maximum elevation between $\sim 33^\circ$ and $\sim 43^\circ$, depending on this cycle; at Mauna Kea, the Moon can pass through the zenith, independent of nodal cycle.

To quantify the effect of the different range of Moon elevation at Dome C and Mauna Kea, we calculated the moonlight brightness using the model of Krisciunas & Schaefer (1991). The lunar phase (from full Moon to new Moon and back) cycles over 1 month; for each month in 2005, we calculated the sky brightness when (1) the full Moon was at the highest elevation for that month and (2) the Moon was at the highest altitude, regardless of phase. A cross section of the sky, cutting through the position of the Moon and the zenith at those times, is plotted in Figure 3. In the calculation, we set the extinction coefficient for both sites to the median value for Mauna Kea (0.12 mag per air mass at 550 nm).

The full-Moon contribution at Dome C is less than that at Mauna Kea by several magnitudes at zenith, with little difference at the horizon. For the second case, excluding the sky close to the Moon, the contribution is once again less at Dome C than at Mauna Kea. As at all sites, this contribution reaches a minimum between 60° and 90° away from the Moon (Patat 2004). This advantage to Dome C is reduced to some extent by the fact that the fullness of the Moon and its maximum elevation are highly correlated at Dome C (as seen in Fig. 2) but only weakly so at Mauna Kea. Skies that would otherwise be dark are brightened at zenith by moonlight by a median value of $1.7 V \text{ mag arcsec}^{-2}$ at Dome C and $2.1 V \text{ mag arcsec}^{-2}$ at Mauna Kea, averaged over the epoch 2005–2015.

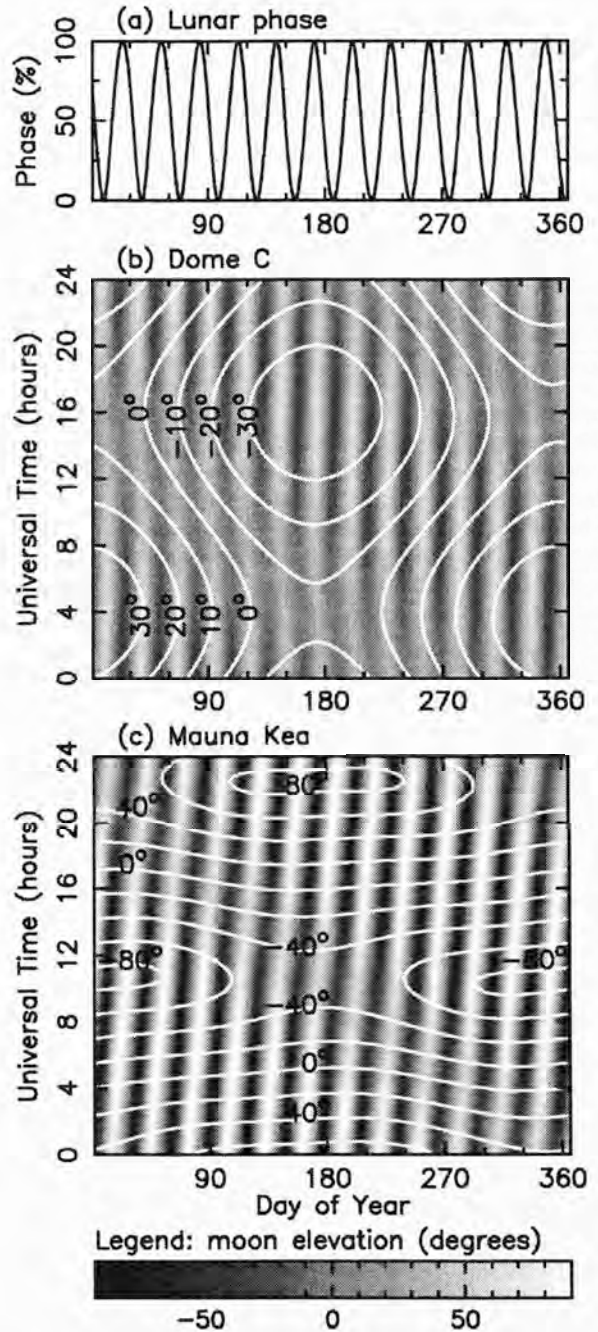


FIG. 2.—(a) Lunar phase and (b, c) solar and lunar elevation angles at Dome C and Mauna Kea over the course of 1 year (2005). In (b) and (c), the contours show the solar elevation angles, and the gray scale shows the lunar elevation angles according to the scale below.

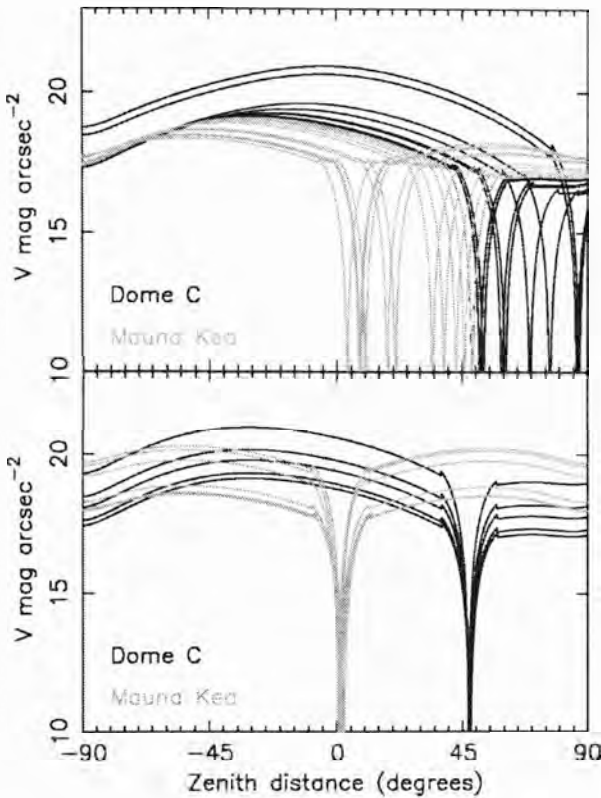


FIG. 3.—*Top*: Scattered moonlight brightness as a function of zenith angle when the full Moon reaches its highest altitude in each month (in 2005). *Bottom*: Scattered moonlight contribution for the highest altitude of the Moon in each month, regardless of phase. Each plot shows the moonlight contribution for a cross section of the sky that passes through the Moon and the zenith, for Dome C (black) and Mauna Kea (gray), and each curve represents a different month.

2.3. Aurorae

Aurorae are the spectacular lights seen dancing across the skies in (mainly) polar regions. As highly energetic particles from the Sun travel into the atmosphere, they collide with upper atmosphere atoms and molecules, exciting them to higher energy levels. The excited atoms and molecules then decay radiatively. Aurorae are generally (though not exclusively) confined to an annular region 15–25° from the geomagnetic poles (see Fig. 4) and have a strong dependence on the 11 yr solar sunspot cycle. The geomagnetic poles are the two positions where the Earth’s theoretical magnetic dipole intersects the Earth’s surface. The positions of the geomagnetic poles move around, and in 2005 January the geomagnetic south pole was at a geographic position of 79°3 south, 108°5 east.¹ The size and position of the auroral oval changes with solar activity;

see the OVATION Web site² for plots of the size and position of the auroral oval from 1983 December to the present. Aurorae typically occur 100–250 km above the ground but can occur at altitudes anywhere between 80 and 1000 km. In the V band, the strongest auroral emission is from neutral oxygen at 557.7 nm. Aurorae can vary rapidly in intensity and position across the sky.

Dome C lies about 10° away from the inner edge of the typical auroral oval, so little auroral activity is expected. In comparison, the South Pole is located very close to the inner edge of the auroral oval and experiences considerable auroral activity. The position of Dome C relative to the auroral oval means that most auroral activity will be close to the horizon, and also low in intensity. Figure 4 shows the geographic positions of Dome C, the South Pole (geographic), the typical auroral oval, and the geomagnetic south pole. Using simple geometry, we calculated the sky position at Dome C for aurorae occurring at altitudes of 100 and 250 km in the auroral oval as a function of angular separation between Dome C and the aurora. Aurorae at 100 km altitude will usually be below the horizon at Dome C; at 250 km altitude, this occurs at 16° separation. The dashed circle in Figure 4 shows this range. The results of the calculations are shown in Table 3. The first column gives the angular separation between the aurora and Dome C, *D* is the distance in kilometers from Dome C to the aurora, and *E* is the elevation angle of the aurora at Dome C. The elevation angle of typical aurorae seen from Dome C will be between the horizon and 7° elevation, and they will be between 1160 and 2000 km away. Sun-aligned quiet arcs will not decrease with increasing magnetic latitude in the same fashion as normal aurorae; however, they are significantly less intense than the aurorae occurring within the auroral oval (G. Burns 2005, private communication).

Dempsey et al. (2005) used satellite measurements of the electron flux above Dome C to calculate the expected intensity of aurorae. They found that in the V band the intensity of the auroral contribution to sky background was less than 22.7 mag arcsec⁻² for 50% of the wintertime during a solar maximum year, and below 23.5 mag arcsec⁻² during solar minimum.

Aurorae are therefore expected to have a minor impact on optical astronomy at Dome C, even without the use of narrowband filters to remove the brightest emission lines. The contribution to sky brightness at Mauna Kea by aurorae is of course negligible.

2.4. Zodiacal Light

Zodiacal light is caused by sunlight scattering from the diffuse cloud of interplanetary dust that lies largely in the plane of the solar system. Zodiacal light is strongest near the Sun

¹ Obtained from the National Geophysical Data Center Web page “Estimated Values of Magnetic Field Properties.” at <http://www.ngdc.noaa.gov/ngdc.html>.

² OVATION ([Auroral] Oval Variation, Assessment, Tracking, Intensity, and Online Nowcasting) is a project of the Auroral Particles and Imagery Group and the John Hopkins University; see <http://sd-www.jhuapl.edu/Aurora/index.html>.

494 KENYON & STOREY

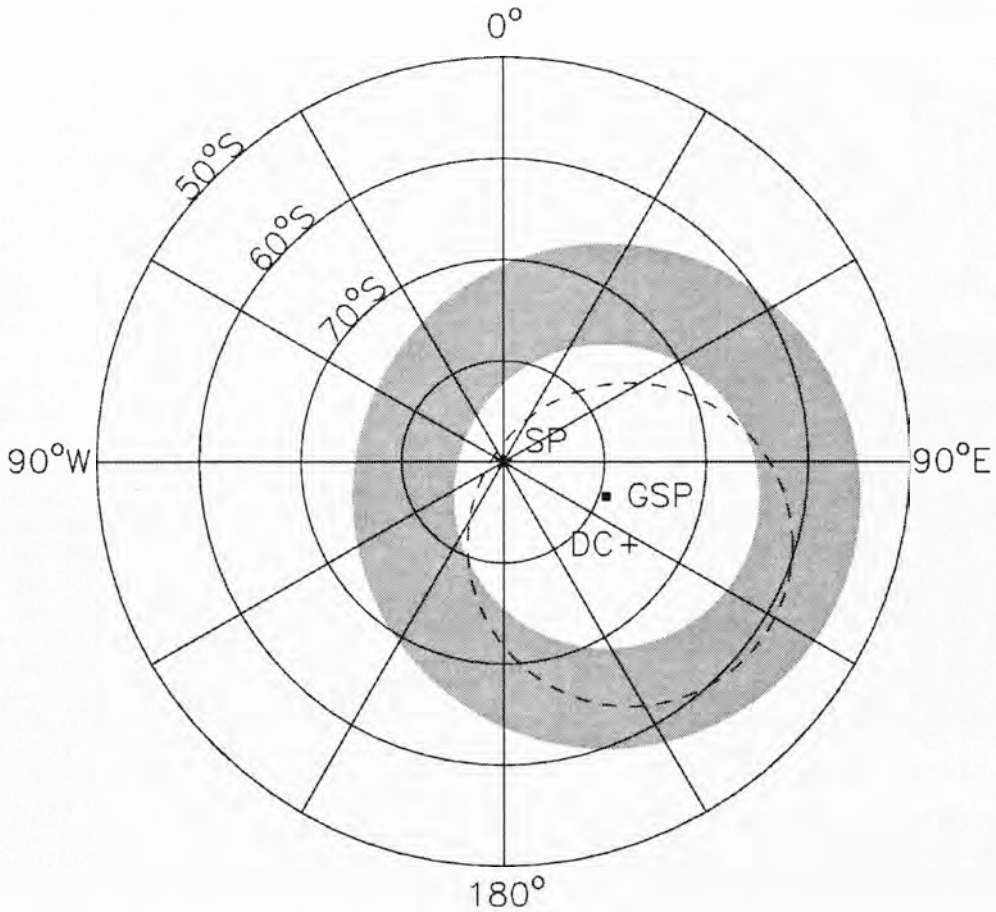


FIG. 4.—Schematic of the typical southern auroral oval, showing the geographic South Pole (SP), Dome C (DC), and the geomagnetic south pole (GSP). The auroral oval, shown in gray, is typically located 15°–25° from the GSP. Aurorae at 250 km altitude will be above the horizon at Dome C only if they lie within the dashed line.

TABLE 3
ALTITUDES OF AURORAE AT DOME C

ANGULAR SEPARATION (deg)	100 km		250 km	
	<i>D</i> (km)	<i>E</i> (deg)	<i>D</i> (km)	<i>E</i> (deg)
10	1125	0	1161	7
11	1236	-1	1271	6
12	1347	-2	1382	4
13	1459	-3	1493	3
14	1570	-3	1604	2
15	1681	-4	1716	1
16	1792	-5	1827	0
17	1903	-6	1938	-1

NOTE.—The first column is the angular separation between the aurora and Dome C. From this we derive the distance *D* from Dome C to the aurora and the elevation angle *E* of the aurora at Dome C.

and is generally seen as a cone of light with its base at the horizon, decreasing in intensity toward the zenith, with another maximum sometimes seen at the antisolar point. The intensity is dependent on wavelength, observer position, and sky position. Zodiacal light is polarized, reaching a maximum polarization of about 20% (Leinert et al. 1998).

The zodiacal contribution to sky brightness at Dome C and Mauna Kea was calculated over 1 year, using the method described by Leinert et al. (1998). All correction factors in the model were set to unity; thus, there is a possible variation in flux of up to 30%. Calculations were limited to astronomical nighttime. Two sky positions were looked at: the zenith and a zenith distance of 60° at the same azimuthal position as the Sun. The results are shown in Figure 5.

In the *V* band, the zenith brightness of zodiacal light at Dome C is always darker than 23.1 mag arcsec⁻² because the zodiac

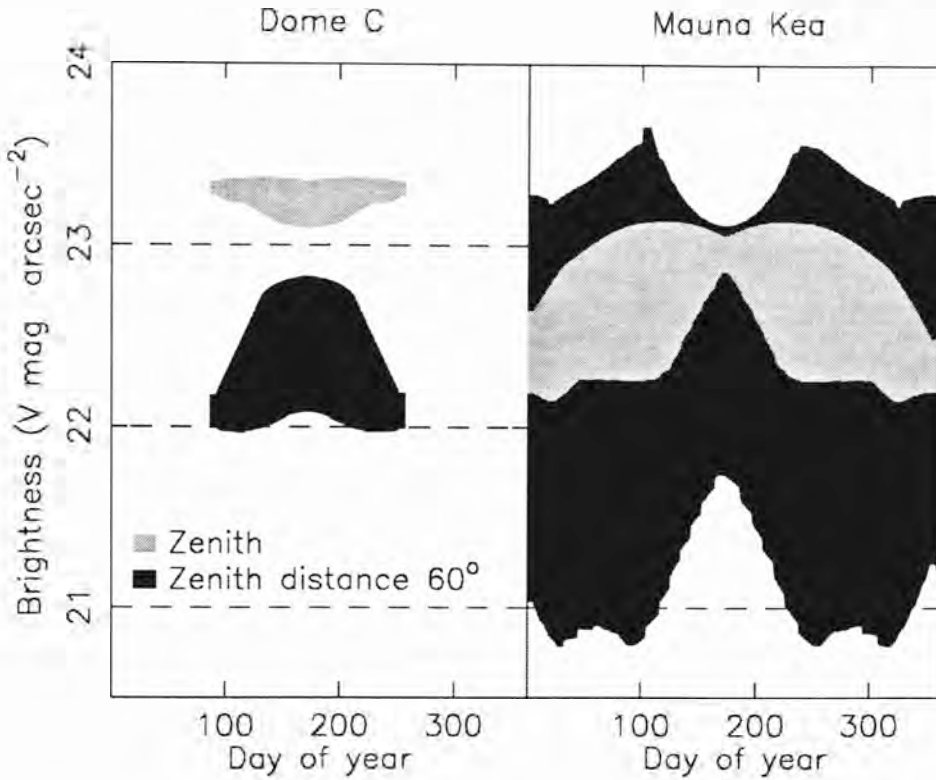


FIG. 5.—Range of zodiacal contribution to sky brightness (V mag arcsec $^{-2}$) at Dome C (left) and Mauna Kea (right), over 1 year, for Sun elevations less than -18° . The gray shading is for observations at zenith, and the black is for a zenith distance of 60° at the same azimuthal position as the Sun.

is always fairly low on the horizon. In contrast, at Mauna Kea the zodiacal sky brightness at zenith is always *brighter* than about 23.1 mag arcsec $^{-2}$, reaching a maximum contribution of about 22.1 mag arcsec $^{-2}$. At a zenith distance of 60° and in the azimuthal direction of the Sun, the zodiacal light at Dome C is always darker than about 22 mag arcsec $^{-2}$; at Mauna Kea, it can get as bright as about 20.8 mag arcsec $^{-2}$. This reduced contribution from zodiacal light is of course not a characteristic of the site per se, but rather a reflection of the fact that a different part of the sky passes overhead at Dome C than at Mauna Kea.

2.5. Airglow

Airglow, observed at night, is the chemiluminescence of upper atmosphere molecules and atoms. This so-called nightglow includes a quasi continuum from NO $_2$, and a number of discrete emission lines, the strongest by far being from the hydroxyl radical. A number of visible nightglow emission lines are listed in Table 4, along with the typical altitude of the emitting atmospheric layer and typical intensities.

Nightglow is unpolarized and on a large scale increases from

zenith to the horizon, as described by the van Rhijn function. On a small spatial scale, nightglow emissions are uneven and blotchy across the sky. Nightglow emissions vary over short and long timescales.

Nightglow emissions are mainly from the thin mesospheric layer, centered at an altitude of 85–90 km. OH Meinel bands are primarily excited by a reaction between ozone and atomic hydrogen (Le Texier et al. 1987). The concentrations of O $_3$ and H depend on the atomic oxygen mixing ratio (Le Texier et al. 1987), which is largely controlled by the transport processes in the mesosphere and lower thermosphere (Garcia & Solomon 1985). At low and middle latitudes, there is a semiannual variation in atomic hydrogen and hence OH nightglow (Le Texier et al. 1987).

Because of the efficient mechanisms that transport reactants from sunlit locations to the poles, there is no reason to expect a diminution in the chemiluminescence of species such as OH and O $_2$ during the long polar night. Phillips et al. (1999) observed a small reduction in OH emission at the South Pole in 1995 relative to temperate sites, but this is more likely explained by the known highly variable nature of OH emission. Continuous monitoring of the Meinel bands of OH in the *J*

496 KENYON & STOREY

TABLE 4
AIRGLOW EMISSIONS AT ZENITH IN THE VISIBLE RANGE

Wavelength (nm)	Source	Height (km)	Typical Intensity (R)	Comments
Nightglow from Chemical Association				
260–380	O ₂	90	0.5 Å ⁻¹	Herzberg bands
600–4500	OH	85	4.5 × 10 ⁶	Strongest bands in near-infrared
500–650	NO ₂	90	250	Nightglow continuum
557.7	O I	95	250	
589.0, 589.6	Na D	~92	50	Strong seasonal variation
761.9	O ₂	~80	1000	Atmospheric bands
864.5	O ₂	~80	1000	Atmospheric bands
Nightglow from Ionic Reactions				
519.8, 520.1	N I	1		
557.7	O I	250–300	20	High atmospheric, chiefly in tropics during enhancement of O I λλ630.0, 636.4
630.0	O I	250–300	100	Sporadic enhancements in tropics associated with ionospheric disturbances
636.4	O I	250–300	20	

NOTE.—IR = $1/(4\pi) \times 10^{10}$ photons m⁻² s⁻¹ sr⁻¹.

REFERENCES.—Roach & Gordon 1973; Leinert et al. 1998 and references therein.

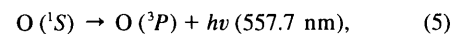
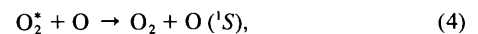
band with a Michelson interferometer has been carried out at the pole since 1992 January, and the data are now publicly available online.³ As expected, these data show very large hourly and nightly variations, with no diminution in average intensity as the winter progresses.

Zaragoza et al. (2001) measured the OH nightglow emissions in a narrow spectral band near 4.6 μm for just under 1 year. Using the Improved Stratospheric and Mesospheric Sounder on the *Upper Atmosphere Research Satellite (UARS)*, they have almost full global coverage (80° north to 80° south). They find at high latitudes a springtime minimum in the OH emission ~30% below the global mean, although this is only for 1 year of data. During the Northern Hemisphere winter solstice period, their averaged measured intensities of OH nightglow at high latitudes and midlatitudes are the same to within the errors.

Measurements of OH nightglow between 837.5 and 856.0 nm at Davis, Antarctica (68°35' south, 77°58' east), over 7 years (Burns et al. 2002) show a barely significant seasonal variation in emission intensity, although there are large day-to-day variations (G. Burns & J. French 2005, private communication). We therefore expect that the Dome C sky brightness in those bands (650 nm–2.2 μm) that are dominated by OH emission will be essentially identical to that at all other observatory sites, including Mauna Kea.

The strongest nightglow emission in the visible is the 557.7 nm line of O (¹S). As discussed in Shepherd et al. (1997),

the 557.7 nm emission is caused by the reactions



where *M* is usually N₂. O₂^{*} and O (¹S) have very short lifetimes; however, atomic oxygen above an altitude of 100 km has a long lifetime and can be transported globally before recombination.

Using a model of global tides in the thermosphere, ionosphere, and mesosphere, Yee et al. (1997) predict an *increase* of some 50% in the O (¹S) 557.7 nm emissions toward the poles, although more data are needed to confirm this model. Note, however, that this single strong line can be easily filtered from astronomical measurements. In general, we expect that there will be little difference in overall airglow emissions between Antarctic and temperate sites.

2.6. Integrated Starlight, Diffuse Galactic Light, and Integrated Cosmic Light

Telescopes can only identify as individual objects those stars that are brighter than a certain magnitude. The integrated flux from all stars fainter than this magnitude contributes to the sky background. The limiting magnitude of a telescope depends on the *seeing* of the site, the atmospheric extinction, and the size of the telescope. The expected excellent seeing and low atmo-

³ See the South Pole Michelson Interferometer Web page: <http://cedarweb.hao.ucar.edu>.

spheric extinction at Dome C will ensure that the limiting magnitude of even a small telescope will be sufficient to reduce the integrated unresolved starlight to negligible levels.

Diffuse Galactic light is a result of the scattering of starlight by interstellar dust and is brightest toward the center of the Milky Way, where the concentrations of stars and dust are highest. The typical zenith value of diffuse Galactic light in the *V* band is about 23.6 mag arcsec⁻² (Roach & Gordon 1973). At Dome C, the Galactic plane continuously circles close to the zenith, leading to a relatively high contribution from integrated starlight and diffuse Galactic light, compared to other sites. At Dome C, the Galactic latitude of the zenith ranges between -10° and -40° , whereas at Mauna Kea the range is much larger, -40° to $+85^\circ$, with the Galactic plane being close to the horizon for some of the time.

The integrated cosmic light contribution (redshifted starlight from unresolved galaxies) is very small at all sites, compared to all other sources of sky brightness. No firm measurement exists for its value; however, upper and lower limits have been measured and estimated from models, giving a range of about 25 to 30 mag arcsec⁻² at 550 nm (Leinert et al. 1998 and references therein).

Dome C will receive a comparatively higher contribution of light from the Galactic plane than lower latitude sites. However, this contribution is small when compared to other sources of sky brightness and, as with zodiacal light, depends on the sky position being observed.

2.7. Light Pollution

Light pollution from towns and cities can cause a considerable increase in the brightness of the night sky. Light pollution is mostly caused by light from vapor lamps (Hg-Na emission lines in the blue-visible spectrum) and incandescent lamps (weak continuum) (Benn & Ellison 1998 and references therein). Garstang (1989a) modeled the increase of the zenith sky brightness caused by light pollution at various sites. Garstang (1989b) further predicts the increase in light pollution at various sites over time. For example, Garstang (1989b) predicts that artificial sky brightness will increase the total sky brightness by between 0.04 and 0.53 mag arcsec⁻² at Mauna Kea by the year 2020. This estimate is based on projections of population increase and does not take into account changes in light sources and systems or unforeseen circumstances, such as major tourist or housing developments nearby the sites, as noted in the paper. Light pollution can significantly increase the brightness of the night sky. For further discussions of night-sky brightness modeling and world maps of the artificial sky brightness, see Cinzano & Elvidge (2001, 2004) and references within.

The closest station to Dome C (Vostok, at $78^\circ 27' 51''$ south, $106^\circ 51' 57''$ east) is 560 km away. The placement of external lighting at the Dome C station itself will be carefully considered

in relation to astronomical observations. With proper planning, there should continue to be no artificial-light pollution at Dome C, while the light pollution at other sites is likely to increase.

3. ATMOSPHERIC EXTINCTION

Atmospheric extinction is caused by the scattering and absorption of light as it travels through the atmosphere. Extinction in the atmosphere decreases the amount of light received by an observer and lowers the limiting magnitude of a telescope.

As radiation travels from the top of the atmosphere to the surface of the Earth, it may be transmitted directly to the surface, with no attenuation or scattering. Alternatively, it may undergo one or more of the following processes: single or multiple scattering, reflection from the Earth's surface, or absorption by an atmospheric particle or molecule. Scattering is described by Rayleigh scattering ($2\pi r \ll \lambda$) from gaseous molecules, Mie scattering ($2\pi r \sim \lambda$) from aerosol particles (where r is the radius of the particle and λ is the wavelength of the light interacting with the particle), and a small amount of scattering due to turbulent cells. Radiation is absorbed in the atmosphere by molecules (especially water vapor and ozone), aerosol particles, and liquid or frozen water in clouds (Coulson 1988). All these processes of scattering and absorption are strong functions of altitude and wavelength, and their effect, with the exception of Rayleigh scattering, is highly variable with location and time.

Scattering has two effects on astronomical observations: it increases the overall sky brightness and decreases the flux received from the object being observed. Atmospheric absorption will also decrease the signal flux. Beer's law describes the attenuation of light caused by the atmosphere:

$$I_\lambda = I_0 \exp(-\tau_\lambda^R - \tau_\lambda^A - \tau_\lambda^W - \tau_\lambda^O - \tau_\lambda^C), \quad (6)$$

where I_λ is the flux received by the observer, I_0 is the flux outside the atmosphere, and τ is the wavelength-dependent optical thickness of the atmosphere; a sum of the Rayleigh *R*, aerosol *A*, water vapor *W*, ozone *O*, and cloud *C* optical thicknesses.

3.1. Rayleigh Optical Depth

Rayleigh optical depth is dependent on the molecular composition of the atmosphere and is proportional to λ^{-4} . The molecular composition varies with the pressure, temperature, and refractive index of the atmosphere above the Earth's surface. Rayleigh optical depth is essentially constant between sites of similar elevation (see Bodhaine et al. [1999] and Tomasi et al. [2005] for further details on Rayleigh optical depth calculations).

3.2. Aerosol Optical Depth

Aerosol optical depth is extremely variable with geography and time and is dependent on the concentration, size, refractive

498 KENYON & STOREY

index, and chemical composition of the aerosol particles. The complex refractive index of a particle is $m = n - ik$, where n is the real part (1.45–1.60) and k the imaginary part (0.001–0.1); the bracketed ranges are typical values for most “dry” atmospheric aerosols (Coulson 1988). High humidity in the air can cause condensation to occur on aerosol particles, which changes the index of refraction, size, and mean density of the particle. The vertical profile of the aerosol content of the atmosphere can be derived from intensity measurements during twilight as different levels of the atmosphere are illuminated by sunlight. For the best sites, the aerosol optical depth needs to be as small as possible.

No aerosol measurements have been taken yet at Dome C; however, aerosol measurements at the South Pole and Mauna Loa, Hawaii, have been taken since 1974 (Bodhaine 1995 and references therein). The wavelength-dependent aerosol scattering coefficient is defined as $\beta_s = N_s \sigma_s$, where N_s is the number concentration of aerosol particles and σ_s is the scattering cross section. At the South Pole, β_s (550 nm) is very low, varying between 1×10^{-7} and $4 \times 10^{-7} \text{ m}^{-1}$. The maximum values are seen in winter and are associated with long-range mid-tropospheric transport of sea salt from the coast. Scattering from polar stratospheric clouds may also contribute to the maximum seen in winter (Collins et al. 1993). In comparison, at Mauna Loa, β_s (550 nm) varies between 6×10^{-7} and $60 \times 10^{-7} \text{ m}^{-1}$, showing maximum values during winter and spring that are associated with dust transport.

3.3. Absorption Optical Depths

The absorption of visible and infrared radiation in the atmosphere is dependent on pressure, temperature, and concentrations of the absorbing gas (largely water vapor and ozone) and aerosol, all of which vary with location, height, and time (Zuev 1974). Atmospheric absorption is described by the imaginary part k of the refractive index of the atmospheric particles such that the absorption coefficient (m^{-1}) is

$$\beta_a = \frac{4\pi k}{\lambda} = \sigma_a N_a, \quad (7)$$

where σ_a is the absorption cross section (m^2) and N_a is the concentration of absorbers (m^{-3}). At most wavelengths, water vapor is the primary absorber in the atmosphere, and its concentration is highly variable. The optical thicknesses for water vapor and clouds show complicated and highly variable changes in magnitude with wavelength and time. The aerosol absorption coefficient for light at 550 nm at the South Pole varies between 2×10^{-10} and $5 \times 10^{-7} \text{ m}^{-1}$, comparatively lower than at Mauna Loa (from 1×10^{-8} to $3 \times 10^{-7} \text{ m}^{-1}$; Bodhaine 1995 and references therein).

To minimize the total optical depth, a site with low water vapor concentration, few clouds, and low aerosol concentration is required. Dome C fits all these criteria and may have an

even lower atmospheric aerosol content than the South Pole, because of its greater distance from the coast. We therefore expect both the scattering and absorption by aerosols to be typically an order of magnitude less at Dome C than at Mauna Kea, and that the overall atmospheric extinction will be the lowest possible.

At ultraviolet wavelengths, the reduced atmospheric aerosol content should lead to improved transmission. However, the infamous “ozone hole” is unlikely to be of significant benefit to astronomers. From January until August, the column density of ozone in the atmosphere above the South Pole is typically the same as at other sites around the world. It is only during the spring months that the ozone content falls to as low as 40% of its normal value. Unfortunately, these low ozone values do not occur in the dark winter months. Furthermore, because the Hartley bands of ozone are heavily saturated, even a reduction in ozone column density by a factor of 3 (i.e., somewhat greater than is actually observed over the South Pole) would shift the UV cutoff wavelength of the atmosphere by only about 5 nm.

4. USING A POLARIZER DURING TWILIGHT

Dome C experiences long periods of twilight, where the solar depression angle is between 0° and -18° . Baldry & Bland-Hawthorn (2001) have suggested using a polarizing filter to reduce the scattered sunlight contribution to sky brightness during twilight in order to achieve “dark time” observing. At sites close to the equator, this probably would not be worthwhile, because twilight only lasts a few hours. However, the use of a filter during twilight in Antarctica could be very beneficial, as noted in that paper. For example, if dark-time conditions at Dome C could be achieved at a solar depression angle of 15° , the available “dark” observing time would increase by 18%.

In § 4.1 we discuss the intensity and polarization of twilight, and in § 4.2 we review the filter proposal by Baldry & Bland-Hawthorn (2001). In § 4.3 we look at measurements of the polarization of *daylight* at the South Pole. In § 4.4 we look in some detail at measurements of the total polarization of *twilight* in the atmosphere as a function of solar zenith angle Z_\odot and wavelength λ and explore the benefit that might be gained by using a polarizer on an Antarctic telescope.

4.1. Intensity and Polarization of Twilight

During twilight, the total background light I_B reaching the surface consists of singly scattered sunlight I_S , multiply scattered sunlight I_M , and the night-sky illuminance I_N :

$$I_B = I_S + I_M + I_N. \quad (8)$$

The night-sky illuminance includes all the sources of sky brightness discussed in § 2, except for moonlight and sunlight. Sunlight becomes polarized in the atmosphere through scattering interactions with permanent atmospheric gases, variable

gases, and solid and liquid particles suspended in the atmosphere. The total degree of polarization of twilight is given by

$$P = \frac{I_S}{I_B} P_S + \frac{I_M}{I_B} P_M, \quad (9)$$

where P_S and P_M are the degrees of polarization of singly and multiply scattered light, respectively. The polarized component of the background night-sky flux is assumed to be negligible with respect to that of the scattered sunlight.

Singly scattered sunlight is a combination of sunlight scattered from molecules and aerosols. The polarization of sunlight that is singly scattered from molecules can be modeled (see Coulson 1988). In such a model, the atmosphere is considered to contain only permanent gases, with no aerosols, clouds, water vapor, or ionized particles, and it is assumed that the scattering particles are spherical and that the refractive index is very close to unity.

Figure 6 shows the results of a calculation using this model for $Z_\odot = 90^\circ, 96^\circ, 102^\circ,$ and 108° (i.e., from sunset to the end of astronomical twilight). The light shading shows that a large section of the singly scattered sunlight perpendicular to the Sun is polarized to a high degree, whereas in the direction parallel to the Sun, the polarization rapidly drops off with zenith angle. The bottom panel of the figure shows the polarization at zenith as a function of increasing solar zenith angle for $P_S^{\max} = 85\%$ and 100% . This indicates that singly scattered light (in an ideal atmosphere) is highly polarized over a substantial fraction of the sky during twilight.

The degree of polarization (although not the pattern) in the real atmosphere differs from this model because of nonisotropic molecular scattering, aerosol scattering, and reflection from the Earth's surface.

Multiply scattered sunlight is polarized to a lesser degree than singly scattered light. Multiple scattering is confined to a thin atmospheric layer that is much closer to the Earth's surface than the single-scattering layer (Ougolnikov 1999). The polarization of sunlight can be further reduced by reflection from high-level clouds and cloud-forming particles (e.g., Pomozi et al. 2001).

The highest polarization of light occurs when water vapor and aerosol concentrations are very low and the Rayleigh optical depth is as small as possible, suggesting that scattered sunlight at Dome C should in general be more highly polarized than at temperate or tropical sites.

4.2. Potential Improvements with a Polarizer

Use of an appropriately oriented polarizer will reduce the sky background to

$$I'_B = \tau I_B [1 - P(1 + 2\gamma)], \quad (10)$$

where τ is the transmission of the polarizer with unpolarized

light and γ is the extinction of the polarizer (Baldry & Bland-Hawthorn 2001).

Assuming photon-noise-limited observations, a perfect polarizer, and no change in instrument response with polarization, a polarizer will be beneficial whenever

$$P \gtrsim (1 - \tau) \frac{I_O + I_B}{I_B}, \quad (11)$$

where I_O is the magnitude of the object. Objects that are very dark compared to the sky background require $P > 52\%$ for $\tau = 0.48$; for a sky background of $20.5 \text{ mag arcsec}^{-2}$ and object of $22 \text{ mag arcsec}^{-2}$, the polarization must be greater than 65% for a polarizer to be beneficial.

Baldry & Bland-Hawthorn (2001) assume the polarization of twilight is always 85% , independent of solar elevation angle. Although the polarization of singly scattered light is probably always above 85% (for a clear atmosphere), the total polarization depends on the relative intensity of the singly and multiply scattered light with respect to the total sky intensity, as in equation (9).

4.3. Polarization at the South Pole and Effects of Ice Precipitation

Currently, no measurements of the polarization of twilight at Dome C have been taken. However, Fitch & Coulson (1983) measured the polarization of the sky at the South Pole during summer, under clear sky conditions, and when ice crystals were evident. They found the degree of polarization to be very high under clear sky conditions, and close to the results given by a Rayleigh model. The presence of ice crystals reduced the degree of polarization and had a greater effect at longer wavelengths. We expect that the atmosphere at Dome C will also closely resemble a Rayleigh atmosphere, and therefore at small solar depression angles the scattered light will be highly polarized.

4.4. Spectral Characteristics of Polarization as a Function of Solar Depression Angle

Over the course of twilight, the polarization and intensity of skylight changes as different levels of the atmosphere are illuminated. In this section, we look at measurements of twilight polarization and intensity at various high-altitude, clean sites. The behavior of the total degree of polarization P as a function of solar zenith angle Z_\odot can be roughly divided into three regimes; we assess the benefit of using a polarizer in each regime. The polarization P also behaves somewhat differently for red and blue wavelengths, with a division around $\lambda = 550 \text{ nm}$. Note that $P(Z_\odot)$ usually shows day-to-day variations at each site, and there is some overlap in the three ranges of solar zenith angle. This is probably caused by different weather conditions and vertical aerosol concentrations.

The typical behavior of P as a function of Z_\odot and λ is

500 KENYON & STOREY

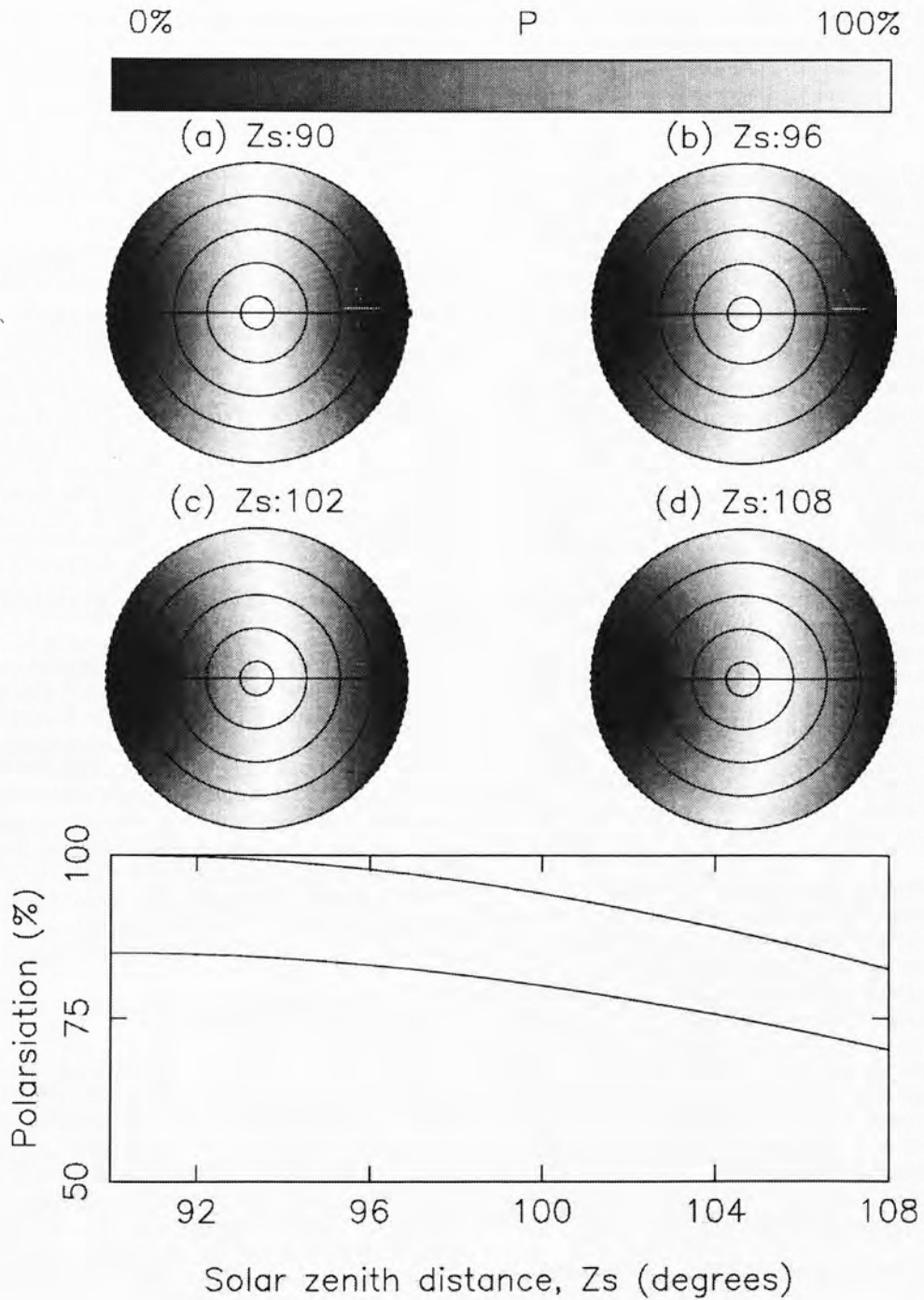


FIG. 6.—*Top*: Full-sky plots of the degree of polarization using the Rayleigh model for Sun zenith angles of (a) 90° , (b) 96° , (c) 102° , and (d) 108° (i.e., from sunset to the end of astronomical twilight). The circles indicate elevation angle and are spaced 20° apart. *Bottom*: Polarization at zenith as a function of solar zenith angle for a Rayleigh atmosphere with assumed maximum polarization of 100% and 85%.

TABLE 5
TYPICAL BEHAVIOR OF THE DEGREE OF POLARIZATION WITH SOLAR ZENITH ANGLE AND WAVELENGTH

Parameter	$Z_{\odot} = 90^{\circ}-96^{\circ}$	$Z_{\odot} = 96^{\circ}-102^{\circ}$	$Z_{\odot} = 102^{\circ}-108^{\circ}$
P (blue λ)	Maximum: $Z_{\odot} = 92^{\circ}-94^{\circ}$; decreases with increasing Z_{\odot} ; λ dependent	Steep decrease with increasing Z_{\odot} , then a flat or a minimum section between 98° and 102°	Steep decrease with increasing Z_{\odot} , then starts to fatten at $Z_{\odot} \sim 104^{\circ}$
P (red λ)	Maximum: $Z_{\odot} = 90^{\circ}$; decreases with increasing Z_{\odot} ; λ independent	Steady decrease; occasional second maximum associated with aerosols	Steep decrease
Processes	I_s dominates over I_M ; I_N negligible	I_M dominates over I_s ; I_N negligible for $Z_{\odot} < 98^{\circ}$; $P < 60\%$ for both ranges	I_s dominates over I_M for $Z_{\odot} > 104^{\circ}$; I_N dominates over I_s and I_M ; P strongly λ dependent; aerosol scattering important; $P < 50\%$ for both ranges
Polarizer advantage	$Z \sim 90^{\circ}$, $I_o > 5.3$; $Z \sim 92^{\circ}$, $I_o > 5.7$; $Z \sim 94^{\circ}$, $I_o > 7.2$; $Z \sim 96^{\circ}$, $I_o > 9.9^a$	$Z \sim 98^{\circ}$, $I_o > 14.3$; $Z \sim 100^{\circ}$, $I_o > 18.3$	No advantage in using a polarizer

^a Maximum object brightness (mag arcsec⁻²) for which a polarizer will yield an advantage at 690 nm, based on the results of Pavlov et al. (1995). REFERENCES.—Bondarenko 1964; Coulson 1980, 1988; Pavlov et al. 1995.

summarized in Table 5, which is derived from the work of Bondarenko (1964), Coulson (1980), Pavlov et al. (1995), Ougolnikov & Maslov (2003), and Postlyakov et al. (2003). Figure 7, from Pavlov et al. (1995), shows the typical variations of single, multiple, and total polarization as a function of solar zenith angle during twilight.

The $Z_{\odot} = 102^{\circ}-108^{\circ}$ regime is where one might have hoped to turn twilight into dark time. However, as shown in Table 5, measurements at other sites show the polarization in this range to be less than about 50%, and hence, as discussed in § 4.2, the

use of a polarizer would not be beneficial. The total polarization at Dome C at these solar zenith angles is likely to be similar to the sites discussed, because all measurements were taken at clean, high-altitude sites (therefore with small Rayleigh optical depths) on visibly clear days. We therefore conclude that there is likely to be no gain in using a polarizer in this regime.

For observations of bright stars (for example, direct imaging of exoplanets around host stars with typical magnitudes of $V = 11$), a high sky background can be tolerated. Using a polarizer for this type of observation could be advantageous during those times when the Sun is up to 6° below the horizon.

5. CONCLUSIONS

Dome C has a similar number of cloud-free, astronomically dark hours compared to a more temperate site, such as Mauna Kea. Nevertheless, the fraction of observable sky at Dome C is considerably lower than at Mauna Kea. Atmospheric scattering at Dome C should be close to the lowest anywhere on Earth, reducing the sky brightness contributions from sunlight, moonlight, and tropospheric scattering, and reducing the extinction throughout the optical. The moonlight contribution to sky brightness over the year is less than at lower latitude sites. Aurorae will rarely be more than 7° above the horizon and will typically be more than about 1160 km away; they will generally be unobservable. Zodiacal light is darker at both zenith and 60° from zenith than at equatorial sites and will always be darker in V than 23.1 mag arcsec⁻² at zenith. Airglow is essentially the same at all sites. The integrated starlight and diffuse Galactic light will be slightly brighter at Dome C than at other sites, because the Galactic plane is always close to zenith. There is no artificial-light pollution at Dome C, a condition that should continue indefinitely.

In early evening twilight and late morning twilight, some advantage could be gained through the use of polarizing filters. However, as the sky becomes darker, such filters are of less benefit.

Dome C thus appears to be an attractive site for optical as

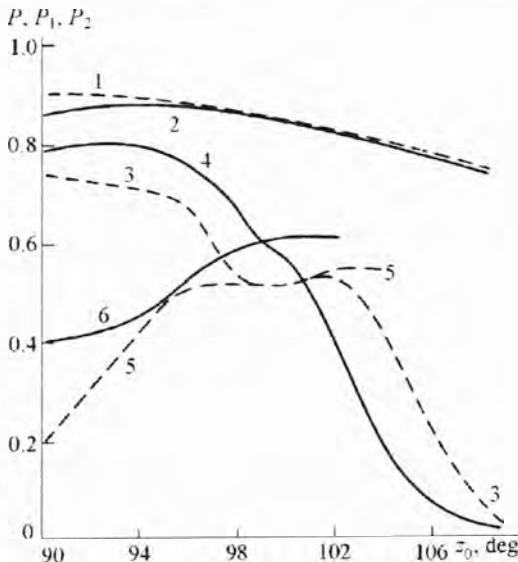


FIG. 7.—Polarization as a function of solar zenith angle. Curves 1 and 2 are calculated for singly scattered light (P_s) in a clear atmosphere, curves 3 and 4 are averaged measurements of the total polarization (P), and curves 5 and 6 are the calculated polarization for multiply scattered light (P_M). The dashed lines are for polarization at 480 nm, and the solid lines are for 690 nm. (Reproduced from Pavlov et al. 1995, courtesy of the American Geophysical Union.)

502 KENYON & STOREY

well as infrared astronomy. Versatile facilities such as the proposed 2 m telescope PILOT (Pathfinder for an International Large Optical Telescope; Burton et al. 2005) should therefore be able to achieve their scientific potential at Dome C across the full observable spectrum.

This research is supported by the Australian Research Council. S. L. K. is supported by an Australian Postgraduate Award

and by an Australian Antarctic Division top-up scholarship. The authors would like to thank Anna Moore for helpful discussions, and Eric Aristidi for permission to quote the results of the University of Nice group prior to publication. We would especially like to thank Gary Burns for very helpful comments on an earlier draft, and the referee, Ferdinando Patat, for his useful suggestions, which have significantly improved the paper.

REFERENCES

- Agabi, A., et al. 2006, *PASP*, 118, 344
 Anderson, D. E., & Lloyd, S. A. 1990, *J. Geophys. Res.*, 95, 7429
 Aristidi, E., et al. 2005a, *A&A*, 430, 739
 ———. 2005b, *A&A*, 444, 651
 ———. 2006, *Acta Astron. Sinica Suppl.*, in press
 Ashley, M. C. B., Burton, M. G., Calisse, P. G., Phillips, A., & Storey, J. W. V. 2005, *Highlights Astron.*, 13, 936
 Baldry, I. K., & Bland-Hawthorn, J. 2001, *MNRAS*, 322, 201
 Benn, C. R., & Ellison, S. L. 1998, *La Palma Night-Sky Brightness*, La Palma Tech. Note 115 (La Palma: Issac Newton Group)
 Bodhaine, B. A. 1995, *J. Geophys. Res.*, 100, 8967
 Bodhaine, B. A., Wood, N. B., Dutton, E. G., & Slusser J. R. 1999, *J. Atmos. Ocean. Tech.*, 16, 1854
 Bondarenko, L. N. 1964, *Soviet Astron.*, 8, 299
 Burns, G. B., French, W. J. R., Greet, P. A., Phillips, F. A., Williams, P. F. B., Finlayson, K., & Klich, G. 2002, *J. Atmos. Sol.-Terr. Phys.*, 64, 1167
 Burton, M. G., et al. 2005, *PASA*, 22, 199
 Calisse, P. G., Ashley, M. C. B., Burton, M. G., Phillips, M. A., Storey, J. W. V., Radford, S. J. E., & Peterson, J. B. 2004, *PASA*, 21, 256
 Candidi, M., & Lori, A. 2003, *Mem. Soc. Astron. Italiana*, 74, 29
 Cinzano, P., & Elvidge, C. D. 2001, *MNRAS*, 328, 689
 ———. 2004, *MNRAS*, 353, 1107
 Collins, R. L., Bowman, K. P., & Gardner, C. S. 1993, *J. Geophys. Res.*, 98, 1001
 Coulson, K. L. 1980, *Appl. Opt.*, 19, 3469
 ———. 1988, *Polarization and Intensity of Light in the Atmosphere* (Hampton, VA: A. Deepak)
 Deeg, H. J., Belmonte, J. A., Alonso, R., Horne, K., Alsubai, K., & Doyle, L. R. 2005, in *EAS Publ. Ser. 14, Dome C Astronomy and Astrophysics Meeting*, ed. M. Giard, F. Casoli, & F. Paletou (Les Ulis: EDP Sci.), 303
 Dempsey, J. T., Storey, J. W. V., & Phillips, A. 2005, *Proc. Astron. Soc. Australia*, 22, 91
 Fitch, B. W., & Coulson, K. L. 1983, *Appl. Opt.*, 22, 71
 Garcia, R. R., & Soloman, S. 1985, *J. Geophys. Res.*, 90, 3850
 Garstang, R. H. 1989a, *PASP*, 101, 306
 ———. 1989b, *ARA&A*, 27, 19
 Krisciunas, K., & Schaefer, B. E. 1991, *PASP*, 103, 1033
 Lawrence, J. S. 2004, *PASP*, 116, 482
 Lawrence, J. S., Ashley, M. C. B., Tokovinin, A., & Travouillon, T. 2004, *Nature*, 431, 278
 Leinert, C., et al. 1998, *A&AS*, 127, 1
 Le Texier, H., Soloman, S., & Garcia, R. R. 1987, *Planet. Space Sci.*, 35, 977
 Ortolani, S., ed. 2003, *ESPAS Site Summary Ser. 1.2, Mauna Kea* (Garching: ESO), 2
 Ugolnikov, O. S. 1999, *Cosmic Res.*, 37, 168
 Ugolnikov, O., & Maslov, I. 2003, *Proc. SPIE*, 5026, 219
 Patat, F. 2003, *A&A*, 400, 1183
 ———. 2004, *Messenger*, No. 118, 11
 Pavlov, V. E., Egorova, L. A., Kardopolo, V. I., Rspav, F. K., & Ukhinov, S. A. 1995, *Izvestiya, Atmospheric and Oceanic Physics*, 30, 449
 Phillips, A., Burton, M. G., Ashley, M. C. B., Storey, J. W. V., Lloyd, J. P., Harper, D. A., & Bally, J. 1999, *ApJ*, 527, 1009
 Pomozi, I., Horvath, G., & Wehner, R. 2001, *J. Exp. Bio.*, 204, 2933
 Postlyakov, O. V., Ugolnikov, O. S., Maslov, I. A., & Sidorchuk, A. A. 2003, in *Proc. EGS-AGU-EUG Joint Assembly*, abstract 13842
 Rayleigh, L. 1928, *Proc. R. Soc. London A*, 119, 11
 Roach, F. E., & Gordon, J. L. 1973, *The Light of the Night Sky* (Dordrecht: Reidel)
 Rozenberg, G. V. 1966, *Twilight: A Study in Atmospheric Optics* (New York: Plenum)
 Shepherd, G. G., Roble, R. G., McLandress, C., & Ward, W. E. 1997, *J. Atmos. Sol-Terr. Phys.*, 59, 655
 Storey, J. W. V., Ashley, M. C. B., Burton, M. G., & Lawrence, J. S. 2005, in *EAS Publ. Ser. 14, Dome C Astronomy and Astrophysics Meeting*, ed. M. Giard, F. Casoli, & F. Paletou (Les Ulis: EDP Sci.), 7
 Storey, J. W. V., Ashley, M. C. B., Lawrence, J. S., & Burton, M. G. 2003, *Mem. Soc. Astron. Italiana Suppl.*, 2, 13
 Tomasi, C., Vitale, V., Petkov, B., Lupi, A., & Cacciari, A. 2005, *Appl. Opt.*, 44, 3320
 Ugolnikov, O. S., Postlyakov, O. V., & Maslov, I. A. 2004, *Mem. Soc. Astron. Italiana*, 88, 233
 Valenziano, L., & dall'Oglio, G. 1999, *Proc. Astron. Soc. Australia*, 16, 167
 Walden, V. P., Town, M. S., Halter, B., & Storey, J. W. V. 2005, *PASP*, 117, 300
 Walker, M. F. 1988, *PASP*, 100, 496
 Yee, J.-H., Crowley, G., Roble, R. G., Skinner, W. R., Burrage, M. D., & Hays, P. B. 1997, *J. Geophys. Res.*, 102, 19949
 Zaragoza, G., Taylor, F. W., & López-Puertas, M. 2001, *J. Geophys. Res.*, 106, 8027
 Zuev, V. E. 1974, *Propagation of Visible and Infrared Radiation in the Atmosphere* (transl. ed.; Jerusalem: Keter Press)

C-2 Atmospheric scintillation at Dome C, Antarctica

PUBLICATIONS OF THE ASTRONOMICAL SOCIETY OF THE PACIFIC, 118: 924–932, 2006 June
 © 2006. The Astronomical Society of the Pacific. All rights reserved. Printed in U.S.A.

Atmospheric Scintillation at Dome C, Antarctica: Implications for Photometry and Astrometry

S. L. KENYON, J. S. LAWRENCE, M. C. B. ASHLEY, AND J. W. V. STOREY

School of Physics, University of New South Wales, Sydney, NSW 2052, Australia; suzanne@phys.unsw.edu.au

A. TOKOVININ

Cerro Tololo Inter-American Observatory, Casilla 603, La Serena, Chile

AND

E. FOSSAT

Laboratoire Universitaire d'Astrophysique de Nice, Université de Nice, France

Received 2006 April 5; accepted 2006 April 26; published 2006 June 21

ABSTRACT. We present low-resolution turbulence profiles of the atmosphere above Dome C, Antarctica, measured with the MASS instrument during 25 nights in 2004 March–May. Except for the lowest layer, Dome C has significantly less turbulence than Cerro Tololo and Cerro Pachón. In particular, the integrated turbulence at 16 km is *always less* than the median values at the two Chilean sites. From these profiles we evaluate the photometric noise produced by scintillation, and the atmospheric contribution to the error budget in narrow-angle differential astrometry. In comparison with the two midlatitude sites in Chile, Dome C offers a potential gain of about 3.6 in both photometric precision (for long integrations) and narrow-angle astrometry precision. These gain estimates are preliminary, being computed with average wind-speed profiles, but the validity of our approach is confirmed by independent data. Although the data from Dome C cover a fairly limited time frame, they lend strong support to expectations that Dome C will offer significant advantages for photometric and astrometric studies.

1. INTRODUCTION

The potential of the Antarctic plateau for astronomy has been recognized for many years. In the early 1990s Gillingham (1991, 1993) suggested that the atmospheric turbulence above a thin boundary layer would generally be very weak. This was confirmed by the first measurements at the South Pole by Marks et al. (1999). These showed that most turbulence is found close to the surface, in this case confined to a 200 m thick layer, with very weak turbulence at high altitudes. In comparison, at most temperate sites the turbulence is strong in the tropopause and above, caused by the interactions of the jet stream with temperature gradients in the tropopause. A brief history of astrophysics in Antarctica is presented by Indermuehle et al. (2005).

Dome C, Antarctica is potentially one of the best astronomical sites in the world. As a local maximum in elevation on the plateau, Dome C enjoys very low surface wind speeds, on average 2.9 m s^{-1} (Aristidi et al. 2005).

The atmospheric turbulence at Dome C has now been studied with four different techniques: acoustic radar, MASS (a scintillation profiling technique; see below), DIMM, and microthermal sensors. An acoustic radar, or SODAR, emits sound

pulses into the air and derives the strength of the atmospheric turbulence as a function of height from the intensity and delay time of the reflected sound. A DIMM, or differential image motion monitor, observes the relative motion of two images of the same star viewed through two subapertures of a small telescope. From this, the DIMM can derive the integrated atmospheric seeing. Microthermal sensors, carried aloft on a weather balloon, make an in situ measurement of the temperature fluctuations of the air as a function of height all the way to the top of the atmosphere.

SODAR measurements in the early months of 2003 by Travouillon (2005) showed that, as expected, the surface turbulent layer at Dome C was much thinner than at the South Pole. Combined MASS and SODAR measurements of the turbulence in winter 2004 gave an average seeing of $0''.27$ above 30 m, with the seeing below $0''.15$ for 25% of the time (Lawrence et al. 2004b). DIMM measurements in winter 2005 (Agabi et al. 2006) confirmed these results, showing an average seeing of $0''.25$ above the ground layer (Agabi et al. 2006, Fig. 1e), and balloon microthermal measurements by the same authors imply a median seeing of $0''.36 \pm 0''.19$ at a height of 30 m. They also showed the existence of an intense turbulent boundary layer, finding a median seeing of $1''.9$ from ground level, with 87%

of the total atmospheric turbulence confined to the first 36 m of atmosphere.

As expected, at Dome C the sky background in the infrared (Walden et al. 2005) is lower than at temperate sites because of the extremely cold temperatures and lower precipitable water vapor. For the same reason, the atmospheric transmission in the submillimeter is higher than at temperate sites (Calisse et al. 2004). An assessment of the optical sky brightness has been recently published by Kenyon & Storey (2006).

To date, the winter time scintillation at Dome C has only been estimated from atmospheric models (e.g., Swain et al. 2003). Scintillation is an important factor in measurements requiring high-precision photometry (e.g., extrasolar planet detection) and astrometry, and of objects with very fast intensity changes (e.g., asteroseismology; Heasley et al. 1996; Fossat 2005).

Here we evaluate the scintillation noise contribution to photometry and the atmospheric noise contribution to narrow-angle astrometry, using a set of low-resolution turbulence profiles measured at Dome C in 2004. The instrument and data are described in § 2. In § 3 we outline the theory of atmospheric turbulence, scintillation, and interferometry. In § 4 we present our results and discussion.

2. MASS MEASUREMENTS

The turbulence profile of the atmosphere at Dome C was monitored with a MASS (multiaperture scintillation sensor) instrument during the first 2 months of the 2004 night time: 2004 March 23 to 2004 May 16. The analysis of these data in terms of seeing has been reported by Lawrence et al. (2004b).

The MASS instrument and theory are described in detail in Kornilov et al. (2003) and Tokovinin et al. (2003). In brief, starlight is directed via a telescope onto four concentric annular mirrors that split the entrance aperture into rings with projected outer diameters of 19, 32, 56, and 80 mm. Each of the four beams is directed to a miniature Hamamatsu photomultiplier that samples the stellar intensity at a 1 kHz rate. Four normal and six differential scintillation indices are calculated for each 1 s integration and further averaged during 1 minute. The set of 10 indices is fitted to a model of six fixed layers at heights 0.5, 1, 2, 4, 8, and 16 km above the observatory. For each layer i , the integrated turbulence J_i ($m^{1/3}$) is calculated:

$$J_i = \int_{\text{Layer } i} C_n^2(h) dh, \quad (1)$$

where $C_n^2(h)$ ($m^{-2/3}$) is the refractive index structure constant and h is the height above the site. The spectral response of MASS is from 400 to 550 nm with a FWHM bandwidth of 100 nm.

The profile restoration from scintillation indices is a delicate procedure, and errors may reach 10% of the total turbulence

integral. The errors are larger for the lower layers, while the two highest layers (8 and 16 km) are measured well. The second moment of the turbulence profile used in this paper is measured by MASS with high reliability, as well as lower moments. This has been demonstrated by intercomparing MASS and SCIDAR instruments (Tokovinin et al. 2005).

The Dome C MASS (Lawrence et al. 2004a), operated in the AASTINO (Automated Astrophysical Site Testing International Observatory; Lawrence et al. 2005), uses a gimbal-mounted siderostat mirror feeding a fixed 85 mm refracting telescope.

MASS instruments also operate at a number of other sites. To provide a comparison to the Dome C results, we have also included the publicly available data¹ from the Cerro Tololo and Cerro Pachón observatories in Chile. The profiles for Cerro Pachón have been discussed and modeled by Tokovinin & Travouillon (2006).

3. THEORY

3.1. Turbulence

Many astronomical measurements are limited by the Earth's atmosphere. A wave front located at height h and horizontal position vector \mathbf{x} in the atmosphere can be described by its complex amplitude $\Psi_h(\mathbf{x})$ (Roddier 1981),

$$\Psi_h(\mathbf{x}) = e^{\chi_h(\mathbf{x}) + i\psi_h(\mathbf{x})}, \quad (2)$$

where $\chi_h(\mathbf{x})$ is the logarithm of the amplitude and $\psi_h(\mathbf{x})$ is the phase of the wave.

Atmospheric turbulence introduces pure phase distortions. As the wave front propagates through the atmosphere, amplitude modulations appear as well. In the geometric optics approximation, phase perturbations act as positive or negative lenses, changing the wave front curvature and producing intensity modulation at the ground. Diffraction is also important and defines the size of the most effective atmospheric 'lenses' to be of the order of the Fresnel radius,

$$r_F \approx (\lambda h)^{1/2}, \quad (3)$$

where λ is the wavelength of light and h is the height of the turbulent layer above the observatory site. For example, if the dominant turbulence layer is at 10 km, then at 500 nm, $r_F = 7$ cm.

Dravins et al. (1997a, 1997b, 1998) present detailed discussions of stellar scintillation, including statistical distributions and temporal properties, dependence on wavelength, and effects for different telescope apertures.

¹ Obtained from the National Optical Astronomy Observatory Web page 'Sites Data Access' at <http://139.229.11.21>.

926 KENYON ET AL.

3.2. Scintillation Noise

The scintillation index σ_I^2 is used as a measure of the amount of scintillation and is defined (for small intensity fluctuations) as the variance of $\Delta I / \langle I \rangle$. In the weak-scintillation regime, $\sigma_I^2 \ll 1$, the effects of all turbulence layers are additive. In this case, the scintillation index is related to the refractive index structure constant $C_n^2(h)$ by (Krause-Polstorff et al. 1993; Roddier 1981)

$$\sigma_I^2 = \int_0^\infty C_n^2(h) W(h) dh, \quad (4)$$

where the weighting function $W(h)$ is given by

$$W(h) = 16\pi^2 0.033 \left(\frac{2\pi}{\lambda}\right)^2 \int_0^\infty |A(f)|^2 f^{-8/3} \sin^2\left(\frac{\lambda h f^2}{4\pi}\right) df. \quad (5)$$

Here h is the height above the observatory, λ is the wavelength, f is the spatial frequency, and $|A(f)|^2$ is an aperture filtering function. This expression is valid for monochromatic light and has to be modified for wide-band radiation.

For telescope apertures with diameter $D \ll r_F$, the monochromatic scintillation index is (Roddier 1981)

$$\sigma_I^2 = 19.2\lambda^{-7/6} (\cos \gamma)^{-11/6} \int_0^\infty h^{5/6} C_n^2(h) dh, \quad (6)$$

where γ is the zenith angle.

The scintillation index for a large circular aperture with diameter $D \gg r_F$ is

$$\sigma_I^2 = 17D^{-7/3} (\cos \gamma)^{-3} \int_0^\infty h^2 C_n^2(h) dh. \quad (7)$$

Large apertures effectively average small-scale intensity fluctuations, so that only atmospheric lenses of the order of the aperture diameter D contribute to the flux modulation. In this case, geometric optics applies and the scintillation becomes independent of both the wavelength and the spectral bandwidth.

The above expressions are for very short timescale exposures. For exposure times that are longer than the time taken for a scintillation pattern to cross the telescope aperture [i.e., $t > (\pi D)/V_\perp$, where D the telescope diameter and V_\perp the speed of the turbulence layer], the scintillation index can be calculated from (Dravins et al. 1998)

$$\sigma_I^2(t) = \int_0^\infty P(\nu) \text{sinc}^2(\pi \nu t) d\nu, \quad (8)$$

where ν (s^{-1}) is the temporal frequency and $P(\nu)$ is the temporal power spectrum, given by Yura & McKinley (1983) and references therein as

$$P(\nu) \approx 8.27k^{2/3} \int_0^\infty \frac{C_n^2(h) h^{4/3}}{V_\perp(h)} Q(h) dh \quad (9)$$

at the zenith, where $k = 2\pi/\lambda$ and

$$Q(h) = \int_0^\infty |A(f_x, f_y)|^2 \left[x^2 + \frac{\nu^2}{\nu_0^2(h)} \right]^{-11/6} \sin^2 \left[x^2 + \frac{\nu^2}{\nu_0^2(h)} \right] dx. \quad (10)$$

Here $f_x = \nu/V_\perp(h)$, $f_y = (2k/h)^{1/2} x$, $\nu_0(h) = (2k/h)^{1/2} V_\perp(h)$, and $A(f) = [2J_1(fD/2)]/(fD/2)$ for a circular aperture with diameter D and $f^2 = f_x^2 + f_y^2$.

For large t , Dravins et al. (1998) simplify equation (8) to

$$\sigma_I^2(t) = \frac{P(0)}{2t}. \quad (11)$$

In the limit of large apertures $D \ll r_F$, we can replace the sine in equation (10) by its argument. By setting $\nu = 0$ and introducing a new variable $y = f_y D$, we can show that

$$P(0) \approx 21.3D^{-4/3} \int_0^\infty \frac{C_n^2(h) h^2}{V_\perp(h)} dh \quad (12)$$

and is independent of the wavelength.

For a particular set of turbulence and wind profiles, the scintillation noise σ_I at zenith can be expressed as

$$\sigma_I = \begin{cases} S_1, & D \ll r_F, \\ S_2 D^{-7/6}, & D \gg r_F, \\ S_3 D^{-2/3} t^{-1/2}, & D \gg r_F, t \gg (\pi D)/V_\perp, \end{cases} \quad (13)$$

where

$$S_1 = \left[19.2\lambda^{-7/6} \int_0^\infty h^{5/6} C_n^2(h) dh \right]^{1/2}, \quad (14)$$

$$S_2 = \left[17.3 \int_0^\infty h^2 C_n^2(h) dh \right]^{1/2}, \quad (15)$$

$$S_3 = \left[10.7 \int_0^\infty \frac{C_n^2(h) h^2}{V_\perp(h)} dh \right]^{1/2}. \quad (16)$$

The scintillation error can be expressed in magnitudes as $\sigma_I(\text{mag}) = 2.5 \log(\sigma_I + 1)$.

In all cases the scintillation noise is dominated by the high-altitude turbulence, more so in the case of large apertures be-

cause of the h^2 weighting. It is the large-aperture case that is generally of more relevance to astronomical photometry.

3.3. Astrometric Interferometry

The Antarctic plateau has been recognized as a potentially favorable site for interferometry because the high-altitude turbulence is very weak (Lloyd et al. 2002). In particular, high precision, very-narrow angle differential astrometry should be attainable at Dome C using long-baseline interferometry techniques. This would benefit a number of science programs, including extrasolar planet searches and the study of close binary and multiple star systems (for other examples, see Swain et al. 2003; Lloyd et al. 2002; Sozzetti 2005).

Differential astrometric measurement requires simultaneous observations of the target and reference object. To achieve this, each telescope has a dual feed to direct the beam from each star to the beam combiner (Shao & Colavita 1992). On combination of the beams, a fringe pattern is produced if the difference between the optical path lengths from each arm of the interferometer to the beam combiner is within $\lambda^2/\Delta\lambda$ (Lane & Muterspaugh 2004). The difference between the fringe positions of the two stars is measured. Phase referencing can be used to improve the limiting magnitude of the interferometer if the target star and reference object are within the isoplanatic patch (Shao & Colavita 1992).

Uncertainties in astrometric position measurements arise from instrumental effects (noise, systematic) and atmospheric effects associated with temporal incoherence and anisoplanatism. See Shao & Colavita (1992), Sozzetti (2005), and Lane & Muterspaugh (2004) for further details.

The variance in an astrometric position measurement caused by anisoplanatism (assuming a Kolmogorov turbulence spectrum) is described by Shao & Colavita (1992) as

$$\sigma_{\text{atm}}^2 \approx 5.25t^{-1} \begin{cases} \theta^2 B^{-4/3} \int_0^\infty \frac{C_n^2(h)h^2}{V(h)} dh & \text{(case 1),} \\ \theta^{2/3} \int_0^\infty \frac{C_n^2(h)h^{2/3}}{V(h)} dh & \text{(case 2),} \end{cases} \quad (17)$$

where t is the integration time, θ is the angular separation between two stars, $C_n^2(h)$ and $V(h)$ are the vertical turbulence and wind profiles, h is the height above the site, and B is the baseline or diameter of the entrance pupil. These formulae are only approximate, but the exact coefficient is not needed for the purpose of site intercomparison.

Case 1 applies to interferometry when the integration time $t \gg B/\bar{V}$ and $\theta\bar{h} \ll B$, where \bar{h} and \bar{V} are the turbulence-weighted effective atmospheric height and wind speed. Because of the h^2 weighting, σ_{atm} in this regime is very sensitive to high-altitude turbulence.

Case 2 is applicable to single-dish astrometry and is inde-

ATMOSPHERIC SCINTILLATION AT DOME C 927

pendent of the size of the telescope when $\theta\bar{h} \gg B$ and $t \gg \theta\bar{h}/\bar{V}$.

For a particular set of turbulence and wind profiles, the error σ_{atm} (arcseconds) can be expressed as

$$\sigma_{\text{atm}} = \begin{cases} C_1 t^{-1/2} \theta B^{-2/3} & \text{(case 1),} \\ C_2 t^{-1/2} \theta^{1/3} & \text{(case 2),} \end{cases} \quad (18)$$

where

$$C_1 = 472,000 \left[\int_0^\infty \frac{C_n^2(h)h^2}{V(h)} dh \right]^{1/2} \quad (19)$$

and

$$C_2 = 472,000 \left[\int_0^\infty \frac{C_n^2(h)h^{2/3}}{V(h)} dh \right]^{1/2}. \quad (20)$$

Note that the expression for C_1 contains the same combination of atmospheric parameters as the expression for the photometric error S_3 . This is not a coincidence, as both narrow-angle astrometry and large-aperture photometry are affected by the same physical phenomenon: large-scale curvature fluctuations of wave fronts. Hence, scintillation in large apertures contains information on the potential accuracy of narrow-angle astrometry at a given site.

4. RESULTS

Using the eight weeks of MASS data from Dome C, we extracted 11,532 turbulence profiles spread over 51 nights (we use ‘night’ to mean the period within 24 hr when the Sun is farther than 10° below the horizon). These data were filtered according to the criteria $B_D/F_D < 0.03$, $F_D > F_{\text{limit}}$, $\delta F_D < 0.003$, $0.7 < F_C/F_D < 0.9$, and $\chi^2 < 100$, where F_D and B_D are the star flux and background measurements in aperture D (largest aperture). Here F_{limit} is a cutoff flux limit set to 100 counts for α Trianguli and 200 counts for β Crucis and β Carinae. The parameter δF_D shows slow flux variations, used here to eliminate data affected by the guiding errors. The flux ratio F_C/F_D serves to control the aperture vignetting by the entrance window, which was sometimes covered by snow or frost. The χ^2 is a measure of the fit quality. After filtering, 1853 profiles over 26 nights remained for further analysis.

Each profile includes the integrated turbulence J_i (see eq. [1]) in layers centered at elevations of 0.5, 1, 2, 4, 8, and 16 km above the site with vertical resolution $\Delta h/h \sim 0.5$. Finally, we calculated the scintillation noise and implied astrometric error from each profile. In this section, we compare these results with similar data for the Cerro Tololo and Cerro Pachón observatories in Chile (see Table 1 for information on each data set).

928 KENYON ET AL.

TABLE 1
DATA SETS

Site	Location*	Altitude (m)	Date Range	Number of Nights	Number of Profiles
Dome C	123 21 E, 75 06 S	3260	2005 Mar 23–2004 May 16	26	1853
Cerro Tololo	70 48 W, 30 09 S	2215	2002 Mar 19–2006 Feb 2	573	98887
Cerro Pachón	70 44 W, 30 14 S	2738	2003 Jan 9–2006 Jan 30	293	39819

NOTE.—We use “night” to mean the period within 24 hr when the Sun is farther than 10° below the horizon.

* Location is given in degrees and arcminutes.

4.1. Turbulence Profiles

Figure 1 shows the cumulative probability that the integrated turbulence for each height is less than the given J_r .

Cerro Tololo has the lowest turbulence in the 0.5 km layer. At 1 km the turbulence at Dome C is so low that, for most of the time, it cannot be reliably measured with MASS. Dome C has a slightly higher probability of smaller turbulence in the 4 and 8 km layers. However, the most significant difference between the sites is in the 16 km layer; at Dome C the integrated turbulence in this high-altitude layer is *always less* than the median values at Cerro Tololo and Cerro Pachón.

The Cerro Tololo and Cerro Pachón sites are only 10 km apart and have a 400 m altitude difference. Hence, we expect identical high-altitude turbulence for those sites. The differences seen in Figure 1 reflect mostly different seasonal coverage of the data sets (more winter-spring data for Cerro Tololo) coupled to the systematic seasonal trends in high-altitude turbulence. Similar caution is warranted for the Dome C data that cover only 25 nights.

4.2. Wind Profiles

The photometric error for long integration times (eqs. [13] and [16]) and the astrometric errors (eqs. [19] and [20]) depend not only on the turbulence but also on the wind speed profile. As these quantities are likely correlated, the correct way to estimate the errors requires simultaneous data on wind and turbulence. The wind profiles can, in principle, be retrieved from the global meteorological databases like NCEP (National Centers for Environmental Prediction). However, here we adopt a simplified approach and use fixed wind profile models instead. Hence, the distributions derived here may be not realistic.

Owing to the strong h^2 weighting, the astrometric and photometric errors are almost entirely determined by the highest MASS layer at 16 km. Hence, the adopted wind speed in this layer critically influences our results.

The wind speed profiles for Cerro Pachón and Cerro Tololo were modeled using a constant ground layer speed V_g plus a Gaussian function to represent the jet stream contribution (Greenwood 1977):

$$V(h) = V_g + V_r \exp \left[- \left(\frac{h - H}{T} \right)^2 \right], \quad (21)$$

where h is the altitude above the observatory. We set $V_g = 8 \text{ m s}^{-1}$, $V_r = 30 \text{ m s}^{-1}$, $H = 8 \text{ km}$, and $T = 4 \text{ km}$ by comparing the model to the Cerro Pachón wind profiles in Avila et al. (2000, 2001).

The summer wind speed profile at Dome C also shows a Gaussian peak at the (somewhat lower) tropopause layer ($\sim 5 \text{ km}$) and fairly constant wind speed at other elevations (see Fig. 4 of Aristidi et al. 2005). In the winter, the wind speed profile is different, showing an increase in stratospheric wind speeds and no peak at the tropopause. So far only three profiles of the winter wind speed have been published (Agabi et al. 2006). Figure 2 shows the average wintertime and summertime wind profiles; we used the wintertime wind profile in this work.

4.3. Scintillation Noise

The scintillation noise was calculated for the three regimes discussed in § 3.2, using the results from each site. Figure 3 shows the cumulative probabilities for S_1 , S_2 , and S_3 .

For short timescales, the median scintillation noise at Dome C is a factor of ~ 2 less than at Cerro Tololo and Cerro Pachón, in the small-aperture regime. For larger apertures the gain is slightly higher, ~ 2.4 , because of the weaker high-altitude turbulence at Dome C. As an example, for a 4 m diameter telescope, the median values of the scintillation noise at each site are 1.2 mmag (Dome C), 3.2 mmag (Cerro Tololo), and 2.8 mmag (Cerro Pachón).

The more relevant figure is the scintillation noise for long exposure times. We used the wind speed models discussed above to calculate this parameter. Dome C offers a potential gain of about 3.6 in photometric precision compared to Cerro Tololo and Cerro Pachón. From the results we calculate the median photometric error expected on a 4 m telescope for $t = 60 \text{ s}$ to be $\sim 53 \text{ } \mu\text{mag}$ at Dome C, $\sim 200 \text{ } \mu\text{mag}$ at Cerro Tololo, and $\sim 180 \text{ } \mu\text{mag}$ at Cerro Pachón.

As a comparison, Dravins et al. (1998) measured $P(\nu)$ at La Palma using various small apertures. From their results they extrapolate $P(0) = 5 \times 10^{-6} \text{ s}$ for a 4 m aperture at zenith, which gives $\sigma_t = 220 \text{ } \mu\text{mag}$ for a 60 s integration, similar to the typical values for Cerro Tololo and Cerro Pachón. Our results are also consistent with those measured at Kitt Peak and Mauna Kea by Gilliland et al. (1993).

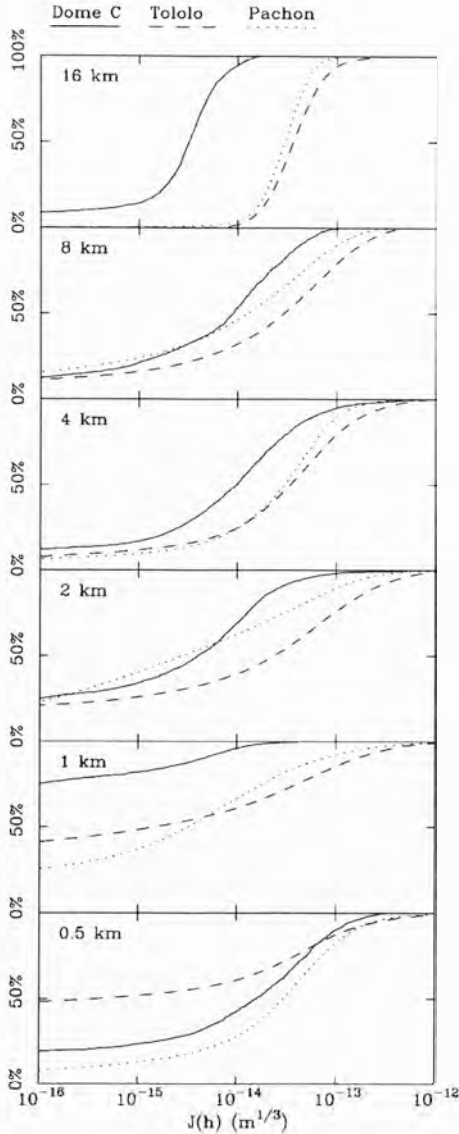


FIG. 1.—Cumulative probabilities that the integrated turbulence for each height (above the surface) is less than the given J_i for Dome C (solid curve), Cerro Tololo (dashed curve), and Cerro Pachón (dotted curve). The large fraction of very low J_i values for the 0.5 and 1 km layers is an artifact of the MASS profile restoration method in situations when these layers do not dominate.

4.4. Astrometry

The constants C_1 and C_2 (§ 3.3) were calculated for each site; cumulative probabilities are shown in Figure 4. The median astrometric error σ_{atm} at Dome C is ~ 3.5 times less than the median values at Cerro Tololo and Cerro Pachón. In Figure 5,

ATMOSPHERIC SCINTILLATION AT DOME C 929

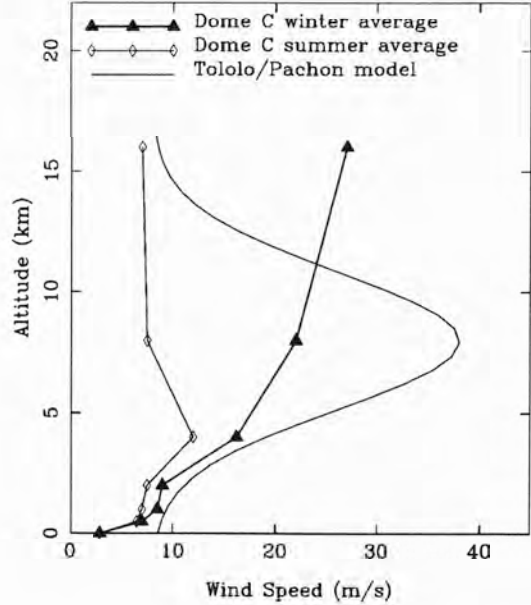


FIG. 2.—Average wind speed profiles at Dome C in the winter (Agabi et al. 2006) and summer (Aristidi et al. 2005), and a model of the wind profile at Cerro Tololo and Cerro Pachón.

σ_{atm} at Dome C is plotted for several baselines as a function of separation angle θ for an integration time of 1 hr.

We note that the advantage of Dome C for narrow-angle astrometry over midlatitude sites is even larger than its advantage in the fast scintillation. This difference is related to the adopted wind speed at 16 km altitude (27 and 8.5 m s^{-1} for Dome C and Cerro Pachón, respectively). Turbulence at Dome C is known to be slow (large time constant; see below), but the h^2 weighting in the expressions for the photometric and astrometric errors reverses this conclusion because the high-altitude turbulence dominates the calculation.

Our conclusions are conditional on the adopted wind-speed models. Using the mean Dome C winter wind speed we calculated a median C_1 value of 140 $\text{arcsec rad}^{-1} \text{m}^{2/3} \text{s}^{1/2}$; decreasing the 16 km wind speed to 7 m s^{-1} gave a median C_1 value of 200 $\text{arcsec rad}^{-1} \text{m}^{2/3} \text{s}^{1/2}$, still well below the median values at Cerro Tololo and Cerro Pachón. As an additional check, we computed C_1 from a set of six balloon profiles of C_n^2 and wind measured at Cerro Pachón in 1998 October (see Avila et al. 2000, 2001 for the discussion of these data). The C_1 values range from 380 to 660 $\text{arcsec rad}^{-1} \text{m}^{2/3} \text{s}^{1/2}$, with a median of 480. This is close to the median value for Cerro Pachón given in Figure 4. Shao & Colavita (1992) calculate C_1 at Mauna Kea to be 300 $\text{arcsec rad}^{-1} \text{m}^{2/3} \text{s}^{1/2}$, using the results from two short observing campaigns.

The fringe phase of an interferometric measurement must be determined within the atmospheric coherence time. Table 2

930 KENYON ET AL.

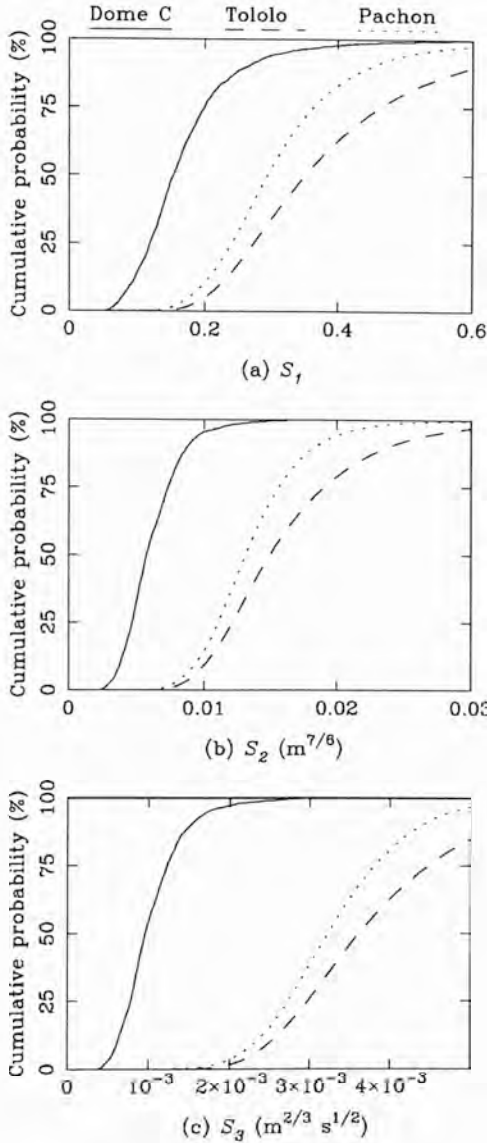


FIG. 3.—Cumulative probabilities of the constants (a) S_1 , (b) S_2 ($m^{7/6}$), and (c) S_3 ($m^{2/3} s^{1/2}$) for Dome C, Cerro Tololo, and Cerro Pachón. The scintillation noise σ_I is the standard deviation of $\Delta I/I$, where I is the stellar flux, and is equal to S_1 for $D \ll r_F$, $S_2 D^{-7/6}$ for $D \gg r_F$, and $S_3 D^{-2/3} t^{-1/2}$ for $D \gg r_F$ and $t \gg (\pi D)/V$, where D is the telescope diameter, r_F is radius of the Fresnel zone, and t is the integration time.

shows the median coherence times τ_0 (Roddier et al. 1982a) and isoplanatic angles θ_0 (Roddier et al. 1982b) at each site for wavelengths 500 nm and 2.2 μm . The median coherence time at Dome C, measured with MASS, is 7.2 ms at $\lambda = 500$ nm and 42 ms at $\lambda = 2.2 \mu m$. Using the measured turbulence

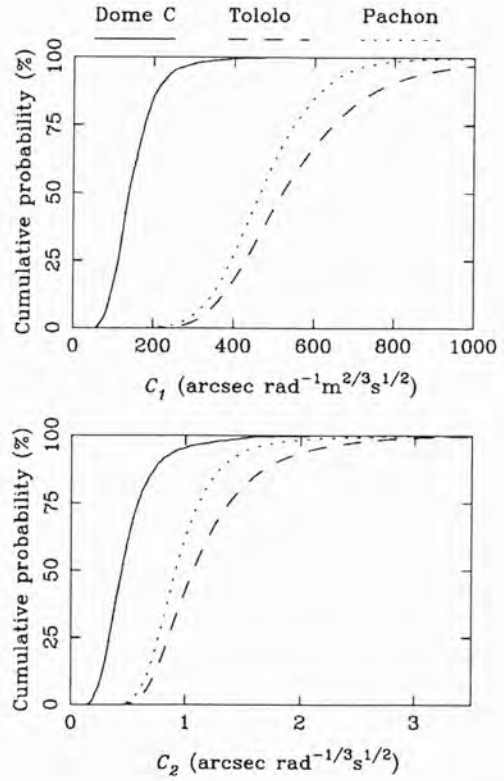


FIG. 4.—Cumulative probabilities that the constants C_1 and C_2 are less than the value given, for Dome C, Cerro Tololo, and Cerro Pachón. The astrometric error σ_{ast} (arcseconds) is equal to $C_1 t^{-1/2} \theta B^{-2/3}$ for $t \gg B/\bar{V}$ and $\theta \bar{h} \ll B$, and $C_2 t^{1/2} \theta^{1/3}$ for $t \gg \theta \bar{h}/\bar{V}$ and $\theta \bar{h} \gg B$. Here t is the integration time, B is the baseline length, \bar{h} and \bar{V} are the turbulence-weighted effective atmospheric height and wind speed, and θ is the stellar separation.

profiles and assumed wind profile at Dome C, we calculated $\tau_0 = 9.4$ ms at $\lambda = 500$ nm.

Phase referencing during the measurement (Shao & Colavita 1992) effectively increases the coherence time, with the condition that the target and reference objects are within the same isoplanatic patch. The median isoplanatic angle at Dome C is ~ 3 times larger than at Cerro Tololo and Cerro Pachón, allowing wider fields to be used for phase referencing.

5. CONCLUSIONS

The scintillation noise at Dome C for fast exposures is typically a factor 1.9–2.6 times lower than at Cerro Tololo and Cerro Pachón, leading to a corresponding reduction in this ultimate limit for high-precision photometry. The “small aperture” scintillation index becomes important for adaptive optics when the distance between the actuators approaches the Fresnel zone size r_F and shadow patterns start becoming re-

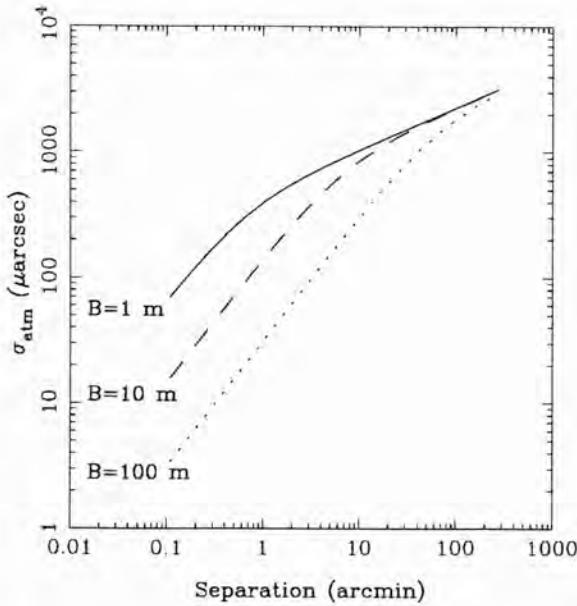


FIG. 5.—Median error σ_{atm} for three baseline lengths at Dome C, with an integration time of 1 hr.

solved (Masciadri et al. 2004). Adaptive optics will also benefit from the long coherence time and large isoplanatic angle at Dome C, particularly in the infrared.

For longer exposures, σ_i at Dome C is typically 3.4–3.8 times less than at Cerro Tololo and Cerro Pachón. For a 60 s integration on a 4 m telescope, the median photometric error is $\sim 53 \mu\text{mag}$ at Dome C. This parameter is important for exoplanet transit measurements because the change in flux, caused by a transiting planet, is related to the planet R_p and star R_s radii by $\Delta F/F = (R_p/R_s)^2$. For example, for a Jupiter-size planet transiting a Sun-size star $\Delta F/F = 0.01$; for an Earth-size planet this ratio is 0.0001. The lower scintillation noise at Dome C will allow for the transits of smaller planets to be detected than at the Chilean sites.

The atmospheric contribution to the positional error in a differential astrometric measurement using a long-baseline interferometer at Dome C is always less than the median values at Cerro Tololo and Cerro Pachón. This conclusion is obtained

ATMOSPHERIC SCINTILLATION AT DOME C 931

TABLE 2
ISOPLANATIC ANGLES AND COHERENCE TIMES FOR ADAPTIVE OPTICS

Site	$\theta_0(500 \text{ nm})$ (arcsec)	$\tau_0(500 \text{ nm})$ (ms)	$\theta_0(2.2 \mu\text{m})$ (arcsec)	$\tau_0(2.2 \mu\text{m})$ (ms)
Median Values				
Dome C	5.4	7.2	32	42
Cerro Tololo	1.8	2.0	11	12
Cerro Pachón	2.0	2.6	12	16
Average Values				
Dome C	5.9	8.8	35	52
Cerro Tololo	1.9	2.8	11	17
Cerro Pachón	2.1	3.3	13	20

NOTE.—The values of τ_0 and θ_0 at 500 nm are taken from the MASS data files, and the values at 2.2 μm are scaled by $\lambda^{6/5}$.

using average wind profiles and remains provisional until a more complete analysis is done.

Based on the expected low astrometric error at Dome C, a number of interferometric projects have already been proposed. These include the Antarctic Planet Interferometer (API; Swain et al. 2004), the Kiloparsec Explorer for Optical Planet Search (KEOPS; Vakili et al. 2004), and the Antarctic L-band Astrophysics Discovery Demonstrator for Interferometric Nulling (ALADDIN; Coudé du Foresto et al. 2006). Many science programs would benefit from an Antarctic interferometer, including exoplanet detection and orbit determination and measurement of microlensing events (Lloyd et al. 2002).

The UNSW AASTINO project is indebted to the French and Italian Antarctic Programs (IPEV, PNRA) for logistics support and to the Australian Research Council and the Australian Antarctic Division for financial support. S. L. K. is supported by an Australian Postgraduate Award and by an Australian Antarctic Division top-up scholarship. We thank James Lloyd and Mark Swain for particularly useful discussions that led to the concept of a ‘warm MASS’ for making these measurements, and Victor Kornilov and Nicolai Shatsky for helpful advice on the data reduction software. We thank the LUAN team at the University of Nice, in particular Eric Aristidi and Karim Agabi, for their assistance in setting up the AASTINO at Dome C. We also thank Colin Bonner, Jon Everett, and Tony Travouillon of the University of New South Wales Antarctic Research Group and Anna Moore of the Anglo-Australian Observatory for valuable contributions to the Dome C MASS project.

932 KENYON ET AL.

REFERENCES

- Agabi, A., Aristidi, E., Azouit, M., Fossat, E., Martin, F., Sadibekova, T., Vermin, J., & Ziad, A. 2006, *PASP*, 118, 344
- Aristidi, E., et al. 2005, *A&A*, 430, 739
- Avila, R., Vermin, J., Chun, M. R., & Sanchez, L. J. 2000, *Proc. SPIE*, 4007, 721
- Avila, R., Vermin, J., & Sánchez, L. J. 2001, *A&A*, 369, 364
- Calisse, P. G., Ashley, M. C. B., Burton, M. G., Phillips, M. A., Storey, J. W. V., Radford, S. J. E., & Peterson, J. B. 2004, *Publ. Astron. Soc. Australia*, 21, 256
- Coudé du Foresto, V., Absil, O., Barillot, M., & Swain, M. 2006, in *IAU Colloq. 200, Direct Imaging of Exoplanets: Science and Techniques*, ed. C. Aime & F. Vakili (Cambridge: Cambridge Univ. Press), 305
- Dravins, D., Lindegren, L., Mezey, E., & Young, A. T. 1997a, *PASP*, 109, 173
- . 1997b, *PASP*, 109, 725
- . 1998, *PASP*, 110, 610
- Fossat, E. 2005, in *Dome C Astronomy and Astrophysics Meeting*, ed. M. Giard, F. Casoli, & F. Paletou (Les Ulis: EDP Sci.), 121
- Gilliland, R. L., et al. 1993, *AJ*, 106, 2441
- Gillingham, P. R. 1991, *Publ. Astron. Soc. Australia*, 9, 55
- . 1993, *ANARE Research Notes*, No. 88, 290
- Greenwood, D. P. 1977, *J. Opt. Soc. Am.*, 67, 390
- Heasley, J. N., Janes, K., Labonte, B., Guenther, D., Mickey, D., & Demarque, P. 1996, *PASP*, 108, 385
- Indermuehle, B. T., Burton, M. G., & Maddison, S. T. 2005, *Publ. Astron. Soc. Australia*, 22, 73
- Kenyon, S. L., & Storey, J. W. V. 2006, *PASP*, 118, 489
- Kornilov, V., Tokovinin, A. A., Vozyakova, O., Zaitsev, A., Shatsky, N., Potanin, S. F., & Sarazin, M. S. 2003, *Proc. SPIE*, 4839, 837
- Krause-Polstorff, J., Murphy, E. A., & Walters, D. L. 1993, *Appl. Opt.*, 32, 4051
- Lane, B. F., & Muterspaugh, M. W. 2004, *ApJ*, 601, 1129
- Lawrence, J. S., Ashley, M. C., Kenyon, S. L., Storey, J. W. V., Tokovinin, A. A., Lloyd, J. P., & Swain, M. R. 2004a, *Proc. SPIE*, 5489, 174
- Lawrence, J. S., Ashley, M. C., & Storey, J. W. V. 2005, *J. Electrical Electron. Eng. Australia*, 2, 1
- Lawrence, J. S., Ashley, M. C. B., Tokovinin, A., & Travouillon, T. 2004b, *Nature*, 431, 278
- Lloyd, J. P., Oppenheimer, B. R., & Graham, J. R. 2002, *Publ. Astron. Soc. Australia*, 19, 318
- Marks, R. D., Vermin, J., Azouit, M., Manigault, J. F., & Clevelin, C. 1999, *A&AS*, 134, 161
- Masciadri, E., Feldt, M., & Hippler, S. 2004, *ApJ*, 613, 572
- Roddier, F. 1981, *Prog. Opt.*, 19, 281
- Roddier, F., Gilli, J. M., & Lund, G. 1982a, *J. Optics*, 13, 263
- Roddier, F., Gilli, J. M., & Vermin, J. 1982b, *J. Optics*, 13, 63
- Shao, M., & Colavita, M. M. 1992, *A&A*, 262, 353
- Sozzetti, A. 2005, *PASP*, 117, 1021
- Swain, M. R., Coude du Foresto, V., Fossat, E., & Vakili, F. 2003, *Mem. Soc. Astron. Italiana Supp.*, 2, 207
- Swain, M. R., et al. 2004, *Proc. SPIE*, 5491, 176
- Tokovinin, A., Kornilov, V., Shatsky, N., & Voziakova, O. 2003, *MNRAS*, 343, 891
- Tokovinin, A., & Travouillon, T. 2006, *MNRAS*, 365, 1235
- Tokovinin, A., Vermin, J., Ziad, A., & Chun, M. 2005, *PASP*, 117, 395
- Travouillon, T. 2005, in *Dome C Astronomy and Astrophysics Meeting*, ed. M. Giard, F. Casoli, & F. Paletou (Les Ulis: EDP Sci.), 31
- Vakili, F., et al. 2004, *Proc. SPIE*, 5491, 1580
- Walden, V. P., Town, M. S., Halter, B., & Storey, J. W. V. 2005, *PASP*, 117, 300
- Yura, H. T., & McKinley, W. G. 1983, *Appl. Opt.*, 22, 3353

C-3 Nigel and the optical sky brightness at Dome C, Antarctica

Suzanne L. Kenyon*, Michael C. B. Ashley, Jon Everett, Jon S. Lawrence and
John W. V. Storey

School of Physics, University of New South Wales, Sydney 2052, Australia

ABSTRACT

The brightness of the night sky at an astronomical site is one of the principal factors that determine the quality of available optical observing time. At any site the optical night sky is always brightened with airglow, zodiacal light, integrated starlight, diffuse Galactic light and extra-galactic light. Further brightening can be caused by scattered sunlight, aurorae, moonlight and artificial sources. Dome C exhibits many characteristics that are extremely favourable to optical and IR astronomy; however, at this stage few measurements have been made of the brightness of the optical night sky. Nigel is a fibre-fed UV/visible grating spectrograph with a thermoelectrically cooled 256×1024 pixel CCD camera, and is designed to measure the twilight and night sky brightness at Dome C from 250 nm to 900 nm. We present details of the design, calibration and installation of Nigel in the AASTINO laboratory at Dome C, together with a summary of the known properties of the Dome C sky.

Keywords: Site testing, Antarctica, sky brightness

1. INTRODUCTION

Dome C, Antarctica ($75^{\circ}6'$ south, $123^{\circ}21'$ east, 3250 m) has been recognised as a promising optical and infrared astronomical site for a number of years.¹ Above a thin boundary layer the atmospheric turbulence is very weak, leading to exceptionally good seeing. Measurements of the turbulence using a MASS and a SODAR in winter 2004 showed an average seeing above 30 m of $0.27''$, with the seeing better than $0.15''$ for 25% of the time.² These results were independently confirmed in winter 2005; DIMM measurements showed an average seeing of $0.25''$ above the ground layer with 87% of the turbulence confined to the first 36 m of the atmosphere.³ The extremely cold temperatures and low precipitable water vapour at Dome C also result in an infrared sky background that is very much lower than at temperate sites.⁴

To date the optical sky brightness of Dome C has not been monitored during the winter. Because of the high latitude of Dome C, the Sun spends a relatively small amount of time a long way below the horizon, resulting in long periods of twilight. There is thus a need to evaluate both the quality and quantity of dark time at Dome C. Nigel is a spectrograph designed to measure both the optical twilight and the nighttime sky brightness at Dome C. Nigel was installed in the AASTINO (Automated Astrophysical Site Testing International Observatory⁵) in November 2004 and collected data until 13 February 2005.

In Section 2 we discuss the various contributions to sky brightness at Dome C and discuss the amount of usable dark time. In Section 3 we discuss the aims, design and installation of Nigel. Finally, in Section 4 we summarise future plans for Nigel.

2. SKY BRIGHTNESS

The sky is never completely dark in optical wavelengths. At the darkest sites, long after sunset, the sky background is on the order of $22.0\text{--}21.1$ V mag arcsec⁻² at zenith.⁶ Sky brightening is caused by sunlight, moonlight, airglow, aurorae, zodiacal light, integrated starlight, diffuse Galactic light, extra-galactic light and artificial sources. Kenyon & Storey (2006)⁷ present a detailed analysis of the sky brightness at Dome C and provide a comparison to Mauna Kea, Hawaii. In this section we summarise the main conclusions of that paper.

* suzanne@phys.unsw.edu.au

Sunlight No direct sunlight reaches the surface of the Earth after sunset, however, sunlight is *scattered* off atmospheric molecules and aerosol particles towards the surface. This is the highest contributor to sky brightness until the Sun is about 8° below the horizon. Scattering from atmospheric molecules is essentially the same at all sites of similar elevation, so little advantage is expected at Dome C in this respect. However, aerosol scattering is extremely variable between sites. Because of the extremely clear atmosphere at Dome C it is expected that aerosol scattering will be minimal. No measurements of aerosols have been taken at Dome C, however the annual average scattering coefficient at South Pole is 5 times less than at Mauna Loa, Hawaii.^{8,9} The main aerosol in the atmosphere at South Pole is sea salt that has been transported from the coast. As Dome C is further from the coast than South Pole, it is expected that the aerosol content of the atmosphere there will be even lower. Astronomical nighttime is formally defined to begin when the Sun reaches a depression angle of 18° . Using this definition, Dome C has about 50% the dark-time of Mauna Kea. When the cloud cover at each site is taken into account, however, it appears that Dome C may have a comparable number of cloud-free dark hours to Mauna Kea.

Moonlight Moonlight brightens the sky in much the same way as the Sun, by direct transmission and scattering. At Dome C, the maximum elevation of the Moon ranges between about 33° and 43° over the 18 yr lunar nodal cycle. At sites closer to the equator, such as Mauna Kea, the Moon can always pass through the zenith, regardless of the lunar nodal cycle. Models of the sky brightening caused by the Moon show that, averaged over the epoch 2005–2015, moonlight brightens the sky at zenith by a median value of $1.7 V \text{ mag arcsec}^{-2}$ at Dome C, and $2.1 V \text{ mag arcsec}^{-2}$ at Mauna Kea.⁷

Aurorae Aurorae are caused by the collisions of highly energetic solar particles with upper atmosphere atoms and molecules. The collisions excite the atoms and molecules to higher energy states, from which they radiatively decay. Dome C is about 10° from the inner edge of the southern auroral oval; aurorae are therefore expected to be low on the horizon and of low intensity. Using geometric calculations, aurorae at Dome C are generally expected to be lower than 7° elevation and 1100–2000 km away.

Airglow Airglow, at night, is the chemiluminescence of upper atoms and molecules. Airglow emissions in the visible are shown in Table 1. In general, little difference in overall airglow emission between Antarctic and temperate sites is expected.

Table 1. Airglow emissions at zenith in the visible range [7, and ref. therein].

Wavelength (nm)	Source	Height (km)	Typical intensity (R)
260 – 380	O ₂	90	0.5 \AA^{-1}
500 – 650	NO ₂	90	250
519.8, 520.1	N	1	
557.7	O _I	95	250
557.7	O _I	250 – 300	20
589.0, 589.6	Na D	~ 92	50
600 – 4500	OH	85	4500 k
630.0	O _I	250 – 300	100
636.4	O _I	250 – 300	20
761.9	O ₂	~ 80	1000
864.5	O ₂	~ 80	1000

Zodiacal light Zodiacal light is caused by sunlight scattering from the diffuse cloud of interplanetary dust that lies in the plane of the solar system. Models of the zodiacal light at Dome C show it is expected to be always darker than $23.1 V \text{ mag arcsec}^{-2}$, at zenith. Similar models for Mauna Kea estimate the zodiacal light to be always brighter than $23.1 V \text{ mag arcsec}^{-2}$. The reduced zodiacal light at Dome C is not a characteristic of the site per se, but rather due to the different parts of the sky that are observed, i.e., the zodiac is always lower on the horizon at Dome C.

Integrated starlight Integrated starlight is from all the stars fainter than the limiting magnitude of the telescope. The limiting magnitude of even a small telescope at Dome C should be dark enough for the integrated starlight to be reduced to negligible levels.

Diffuse Galactic light Diffuse Galactic light is starlight scattered off interstellar dust. Diffuse Galactic light is typically about $23.6 V \text{ mag arcsec}^{-2}$ at zenith.¹⁰ The Galactic plane is always close to the zenith at Dome C and this may result in a relatively higher contribution of diffuse Galactic light and integrated starlight, compared to lower latitude sites. This contribution is rather smaller than other sources of sky brightness and, similarly to zodiacal light, depends on the celestial coordinates.

Integrated cosmic light Integrated cosmic light is the redshifted starlight from unresolved galaxies. This contribution, at all sites, is very small compared to other sources of sky brightness, and is expected to be in the range of $25\text{--}30 \text{ mag arcsec}^{-2}$ at 550 nm .⁶

Artificial sources The night sky can be brightened considerably by light pollution from towns and cities. At Dome C, light pollution from other stations will not be a problem; the nearest station (Vostok) is about 560 km away. With thoughtful planning in regards to external lighting at Dome C there should be no artificial light pollution, whereas the light pollution at other astronomical observatories, with close-by towns, is likely to increase.

3. NIGEL

Nigel is a fibre-fed spectrograph for the measurement of the optical brightness, temporal characteristics and spectrum of the twilight and nighttime sky, including auroral events. Nigel was developed from the Antarctic Fibre Optic Spectrograph (AFOS)¹¹ which operated at the South Pole from 2002–2003.¹² Nigel was installed in the AASTINO at Dome C in November 2004, and operated until 13 February 2005, at which time the entire AASTINO system was shut down. Unfortunately this means that the darkest sky we recorded was when the Sun was barely below the horizon.

In this section we describe the instrument design, installation and calibration.

3.1. Instrument Design

Nigel has six optical fibres that collect light from three directions in the sky and direct it into a spectrograph; the resulting image is recorded on a CCD. The spectrograph, CCD and control computer were located inside the AASTINO and the fibres fed outside through a roof port. Nigel is designed to operate in the wavelength range 250 nm–900 nm, so to ensure good efficiency over the whole spectral range we used two sets of fibres, optimised in red and blue wavelength ranges. Both sets of fibres were supplied by Ceramoptec and have a standard numerical aperture of 0.22 ± 0.02 with a core diameter of $100 \mu\text{m}$. The 6 fibres are paired into blue and red optimised combinations. The fibre numerical aperture corresponds to an f-ratio of $f/2.2$; each fibre thus sees a field of view of 25° on the sky. Each pair of fibres was pointed in a different direction, one pair towards the zenith and the other two pairs elevated to 30° and pointed in northerly and southerly directions.

The “sky” end of each fibre is held in an SMA connector, with a coaxial copper tube to hold the fibres in place on the top of the AASTINO. The tube can be electrically heated to prevent ice build up near the fibres. Each fibre is threaded into Teflon tubing for protection; Teflon was chosen as it remains flexible at the cold temperatures

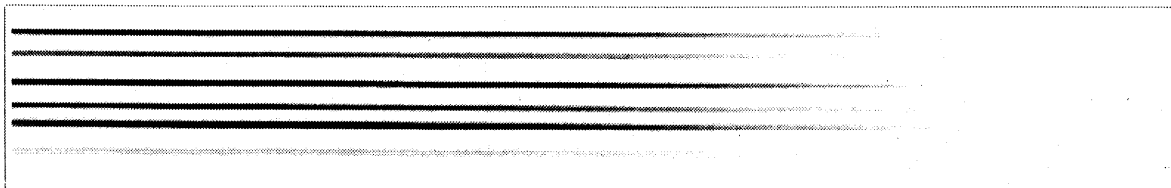


Figure 1. Raw CCD image taken with Nigel. Each horizontal line corresponds to the spectrum from one fibre; wavelength decreases to the right.

experienced at Dome C. Inside the AASTINO the tubes were bundled together and threaded into a rubber tube for further protection. The spectrograph end of the fibres is held in a brass connector. The connector is machined with six parallel and evenly spaced V-grooves. Each fibre was glued into a groove and cut flush with the edge of the connector. The resulting linear array of fibres forms a pseudo-slit to the spectrograph, with the spectrum from each fibre separated by about 20 pixels on the spectrograph. The fibre ends were hand-polished.

We used a commercial spectrometer (Jobin Yvon model CP200). The grating is concave holographic and produces a linear dispersion that varies from 24.6 nm/mm in the blue to 25.7 nm/mm in the red. With the 100 μm fibres, the resulting resolution is 2.5 nm full width half maximum. The 1024 \times 256 pixel CCD camera was an Andor unit supplied by Oriel Instruments (model Instaspec IV, open electrode) and is cooled by a single air-cooled Peltier stage. With a wavelength range of 250–900 nm spread across the 1024 pixel CCD camera, each resolution element is spread across about 4 pixels. The images on the CCD are saved in the FITS file format. Figure 1 shows a CCD image taken with Nigel; each horizontal line corresponds to the spectrum from one fibre, and the wavelength decreases to the right.

3.2. Control

Ultimate control over the operation of Nigel is by the “Supervisor” computer in the AASTINO. The Supervisor controls the power and heat in the AASTINO as well as the operation of various instruments and communications. Communications to the Supervisor from off-site are via the Iridium satellite network. Nigel has a separate PC104 computer to control the CCD. The two computers are connected via ethernet and communicate using the ERIC software package.¹³

The observing sequence of Nigel is controlled by a Perl script on the Supervisor that automatically starts each day by a crontab file. This script controls the frequency of exposures and the exposure times, depending on the azimuth and altitude of the Sun and Moon, and the phase of the Moon. If the Sun is in the field of view of a pair of fibres no exposure is taken. If the Moon is in the field, then exposures are taken every 15 minutes, otherwise every 3 hours. The number of exposures taken is limited by the storage capacity available, when compressed each FITS file is about 125 KBytes in size. If an exposure is to be taken, a shell script is started that communicates and controls the CCD computer, including cooling the CCD, setting the read out area and time and taking the exposure. All exposures are saved on the Supervisor and timestamped.

3.3. Calibration

3.3.1. Wavelength calibration

The wavelength scale of the spectrograph was initially calibrated using a domestic fluorescent light tube. The tube of a fluorescent light contains a rare gas (usually Argon) and a small amount of mercury. The tube is coated on the inside with phosphor. Typically a combination of three rare earth phosphors is used, emitting in the red (e.g. $\text{Y}_2\text{O}_3:\text{Eu}^{3+}$), green (e.g. $\text{CeMgAl}_{11}\text{O}_{19}:\text{Tb}^{3+}$, $\text{LaPO}_4:\text{Ce}^{3+},\text{Tb}^{3+}$, $\text{GdMgB}_5\text{O}_{10}:\text{Ce}^{3+},\text{Tb}^{3+}$) and blue (e.g. $\text{BaMgAl}_{10}\text{O}_{17}:\text{Eu}^{2+}$, $(\text{Sr},\text{Ba},\text{Ca})_5(\text{PO}_4)_3:\text{Eu}^{2+}$).^{14,15} Table 2 shows the nominal wavelengths and probable identifications of each fluorescent peak used for wavelength calibration.

Additional wavelength calibration was from known Fraunhofer absorption lines in daytime sky spectra. Figure 2 shows a fluorescent and daytime sky spectrum taken with Nigel, with the calibration lines marked.

Table 2. Probable identification of fluorescent lines¹⁶⁻¹⁹

Peak label	Nominal wavelength (nm)	Probable identification	Peak label	Nominal wavelength (nm)	Probable identification
a	405	Hg I	i	625	Tb IV $^5D_4 \rightarrow ^7F_3$
b	436	Hg I	j	631	Eu IV $^5D_0 \rightarrow ^7F_3$
c	488	Tb IV $^5D_4 \rightarrow ^7F_6$	k	651	Eu IV $^5D_0 \rightarrow ^7F_3$
d	544	Tb IV $^5D_4 \rightarrow ^7F_5$	l	662	?
	546	Hg I	m	688	Eu IV $^5D_0 \rightarrow ^7F_4$
e	588	Eu IV $^5D_0 \rightarrow ^7F_1$	n	694	Eu IV $^5D_0 \rightarrow ^7F_4$
f	594	Tb IV $^5D_4 \rightarrow ^7F_4$	o	708	?
g	599	Eu IV	p	742	Eu IV $^5D_0 \rightarrow ^7F_5$
h	611	Eu IV $^5D_0 \rightarrow ^7F_2$	q	809	Eu IV $^5D_0 \rightarrow ^7F_6$

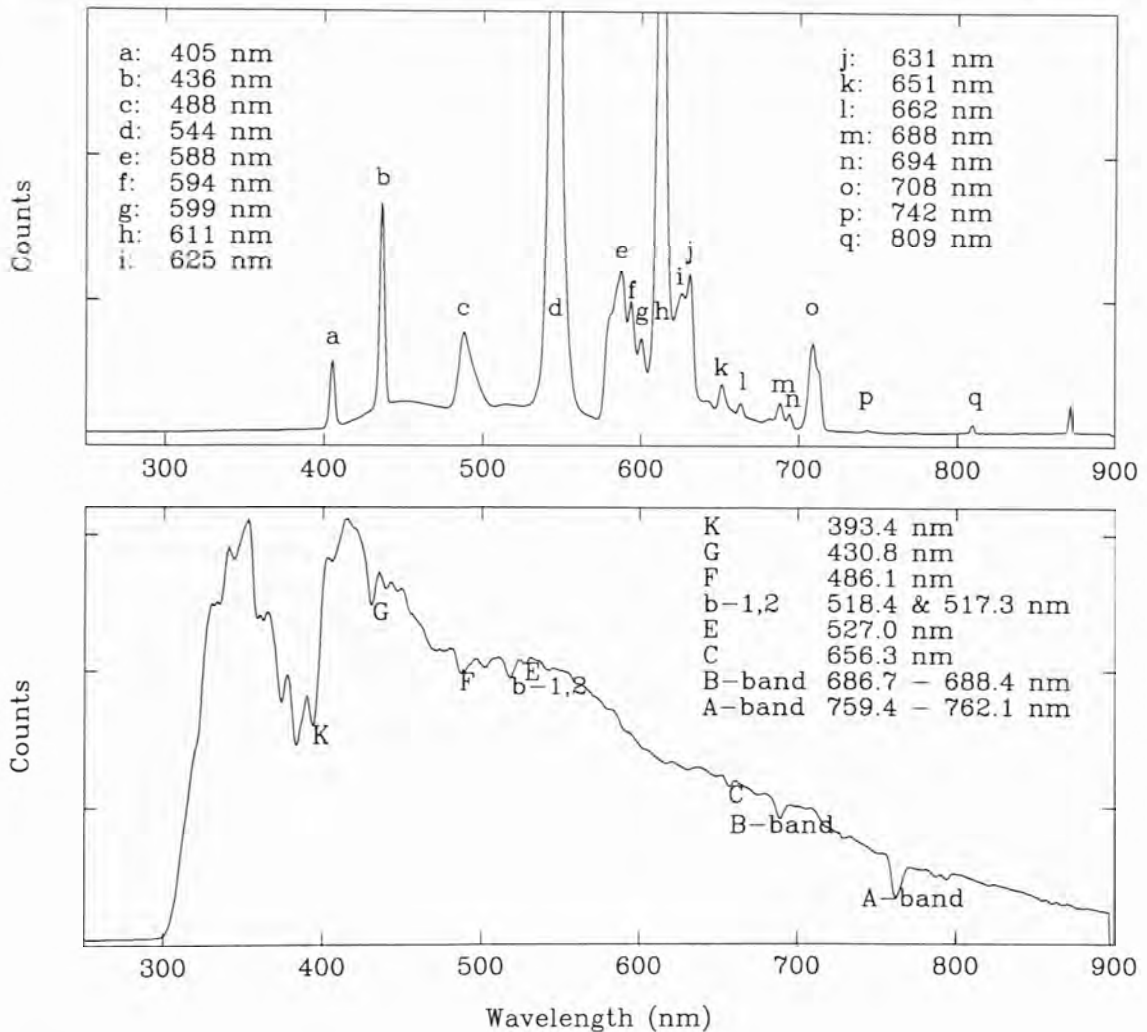


Figure 2. Spectrum of a compact fluorescent tube (top) and the daytime sky (bottom) showing the calibration wavelengths.

3.3.2. Flux calibration

To achieve an absolute flux calibration of Nigel we explored a method using light from a tungsten bulb reflected off a diffuse white surface.^{20,21} We also planned to use lunar spectra to check the flux calibration during the year, as the Moon would pass through the field of view of all but the zenith fibres on several occasions.

The idea behind the first method is to illuminate a Lambertian surface with a tungsten globe and observe the reflected light with the spectrograph. The spectral luminance (photons $\text{s}^{-1}\text{m}^{-2}\text{sr}^{-1}(\text{m})^{-1}$) of the Lambertian surface can be calculated from

$$B(\lambda, T) = a_f E(\lambda, T) \alpha(\lambda) \frac{1}{4\pi^2 L^2} \cos \theta, \quad (1)$$

where λ is the wavelength; T , a_f and $E(\lambda, T)$ are the temperature, area and spectral emittance of the filament; $\alpha(\lambda)$ is the albedo of the surface, L is the distance between the filament and the surface, and θ is the angle between the filament and the normal to the Lambertian surface. The temperature of the bulb is estimated from the known temperature-resistivity relationship for tungsten. The surface area of the filament is calculated from the power, total emissivity and temperature.

Because of the large wavelength range, we have to take into account light from wavelengths between 245 and 450 nm that will pass through the grating in the second order and contaminate the wavelength range 490 – 900 nm. To account for this we took calibration images with and without a 515 nm long-pass glass filter in front of the fibres.

Figures 3a and 3b show the response of the system to the illuminated Lambertian screen, unfiltered and filtered with a long-pass 515 nm filter, respectively. Figures 3c and 3d show the same data, but with the intensity axis zoomed in to show the behaviour at short wavelengths. These plots show that even in the filtered case, the intensity does not drop to zero at shorter wavelengths but has a pedestal of about 215 counts per second. This is probably caused by scattering within the spectrometer. On average this pedestal accounts for about 5×10^{-5} of the total flux recorded in a fibre, close to the expected stray light rejection ratio of 10^{-4} . We calculated the expected output from the tungsten globe using Equation (1), this spectrum is shown as the dashed line in Figures 3a and 3b.

After removing the scattered light contribution (assumed to be a constant 215 counts per second) from the measured spectra, we took the ratio between the measured response and the tungsten spectrum (see Figures 3e and 3f). Also plotted is the transmission expected from the quantum efficiency of the CCD²² convolved with the grating efficiency.²³ The system transmission we obtain for the “best” fibre agrees reasonably well both in shape and in absolute terms with the expected transmission at all wavelengths longer than about 500 nm. However, the absolute transmission of the other fibres is considerably less. This is probably because of bad coupling efficiency between the fibre ends and the grating, possibly a result of the polishing technique, or the fibre ends could have been damaged in transit.

As shown in Figure 3e, this technique of flux calibration becomes unreliable at short wavelengths because the flux radiated from the bulb is too weak and the response becomes dominated by scattered light. In addition, the glass bulb will be absorbing some UV light.²¹

Figure 4 shows the measured transmission of each fibre, divided by the transmission through the brightest fibre F_4 . Each ratio is fairly constant, showing that as a means of calibrating the transmission between each fibre, this method is quite useful.

3.3.3. Conclusions on calibration methods

We found that the incandescent bulb method can potentially be used for absolute flux calibration at visible and near infrared wavelengths. If delicate calibration standards cannot be taken into the field with the instrument, careful calibration could be carried out in a laboratory and this method could be used to check the calibrations in the field. Coupled with the wavelength calibration using a fluorescent bulb, this incandescent bulb method is a cheap and easy way to test the calibration. This technique could be improved by using a hotter filament in conjunction with a short-pass filter, although at very short wavelengths absorption of UV by the glass bulb becomes a problem.

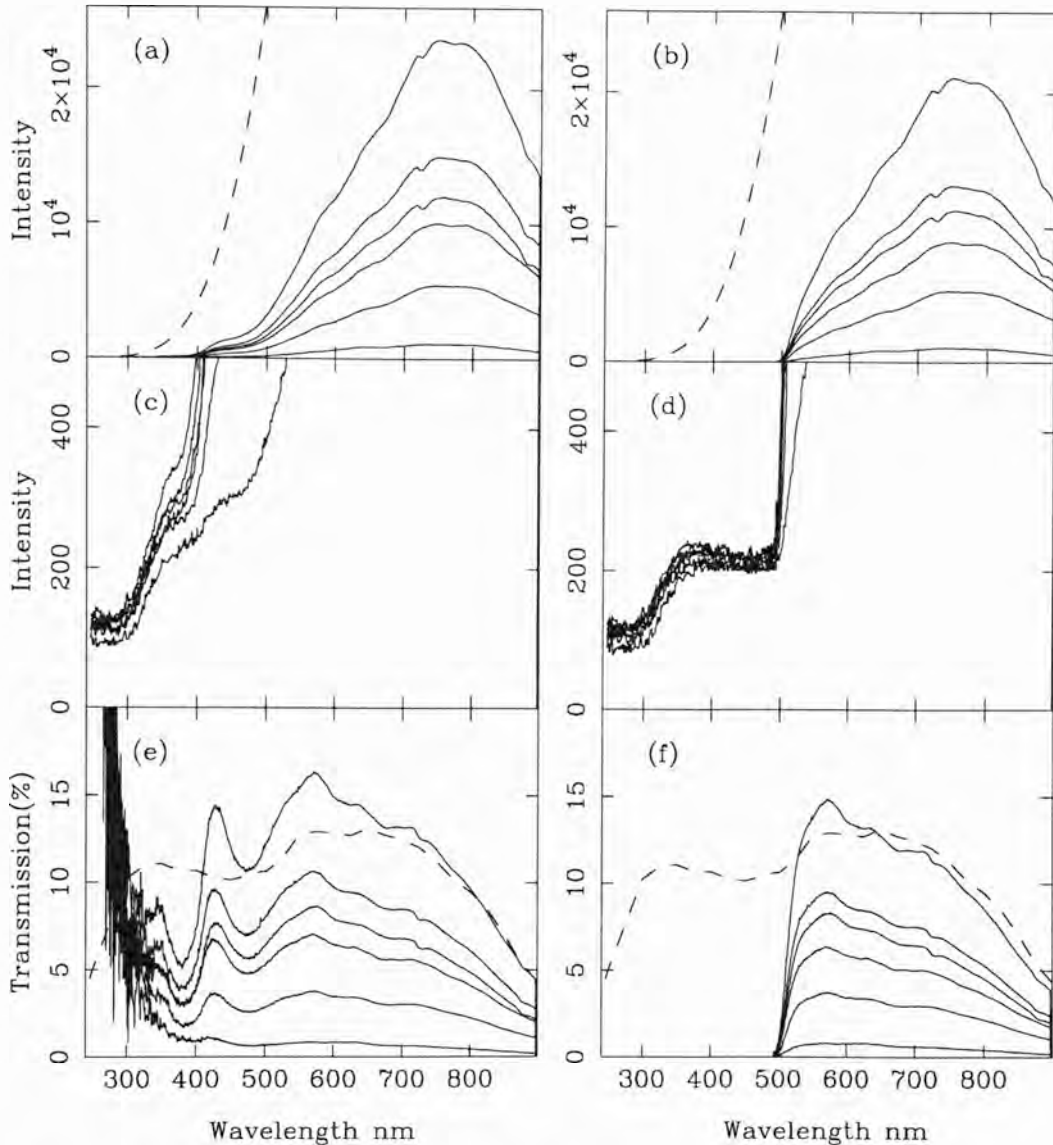


Figure 3. (a) Intensity as a function of wavelength for an exposure of the Lambertian screen without a filter and (b) with a 515 nm long-pass filter; the solid lines show the measured response through each of the six fibres and the dashed line shows the calculated emission from the tungsten filament. Plots (c) and (d) are the same, with the intensity axis zoomed in. Plots (e) and (f) show the ratio of the measured response to the tungsten spectrum, for the unfiltered and filtered set-ups, respectively. Also shown (dashed) is the expected quantum efficiency of the CCD convolved with the grating efficiency. In all cases the order of fibres from brightest is F_4 , F_2 , F_6 (red), then F_3 , F_5 and F_1 (blue).

4. DISCUSSION AND NIGEL'S PLANS FOR THE FUTURE

The large field of view (25°) of Nigel will mean that at times when the Galactic plane is passing through the field, the contribution from starlight will be comparatively large. This means that each measurement needs to be carefully analysed according to what part of the sky is being observed. In this respect Nigel is an ideal companion instrument to the Gattini-Sky Background (Gattini-SBC) and Gattini-All Sky cameras,²⁴ currently in operation at Dome C. The Gattini-SBC is designed to measure the optical sky brightness between the stars

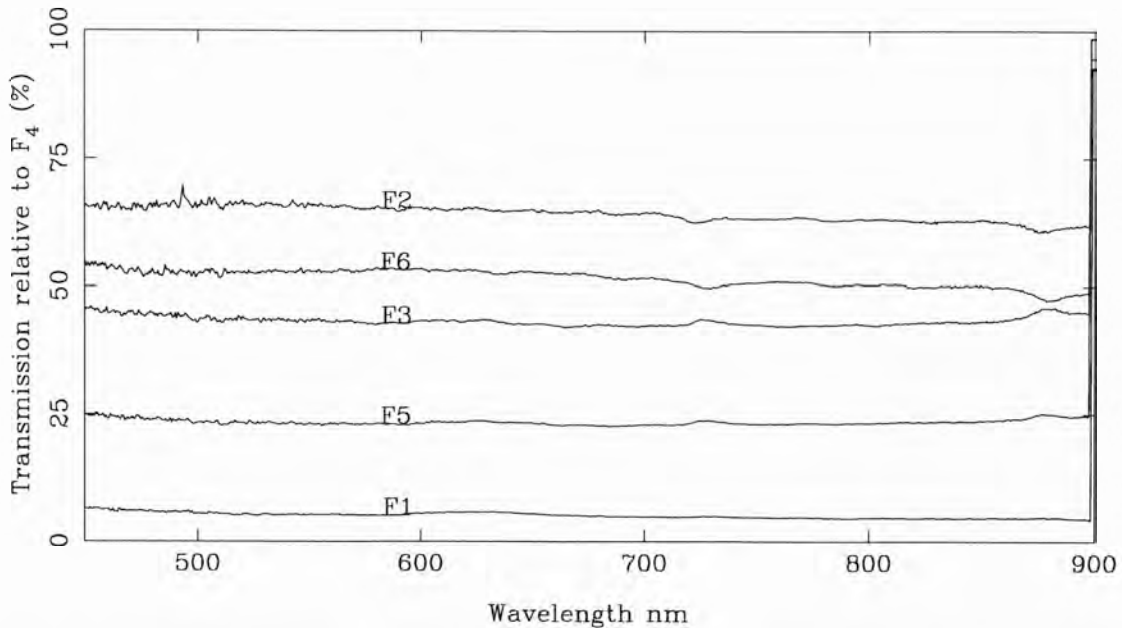


Figure 4. Measured transmission of each fibre relative to the brightest fibre (F_4). Most of the difference is probably due to coupling losses at the ends of the fibres.

in a 6° by 4° field centred on the South Pole. Gattini-SBC will also pick up auroral events, and combination of these data with spectra from Nigel would allow these events to be identified. Using the spectra from Nigel we may also be able to identify periods of cloud cover. Twilight spectra from Nigel will be useful for analysis of the profile of the atmosphere, and could be compared to similar measurements at ESO-Paranal.²⁵

Nigel was removed from Dome C during the summer 2005/2006 season and returned to Sydney. The instrument will be upgraded and sent to either Dome C for the 2007 winter or to Dome A for the 2008 winter. Before redeployment we plan to upgrade the fibres and connectors, and include an inline long-pass filter on each of the red fibres to eliminate second order contamination from the shorter wavelengths. We will also further improve the calibration system, including careful tests on the absolute flux calibration method outlined above. If the instrument is deployed to Dome A, we will need to ensure it is completely autonomous and may need to include a system to test the calibration throughout the year. Dome C is now manned all year around and the calibration could be regularly checked by the winterover person in charge of the site testing experiments. Before redeployment the upgraded Nigel will be tested at an observatory in Australia to test the response to the night sky brightness and to refine the data reduction process; in addition, we may test Nigel at another high latitude site to assess the response to aurorae.

ACKNOWLEDGMENTS

We would like to thank the Australian Research Council and the Australian Antarctic Division for financial support, and the French (IPEV) and Italian (PNRA) Antarctic programs for logistical support. We thank our colleagues from the University of Nice for their assistance when we were setting up the experiment at Dome C. SLK is supported by an Australian Postgraduate Award and by an Australian Antarctic Division top-up scholarship.

REFERENCES

1. J. W. V. Storey, M. C. B. Ashley, J. S. Lawrence, and M. G. Burton, "Dome C—the best astronomical site in the world?," *Mem. Soc. Astron. Ital. Suppl.* **2**, pp. 13–18, 2003.

2. J. S. Lawrence, M. C. B. Ashley, A. Tokovinin, and T. Travouillon, "Exceptional astronomical seeing conditions above Dome C in Antarctica," *Nature* **431**, pp. 278–281, 2004.
3. A. Agabi, E. Aristidi, M. Azouit, E. Fossat, F. Martin, T. Sadibekova, J. Vernin, and A. Ziad, "First whole atmosphere night-time seeing measurements at Dome C, Antarctica," *Publ. Astron. Soc. Pac.* **118**, pp. 344–348, 2006.
4. V. P. Walden, M. S. Town, B. Halter, and J. W. V. Storey, "First measurements of the infrared sky brightness at Dome C, Antarctica," *Publ. Astron. Soc. Pac.* **117**, pp. 300–308, 2005.
5. J. S. Lawrence, M. C. Ashley, and J. W. V. Storey, "A remote, autonomous laboratory for Antarctica with hybrid power generation," *Aust. Journal Elec. & Electronic Eng.* **2**, pp. 1–12, 2005.
6. C. Leinert, S. Bowyer, L. K. Haikala, M. S. Hanner, M. G. Hauser, A.-C. Levasseur-Regourd, I. Mann, K. Mattila, W. T. Reach, W. Schlosser, H. J. Staude, G. N. Toller, J. L. Weiland, J. L. Weinberg, and A. N. Witt, "The 1997 reference of diffuse night sky brightness," *Astron. Astrophys. Suppl. Ser.* **127**, pp. 1–99, 1998.
7. S. L. Kenyon and J. W. V. Storey, "A review of optical sky brightness and extinction at Dome C, Antarctica," *Publ. Astron. Soc. Pac.* **118**, p. 489, 2006.
8. E. Andrews, D. Jackson, A. Jefferson, S. Kim, J. Ogren, P. Sheridan, and J. Wendell, "Aerosols and radiation: Aerosol monitoring," in *CMDL Summary Report #27*, A. McComiskey, ed., pp. 58–66, CMDL, 2002–2003.
9. B. A. Bodhaine, "Aerosol absorption measurements at Barrow, Mauna Loa and the South Pole," *J. Geo. Res.* **100**, pp. 8967–8976, 1995.
10. F. E. Roach and J. L. Gordon, *The Light of the Night Sky*, D.Reidel Publishing Company, Dordrecht, Holland, 1973.
11. M. Boccas, M. C. B. Ashley, A. Phillips, A. Schinckel, and J. W. V. Storey, "Antarctic Fiber Optic Spectrometer," *Publ. Astron. Soc. Pac.* **110**, pp. 306–316, 1998.
12. J. T. Dempsey, J. W. V. Storey, M. C. B. Ashley, M. G. Burton, P. G. Calisse, and M. A. Jarnyk, "AFOS: probing the UV-visible potential of the Antarctic plateau," *Proc. SPIE* **5492**, pp. 811–821, 2004.
13. M. C. B. Ashley, P. W. Brooks, and J. P. Lloyd, "Remote control of astronomical instruments via the Internet," *Publ. Astron. Soc. Aust.* **13**, pp. 17–21, 1996.
14. A. Srivastava and T. Sommerer, "Fluorescent lamp phosphors," *The Electrochemical Society Interface* **7**, pp. 28–31, 1998.
15. Dejneka, M. J., et. al, "Rare earth-doped glass microbarcodes," *Publ. Natl. Acad. Sci USA* **100**, pp. 389–393, 2003.
16. G. Ofelt, "Structure of the f_6 configuration with application to rare-earth ions," *J. Chem. Phys.* **38**, pp. 2171–2180, 1963.
17. L. G. DeShazer and G. H. Dieke, "Spectra and energy levels of Eu^{3+} in LaCl_3 ," *J. Chem. Phys.* **38**, pp. 2190–2199, 1963.
18. L. Thompson, O. A. Serra, J. P. Riehl, F. S. Richardson, and R. W. Schwartz, "Emission spectra of $\text{Cs}_2\text{NaTbCl}_6$ and $\text{Cs}_2\text{NaYCl}_6: \text{Tb}^{3+}$," *Chem. Phys.* **26**, pp. 393–401, 1977.
19. J. Koningstein, "Energy levels and crystal-field calculations of europium and terbium in yttrium aluminum garnet," *Phys. Rev.* **136**, pp. A717–A725, 1964.
20. O. Harang and M. Kosch, "Absolute optical calibrations using a simple tungsten bulb: theory," *Sodankylä Geophysical Observatory Publications* **92**, pp. 121–123, 2003.
21. O. Harang, private communication, 2004.
22. Oriel Instruments, *Catalog, New Products for Light Research*, 1995.
23. Jobin Yvon, *CP 200 Technical Manual*, 1989.
24. A. Moore, E. Aristidi, M. C. B. Ashley, M. Candidi, J. Everett, S. L. Kenyon, J. S. Lawrence, A. Phillips, B. Le Rouxe, R. Ragazzonie, P. Salinarie, J. W. V. Storey, M. Taylor, and T. Travouillon, "The Gattini cameras for optical sky brightness measurements in Antarctica," *these proceedings*, 2006.
25. F. Patat, O. Ugolnikov, and O. Postlyako, "UBVRI twilight sky brightness at ESO-Paranal," *Astron. Astrophys.*, *in press*, 2006.

References

- Agabi, A., Aristidi, E., Azouit, M., Fossat, E., Martin, F., Sadibekova, T., Vernin, J., and Ziad, A. 2006, *PASP*, 118, 344
- Anderson, D. E. and Lloyd, S. A. 1990, *J. Geophys. Res.*, 95, 7429
- Angel, J. R. P., Lawrence, J. S., and Storey, J. W. 2004, in *Proc. SPIE*, Vol. 5382, pp 76–84
- Aristidi, E., Agabi, A., Azouit, M., Fossat, E., Martin, F., Sadibekova, T., Vernin, J., and Ziad, A. 2005a, *Acta Astron. Sinica Suppl.*, in press
- Aristidi, E., Agabi, A., Fossat, E., Azouit, M., Martin, F., Sadibekova, T., Travouillon, T., Vernin, J., and Ziad, A. 2005b, *A&A*, 444, 651
- Aristidi, E., Agabi, K., Azouit, M., Fossat, E., Vernin, J., Travouillon, T., Lawrence, J. S., Meyer, C., Storey, J. W. V., Halter, B., Roth, W. L., and Walden, V. 2005c, *A&A*, 430, 739
- Ashburn, E. V. 1952, *J. Geophys. Res.*, 57, 85
- Ashley, M. C. B., Brooks, P. W., and Lloyd, J. P. 1996, *PASA*, 13, 17
- Ashley, M. C. B., Burton, M. G., Calisse, P. G., Phillips, A., and Storey, J. W. V. 2005, *Highlights of Astronomy, ASP Conference Series*, 13, 936
- Avila, R., Vernin, J., Chun, M. R., and Sanchez, L. J. 2000, in *Proc. SPIE*, Vol. 4007, pp 721–732
- Avila, R., Vernin, J., and Sánchez, L. J. 2001, *A&A*, 369, 364
- Baldry, I. K. and Bland-Hawthorn, J. 2001, *MNRAS*, 322, 201

- Benn, C. R. and Ellison, S. L. 1998, Technical Report 115, *La Palma night sky brightness*.
Issac Newton Group, La Palma
- Boccas, M., Ashley, M. C. B., Phillips, A., Schinckel, A., and Storey, J. W. V. 1998,
PASP, 110, 306
- Bodhaine, B. A. 1995, *J. Geophys. Res.*, 100, 8967
- Bodhaine, B. A., Wood, N. B., Dutton, E. G., and Slusser, J. R. 1999, *J. Atmos. Ocean. Tech.*, 16, 1854
- Bondarenko, L. N. 1964, *Soviet Astron.*, 8, 299
- Briguglio, R., Cacciani, A., and Antonello, E. 2005, in *EAS Publ. Ser. 14, Dome C Astronomy and Astrophysics Meeting*, pp 313–320
- Burns, G. B., French, W. J. R., Greet, P. A., Phillips, F. A., Williams, P. F. B., Finlayson, K., and Klich, G. 2002, *J. Atmos. Terr. Phys.*, 64, 1167
- Burton, M. G., Lawrence, J. S., Ashley, M. C. B., Bailey, J. A., Blake, C., Bedding, T. R., Bland-Hawthorn, J., Bond, I. A., Glazebrook, K., Hidas, M. G., Lewis, G., Longmore, S. N., Maddison, S. T., Mattila, S., Minier, V., Ryder, S. D., Sharp, R., Smith, C. H., Storey, J. W. V., Tinney, C. G., Tuthill, P., Walsh, A. J., Walsh, W., Whiting, M., Wong, T., Woods, D., and Yock, P. C. M. 2005, *PASA*, 22, 199
- Calisse, P. G., Ashley, M. C. B., Burton, M. G., Phillips, M. A., Storey, J. W. V., Radford, S. J. E., and Peterson, J. B. 2004, *PASA*, 21, 256
- Candidi, M. and Lori, A. 2003, *Mem. Soc. Astron. Italiana*, 74, 29
- Chadid, M., Vernin, J., and Fossat, E. 2005, in *EAS Publ. Ser. 14, Dome C Astronomy and Astrophysics Meeting*, pp 281–284
- Cinzano, P. and Elvidge, C. D. 2004, *MNRAS*, 353, 1107
- Cinzano, P., Falchi, F., and Elvidge, C. D. 2001, *MNRAS*, 328, 689
- Collins, R. L., Bowman, K. P., and Gardner, C. S. 1993, *J. Geophys. Res.*, 98, 1001
- Coudé du Foresto, V., Absil, O., Barillot, M., and Swain, M. 2006, in *IAU Colloq. 200: Direct Imaging of Exoplanets: Science & Techniques*, pp 305–308

- Coulson, K. L. 1980, *Appl. Opt.*, 19, 3469
- Coulson, K. L. 1983, *Appl. Opt.*, 22, 1036
- Coulson, K. L. 1988, *Polarization and Intensity of Light in the Atmosphere*. A. Deepak Publishing, Hampton, Virginia USA
- Deeg, H. J., Belmonte, J. A., Alonso, R., Horne, K., Alsubai, K., and Doyle, L. R. 2005, in *EAS Publ. Ser. 14, Dome C Astronomy and Astrophysics Meeting*, pp 303–308
- Dejneka, M. J., Streltsov, A., Pal, S., Frutos, A. G., Powell, C. L., Yost, K., Yuen, P. K., Müller, U., and Lahiri, J. 2003, *Proc. Nat. Aca. Sci.*, 100, 389
- Delbouille, L., Neven, L., and Roland, C. 1973, *Photometric Atlas of the Solar Spectrum from 3000 to 10,000 Å*. Institut d'Astrophysique de l'Universite de Liege. Observatoire Royal de Belgique, Liege, Belgique
- Dempsey, J. T., Storey, J. W. V., and Ashley, M. C. B. 2003, *Mem. Soc. Astron. Italiana Suppl.*, 2, 70
- Dempsey, J. T., Storey, J. W. V., Ashley, M. C. B., Burton, M. G., Calisse, P. G., and Jarnyk, M. A. 2004, in *Proc. SPIE*, Vol. 5492, pp 811–821
- Dempsey, J. T., Storey, J. W. V., and Phillips, A. 2005, *PASA*, 22, 91
- Diets, R. S. 1948, *Popular Astronomy*, 56, 202
- Dravins, D., Lindegren, L., Mezey, E., and Young, A. T. 1997a, *PASP*, 109, 173
- Dravins, D., Lindegren, L., Mezey, E., and Young, A. T. 1997b, *PASP*, 109, 725
- Dravins, D., Lindegren, L., Mezey, E., and Young, A. T. 1998, *PASP*, 110, 610
- ESO Working Group 2003, in M. Sarazin, S. Ortolani, P. Casals, M. Beniston, and M. Quattri (eds.) *ESPAS Site Summary Series 1.2: Mauna Kea*, Garaching: ESO
- Fitch, B. W. and Coulson, K. L. 1983, *Appl. Opt.*, 22, 71
- Fossat, E. 2005, in M. Giard, F. Casoli, and F. Paletou (eds.) *EAS Publ. Ser. 14, Dome C Astronomy and Astrophysics Meeting*, pp 121–126
- Fried, D. L. 1965, *J. Opt. Soc. Am.*, 55, 1427

- Fried, D. L. 1966, *J. Opt. Soc. Am.*, 56, 1372
- Garcia, R. R. and Solomon, S. 1985, *J. Geophys. Res.*, 20, 3850
- Garstang, R. H. 1989a, *PASP*, 101, 306
- Garstang, R. H. 1989b, *ARA&A*, 27, 19
- Geissler, K. and Masciadri, E. 2006, *PASP*, 118, 1048
- Gilliland, R. L., Brown, T. M., Kjeldsen, H., McCarthy, J. K., Peri, M. L., Belmonte, J. A., Vidal, I., Cram, L. E., Palmer, J., Frandsen, S., Parthasarathy, M., Petro, L., Schneider, H., Stetson, P. B., and Weiss, W. W. 1993, *AJ*, 106, 2441
- Gillingham, P. R. 1991, *PASA*, 9, 55
- Gillingham, P. R. 1992, in G. Burns and M. Duldig (eds.) *ANARE Research Notes Number 88*, pp 290–292, Australian Antarctic Division
- Greenwood, D. P. 1977, *J. Opt. Soc. Am.*, 67, 390
- Harang, O., 2004, private communication
- Harang, O. and Kosch, M. 2003, *Sodankylä Geophysical Observatory Publications*, 92, 121
- Heasley, J. N., Janes, K., Labonte, B., Guenther, D., Mickey, D., and Demarque, P. 1996, *PASP*, 108, 385
- Herber, A., Gröschke, A., Vitale, V., and Strassmeier, K. 2006, *26th IAU Meeting, 22–23 August, 2006 in Prague, Czech Republic, Special Session 7*, abstract #34
- Holben, B. N., Tanré, D., Smirnov, A., Eck, T. F., Slutsker, I., Abuhassan, N., Newcomb, W. W., Schafer, J. S., Chatenet, B., Lavenu, F., Kaufman, Y. J., Castle, J. V., Setzer, A., Markham, B., Clark, D., Frouin, R., Halthore, R., Karneli, A., O'Neill, N. T., Pietras, C., Pinker, R. T., Voss, K., and Zibordi, G. 2001, *J. Geophys. Res.*, 106, 12067
- Hussain, N. S., Reddy, Y. P., and Buddhudu, S. 2002, *Materials Letters*, 53, 25
- Indermuehle, B. T., Burton, M. G., and Maddison, S. T. 2005, *PASA*, 22, 73

- Kalnay, E., Kanamitsu, M., Kistler, R., Collins, W., Deaven, D., Gandin, L., Iredell, M., Saha, S., White, G., Woollen, J., Zhu, Y., Leetmaa, A., Reynolds, B., Chelliah, M., Ebisuzaki, W., Higgins, W., Janowiak, J., Mo, K. C., Ropelewski, C., Wang, J., Jenne, R., and Joseph, D. 1996, *Bulletin American. Met. Soc.*, 77, 437
- Keeling, C. D. and Whorf, T. P. 2004, in *Trends: A Compendium of Data on Global Change*, Carbon Dioxide Information Analysis Center, Oak Ridge National Laboratory, U.S. Department of Energy, Oak Ridge, Tennessee, U.S.A.
- Kenyon, S. L., Ashley, M. C. B., Everett, J., Lawrence, J. S., and Storey, J. W. V. 2006a, in *Proc. SPIE*, Vol. 6267, p. 62671M
- Kenyon, S. L., Lawrence, J. S., Ashley, M. C. B., Storey, J. W. V., Tokovinin, A., and Fossat, E. 2006b, *PASP*, 118, 924
- Kenyon, S. L. and Storey, J. W. V. 2006, *PASP*, 118, 489
- Kolmogorov, A. N. 1941, *Doklady Akademii Nauk SSSR*, 30, 299
- Kolmogorov, A. N. 1991, *Royal Society of London Proceedings Series A*, 434, 9
- Koningstein, J. 1964, *Phys. Rev*, 136, A717
- Kornilov, V., Shatsky, N., and Voziakova, O. 2003a, *MASS Software User Guide*, version 2.04. Sternberg Astronomical Institute
- Kornilov, V., Tokovinin, A. A., Vozyakova, O., Zaitsev, A., Shatsky, N., Potanin, S. F., and Sarazin, M. S. 2003b, in *Proc. SPIE*, Vol. 4839, pp 837–845
- Kosch, M. J., Mäkinen, S., Sigernes, F., and Harang, O. 2003, in *30th Annual European Meeting on Atmospheric Studies by Optical Methods*, Norway
- Krause-Polstorff, J., Murphy, E. A., and Walters, D. L. 1993, *Appl. Opt.*, 32, 4051
- Krisciunas, K. and Schaefer, B. E. 1991, *PASP*, 103, 1033
- Lane, A. P. 1998, in *ASP Conf. Ser. 141: Astrophysics From Antarctica*, p. 289
- Lane, B. F. and Muterspaugh, M. W. 2004, *ApJ*, 601, 1129
- Lawrence, J. S. 2004, *Appl. Opt.*, 43, 1435

- Lawrence, J. S., Ashley, M. C., Kenyon, S. L., Storey, J. W. V., Tokovinin, A. A., Lloyd, J. P., and Swain, M. R. 2004, in *Proc. SPIE*, Vol. 5489, pp 174–179
- Lawrence, J. S., Ashley, M. C., and Storey, J. W. V. 2005, *Aust. J. Elec. & Electronic Eng.*, 2, 1
- Lawrence, J. S., Ashley, M. C. B., Bonner, C. S., Bradley, S., Luong-Van, D., and Storey, J. W. V. 2006a, in *EAS Publ. Ser.*, *in press*, Roscoff, France
- Lawrence, J. S., Ashley, M. C. B., Burton, M. G., Calisse, P. G., Dempsey, J. T., Everett, J. R., Maher, O., Storey, J. W. V., and Travouillon, T. 2003, *Mem. Soc. Astron. Italiana Suppl.*, 2, 217
- Lawrence, J. S., Ashley, M. C. B., Burton, M. G., Cui, X., Everett, J. R., Indermuehle, B. T., Kenyon, S. L., Luong-Van, D., Moore, A. M., Storey, J. W. V., Tokovinin, A., Travouillon, T., Pennypacker, C., Wang, L., and York, D. 2006b, in *Proc. SPIE*, Vol. 6267, p. 62671L
- Lawrence, J. S., Ashley, M. C. B., Tokovinin, A., and Travouillon, T. 2004, *Nature*, 431, 278
- Le Texier, H., Solomon, S., and Garcia, R. R. 1987, *Planet. Space Sci.*, 35, 977
- Leinert, C., Bowyer, S., Haikala, L. K., Hanner, M. S., Hauser, M. G., Lvasseur-Regourd, A.-C., Mann, I., Mattila, K., Reach, W. T., Schlosser, W., Staude, H. J., Toller, G. N., Weiland, J. L., Weinberg, J. L., and Witt, A. N. 1998, *A&AS*, 127, 1
- Lide, D. R. and Frederikse, H. P. R. (eds.) 1995–1996, *CRC Handbook of Chemistry and Physics*, 76th edition. CRC Press, Boca Raton, Florida, USA
- Lloyd, J. P. 2004, in *Proc. SPIE*, Vol. 5491, pp 190–198
- Lloyd, J. P., Lane, B. F., Swain, M. R., Storey, J. W., Travouillon, T., Traub, W. A., and Walker, C. K. 2003, in *Proc. SPIE*, Vol. 5170, pp 193–199
- Lloyd, J. P., Oppenheimer, B. R., and Graham, J. R. 2002, *PASA*, 19, 318
- Marks, R. D., Vernin, J., Azouit, M., Manigault, J. F., and Clevelin, C. 1999, *A&AS*, 134, 161

- Masciadri, E., Feldt, M., and Hippler, S. 2004, *ApJ*, 613, 572
- Massey, P. and Foltz, C. B. 2000, *PASP*, 112, 566
- McComiskey, A., Andrews, E., Jackson, D., Jefferson, A., Kim, S., Ogren, J., Sheridan, P., and Wendell, J. 2002-2003, in *CMDL Summary Report #27*, pp 58–66, Climate Monitoring and Diagnostics Laboratory, National Oceanic and Atmospheric Administration
- McDade, I. C., Murtagh, D. P., Greer, R. G. H., Dickinson, P. H. G., Witt, G., Stegman, J., Llewellyn, E. J., Thomas, L., and Jenkins, D. B. 1986, *Planet. Space Sci.*, 34, 789
- McEwan, M. J. and Phillips, L. F. 1975, *Chemistry of the Atmosphere*. Edward Arnold, London
- Midya, S. K. and Midya, D. 1993, *Earth Moon and Planets*, 61, 175
- Moore, A., Aristidi, E., Ashley, M., Busso, M., Candidi, M., Everett, J., Kenyon, S., Lawrence, J., Luong-Van, D., Phillips, A., Le Roux, B., Ragazzoni, R., Salinari, P., Storey, J., Taylor, M., Tosti, G., and Travouillon, T. 2006b, in *Proc. SPIE*, Vol. 6269, p. 62695U
- Moore, A., Aristidi, E., Ashley, M., Busso, M., Candidi, M., Everett, J., Kenyon, S., Lawrence, J., Luong-Van, D., Phillips, A., Le Roux, B., Ragazzoni, R., Salinari, P., Storey, J., Taylor, M., Tosti, G., and Travouillon, T. 2006a, in *Proc. SPIE*, Vol. 6267, p. 62671N
- Morrison, D., Murphy, R. E., Cruikshank, D. P., Sinton, W. M., and Martin, T. Z. 1973, *PASP*, 85, 255
- Mosser, B. and Aristidi, E. 2007, *PASP*, 119, 127
- Ng, S. L., Lam, Y. L., Zhou, Y., Ooi, B. S., Kam, C. H., Wong, K. S., Rambabu, U., and Buddhudu, S. 2000, *J. Mat. Sci. Lett.*, 19, 495
- NIST, Web site accessed 2006, *NIST Atomic Spectra Database Lines Form*, <http://physics.nist.gov/PhysRefData/ASD/lines.form.html>, National Institute of Standards and Technology, Physics Laboratory

- Ofelt, G. 1963, *J. Chem. Phys.*, 38, 2171
- Ougolnikov, O. and Maslov, I. 2003, in *Proc. SPIE*, Vol. 5026, pp 219–231
- Ougolnikov, O. S. 1999, *Cosmological Research*, 37, 159
- Patat, F. 2003, *A&A*, 400, 1183
- Patat, F., 2004, *Hints and tricks for observing in brighttime*, ESO Messenger, 118, 11
- Patat, F., Ugolnikov, O. S., and Postylyakov, O. V. 2006, *A&A*, 455, 385
- Pavlov, V., Egorova, L., Kardopolov, V., Rspaev, F., and Ukhinov, S. 1995, *Atmos. Ocean. Phys.*, 30, 449
- Phillips, A., Burton, M. G., Ashley, M. C. B., Storey, J. W. V., Lloyd, J. P., Harper, D. A., and Bally, J. 1999, *ApJ*, 527, 1009
- Phillips, R. R., Naylor, D. A., Knee, L. B., Dahl, R. E., and Sirbu, D. 2006, *26th IAU Meeting, 22–23 August, 2006 in Prague, Czech Republic, Special Session 7*, abstract #14
- Pomozi, I., Horvath, G., and Wehner, R. 2001, *J. Exp. Bio*, 204, 2933
- Postylyakov, O. V., Ugolnikov, O. S., Maslov, I. A., and Sidorchuk, A. A. 2003, *EGS-AGU-EUG Joint Assembly, Abstracts from the meeting held in Nice, France, 6–11 April 2003*, p. 13842
- Ratnam, V. M., Shen, C. M., Chen, W. N., and Nee, d. J. B. 2004, *J. Atmos. Solar-Terr. Phys.*, 66, 209
- Rayleigh, L. 1928, *Royal Society of London Proceedings Series A*, 119, 11
- Richardson, L. F. 1922, *Weather Prediction by Numerical Processes*. Cambridge University Press
- Roach, F. E. and Gordon, J. L. 1973, *The Light of the Night Sky*. D.Reidel Publishing Company, Dordrescht, Holland
- Roddier, F. 1981, in *Progress in optics. Volume 19. Amsterdam, North-Holland Publishing Co.*, pp 281–376

- Roddier, F., Gilli, J. M., and Lund, G. 1982a, *J. Optics*, 13, 263
- Roddier, F., Gilli, J. M., and Vernin, J. 1982b, *J. Optics*, 13, 63
- Rozenberg, G. 1966, *Twilight, A Study in Atmospheric Optics*. Plenum Press, New York
- Satoh, Y., Najafov, H., Ohshio, S., and Saitoh, H. 2005, *Azajomo Journal of Materials Online*, 1, 1
- Shao, M. and Colavita, M. M. 1992, *A&A*, 262, 353
- Sivjee, G., Azeem, S., and Emery, B. A., Web site accessed 2005, *South Pole Michelson Interferometer*, <http://cedarweb.hao.ucar.edu>, CEDARweb, University Corporation for Atmospheric Research
- Six, D., Fily, M., Blarel, L., and Goloub, P. 2005, *Atmospheric Environment*, 39, 5041
- Skidmore, W., Travouillon, T., and Riddle, R. 2006, in *Proc. SPIE*, Vol. 6267, p. 62671Z
- Sozzetti, A. 2005, *PASP*, 117, 1021
- Srivastava, A. and Sommerer, T. 1998, *The Electrochemical Society Interface*, 7, 28
- Sterner, R., Web site accessed 2006, *Liege Solar Spectral Atlas*, <http://fermi.jhuapl.edu/liege/intro.html>, John Hopkins University Applied Physics Laboratory
- Storey, J. W. V., Angel, R., Lawrence, J., Hinz, P., Ashley, M. C. B., and Burton, M. G. 2006, in *Proc. SPIE*, Vol. 6267, p. 62671E
- Storey, J. W. V., Ashley, M. C. B., Burton, M. G., and Lawrence, J. S. 2005, in M. Giard, F. Casoli, and F. Paletou (eds.) *EAS Publ. Ser. 14, Dome C Astronomy and Astrophysics Meeting*, pp 7–12
- Storey, J. W. V., Ashley, M. C. B., Lawrence, J. S., and Burton, M. G. 2003, *Mem. Soc. Astron. Italiana Suppl.*, 2, 13
- Swain, M. R., Coude du Foresto, V., Fossat, E., and Vakili, F. 2003, *Mem. Soc. Astron. Italiana Suppl.*, 2, 207

- Swain, M. R., Walker, C. K., Traub, W. A., Storey, J. W. V., Coude Du Foresto, V., Fossat, E., Vakili, F., Stark, A. A., Lloyd, J. P., Lawson, P. R., Burrows, A. S., Ireland, M., Millan-Gabet, R., van Belle, G. T., Lane, B. F., Vasisht, G., and Travouillon, T. 2004, in *Proc. SPIE*, Vol. 5491, p. 176
- Tatarski, V. I. 1961, *Wave Propagation in a Turbulent Medium*. McGraw-Hill, New York
- Thompson, L., Serra, O. A., Riehl, J. P., Richardson, F. S., and Schwartz, R. W. 1977, *Chem. Phys.*, 26, 393
- Tokovinin, A., Baumont, S., and Vasquez, J. 2003a, *MNRAS*, 340, 52
- Tokovinin, A. and Kornilov, V. 2002, in *ASP Conf. Ser. 266: Astronomical Site Evaluation in the Visible and Radio Range*, p. 104
- Tokovinin, A., Kornilov, V., Shatsky, N., and Voziakova, O. 2003b, *MNRAS*, 343, 891
- Tokovinin, A. and Travouillon, T. 2006, *MNRAS*, 365, 1235
- Tomasi, C., Vitale, V., Petkov, B., Lupi, A., and Cacciari, A. 2005, *Appl. Opt.*, 44, 3320
- Travouillon, T. 2004, PhD thesis, University of New South Wales
- Travouillon, T. 2005, in *EAS Publ. Ser. 14, Dome C Astronomy and Astrophysics Meeting*, pp 31–36
- Travouillon, T., Ashley, M. C. B., Burton, M. G., Lawrence, J., and Storey, J. W. V. 2003a, *Mem. Soc. Astron. Italiana Suppl.*, 2, 150
- Travouillon, T., Ashley, M. C. B., Burton, M. G., Storey, J. W. V., and Loewenstein, R. F. 2003b, *A&A*, 400, 1163
- Ugolnikov, O. S., Postlyakov, O. V., and Maslov, I. A. 2004, *J. Quant. Spec. Radiat. Transf.*, 88, 233
- Vakili, F., Belu, A., Aristidi, E., Fossat, E., Maillard, A., Abe, L., Agabi, K., Vernin, J., Baptiste Daban, J., Hertmanni, W., Schmider, F.-X., Assus, P., Coude Du Foresto, V., and Swain, M. R. 2004, in *Proc. SPIE*, Vol. 5491, p. 1580
- Valenziano, L. and dall'Oglio, G. 1999, *PASA*, 16, 167

- Vernin, J., Chadid-Vernin, M., Aristidi, E., Trinquet, H., and Sadibekova, T. 2006. in *26th IAU Meeting, 22-23 August, 2006 in Prague, Czech Republic, Special Session 7*. Vol. abstract #8
- Walden, V. P., Town, M. S., Halter, B., and Storey, J. W. V. 2005, *PASP*, 117, 300
- Walker, M. F. 1988, *PASP*, 100, 496
- Wang, Q. M. and Yan, B. 2005, *Applied Organometallic Chemistry*, 19, 952
- Wendler, G., Stearns, C., Weidner, G., Dargaud, G., and Parish, T. 1997. *J. Geophys. Res.*, 102, 4463
- Yee, J.-H., Crowley, G., Roble, R. G., Skinner, W. R., Burrage, M. D., and Hays, P. B. 1997, *J. Geophys. Res.*, 102, 19949
- Yura, H. T. and McKinley, W. G. 1983, *Appl. Opt.*, 22, 3353
- Zaragoza, G., Taylor, F., and López-Puertas, M. 2001, *J. Geophys. Res.*, 106, 8027

